TECHNISCHE UNIVERSITÄT MÜNCHEN
Physik-Department
Institut für Theoretische Physik
Lehrstuhl Univ.-Prof. Dr. Peter Vogl

Theory of the Electronic Structure of Quantum Dots in External Fields

Thomas Eißfeller

Vollständiger Abdruck der von der Fakultät für Physik der Technischen Universität München zur Erlangung des akademischen Grades eines

Doktors der Naturwissenschaften (Dr. rer. nat.)

genehmigten Dissertation.

Vorsitzender:	Univ.-Prof. Jonathan J. Finley, Ph.D.
Prüfer der Dissertation:	1. Univ.-Prof. Dr. Peter Vogl 2. Univ.-Prof. Paolo Lugli, Ph.D.

Die Dissertation wurde am 05.07.2012 bei der Technischen Universität München eingereicht und durch die Fakultät für Physik am 17.09.2012 angenommen.

1. Auflage Oktober 2012

Titelbild: Electrical g-factor tuning in In-dilute InGaAs/GaAs quantum dots

(left) Independent components of the hole g-tensor as functions of an external vertical electric field for an In-dilute quantum dot with a height of 6 nm above a 2 nm wetting layer, a diameter of 24 nm and an In-concentration at the apex of 35%. The g-factors of the principal axes *[001]*, *[110]*, and *[1$\underline{1}$0]* of the g-tensor are denoted by g_{001} (solid red line), g_{110} (solid black line), and $g_{1\underline{1}0}$ (dashed black line), respectively.

(right) Schematic illustration of the two orthogonal precession axes Ω_1 and Ω_2 for a vertical electric field of -24 kV/cm and 24 kV/cm, respectively, and a magnetic field **B** in the *[111]* direction. The red arrow indicates an exemplary spin precessing around the Ω_1 axis.

Druck: Printy Digitaldruck, München (http://www.printy.de)

ISBN: 978-3-941650-46-6

Contents

Introduction and Motivation **xi**

I Model 1

1 Review of the continuum model of semiconductor heterostructures 3
1.1 Introduction . . . 3
1.2 Luttinger-Kohn $k \cdot p$ theory . . . 3
1.2.1 Bloch's theorem . . . 4
1.2.2 Luttinger-Kohn representation . . . 4
1.2.3 Luttinger-Kohn Hamiltonian . . . 5
1.2.4 Envelope function theory . . . 6
1.2.5 Luttinger-Kohn momentum operator . . . 6
1.2.6 Loewdin's perturbation theory . . . 7
1.2.7 Momentum operator in Loewdin's basis . . . 10
1.3 Linear optical response theory . . . 11
1.4 Continuum strain . . . 13
1.5 Piezoelectric effect . . . 15

2 New derivation of the zincblende multi-band $k \cdot p$-Hamiltonian 17
2.1 Introduction . . . 17
2.2 Review of symmetry properties of the zincblende Hamiltonian . . . 18
2.2.1 Irreducible representations of T_d . . . 18
2.2.2 Luttinger-Kohn Hamiltonian in T_d symmetry . . . 19
2.3 Derivation of the second-order $k \cdot p$ Hamiltonian . . . 20
2.3.1 Review of the first-order extended Kane model . . . 20
2.3.2 Operator ordering in the envelope function approximation . . . 24
2.3.3 Coupling of the free electron spin to a magnetic field . . . 26
2.3.4 Perturbative coupling to remote bands . . . 27
2.4 Linear response theory of the g-tensor . . . 29
2.5 Relation to $k \cdot p$ models with fewer bands . . . 33
2.5.1 The eight-band model . . . 33
2.5.2 The single-band model of the conduction band . . . 34

2.5.3 The six-band model of the valence band . . . 35
2.6 Cartesian representation of the $k \cdot p$ Hamiltonian . . . 35
2.7 Material parameters of the $k \cdot p$ Hamiltonian . . . 39
2.7.1 Elliptic parameter sets . . . 39
2.7.2 Temperature dependency . . . 39
2.7.3 Interpolation of ternary alloys . . . 40
2.8 Rotations of the $k \cdot p$ Hamiltonian . . . 40

3 Novel Symmetry Adapted Finite Element method (SAFE) 43
3.1 Introduction . . . 43
3.2 Method . . . 44
3.2.1 The problem: spurious solutions in discrete effective mass theory 44
3.2.2 The solution: the SAFE method . . . 45
3.2.3 SAFE method for eight- and 14-band Hamiltonians . . . 48
3.2.4 Gauge-invariant SAFE method for magnetic fields . . . 50
3.3 Results . . . 53
3.4 Summary . . . 55

4 Concrete numerical implementation 57
4.1 Introduction . . . 57
4.2 Implementation of the finite element method . . . 57
4.2.1 Finite element space . . . 58
4.2.2 Isoparametric finite elements . . . 62
4.2.3 Efficient implementation . . . 63
4.2.4 Hermite finite elements . . . 65
4.2.5 Boundary conditions . . . 66
4.3 Solution of linear systems of equations . . . 67
4.4 Solution of eigenvalue problems . . . 69

II Results 71

5 New insights to the symmetry lifting in InGaAs/GaAs quantum dots 73
5.1 Introduction . . . 73
5.2 Method . . . 76
5.3 Results and discussion . . . 78
5.3.1 p-Level splitting . . . 78
5.3.2 Shape anisotropy . . . 81
5.3.3 Sign of the piezoelectric potential . . . 83
5.4 Summary . . . 87

6 Prediction of strong electrical g-Factor tuning in In-dilute quantum dots 89
6.1 Introduction . . . 89
6.2 Method . . . 90
6.2.1 Electron-hole Coulomb interaction . . . 91
6.2.2 Sign convention of the g-factor . . . 92
6.2.3 Valence band g-factor anisotropy . . . 94
6.3 Results and discussion . . . 94
6.3.1 E-Field dependence of the exciton g-factor . . . 94
6.3.2 Orbital angular momentum quenching . . . 96
6.3.3 Universal single-qubit gate . . . 99
6.4 Summary . . . 101

7 Explanation of the non-linear Zeeman splitting in large quantum dots 103
7.1 Introduction . . . 103
7.2 Model . . . 105
7.3 Results and discussion . . . 106
7.3.1 Non-linear Zeeman splitting . . . 106
7.3.2 Degree of polarization . . . 111
7.4 Summary . . . 113

III Appendices 115

A Continuum limit of the gauge-invariant SAFE method 117

B Angular momentum matrices of T_d 119

C Material parameters of InGaAs 121

D Term rewriting system 123
D.1 Definition of the TRS . . . 123
D.2 Application of the TRS . . . 127
D.3 Optimization of the discretization . . . 128

List of publications 129

Acknowledgments 131

Abstract

In the first part of this work, we propose two significant improvements of the $k \cdot p$ envelope function approach for mesoscopic semiconductor heterostructures. Firstly, we present the novel symmetry adapted finite element (SAFE) approach for multi-band $\mathbf{k} \cdot \mathbf{p}$ envelope function Hamiltonians that is manifestly free from spurious solutions which plague mesoscopic electronic structure calculations. We show that these spurious solutions originate in the ill-representation of first-order derivatives in real-space bases and resolve this issue by a particular choice of real-space basis functions. In addition, a gauge-invariant extension to this method is developed for problems involving magnetic fields. We predict the electrical exciton g-factor tuning in single InGaAs/GaAs embedded quantum dots to be significantly larger than previously found. Secondly, we newly derive an eight- and 14-band envelope function Hamiltonian for zincblende-type crystals that, in contrast to previous work, preserves the correct operator ordering for *all* relevant remote-band contributions. This leads to a correct formulation of the envelope function momentum and angular momentum operator derived from the Hamiltonian via the Hellmann-Feynman theorem. In particular, the latter gives rise to the perturbative computation of the g-tensor in linear response theory *without* including the magnetic vector potential explicitly in the Hamiltonian. This circumvents the practical issues of gauge-invariant discretization and is in excellent agreement with the fully detailed non-perturbative calculations for low magnetic fields.

In the second part, we apply our novel methods to overgrown self-assembled InGaAs/GaAs quantum dots, where we first clarify the still controversial origin of the lifting of C_{4v} symmetry on the basis of the electronic p-level splitting. In contrast to previous theoretical work, our calculations reveal that for a realistic graded In:Ga-profile the linear piezoelectric effect contributes dominantly to this splitting in excellent agreement with experiment while the quadratic piezoelectric effect and inversion asymmetry play only a minor role. A previously proposed elongation of the dots combined with the piezoelectric effect is demonstrated to be incompatible with experiment. Next, strong electrically tunable exciton g-factors are predicted in individual quantum dots and the microscopic origin of the effect is explained. Realistic eight-band $\mathbf{k} \cdot \mathbf{p}$ simulations quantitatively account for the observations, simultaneously reproducing the exciton transition energy and g-factor tunability for model dots with the measured size and a comparatively low In-composition of $x_{In} \sim 35\%$ near

the dot apex. We show that the observed g-factor tunability is dominated by the *hole*, the electron contributing only weakly. The electric field-induced perturbation of the *hole* wave function is shown to impact upon the g-factor via orbital angular momentum quenching, the change of the In:Ga composition inside the envelope function and the mixing of heavy hole and light hole bands playing no substantial role. Our results provide the design for a universal single qubit gate via purely electrical g-tensor modulation. Finally, the microscopic origin of the non-linear Zeeman splitting of neutral excitons in large In-dilute quantum dots is explained. Eight-band $\mathbf{k}\cdot\mathbf{p}$ simulations, performed using realistic dot parameters extracted from cross-sectional scanning tunneling microscopy measurements, reveal that a quadratic contribution to the Zeeman energy originates from a spin-dependent mixing of heavy and light hole orbital states in the dot in sharp contrast to the electrical g-tensor tuning. The dilute In-composition ($x < 0.4$) and large lateral size ($40 - 50$ nm) of the quantum dots investigated is shown to strongly enhance the non-linear contribution to the excitonic Zeeman gap, providing a method to control such magnetic non-linearities via growth engineering of the quantum dots.

Zusammenfassung

Im ersten Teil dieser Arbeit schlagen wir zwei bedeutende Weiterentwicklungen des Ansatzes der einhüllenden Funktion in der $k \cdot p$ Näherung für mesoskopische Halbleiterheterostrukturen vor. Zuerst stellen wir die neuentwickelte symmetryangepasste finite Elementemethode (SAFE) für den Mehrband-$k \cdot p$-Hamilton Operatoren der Einhüllenden vor. Diese Methode ist von Natur aus frei von unphysikalischen Lösungen, die mesoskopische elektronischen Strukturrechnungen erschweren oder sogar unmöglich machen. Wir zeigen, dass diese unphysikalischen Lösungen ihren Ursprung in der fehlerhaften Darstellung erster Ableitungen in Ortsraumbasen haben, und lösen dieses Problem durch eine spezielle Wahl von Basisfunktionen im Ortsraum. Darüberhinaus wird eine eichinvariante Erweiterung dieser Methode in der Anwesenheit von Magnetfeldern entwickelt. Wir sagen voraus, dass die Änderung des Exzitonen-g-Tensors durch elektrische Steuerung in einzelnen überwachsenen InGaAs/GaAs-Quantenpunkten deutlich höher ist als zuvor mit herkömmlichen Methoden berechnet. Zweitens leiten wir erstmals einen Acht- und 14-Band-Hamilton Operator der einhüllenden Funktion für zinkblendeartige Kristalle her, der im Gegensatz zu früheren Arbeiten die korrekte Anordnung von Differentialoperatoren für *alle* relevanten Beiträge entfernter Bänder berücksichtigt. Dies führt zu einer korrekten Darstellung des Impuls- und Drehimpulsoperators, die sich über das Hellmann-Feynman Theorem aus dem Hamilton Operator ergeben. Insbesondere ermöglicht dies die perturbative Berechnung des g-Tensors in linearer Antworttheorie, ohne dass ein magnetisches Vektorpotential direkt in den Hamilton Operator eingeht. Dies umgeht die Komplikationen einer eichinvarianten Diskretisierung und liefert Ergebnisse, die für niedrige Magnetfelder hervorragend mit denen einer vollen nichtperturbativen Rechnungen übereinstimmen.

Im zweiten Teil wenden wir diese neuartigen Methoden auf selbstorganisierte InGaAs/GaAs-Quantenpunkte an. Als erstes klären wir den Ursprung der C_{4v} Symmetriebrechung – der in der Literatur noch immer kontroverse diskutiert wird – an Hand der Aufspaltung der elektronischen p-Niveaus. Im Gegensatz zu früheren theoretischen Arbeiten zeigen unsere Rechnungen, dass für ein realistisches abgestuftes In:Ga-Profil der lineare piezoelektrische Effekt den dominanten Beitrag in hervorragender Übereinstimmung mit Experimenten liefert. Der quadratische piezoelektrische Effekt und die fehlende Inversionssymmetrie tragen nur geringfügig bei. Eine zuvor vorgeschlagene Streckung der Quantenpunkte hingegen führt, kombiniert mit dem

piezoelektrischen Effekt, zu einer Aufspaltung, die mit den Experimenten nicht vereinbar ist. Als nächstes sagen wir eine ausgeprägte elektrisch gesteuerte Änderung des Exzitonen-g-Faktors in einzelnen Quantenpunkten voraus und klären den mikroskopischen Ursprung dieses Effekts. Realistische Achtband-$\mathbf{k}\cdot\mathbf{p}$-Rechnungen ergeben gleichzeitig die im Experiment beobachtete Exzitonenenergie und die Änderung des g-Faktor für Quantenpunkte mit den experimentell gemessenen Ausmaßen und einer relativ geringen In-Konzentration von $x_{In} \sim 35\%$ an der Oberseite. Wir zeigen, dass die beobachtete Steuerbarkeit des Exzitonen-g-Faktors hauptsächlich durch den Lochzustand und nur im geringen Maße von dem Elektronenzustand verursacht wird. Es stellt sich heraus, dass die elektrische Störung der Lochwellenfunktion den g-Faktor durch die Unterdrückung des Drehimpulses der Wellenfunktion beeinflusst. Die Änderung des In:Ga-Überlapps der Wellenfunktion und die Mischung der leichten und schweren Lochbänder spielen hingegen keine wesentliche Rolle. Unsere Ergebnisse führen zu dem Vorschlag für ein universelles einzelnes Qubit-Gatter durch eine rein elektrisch gesteuerte Änderung des g-Tensors. Zuletzt wird der Ursprung der nicht-linearen Zeeman Aufspaltung des neutralen Exzitons in ausgedehnten In-armen Quantenpunkten erklärt. Achtband-$\mathbf{k}\cdot\mathbf{p}$-Rechnungen, die auf realistischen Quantenpunktparametern aus Tunnel-Mikroskopie-Messungen (X-STM) beruhen, zeigen, dass der quadratische Beitrag zur Zeeman-Aufspaltung von einer magnetfeldabhängigen Mischung der leichten und schweren Lochbänder versursacht wird. Dies stellt einen deutlichen Unterschied zu dem Mechanismus der elektrisch gesteuerten Änderung des g-Tensors dar. Es wird gezeigt, dass der niedrige In-Gehalt ($x < 0.4$) und der große Durchmesser ($40 - 50$ nm) der untersuchten Quantenpunkte die nicht-lineare exzitonische Zeeman Aufspaltung erheblich verstärkt. Daraus folgen Vorgaben, diese magnetischen Nichtlinearitäten durch den Wachstumsprozess zu steuern.

Introduction and Motivation

There are two cardinal intermediate goals on the way to quantum information processing: the entanglement of multiple qubit and the realization of universal qubits gates. On the one hand, non-solid state systems currently provide the highest degrees of entanglement. The entanglement of eight qubits has been reported for a system of trapped ions. [HHR$^+$05] Moreover, universal gate operations for such a system have been realized. [SKHG$^+$03] Hyper-entangled states of up to ten qubits have been prepared experimentally in photonic systems. [GLY$^+$10] On the other hand, solid-state quantum computing has received much attention since it may provide a scalable implementation of quantum logic. A state of three entangled spin qubits in a diamond crystal with nitrogen defects has been demonstrated to be stable at room-temperature. [NMR$^+$08] The entanglement of three qubits, the implementation of important two-qubit algorithms, and high-fidelity single qubit gates have been realized in superconducting circuits. [DMG$^+$09, DRS$^+$10, CDG$^+$10] However, these superconducting qubits currently suffer from short decoherence times. For the entangled three qubit state in Ref. [DRS$^+$10], a relaxation and dephasing time of the order of a microsecond was reported. Another promising candidate for solid-state qubits are the spins of confined electrons and holes in semiconductor quantum dots (QDs). [HKP$^+$07, GKB10] Extremely long spin life-times of 270 μs and 20 ms have been reported for holes and electrons, respectively. [HSH$^+$07, KDH$^+$04] This is because the coupling of carriers to the environment is suppressed due to the atom-like level structure in the QDs. [KN00] A partially entangled two-qubit state has been produced in a double QD in an inhomogeneous magnetic field. [BSO$^+$11] While general concepts to achieve higher degrees of entanglement still need to be investigated, universal single qubit gates have already been demonstrated experimentally: firstly, a specific spin qubit with a unique resonance frequency can be manipulated by a microwave field. [KBT$^+$06] Secondly, a local time-dependent magnetic field can be applied to address the spin of charge carriers in QDs. [KWB$^+$08] However, a unique resonance frequency for each individual QD contradicts scalability and the generation of nanoscale magnetic fields currently appears unfeasible.

This has recently motivated a different approach. Instead of applying a time-dependent magnetic field to each QD, the response of the spin states to a static magnetic field, the g-tensor, is modulated by a time-dependent electric field that can be realized by a gate contact for each QD. Purely electrical g-tensor tuning has been

shown to allow arbitrary rotations on the Bloch-sphere by controlling the spin precession axis in single QDs [PPF08, PPF11] and QD molecules [AV09, REVP10]. To date, electrical g-factor modulation in semiconductor nanostructures has been demonstrated using parabolically composition graded AlGaAs quantum wells, [SKE$^+$01] vertically coupled InGaAs/GaAs QD-molecules [DSP$^+$06] and single InAs/InP QDs. [KSP$^+$09, vBSK$^+$11] Typically, very weak tuning effects are observed in single InGaAs/GaAs dots. [NTA07] Still, the tuning of the electron g-factor in $In_{0.5}Ga_{0.5}As$ can be exploited to realize universal single qubit operations. [PPF11] Due to the weak tunability of the electron g-factor, however, very large electric fields are required thus limiting the spin-lifetime by the tunneling-time of the carriers. Only recently, strongly electrically tunable exciton g-factors were reported for InGaAs/GaAs self-assembled QDs grown using the partially covered island (PCI) method but the mechanism responsible for the tuning could not be identified. [KJK$^+$10] In this work, we aim to develop a microscopic understanding of how external magnetic and electric fields influence the spin properties of the electronic states in QDs and predict these properties quantitatively.

Accurate predictions of the exciton g-tensor require detailed electronic structure calculations. The leading method for electronic structure calculations of three-dimensional mesoscopic semiconductor heterostructures, which encompass millions of atoms, is the envelope function approximation (EFA). While originally developed in **k**-space for bulk semiconductors, [LK55, Kan57] its usefulness stems from the real-space formulation that is highly successful in predicting a wide variety of semiconductor properties. [BP74, IP97] The main advantage of the real-space EFA is its independence of detailed atomic configurations, which are not relevant for mesoscopic structures of at least nm-scale [BZ05] anyway and its numerical efficiency due to the sparseness of the Hamiltonian matrices. More recent developments consist in more rigorous justifications and a deeper understanding of the approximations involved, [Bur94, For95] as well as a better treatment of interfaces. [For96, For98] Gauge-invariant formulations of the EFA with magnetic fields allow the reliable prediction of magnetic properties in mesoscopic heterostructures. [GU98, PF06, AMV08]

A persisting and still unresolved problem of the multi-band EFA method that we will address in this work is the appearance of spurious, unphysical solutions of the Schrödinger equation. These solutions may show up as highly oscillatory or strongly localized wave functions within the fundamental band gap. To make things worse, even well-behaved physical states can be polluted by a "spurious admixture". Three different sources of spurious solutions are known to plague the EFA formalism and only the first two have been resolved so far. First, material parameter sets obtained from experimental data can lead to ill-posed Hamiltonian operators with wing-band solutions within the fundamental band gap that originate from large-**k** bulk states that are poorly represented in the EFA approach. [WS81, StH85, For97, For07, VSW07, KLN03, ESC87] This problem can be resolved by parameter rescaling procedures. [For97, For07] Second, inconsistent boundary conditions for the multi-

component envelope function at material interfaces can lead to unphysical states localized at the interface. [For97, MGO94, GM96, AEF85, AS94] Such solutions can be eliminated by a proper ordering of differential operators. [Bur92, Bur99, For93, For97, RAE+02]

However, there is a third source of spurious solutions that is still unresolved. For realistic three-dimensional multi-material nanostructures, the real-space EFA Hamiltonian can only be solved by discretizing position space in some way. The simplest scheme is to use a finite difference method with symmetric first-order differences, i.e. $\partial_x F = [F(x+h) - F(x-h)]/(2h)$ with grid spacing h. While it has been noticed earlier that this method fails badly for many relevant semiconductors and alloys, [CTM03] no general cure for this problem has been developed so far.

The discretization induced appearance of spurious solutions has been discussed for the centered finite differences scheme and it was found to be related to the ill-representation of first-order derivatives in standard real-space bases. [CTM03] While this problem is less obvious for eight-band models because second-order terms stabilize the discrete Hamiltonian to some extent, standard discretization schemes fail completely in 14-band calculations where no or only small second-order terms are present. All published proposals to overcome this problem have major drawbacks. It has been shown that the material parameters may be rescaled so that all first-order derivatives vanish. [For07] However, this effectively decouples the bands which causes important band structure features such as non-parabolicity and inversion asymmetry to be lost. A plane-wave basis, which is most appropriate for periodic structures, [WR93] has the advantage of being free of spurious modes. However, the **k**-space multi-band Hamilton matrix is dense leading to unfeasible numerical problems for three-dimensional realistic nanostructures. Small off-diagonal second-order terms may be added to the first-order terms in the Hamiltonian, but this so-called upwinding procedure breaks the symmetry of the Hamiltonian. [KLN03] Finally, a staggered-grid finite differences method has been shown to successfully remove the instabilities of the first-order derivatives. [WXW06] This amounts to shifting the grids of the various components of the eight-band EFA Hamiltonian relative to each other in a particular way. Unfortunately, such complex grids make it more difficult to implement boundary conditions in a transparent way. In addition, a gauge-invariant formulation of finite differences methods relies on unambiguously determined connection paths between grid points and it may be difficult to achieve this goal with staggered grids. [PF06, AMV08]

It is a central achievement of our work to resolve this issue by employing a basis for the variational envelope function space that is inherently free from these spurious solutions and requires no modification of the $k \cdot p$ Hamiltonian itself.

The Zeeman splitting is many orders of magnitude smaller than other energy scales of the band structure like the spacing of energy levels in typical nanostructures, the spin-orbit splitting and the fundamental band gap. Consequently, even seemingly subtle details of the Hamiltonian such as the ordering of operators and material

parameters can have a profound impact on the calculated g-tensor. [AV09] In the literature, the remote-band contributions to the eight- and 14-band $k \cdot p$ Hamiltonian were derived only for bulk semiconductors where operators and material parameter commute. [TRR79, MR91, Win03] To date, the correct ordering of these terms was only regarded for the isotropic remote-band contribution κ to the g-factor of the valence band. [For97, AV09] In this work, we derive an eight- and 14-band $k \cdot p$ envelope function Hamiltonian that also accounts for the remote-band contributions g^* to the conduction band g-factor and the anisotropic remote-band contribution q to the valence band g-factor in the correct operator ordering. This method leads to an accurate representation of the EFA Hamilton, momentum and angular momentum operator. The latter allows the perturbative prediction of the g-tensor in linear response theory.

Another important effect influences the g-tensor indirectly: the lowering of the QD symmetry from C_{4v} to C_{2v}. Although the envelope function Hamiltonian is dominated by terms with C_{4v} symmetry, [Win03] the lifting of this symmetry induces a substantial anisotropy of the in-plane g-factors in QDs and QD molecules. [AV09] While it is clear from fundamental symmetry arguments that a [001]-grown self-assembled QD can at most exhibit C_{2v} symmetry, [BZ05] it is still controversial which effects account for this symmetry lifting and need to be included in accurate calculations: the linear piezoelectric effect, [SGB99] the quadratic piezoelectric effect, [BZWV06, SWB07] atomic asymmetry, [BZ05] a systematic shape anisotropy of the dots, [JKBJ01, KKO$^+$06] or combinations thereof. The g-factors and many other QD properties are impacted only indirectly by these a effects. A direct measure of this symmetry lifting is the splitting of the two first excited electronic p-shaped levels in InGaAs/GaAs QDs which are degenerate in C_{4v} symmetry. The splitting of these p-levels has been accurately measured experimentally. [SBL$^+$02, ZWG$^+$04, CZS$^+$06] The experimental data thus provide a direct test for the various proposed contributions to the symmetry lifting.

Two comprehensive theoretical studies on the symmetry lifting in InGaAs/GaAs QDs were performed employing the $k \cdot p$ envelope function approximation [SWB07] and the empirical pseudo-potential method. [BZWV06] Both works concluded that the piezoelectric effect cannot be accountable for the observed p-level splitting because, firstly, the linear piezoelectric effect would lead to an incorrect sign and, secondly, the quadratic contributions would cancel the linear contributions in the quadratic piezoelectric effect inside the dot. Both works, however, have two major shortcomings. On the one hand, the overall sign of the piezoelectric field was reversed in both works. [Sch, Bes] On the other hand, a homogeneous In:Ga-profile was assumed. This, however, is incompatible with experimental findings that show strong evidence for a graded In:Ga-profile. [OKW$^+$05, BVK$^+$02, MCFJ02, FIM$^+$00] We thus examine the various contributions to the symmetry lifting. Our results reveal that the linear piezoelectric effect is dominant and produces a p-level splitting with the correct sign and the experimentally observed magnitude for a realistic In:Ga-profile.

This work is organized in two main parts. The first part, in which we present our methods, begins with a review of the continuum equations relevant for the electronic structure calculation in Ch. 1. This encompasses the general $k \cdot p$ theory together with Loewdin's perturbation theory, the linear response theory to optical fields, the theory of linear elastic strain and the piezoelectric effect. In Ch. 2, we apply this general $k \cdot p$ theory to derive the 14-band envelope function Hamiltonian of zincblende-type crystals as well in the angular momentum as in the Cartesian representation. Starting from the symmetry properties of zincblende and the invariants that constitute the Hamiltonian, we obtain the remote-band contributions with the correct operator ordering. This finding is then exploited to derive a perturbative formula for the g-tensor in linear response theory. We also discuss material parameters, rotations of the crystal and the relation of the 14-band model to models with fewer bands. A central part of our work is presented in Ch. 3: the symmetry adapted finite element (SAFE) method. We first discuss and resolve the issue of spurious solutions on the basis of White's two-band model of light hole and conduction band. The solution for this model problem is then generalized to the eight- and 14-band model and an extension for the gauge-invariant incorporation of magnetic fields is presented. As an application, the g-factor tuning of excitons in self-assembled QDs is shown to be substantially larger then previously calculated. We complete the presentation of our model in Ch. 4 with the numerical methods we employed to discretize and solve the semiconductor equations. To this end, we give an overview of our implementation of the finite element method which is specialized for an efficient discretization of multi-component partial differential equations. Moreover, the direct method for the solution of linear systems of equations and a variant of the Arnoldi iteration for generalized interior eigenvalue problems are summarized.

In the second part, we present the results of our calculations on self-assembled InGaAs/GaAs QDs. The lifting of C_{4v} symmetry is examined on the basis of the p-level splitting in Ch. 5. Next, Ch. 6 is devoted to the electrical tuning of the X^0 exciton g-factor. We calculate the tuning in a fully detailed eight-band calculation incorporating the magnetic field and compare the results to those obtained by linear response theory. An intuitive picture of the g-factor tuning is developed and a universal single qubit gate is proposed. Finally, we investigate the non-linear Zeeman splitting in Ch. 7. The origin of this effect is discussed along with the polarization properties of the optical excitonic transition in a magnetic field. The main parts are followed by Appendix A in which we prove the correct continuum limit of the gauge-invariant symmetry adapted finite element method. In appendix B, the coupling matrices that constitute the invariants of the Hamiltonian in zincblende symmetry are summarized. The material parameters used in this work are tabulated in appendix C. Appendix D finally gives an overview over the formal term rewriting system that we implemented to perform the setup of matrix operators as well as rotations of the crystal and the automated validation of the symmetry of the Hamiltonian.

Part I

Model

Chapter 1

Review of the continuum model of semiconductor heterostructures

1.1 Introduction

In the following chapter, we give an overview of the continuum equations relevant to the electronic structure calculation of low-dimensional mesoscopic heterostructures. Atomistic effects, which are relevant on a sub-nanometer scale only, are neglected in the continuum approach. Only the symmetry properties of the crystal lattice enter the electronic structure calculations. The atomistic equations are thus replaced by effective continuum equations with effective empirical material parameters. Calculations can be performed on a coarser length-scale which makes the numerical solution highly efficient. A mesoscopic heterostructure that encompasses millions of atoms can be solved within good approximation on discrete grids or variational spaces with only a few 1000 variables.

Firstly, we give an overview of the $k \cdot p$ theory and Loewdin's perturbation theory in Sec. 1.2. Section 1.3 briefly summarizes the linear response to optical fields. Finally, the linear continuum elasticity model for the calculation of strain and the linear and the quadratic piezoelectric effect are recapitulated in Sec. 1.4 and Sec. 1.5, respectively.

1.2 Luttinger-Kohn $k \cdot p$ theory

The following section summarizes the literature on the Hamiltonian and the momentum operator in the Luttinger-Kohn representation. [LK55, For00]

1.2.1 Bloch's theorem

In the presence of a periodic crystal potential $V(\mathbf{r}) = V(\mathbf{r}+\mathbf{R})$ with the Bravais lattice $\{\mathbf{R}\}$, the time-independent relativistic Pauli-Schrödinger equation reads

$$\hat{H}\psi(\mathbf{r}) = \left[\frac{\hat{p}^2}{2m_0} + V(\mathbf{r}) + \frac{1}{4m_0^2c^2}\left(\boldsymbol{\sigma}\times\nabla V(\mathbf{r})\right)\hat{\mathbf{p}} + \mu_B\frac{g_0}{2}\boldsymbol{\sigma}\cdot\mathbf{B}\right]\psi(\mathbf{r}) = E\psi(\mathbf{r}). \quad (1.1)$$

Here, $\psi(\mathbf{r})$ is the single-particle wave function of the two-component electron spinor and $\boldsymbol{\sigma}$ is the vector of the Pauli matrices. The last term is the coupling of the free electron spin to a magnetic field $\mathbf{B}$. The free electron g-factor is denoted by $g_0 \approx 2$ and μ_B is the Bohr magneton. This term has no impact on the following derivations and is dropped throughout this section. It will be discussed in Sec. 2.3.3 explicitly.

The solution to the above equation is given by the Bloch functions

$$\psi_{n,\mathbf{k}}(\mathbf{r}) = e^{i\mathbf{kr}}u_{n,\mathbf{k}}(\mathbf{r}), \quad (1.2)$$

with the cell periodic part

$$u_{n,\mathbf{k}}(\mathbf{r}+\mathbf{R}) = u_{n,\mathbf{k}}(\mathbf{r}). \quad (1.3)$$

For each value of $\mathbf{k}$, the set of functions $\{u_{n,\mathbf{k}}(\mathbf{r})|n\}$ forms an orthonormal basis of cell periodic functions and therefore fulfills the orthonormality and completeness relations

$$\frac{1}{\Omega}\int_\Omega u^*_{n,\mathbf{k}}(\mathbf{r})u_{n',\mathbf{k}}(\mathbf{r})d^3r = \delta_{n,n'}, \quad (1.4)$$

$$\frac{1}{\Omega}\sum_n u_{n,\mathbf{k}}(\mathbf{r})u^*_{n,\mathbf{k}}(\mathbf{r}\,') = \sum_{\mathbf{R}}\delta(\mathbf{r}-\mathbf{r}\,'-\mathbf{R}), \quad (1.5)$$

where Ω is the volume of a unit cell.

Notably, the set of Bloch functions $\{\psi_{n,\mathbf{k}}(\mathbf{r})|n,\mathbf{k}\}$ also forms a complete basis for non-periodic functions.

1.2.2 Luttinger-Kohn representation

It is usually desirable not to calculate the entire band structure within the first Brillouin zone but only in the vicinity of an extremal k-point $\mathbf{k}_0$. The Luttinger-Kohn representation is therefore introduced as

$$\chi_{n,\mathbf{k}}(\mathbf{r}) = e^{i\mathbf{kr}}\psi_{n,\mathbf{k}_0}(\mathbf{r}) = e^{i(\mathbf{k}+\mathbf{k}_0)\mathbf{r}}u_{n,\mathbf{k}_0}(\mathbf{r}), \quad (1.6)$$

in which $\mathbf{k}$ is relative to $\mathbf{k}_0$. In the following, we abbreviate $U_n(\mathbf{r}) \equiv u_{n,\mathbf{k}_0}(\mathbf{r})$ and use the Dirac notation $\langle\mathbf{r}|n\mathbf{k}\rangle \equiv \chi_{n,\mathbf{k}}(\mathbf{r})$.

Exploiting periodicity, $U_n(\mathbf{r})$ can be expanded in a Fourier series

$$U_n(\mathbf{r}) = \sum_G U_{n,\mathbf{G}}e^{i\mathbf{Gr}}, \quad (1.7)$$

$$U_{n,\mathbf{G}} = \frac{1}{\Omega}\int_\Omega U_n(\mathbf{r})e^{-i\mathbf{Gr}}d^3x. \quad (1.8)$$

The orthonormality (1.4) and completeness relations (1.5) in direct-space can be expressed in reciprocal space as well

$$\sum_{\mathbf{G}} U^*_{n,\mathbf{G}} U_{n',\mathbf{G}} = \delta_{n,n'}, \tag{1.9}$$

$$\sum_{n} U_{n,\mathbf{G}} U^*_{n,\mathbf{G}'} = \delta_{\mathbf{G},\mathbf{G}'}. \tag{1.10}$$

For $\mathbf{k}$ and $\mathbf{k}'$ lying in the first Brillouin zone the product of two basis functions becomes

$$\begin{aligned} \langle n\mathbf{k}|n'\mathbf{k}'\rangle &= \sum_{\mathbf{G},\mathbf{G}'} U^*_{n,\mathbf{G}} U_{n',\mathbf{G}'} \delta(\mathbf{k}-\mathbf{k}'+\mathbf{G}-\mathbf{G}') \\ &= \sum_{\mathbf{G}} U^*_{n,\mathbf{G}} U_{n',\mathbf{G}} \delta(\mathbf{k}-\mathbf{k}') \\ &= \delta_{n,n'}\delta(\mathbf{k}-\mathbf{k}'), \end{aligned} \tag{1.11}$$

because the difference of two k-vectors inside the first Brillouin zone is never equal to a reciprocal lattice vector other than $\mathbf{0}$. The set of Luttinger-Kohn functions is also complete and therefore forms an orthonormal basis even for non cell-periodic functions.

1.2.3 Luttinger-Kohn Hamiltonian

The transformation of the Pauli-Schrödinger equation (1.1) to the Luttinger-Kohn representation (1.6) leads to the eigenvalue problem

$$\sum_{n'} H_{n,n'}(\mathbf{k}) c_{m,n'}(\mathbf{k}) = E_m(\mathbf{k}) c_{m,n}(\mathbf{k}), \tag{1.12}$$

for the expansion coefficients $c_{m,n}$ of the m^{th} state and the n^{th} Luttinger-Kohn basis function. The Hamilton matrix $H_{n,n'}(\mathbf{k})$ in the basis $\{\chi_{n,\mathbf{k}}(\mathbf{r}) = e^{i\mathbf{kr}}\psi_{n,\mathbf{k}_0}(\mathbf{r})\}$ is given by

$$H_{n,n'}(\mathbf{k}) = \left[E_{n'}(\mathbf{k}_0) + \frac{\hbar^2 k^2}{2m_0}\right]\delta_{n,n'} + \frac{\hbar}{m_0}\mathbf{k}\cdot\boldsymbol{\pi}_{n,n'}, \tag{1.13}$$

$$\boldsymbol{\pi}_{n,n'} = \int_\Omega U^*_n(\mathbf{r})\left[\hat{\mathbf{p}} + \frac{1}{4m_0c^2}\boldsymbol{\sigma}\times\boldsymbol{\nabla}V(\mathbf{r})\right]U_{n'}(\mathbf{r})d^3r. \tag{1.14}$$

The $\boldsymbol{\pi}_{n,n'}$ are the matrix elements of the kinematic momentum between the cell periodic part of the Bloch functions at $\mathbf{k}_0$. The $E_{n'}(\mathbf{k}_0)$ are the eigenvalues of the Schrödinger equation (1.1) for the Bloch functions $\psi_{n',\mathbf{k}_0}$.

1.2.4 Envelope function theory

Any wave function $\phi(\mathbf{r})$ can be expanded in the basis of Luttinger-Kohn functions as

$$\phi(\mathbf{r}) = \sum_i \int_{\Omega^*} d^3k\, \chi_{n,\mathbf{k}}(\mathbf{r})\phi_n(\mathbf{k}), \tag{1.15}$$

where Ω^* is the volume of the reciprocal unit cell and $\phi_n(\mathbf{k})$ is defined as

$$\begin{aligned} \phi_n(\mathbf{k}) &= \int_{\Omega} d^3r\, \chi^*_{n,\mathbf{k}}(\mathbf{r})\phi(\mathbf{r}) \\ &= \sum_{\mathbf{G}} U^*_{n,\mathbf{G}}\phi(\mathbf{k}+\mathbf{k}_0+\mathbf{G}). \end{aligned} \tag{1.16}$$

Using the definition of the Luttinger-Kohn representation (1.6) in the above expansion of $\phi(\mathbf{r})$ yields

$$\begin{aligned} \phi(\mathbf{r}) &= \sum_n \int_{\Omega^*} d^3k\, \chi_{n,\mathbf{k}}(\mathbf{r})\phi_n(\mathbf{k}) \\ &= \sum_n \int_{\Omega^*} d^3k\, e^{i(\mathbf{k}+\mathbf{k}_0)\mathbf{r}} U_n(\mathbf{r})\phi_n(\mathbf{k}) && (1.17) \\ &= \sum_n e^{i\mathbf{k}_0\mathbf{r}} U_n(\mathbf{r}) \int_{\Omega^*} d^3k\, e^{i\mathbf{k}\mathbf{r}}\phi_n(\mathbf{k}) && (1.18) \\ &= e^{i\mathbf{k}_0\mathbf{r}} \sum_n U_n(\mathbf{r})F_n(\mathbf{r}), && (1.19) \end{aligned}$$

where

$$F_n(\mathbf{r}) \equiv \int_{\Omega^*} d^3k\, e^{i\mathbf{k}\mathbf{r}}\phi_n(\mathbf{k}), \tag{1.20}$$

is called the n^{th} component of the envelope function $F(\mathbf{r})$.

Note, however, that the above derivation is only exact if the Luttinger-Kohn basis functions are the same throughout the entire crystal. This is obviously true for bulk semiconductors, but only an approximation in heterostructures. This problem was intensely discussed in the literature and it was found that even an abrupt change in the cell-periodic Bloch functions at material interfaces induces only a minor error. [Bur94, For96, For98] Equation (1.20) thus justifies replacement $\hat{k} \to -i\nabla$ in the real-space envelope function approximation (EFA).

1.2.5 Luttinger-Kohn momentum operator

Many important observables such as optical matrix elements are related to the momentum operator. Momentum matrix elements of the Luttinger-Kohn basis functions are derived by starting with the eigenfunction $|\mathbf{p}\rangle$ of the momentum operator $\hat{\mathbf{p}}$, i.e.

$$\hat{\mathbf{p}}|\mathbf{p}\rangle = \mathbf{p}|\mathbf{p}\rangle. \tag{1.21}$$

The definition of the Luttinger-Kohn functions (1.6) and the Fourier series expansion for $U_n(\mathbf{r})$ (1.7) then results in

$$\begin{aligned}\langle \mathbf{p}|n\mathbf{k}\rangle &= \int (2\pi)^{-3} e^{\frac{i}{\hbar}\mathbf{p}\mathbf{r}} e^{i(\mathbf{k}+\mathbf{k}_0)\mathbf{r}} U_n(\mathbf{r}) d^3r \\ &= \sum_{\mathbf{G}} \delta(\mathbf{k}+\mathbf{k}_0-\frac{1}{\hbar}\mathbf{p}+\mathbf{G}) U_{n,\mathbf{G}}. \end{aligned} \tag{1.22}$$

Using this relation and the completeness of the basis $\{|\mathbf{p}\rangle\}$, the momentum matrix elements between Luttinger-Kohn basis functions become

$$\begin{aligned}&\langle n\mathbf{k}|\hat{\mathbf{p}}|n'\mathbf{k}'\rangle = \int_{\Omega^*} \langle n\mathbf{k}|\mathbf{p}\rangle\langle \mathbf{p}|\hat{\mathbf{p}}|n'\mathbf{k}'\rangle d^3p \\ &= \int_{\Omega^*} \sum_{\mathbf{G}} \mathbf{p}\, U^*_{n,\mathbf{G}}\, \delta(\mathbf{k}+\mathbf{k}_0+\mathbf{G}-\frac{1}{\hbar}\mathbf{p})\langle \mathbf{p}|n'\mathbf{k}'\rangle d^3p \\ &= \sum_{\mathbf{G}} \hbar(\mathbf{k}+\mathbf{k}_0+\mathbf{G})\, U^*_{n,\mathbf{G}} \langle \mathbf{k}+\mathbf{k}_0+\mathbf{G}|n'\mathbf{k}'\rangle \\ &= \sum_{\mathbf{G},\mathbf{G}'} \hbar(\mathbf{k}+\mathbf{k}_0+\mathbf{G})\, U^*_{n,\mathbf{G}} U_{n',\mathbf{G}'}\, \delta(\mathbf{k}'+\mathbf{G}'-\mathbf{k}-\mathbf{G}). \end{aligned} \tag{1.23}$$

For k-vectors inside the same Brillouin, the difference $\mathbf{k}'-\mathbf{k}$ is never equal to a non-zero reciprocal lattice vector. Therefore, $\delta(\mathbf{k}'+\mathbf{G}'-\mathbf{k}-\mathbf{G})$ becomes $\delta(\mathbf{k}'-\mathbf{k})\delta_{\mathbf{G}',\mathbf{G}}$ and

$$\begin{aligned}\langle n\mathbf{k}|\hat{\mathbf{p}}|n'\mathbf{k}'\rangle &= \sum_{\mathbf{G}} [\hbar(\mathbf{k}_0+\mathbf{G})+\hbar\mathbf{k}]\, U^*_{n,\mathbf{G}} U_{n',\mathbf{G}}\, \delta(\mathbf{k}'-\mathbf{k}) \\ &= [\mathbf{p}_{n,n'}(\mathbf{k}_0)+\hbar\mathbf{k}\,\delta_{n,n'}]\delta(\mathbf{k}'-\mathbf{k}), \end{aligned} \tag{1.24}$$

in which relation (1.10) has been used and the momentum matrix element at $\mathbf{k}_0$ is defined as

$$\mathbf{p}_{n,n'}(\mathbf{k}_0) = \sum_{\mathbf{G}} \hbar(\mathbf{k}_0+\mathbf{G})\, U^*_{n,\mathbf{G}} U_{n',\mathbf{G}}. \tag{1.25}$$

The momentum operator does not couple different k-vectors and its matrix elements can thus be written as a function of $\mathbf{k}$

$$\mathbf{p}_{n,n'}(\mathbf{k}) = \mathbf{p}_{n,n'}(\mathbf{k}_0) + \hbar\mathbf{k}\,\delta_{n,n'}. \tag{1.26}$$

1.2.6 Loewdin's perturbation theory

The Hamiltonian (1.13) couples an infinite number bands and contains an infinite number of coupling parameters $\boldsymbol{\pi}_{n,n'}$. For practical purposes, only a small number of coupling parameters can be fitted to experimental data and thus only a small

number of bands can be taken into account. One can reduce the number of bands by employing Loewdin's perturbation theory which allows to decouple a finite set of class $\mathcal{A}$ bands from the remaining remote bands in class $\mathcal{B}$. [L̈51] The bands in class $\mathcal{A}$ are considered to be nearly degenerate, i.e. the energy separation among class $\mathcal{A}$ bands is much smaller than the energy separation between any class $\mathcal{A}$ and class $\mathcal{B}$ band. In order to decouple these classes of bands in a controlled manner, a unitary transformation is applied to the Hamiltonian which eliminates all coupling terms between class $\mathcal{A}$ and class $\mathcal{B}$ bands up to the first order in $\mathbf{k}$. In the following, we use the Einstein sum convention for the coordinate indexes i and j.

At first, the Hamiltonian (1.13) is split into coupling and non-coupling terms between class $\mathcal{A}$ and class $\mathcal{B}$ bands,

$$\begin{aligned} H &= \hat{H}_0 + \hat{H}_1 + \hat{H}_2, && (1.27)\\ H_0 &= \left[E_n(\mathbf{k}_0) + \frac{\hbar^2 k^2}{2m_0}\right]\delta_{n,n'}, && (1.28)\\ H_1 &= \frac{\hbar}{m_0} k_i \pi^i_{n,n'} \Theta_{n,n'}, && (1.29)\\ H_2 &= \frac{\hbar}{m_0} k_i \pi^i_{n,n'} (1-\Theta_{n,n'}), && (1.30) \end{aligned}$$

where

$$\Theta_{n,n'} \equiv \begin{cases} 0 & n,n' \in \mathcal{A} \text{ or } n,n' \in \mathcal{B} \\ 1 & \text{otherwise} \end{cases}, \qquad (1.31)$$

is zero for bands in the same class and one for bands in different classes.

In order eliminate H_1, a unitary transformation of the form

$$\begin{aligned} |\overline{nk}\rangle &= e^{-S}|nk\rangle, && (1.32)\\ \bar{H} &= e^{-S} H e^{S}, && (1.33) \end{aligned}$$

is applied, in which $S = -S^H$ is anti-Hermitian. The transformed Hamiltonian $\bar{H}$ couples class $\mathcal{A}$ bands among each other with renormalized coupling constants that account for the class $\mathcal{B}$ bands perturbatively. It can be expanded to

$$\begin{aligned} \bar{H} &= e^{-S} H e^{S} && (1.34)\\ &= H + [H,S] + \frac{1}{2!}[[H,S],S] + \frac{1}{3!}[[[H,S],S],S] + \ldots \\ &= H_0 + H_1 + H_2 + [H_0,S] + [H_1,S] + [H_2,S] \\ &\quad + \frac{1}{2}[[H_0,S],S] + \frac{1}{2}[[H_1,S],S] + \frac{1}{2}[[H_2,S],S] \\ &\quad + \frac{1}{6}[[[H_0,S],S],S] + \ldots . && (1.35) \end{aligned}$$

In order to remove H_1, S is chosen such that $H_1 + [H_0, S] = 0$. If both the states

n and n' are in the same class of bands, S must be 0. Otherwise, this relation yields

$$\begin{aligned} 0 &= \langle n|H_1 + H_0 S - S H_0|n'\rangle \\ \langle n|H_0 S - S H_0|n'\rangle &= -\langle n|H_1|n'\rangle \\ S(E_n - E_{n'}) &= -\frac{\hbar}{m_0} k_i \pi^i_{n,n'} \\ S &= -\frac{\hbar}{m_0}\frac{k_i \pi^i_{n,n'}}{E_n - E_{n'}}, \end{aligned} \tag{1.36}$$

and S is thus given by

$$S = -\frac{\hbar}{m_0}\frac{k_i \pi^i_{n,n'}}{E_n - E_{n'}}\Theta_{n,n'}. \tag{1.37}$$

With this expression for S, the Hamiltonian (1.35) transforms into

$$\begin{aligned} \bar{H} &= e^{-S} H e^{S} \\ &= H_0 + H_2 + [H_1, S] + [H_2, S] \\ &\quad + \frac{1}{2}[[H_0, S], S] + \frac{1}{2}[[H_1, S], S] + \frac{1}{2}[[H_2, S], S] \\ &\quad + \frac{1}{6}[[[H_0, S], S], S] + \ldots. \end{aligned} \tag{1.38}$$

The terms $\frac{1}{6}[[[H_0, S], S], S]$, $\frac{1}{2}[[H_1, S], S]$, and $\frac{1}{2}[[H_2, S], S]$ are of $O(k^3)$ and are thus neglected as are all higher terms in k. $[H_2, S]$ is of $O(k^2)$, but couples bands from class $\mathcal{A}$ and $\mathcal{B}$ only. It is neglected since we aim to decouple the classes $\mathcal{A}$ and $\mathcal{B}$ up to $O(k)$ only. Using $H_1 = -[H_0, S]$, the term $\frac{1}{2}[[H_0, S], S]$ reduces to $-\frac{1}{2}[H_1, S]$. This finally results in the Hamiltonian $\bar{H}$ of $O(k^2)$

$$\begin{aligned} \bar{H} &\approx H_0 + H_2 + \frac{1}{2}[H_1, S] \\ &= \left[E_n(\mathbf{k}_0) + \frac{\hbar^2 k^2}{2m_0}\right]\delta_{n,n'} + \frac{\hbar}{m_0} k_i \pi^i_{n,n'}(1 - \Theta_{n,n'}) \\ &\quad + \frac{1}{2}\sum_m \frac{\hbar^2}{m_0^2}\left[\frac{k_i \pi^i_{n,m}\pi^j_{m,n'} k_j}{E_n - E_m} + \frac{k_j \pi^j_{n,m}\pi^i_{m,n'} k_i}{E'_n - E_m}\right]\Theta_{n,m}\Theta_{m,n'}. \end{aligned} \tag{1.39}$$

Note importantly that the components of the k-vector commute only in the bulk crystal. In heterostructures this is no longer the case due to boundary conditions at the material interfaces. [Bur92, For96] Hence, the ordering of operators and parameters needs to be preserved carefully throughout the following discussion. In fact, we will show in section 2.3.4 that the correct ordering becomes crucial in the presence of a magnetic field.

Since only the class $\mathcal{A}$ bands are of interest, the Hamiltonian for class A is written

as

$$\begin{aligned}\bar{H}_{n,n'} &= \left[E_n(\mathbf{k}_0)+\frac{\hbar^2k^2}{2m_0}\right]\delta_{n,n'}+\frac{\hbar}{m_0}k_i\pi^i_{n,n'} \\ &\quad +\frac{\hbar^2}{2m_0^2}\sum_{m\in\mathcal{B}}k_i\pi^i_{n,m}\left[\frac{1}{E_n-E_m}+\frac{1}{E_{n'}-E_m}\right]\pi^j_{m,n'}k_j. \qquad (1.40)\end{aligned}$$

From this general $k\cdot p$ Hamiltonian, all single band and multi-band $k\cdot p$ Hamiltonians emerge by the corresponding choice of class $\mathcal{A}$ bands. The sum over the remote class $\mathcal{B}$ bands reduces to a set of parameters that depend on n, n', i and j only. Symmetry properties of the crystal lattice at the k-point $\mathbf{k}_0$ can be exploited to reduce the number of parameters substantially. [DKK55] Equation (1.40) can be used to obtain $k\cdot p$ parameters directly from atomistic models. [GV95, JSdAeSLR05] Commonly, however, only the set of symmetry-allowed independent parameters is extracted from Eq. (1.40). These parameters are then fitted to experimental data. [VMRM01]

1.2.7 Momentum operator in Loewdin's basis

In order to obtain the correct $k\cdot p$ momentum operator for class $\mathcal{A}$ bands, the Luttinger-Kohn momentum operator (1.26) has to be transformed to the same basis as the Hamiltonian. This yields

$$\bar{\mathbf{p}} = e^{-S}\mathbf{p}e^{S} = \mathbf{p}+[\mathbf{p},S]+\ldots, \qquad (1.41)$$

The transformation is only expanded up to $O(k)$ since higher terms in $\mathbf{k}$ would require further coupling parameters in addition to the parameters of the according Hamiltonian because higher combinations in the kinematic momentum matrix elements $\boldsymbol{\pi}_{n,n'}$ were involved.

Evaluating the terms of (1.41) by inserting the momentum matrix elements between Luttinger-Kohn basis functions (1.26) and S (1.37) yields

$$\langle n|p^i|n'\rangle = p^i_{n,n'}+\hbar k_i\delta_{n,n'}, \qquad (1.42)$$

$$\begin{aligned}\langle n|[p^i,S]|n'\rangle &= \sum_{m\in\mathcal{B}}\left[p^i_{n,m}+\hbar k^i\delta_{n,m}\right]\left[-\frac{\hbar}{m_0}\frac{k_j\pi^j_{m,n'}}{(E_m-E_{n'})}\right] \\ &\quad -\sum_{m\in\mathcal{B}}\left[-\frac{\hbar}{m_0}\frac{k_j\pi^j_{n,m}}{(E_n-E_m)}\right]\left[p^i_{m,n'}+\hbar k^i\delta_{m,n'}\right] \\ &= -\sum_{m\in\mathcal{B}}\frac{\hbar}{m_0}\frac{p^i_{n,m}\pi^j_{m,n'}k_j}{(E_m-E_{n'})} \\ &\quad +\sum_{m\in\mathcal{B}}\frac{\hbar}{m_0}\frac{k_j\pi^j_{n,m}p^i_{m,n'}}{(E_n-E_m)}, \qquad (1.43)\end{aligned}$$

$$\begin{aligned}\bar{p}^i_{n,n'} &\approx p^i_{n,n'} + \hbar k_i \delta_{n,n'} \\ &\quad + \frac{\hbar}{m_0} \sum_{m \in \mathcal{B}} \left[\frac{p^i_{n,m} \pi^j_{m,n'} k_j}{E_{n',m}} + \frac{k_j \pi^j_{n,m} p^i_{m,n'}}{E_{n,m}} \right]. \end{aligned} \tag{1.44}$$

The problem now is to express the $k \cdot p$ momentum operator (1.44) in the same set of $k \cdot p$ parameters as the $k \cdot p$ Hamiltonian (1.39). A comparison between both operators shows that two issues arise. Firstly, the $k \cdot p$ momentum operator contains not only kinematic but also canonical momentum matrix elements. However, the difference between both operators is of relativistic nature and usually a very small correction which can be neglected. Secondly, the third term that represents the perturbative remote-band contributions in the $k \cdot p$ momentum operator is not symmetric in i and j whereas the corresponding term in the $k \cdot p$ Hamiltonian is.

For the eight-band, six-band and single-band $k \cdot p$ model of zincblende at the Γ-point, it can be proven by symmetry arguments under mild assumptions that indeed the same set of parameters is sufficient for the $k \cdot p$ momentum operator as for the $k \cdot p$ Hamiltonian. [Eis08] Interestingly, this is not the case for the 14-band model. However, the contributions from remote bands are relatively small in this model. Therefore, neglecting the additional perturbative parameters, which occur in the momentum operator, is expected to yield a sound approximation. Clearly, this argument also holds for all models that encompass even more bands.

Under these approximations, Eq. (1.44) and Eq. (1.39) allow to express $\bar{\mathbf{p}}_{n,n'}$ in terms of $H_{n,n'}$ as

$$\bar{\mathbf{p}}_{n,n'} \approx \frac{m_0}{\hbar} \frac{\partial \bar{H}_{n,n'}}{\partial \mathbf{k}}. \tag{1.45}$$

This is an approximate variant of the Hellmann-Feynman theorem. [Fey39]

1.3 Linear optical response theory

In the presence of a time-dependent electromagnetic field, the principle of minimal coupling leads to the time-dependent single particle Schrödinger equation [Chu95]

$$i\hbar \partial_t \phi(\mathbf{r}, t) = \hat{H} \phi(\mathbf{r}, t) = \left[\frac{(\hat{\mathbf{p}} + e\mathbf{A}(\mathbf{r}, t))^2}{2m_0} + V(\mathbf{r}) \right] \phi(\mathbf{r}, t), \tag{1.46}$$

where $\phi(\mathbf{r}, t)$ is the time-dependent wave function and $V(\mathbf{r})$ the crystal potential. Relativistic effects are neglected here because they have only minor impact on the response to optical fields in the linear limit. The vector potential of a electromagnetic plane wave field with wave vector $\mathbf{q}$ and angular frequency ω is [Chu95]

$$\mathbf{A}(\mathbf{r}, t) = \mathrm{Re}\left[\boldsymbol{\epsilon} A_0 e^{i(\mathbf{q} \cdot \mathbf{r} - \omega t)} \right]. \tag{1.47}$$

Note that in general $\mathbf{A}(\mathbf{r}, t)$ can be a superposition of various static and dynamic components. In the linear limit, we neglect any terms of higher order in $\mathbf{A}(\mathbf{r}, t)$ and

thus treat all these components independently. Hence, without restriction we discuss a single plane wave component (1.47) only.

In the optical limit $|\mathbf{r}| \ll 1/|\mathbf{q}|$, we have that

$$\mathbf{A}(\mathbf{r},t) \approx \mathrm{Re}\left[\boldsymbol{\epsilon} A_0 e^{-i\omega t}\right] = \frac{1}{2} A_0 \left(\boldsymbol{\epsilon}^* e^{i\omega t} + \boldsymbol{\epsilon} e^{-i\omega t}\right), \tag{1.48}$$

where we account for general complex polarizations $\boldsymbol{\epsilon}$. The linear response to this field is thus

$$\mathbf{A} \cdot \frac{\delta \hat{H}}{\delta \mathbf{A}} \approx \mathbf{A} \cdot \frac{e\hat{\mathbf{p}}}{m_0} = \frac{eA_0}{2m_0} \boldsymbol{\epsilon}^* \cdot \hat{\mathbf{p}} e^{i\omega t} + \frac{eA_0}{2m_0} \boldsymbol{\epsilon} \cdot \hat{\mathbf{p}} e^{-i\omega t} = \hat{H}_{int}^{\dagger} e^{i\omega t} + \hat{H}_{int} e^{-i\omega t}, \tag{1.49}$$

with the time-independent interaction Hamiltonian

$$\hat{H}_{int} = \frac{eA_0}{2m_0} \boldsymbol{\epsilon} \cdot \hat{\mathbf{p}}. \tag{1.50}$$

In the limit of large time scales ($\gg 1/\omega$), time-dependent perturbation theory yields Fermi's golden rule for the transition probability [Dav98b]

$$\begin{aligned} W_{f,i} &= \frac{2\pi}{\hbar} |\langle f|H_{int}|i\rangle|^2 \delta(E_f - E_i - \hbar\omega) \\ &+ \frac{2\pi}{\hbar} |\langle f|H_{int}^{\dagger}|i\rangle|^2 \delta(E_f - E_i + \hbar\omega), \end{aligned} \tag{1.51}$$

from the initial state $|i\rangle$ to the final state $|f\rangle$ with the corresponding energies E_i and E_f. From the transition probability the absorption coefficient is derived as [Chu95]

$$\alpha(\omega) = \frac{\pi e^2}{nc\epsilon_0 m_0^2 \omega} \frac{1}{V} {\sum_{a,b}}' |\langle a|\boldsymbol{\epsilon} \cdot \hat{\mathbf{p}}|b\rangle|^2 (\rho_a - \rho_b) \delta(E_b - E_a - \hbar\omega), \tag{1.52}$$

where the sum $\sum'$ runs over all state $|a\rangle$ and $|b\rangle$ with $E_b > E_a$. The normalization volume is denoted as V, c is the vacuum speed of light and ϵ_0 the vacuum dielectric constant. The function ρ_a denotes the occupation of the a-th state. In general, the refractive index n is a function of ω. However, for a small range of transition energies it can be considered as constant.

For convenience, we define the oscillator strength

$$f_{b,a} = \frac{1}{2m_0(E_b - E_a)} |\boldsymbol{\epsilon} \cdot \hat{\mathbf{p}}_{b,a}|^2 = \frac{I_{b,a}}{E_b - E_a}, \tag{1.53}$$

and the transition intensity

$$I_{b,a} = \frac{1}{2m_0} |\boldsymbol{\epsilon} \cdot \hat{\mathbf{p}}_{b,a}|^2. \tag{1.54}$$

The oscillator strength fulfills the popular f-sum rule. However, to assess the intensity of inter-band transitions, the transition intensity serves as a more intuitive scale since, for optical transitions in the Γ-point of bulk direct semiconductors, it equals the Kane energy parameter.

1.4 Continuum strain

A lattice mismatch of the constituents of heterostructures causes strain fields when the lattices locally adjust to each other. These strain field affects the electronic structure in mesoscopic systems in two ways. Firstly, the deformation of the crystal changes the distance of atoms and lowers the symmetry of the crystal. This directly alters the energy of the electronic bands. Secondly, the shear strain components of the strain tensor give rise to piezoelectric charges. The according potential can additionally lower the symmetry and split otherwise degenerate states. The accurate prediction of electronic states thus requires the accurate calculation of strain fields. To this end, we employ the linear elastic continuum model. This method has been shown to be in reasonable agreement with the atomistic valence force field method, but is numerically less costly. [SGB99] In the following, we summarize the linear elastic continuum model for zincblende semiconductors given in the literature. [LL91]

In order to describe the deformation of solid continua, a displacement vector $\mathbf{u}(\mathbf{r})$ is associated with each point $\mathbf{r}$. Consequently, the point $\mathbf{r}$ in the *undeformed* solid is displaced to the position $\mathbf{r}'(\mathbf{r}) = \mathbf{r} + \mathbf{u}(\mathbf{r})$ by the deformation. Without external forces, the free elastic energy in the differential volume $\mathrm{d}^3 r$ is given by [LL91]

$$\frac{1}{2} \sum_{ijkl} \partial_i u_j(\mathbf{r}) C_{ijkl}(\mathbf{r}) \partial_k u_l(\mathbf{r}) \, \mathrm{d}^3 r, \tag{1.55}$$

where C_{ijkl} is the fourth order elastic tensor. The $\partial_i u_j(\mathbf{r})$ are called distortion and can be separated in a symmetric and an anti-symmetric part. It can be shown that, in absence of external forces, the anti-symmetric part does not contribute to the elastic energy because it amounts to rotations of the differential volume only. [LL91] The symmetric part is called strain and is determined by the symmetric second-rank tensor $\epsilon_{i,j} \equiv (\partial_i u_j(\mathbf{r}) + \partial_j u_i(\mathbf{r}))/2$.

In equilibrium, the total free elastic energy is minimal. It is convenient to write the free energy functional in Voigt notation

$$F[\boldsymbol{\epsilon}] = \frac{1}{2} \sum_{ij} \int_\Omega \mathrm{d}^3 r \, \epsilon_i(\mathbf{r}) C_{ij}(\mathbf{r}) \epsilon_j(\mathbf{r}), \tag{1.56}$$

where the vector

$$\boldsymbol{\epsilon} = \begin{pmatrix} \epsilon_{xx} \\ \epsilon_{yy} \\ \epsilon_{zz} \\ 2\epsilon_{yz} \\ 2\epsilon_{zx} \\ 2\epsilon_{xy} \end{pmatrix} = \begin{pmatrix} \partial_x u_x \\ \partial_y u_y \\ \partial_z u_z \\ \partial_y u_z + \partial_z u_y \\ \partial_z u_x + \partial_x u_z \\ \partial_x u_y + \partial_y u_x \end{pmatrix}. \tag{1.57}$$

represents the strain and the second-rank elastic tensor is now denoted as C_{ij}. The integration domain Ω is the volume of the solid.

In zincblende-type symmetry, the second-rank elastic tensor reads [Nye85]

$$C = \begin{pmatrix} C_{11} & C_{12} & C_{12} & 0 & 0 & 0 \\ C_{12} & C_{11} & C_{12} & 0 & 0 & 0 \\ C_{12} & C_{12} & C_{11} & 0 & 0 & 0 \\ 0 & 0 & 0 & C_{44} & 0 & 0 \\ 0 & 0 & 0 & 0 & C_{44} & 0 \\ 0 & 0 & 0 & 0 & 0 & C_{44} \end{pmatrix}, \tag{1.58}$$

where only three independent parameters C_{11}, C_{12}, and C_{44} occur.

The free elastic energy is minimal if the functional derivative of the elastic energy by each displacement component i vanishes, namely

$$\frac{\delta F[\mathbf{u}]}{\delta u_i} = 0. \tag{1.59}$$

The displacement in a heterostructure can be split in a part $\mathbf{u}^0$ due to the lattice mismatch and a part $\mathbf{u}^1$ due to the relaxation of the crystal. The lattice mismatch in known and the relaxation has to be calculated. Hence, the functional derivative Eq. (1.59) results in the system of equations

$$\hat{S} \begin{pmatrix} u_x^1 \\ u_y^1 \\ u_z^1 \end{pmatrix} = -\hat{S} \begin{pmatrix} u_x^0 \\ u_y^0 \\ u_z^0 \end{pmatrix}, \tag{1.60}$$

where the so-called stiffness operator $\hat{S}$ results from the functional derivative (1.59) in

$$\hat{S} = \begin{pmatrix} \partial_x C_{11}\partial_x + \partial_y C_{44}\partial_y + \partial_z C_{44}\partial_z & \partial_x C_{12}\partial_y + \partial_y C_{44}\partial_x & \partial_x C_{12}\partial_z + \partial_z C_{44}\partial_x \\ \partial_y C_{12}\partial_x + \partial_x C_{44}\partial_y & \partial_x C_{44}\partial_x + \partial_y C_{11}\partial_y + \partial_z C_{44}\partial_z & \partial_y C_{12}\partial_z + \partial_z C_{44}\partial_y \\ \partial_z C_{12}\partial_x + \partial_x C_{44}\partial_z & \partial_z C_{12}\partial_y + \partial_y C_{44}\partial_z & \partial_x C_{44}\partial_x + \partial_y C_{44}\partial_y + \partial_z C_{11}\partial_z \end{pmatrix}. \tag{1.61}$$

Since the lattice constants are uniform in all Cartesian direction for zincblende-type crystals, the mismatch strain $\boldsymbol{\epsilon}^0$ for a material with lattice constant a within a matrix with lattice constant a^0 is hydrostatic. It is given by

$$\epsilon_1^0(\mathbf{r}) = \epsilon_2^0(\mathbf{r}) = \epsilon_3^0(\mathbf{r}) = \frac{a^0 - a(\mathbf{r})}{a(\mathbf{r})}, \tag{1.62}$$

$$\epsilon_4^0(\mathbf{r}) = \epsilon_5^0(\mathbf{r}) = \epsilon_6^0(\mathbf{r}) = 0. \tag{1.63}$$

Inserting this in the right-hand side of Eq. (1.60), we obtain the stiffness equation

$$\hat{S}\,\mathbf{u}^1(\mathbf{r}) = -\nabla(C_{11} + 2C_{12})\frac{a^0 - a(\mathbf{r})}{a(\mathbf{r})}. \tag{1.64}$$

By solving this system of partial differential equations for $\mathbf{u}^1(\mathbf{r})$, we obtain the total strain as

$$\boldsymbol{\epsilon}(\mathbf{r}) = \boldsymbol{\epsilon}^0(\mathbf{r}) + \begin{pmatrix} \partial_x u_x^1(\mathbf{r}) \\ \partial_y u_y^1(\mathbf{r}) \\ \partial_z u_z^1(\mathbf{r}) \\ \partial_y u_z^1(\mathbf{r}) + \partial_z u_y^1(\mathbf{r}) \\ \partial_z u_x^1(\mathbf{r}) + \partial_x u_z^1(\mathbf{r}) \\ \partial_x u_y^1(\mathbf{r}) + \partial_y u_x^1(\mathbf{r}) \end{pmatrix}. \tag{1.65}$$

1.5 Piezoelectric effect

A displacement of the atoms in a crystal lacking inversion symmetry can induce dipole and quadrupole moments that lead to a piezoelectric polarization $\mathbf{P}$. [Mar72] The position dependence of the strain field in heterostructures causes a divergence of this polarization. This corresponds to an effective polarization charge $\rho(\mathbf{r}) = -\nabla \cdot \mathbf{P}(\mathbf{r})$ and consequently an electrostatic potential which can have a substantial impact on the electronic structure.

In the Voigt notation, the linear piezoelectric tensor e_{ij} is second-rank where $i = 1, 2, 3$ and $j = 1, \ldots, 6$ denote the Cartesian coordinate and the Voigt index, respectively. It has only a single independent component $e_{14} = e_{25} = e_{36}$ in zincblende symmetry resulting in the linear piezoelectric polarization [Mar72, Nye85]

$$\mathbf{P}(\mathbf{r}) = \begin{pmatrix} 0 & 0 & 0 & e_{14}(\mathbf{r}) & 0 & 0 \\ 0 & 0 & 0 & 0 & e_{14}(\mathbf{r}) & 0 \\ 0 & 0 & 0 & 0 & 0 & e_{14}(\mathbf{r}) \end{pmatrix} \boldsymbol{\epsilon}(\mathbf{r}) = e_{14}(\mathbf{r}) \begin{pmatrix} \epsilon_4(\mathbf{r}) \\ \epsilon_5(\mathbf{r}) \\ \epsilon_6(\mathbf{r}) \end{pmatrix}, \tag{1.66}$$

with the piezoelectric material constant e_{14}. The corresponding electrostatic potential $\Phi(\mathbf{r})$ is the solution of Poisson's equation

$$-\nabla \cdot \varepsilon_0 \varepsilon_r(\mathbf{r}) \nabla \Phi(\mathbf{r}) = -\nabla \cdot \mathbf{P}(\mathbf{r}), \tag{1.67}$$

with the vacuum dielectric constant ε_0 and the material-dependent relative dielectric constant $\varepsilon_r(\mathbf{r})$.

Recently, the quadratic piezoelectric effect was proposed. [BZWV06] The corresponding polarization $\mathbf{P}^q(\mathbf{r})$ is quadratic in the strain and reads [BWPB11]

$$\mathbf{P}^q = e_{14}^q \begin{pmatrix} \epsilon_4 \\ \epsilon_5 \\ \epsilon_6 \end{pmatrix} + B_{114}^q \begin{pmatrix} \epsilon_1 \epsilon_4 \\ \epsilon_2 \epsilon_5 \\ \epsilon_3 \epsilon_6 \end{pmatrix} + B_{124}^q \begin{pmatrix} (\epsilon_2 + \epsilon_3)\epsilon_4 \\ (\epsilon_3 + \epsilon_1)\epsilon_5 \\ (\epsilon_1 + \epsilon_2)\epsilon_6 \end{pmatrix} + B_{156}^q \begin{pmatrix} \epsilon_5 \epsilon_6 \\ \epsilon_6 \epsilon_4 \\ \epsilon_4 \epsilon_5 \end{pmatrix}, \tag{1.68}$$

with the piezoelectric constants e_{14}^q, B_{114}^q, B_{124}^q, and B_{156}^q. Here, we dropped the explicit position dependency for the sake of clarity. Again, the solution of Poisson's equation yields the corresponding potential.

Chapter 2

New derivation of the zincblende multi-band $k \cdot p$-Hamiltonian

2.1 Introduction

In this chapter, we derive for the first time the $k \cdot p$ envelope function Hamiltonian preserving the correct ordering of material parameters and differential operators for *all* relevant remote-band contributions. Previously in the literature, this derivation was carried in the bulk case, where material parameters and $\hat{k}$-operators commute. [TRR79, MR91, PZ96, Win03] So far, the correct ordering was regarded only for the Luttinger parameter κ^L which contributes to the isotropic valence band g-factor. [For97, AMV08] It was found that the operator ordering is particularly important for the calculations of effective g-factors. In the presence of spin-orbit coupling, the $k \cdot p$ interaction induces an orbital motion of the wave function. [KIR98] This orbital motion strongly modifies the coupling to a magnetic field. Consequently, the remote bands contribute to the effective g-factors perturbatively. In addition to κ^L, we find that in fact *all* terms that relate to the effective orbital motion depend on the correct ordering of operators in heterostructures.

We apply the general $k \cdot p$ envelope function theory to zincblende-type crystals with a direct band gap at the Γ-point. These crystals encompass the most important materials for opto-electronic devices. At the Γ-point, we have that $\mathbf{k}_0 = (0, 0, 0)$ and the $k \cdot p$ Hamiltonian has the full symmetry of the zincblende-type crystal.

Section 2.2 gives an overview of the symmetry properties of the group T_d and their implications for the Luttinger-Kohn Hamiltonian. Section 2.3 summarizes the first-order 14-band extended Kane Hamiltonian in angular momentum representation that incorporates all symmetry properties of T_d including the lack of inversion symmetry. We newly derive the perturbative second-order remote-band contributions preserving the correct operator ordering by employing Loewdin's perturbation theory. We exploit these results to derive a perturbative formula for the g-tensor in linear response theory in Sec. 2.4. In Sec. 2.5, the 14-band model is related to the

Table 2.1: Correspondence of irreducible representations in various notations.

Koster [KDWS63] (this work)	Pikus/Bir [BP74]	Wigner [BSW36]
Γ_1	A_1	Γ_1
Γ_2	A_2	Γ_2
Γ_3	E	Γ_{12}
Γ_4	F_1	Γ_{25}
Γ_5	F_2	Γ_{15}
Γ_6	E_2'	Γ_6
Γ_7	E_1'	Γ_7
Γ_8	G'	Γ_8

common eight-, six-, and single-band models by rescaling material parameters. Next, we transform the 14-band Hamiltonian to the Cartesian representation in Sec. 2.6. This particular representation is required by our spurious-solution-free discretization method presented in Ch. 3. Finally, the dependence of material parameters on the temperature and the alloy composition as well as rotations of the crystal axes are discussed in Sec. 2.7 and Sec. 2.8, respectively.

2.2 Review of symmetry properties of the zincblende Hamiltonian

2.2.1 Irreducible representations of T_d

The point group of zincblende-type crystals is the group T_d, which consists of the 24 proper and improper rotations that leave a regular tetrahedron invariant. There are five irreducible representations that we label in the notation of Koster as Γ_1, Γ_2, Γ_3, Γ_4, and Γ_5. [KDWS63] Table 2.1 relates various notation commonly found in the literature.

In the crystal field, the electron wave functions transform according to the direct product of the single valued representations Γ_1 through Γ_5 and the double valued representation $D_{1/2}$ of 1/2-spin. [BP74] These products are in general reducible and decompose into the irreducible double group representations Γ_6, Γ_7, and Γ_8 as follows:

$$\begin{aligned} \Gamma_1 \times D_{1/2} &= \Gamma_6, \\ \Gamma_2 \times D_{1/2} &= \Gamma_7, \\ \Gamma_3 \times D_{1/2} &= \Gamma_8, \\ \Gamma_4 \times D_{1/2} &= \Gamma_6 + \Gamma_8, \\ \Gamma_5 \times D_{1/2} &= \Gamma_7 + \Gamma_8. \end{aligned} \tag{2.1}$$

The representation Γ_6 and Γ_7 are two-dimensional and the representation Γ_8 is four-dimensional.

2.2.2 Luttinger-Kohn Hamiltonian in T_d symmetry

As a central result of representation theory, wave functions that belong to the same irreducible representation are degenerate in energy. Further, since the Luttinger-Kohn Hamiltonian (1.13) must be invariant under symmetry operations of the group T_d, its matrix elements are subject to strict selection rules. [DKK55] Hence, the block $H_{i\alpha j\beta}$ of the Luttinger-Kohn Hamiltonian that couples the two irreducible representations $(i\alpha)$ and $(j\beta)$ can be written in terms of a few basis matrices, the so-called invariants. [Lut56, BP74, TRR79] Here, the indices $(i\alpha)$ and $(j\beta)$ denote the α-th occurrence of the irreducible representation Γ_i and the β-th occurrence of the irreducible representation Γ_j, respectively. In summary, the invariants of the Luttinger-Kohn Hamiltonian (1.13) are up to first order in $\mathbf{k}$ and read [MR91]

$$\begin{aligned}
H^{LK}_{6\alpha6\beta}(\mathbf{k}) &= \delta_{\alpha\beta}(E_{6\alpha} + \frac{\hbar^2k^2}{2m_0})\mathbf{1}_2, \\
H^{LK}_{7\alpha7\beta}(\mathbf{k}) &= \delta_{\alpha\beta}(E_{7\alpha} + \frac{\hbar^2k^2}{2m_0})\mathbf{1}_2 + (1-\delta_{\alpha\beta})\Delta_{7\alpha7\beta}\mathbf{1}_2, \\
H^{LK}_{8\alpha8\beta}(\mathbf{k}) &= \delta_{\alpha\beta}(E_{8\alpha} + \frac{\hbar^2k^2}{2m_0})\mathbf{1}_4 \\
&\quad +\bar{P}_{8\alpha8\beta}(\{J_y,J_z\}k_x + \{J_z,J_x\}k_y + \{J_x,J_y\}k_z) \\
&\quad +(1-\delta_{\alpha\beta})\Delta_{8\alpha8\beta}\mathbf{1}_4, \\
H^{LK}_{6\alpha7\beta}(\mathbf{k}) &= \bar{P}_{6\alpha7\beta}(k_x\sigma_x + k_y\sigma_y + k_z\sigma_z), \\
H^{LK}_{6\alpha8\beta}(\mathbf{k}) &= \bar{P}_{6\alpha8\beta}(k_xT_x + k_yT_y + k_zT_z), \\
H^{LK}_{7\alpha8\beta}(\mathbf{k}) &= (1-\delta_{\alpha\beta})\bar{P}_{7\alpha8\beta}(k_xT_{yz} + k_yT_{zx} + k_zT_{xy}).
\end{aligned} \tag{2.2}$$

The Pauli matrices are denoted by σ_i. The angular momentum matrices J_i, T_i, and T_{ij} are found in the literature [TRR79] and are summarized in appendix B. The symmetrized product of two matrices is denoted by $\{A,B\} \equiv \frac{1}{2}(AB+BA)$. The material parameters $\bar{P}_{i\alpha j\beta}$ are momentum matrix element between Bloch functions of the according representations. In the limit of small spin-orbit coupling, they correspond to the momentum matrix elements of the single group representations up to a numeric prefactor due to the expansion coefficients of the angular momentum bases. In general $\bar{P}_{i\alpha j\beta}$ and $\Delta_{i\alpha j\beta}$ are complex.

Note importantly, that, in contrast to Eq. (1.13), each eigenenergy $E_{i\alpha}$ at $\mathbf{k}=0$ includes only the intra-band spin-orbit coupling. The inter-band spin-orbit coupling introduces a small mixing between representations that are otherwise decoupled at $\mathbf{k}=0$. It is convenient to formulate the $k\cdot p$ Hamiltonian in these "pure" representations because, in this case, the momentum matrix elements are those of the single group representations. Therefore, the inter-band spin-orbit coupling is excluded from $E_{i\alpha}$ and thus has to be taken into account explicitly via the term $\Delta_{i\alpha j\beta}$.

2.3 Derivation of the second-order $k \cdot p$ Hamiltonian

2.3.1 Review of the first-order extended Kane model

Most of the technically important III-V and II-VI semiconductors have bonding p-like highest valence bands and anti-bonding s-like lowest conduction bands. [Mad96] Atomic s-symmetry (orbital angular momentum $L = 0\hbar$) is compatible to the Γ_1 irreducible representation. Atomic p-symmetry (orbital angular momentum $L = 1\hbar$) is compatible to the Γ_5 irreducible representation. [BP74] Therefore, we denote the Γ_1 and the Γ_5 bands as s-like and p-like, respectively.

Since the Γ_5 irreducible representation transforms like a vector, the basis functions are labeled X, Y, and Z according to the unit vector they transform like. The basis function of Γ_1 is labeled S with regard to atomic s-symmetry and transforms like a scalar. Since these basis functions transform like vectors and scalars in a Cartesian space, we label theses basis functions Cartesian.

The bonding states are of even and the anti-bonding states of odd parity in O_h. In most III-V semiconductors with T_d symmetry, parity is lifted only weakly. Hence, parity-forbidden matrix elements in O_h are still weak in T_d. [Win03] To describe effects that are due to inversion asymmetry in T_d the anti-bonding p-like conduction bands has to be included in the Hamiltonian explicitly. [TRR79, PZ96] Since inversion asymmetry leads to a lifting of parity, the momentum matrix elements between the anti-bonding p-like conduction and anti-bonding s-like conduction band are allowed and in general non-zero.

The bonding s-like valence bands are usually not included explicitly in the $k \cdot p$ Hamiltonian. These bands couple only weakly to the bonding p-like valence bands due to the weak lifting of parity. Further, they do not couple to the anti-bonding s-bands due to exact selection rules of the momentum matrix elements in T_d. [CCF88] The momentum matrix element between the anti-bonding s-like bands and anti-bonding p-like bands is parity-allowed and thus of substantial magnitude. [CCF88] However, the bands are very remote in energy (commonly $\gtrsim 10$ eV) and this coupling is suppressed. Therefore, their impact on the band structure close to the band gap is negligible.

Together, the p-like valence bands, the s-like and p-like conduction bands result in a 14-band $k \cdot p$ Hamiltonian, the so-called extended Kane model. A typical band structure of the extended Kane model is illustrated for bulk GaAs in Fig. 2.1. Note that the two Γ_8 bands split into two irreducible representations for $\mathbf{k} \neq 0$. Because of spin-orbit coupling, the Γ_5 irreducible representation is split into the Γ_7 and Γ_8 irreducible representations which are compatible with the full rotational group $D_{1/2}$ and $D_{3/2}$ of 1/2 and 3/2 spin, respectively. The direct product of Γ_1 and $D_{1/2}$ simply results in the irreducible representation Γ_6.

The basis functions of Γ_7 and Γ_8 can be written in terms of the vector-like Γ_5

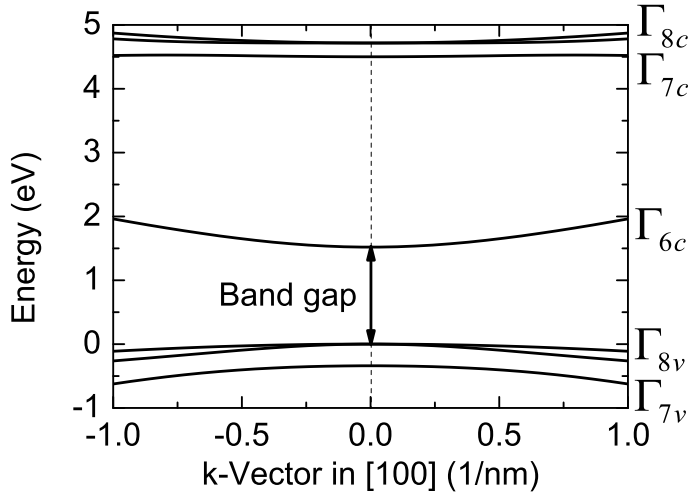

Figure 2.1: Energy dispersion of the extended Kane model for bulk GaAs in the [100] direction.

basis functions and the basis of 1/2-spin $|\uparrow\rangle$ and $|\downarrow\rangle$ as follows [Win03]

$$
\begin{aligned}
|\Gamma_8, +\tfrac{3}{2}\rangle &= |HH\uparrow\rangle = -\frac{1}{\sqrt{2}}|X\uparrow> -\frac{i}{\sqrt{2}}|Y\uparrow>, \\
|\Gamma_8, +\tfrac{1}{2}\rangle &= |LH\uparrow\rangle = \sqrt{\frac{2}{3}}|Z\uparrow> -\frac{1}{\sqrt{6}}|X\downarrow> -\frac{i}{\sqrt{6}}|Y\downarrow>, \\
|\Gamma_8, -\tfrac{1}{2}\rangle &= |LH\downarrow\rangle = \frac{1}{\sqrt{6}}|X\uparrow> -\frac{i}{\sqrt{6}}|Y\uparrow> +\sqrt{\frac{2}{3}}|Z\downarrow>, \\
|\Gamma_8, -\tfrac{3}{2}\rangle &= |HH\downarrow\rangle = \frac{1}{\sqrt{2}}|X\downarrow> -\frac{i}{\sqrt{2}}|Y\downarrow>, \\
|\Gamma_7, +\tfrac{1}{2}\rangle &= |SO\uparrow\rangle = -\frac{1}{\sqrt{3}}|Z\uparrow> -\frac{1}{\sqrt{3}}|X\downarrow> -\frac{i}{\sqrt{3}}|Y\downarrow>, \\
|\Gamma_7, -\tfrac{1}{2}\rangle &= |SO\downarrow\rangle = -\frac{1}{\sqrt{3}}|X\uparrow> \frac{i}{\sqrt{3}}|Y\uparrow> +\frac{1}{\sqrt{3}}|Z\downarrow> .
\end{aligned}
\tag{2.3}
$$

Here, we label the states by their irreducible representations and the projection of the total angular momentum. The quantization direction for the total angular momentum is taken to be the same as for the electron spin but is otherwise arbitrary. In addition, we have included the common termini heavy hole (HH), light hole (LH) and split-off hole (SO). This basis of Bloch functions is denoted as *angular momentum basis*.

Note that in general the Cartesian basis that constitutes the Γ_8 basis needs not be the same as the Cartesian basis that constitutes the Γ_7 basis. However, for most relevant semiconductors, the spin-orbit coupling is much smaller than the coupling of atomic orbitals. [JSBB98] We make the common assumption that the $\Gamma_7 + \Gamma_8$ basis functions emerge from the same Γ_5 basis. [DKK55]

The above expansion can be cast into a transformation matrix from the Cartesian to the angular representation

$$S_{78,5D} = S^H_{5D,78} = \begin{pmatrix} -\frac{1}{\sqrt{2}} & \frac{i}{\sqrt{2}} & 0 & 0 & 0 & 0 \\ 0 & 0 & \sqrt{\frac{2}{3}} & -\frac{1}{\sqrt{6}} & \frac{i}{\sqrt{6}} & 0 \\ \frac{1}{\sqrt{6}} & \frac{i}{\sqrt{6}} & 0 & 0 & 0 & \sqrt{\frac{2}{3}} \\ 0 & 0 & 0 & \frac{1}{\sqrt{2}} & \frac{i}{\sqrt{2}} & 0 \\ 0 & 0 & -\frac{1}{\sqrt{3}} & -\frac{1}{\sqrt{3}} & \frac{i}{\sqrt{3}} & 0 \\ -\frac{1}{\sqrt{3}} & -\frac{i}{\sqrt{3}} & 0 & 0 & 0 & \frac{1}{\sqrt{3}} \end{pmatrix}. \tag{2.4}$$

The index "$5D$" refers to the *reducible* representation $\Gamma_{5D} \equiv \Gamma_5 \times D_{1/2}$. By convention, the first four rows of $S_{78,5D}$ correspond to the Γ_8 representation and the last two rows to the Γ_7 representation in the same order as in Eqs. (2.3). The columns correspond to the $|X\uparrow\rangle$, $|Y\uparrow\rangle$, $|Z\uparrow\rangle$, $|X\downarrow\rangle$, $|Y\downarrow\rangle$, and $|Z\downarrow\rangle$ basis functions in this order.

The basis of Γ_6 is simply the product of the basis function S with the spinor basis, namely $\{|S\uparrow\rangle, |S\downarrow\rangle\}$. Hence, the transformation matrix is the identity

$$S_{6,1D} = S^H_{1D,6} = \begin{pmatrix} 1 & 0 \\ 0 & 1 \end{pmatrix}, \tag{2.5}$$

where again $\Gamma_{1D} \equiv \Gamma_1 \times D_{1/2}$.

We label the representations of the conduction band by c and the representations of the valence band by v. Thus, the 14-band model encompasses the irreducible representations Γ_{7c}, Γ_{8c}, Γ_{6c}, Γ_{7v}, and Γ_{8v}.

The 14-band $k \cdot p$ Hamiltonian without perturbative coupling to remote bands is constructed from the block Luttinger-Kohn Hamiltonians given in Eq. (2.2) and reads [MR91]

$$H^{LK}_{14}(\mathbf{k}) = \begin{pmatrix} H^{LK}_{8c8c} & H^{LK}_{8c7c} & H^{LK}_{8c6c} & H^{LK}_{8c8v} & H^{LK}_{8c7v} \\ & H^{LK}_{7c7c} & H^{LK}_{7c6c} & H^{LK}_{7c8v} & H^{LK}_{7c7v} \\ & & H^{LK}_{6c6c} & H^{LK}_{6c8v} & H^{LK}_{6c7v} \\ & h.c. & & H^{LK}_{8v8v} & H^{LK}_{8v7v} \\ & & & & H^{LK}_{7v7v} \end{pmatrix}, \tag{2.6}$$

where the lower left triangular part is the Hermite conjugate of the upper right triangular part.

The parameters in the block Hamiltonians in Eq. (2.2) are given by [MR91]

$$\begin{aligned}
&\bar{P}_{8c6c} = -i\sqrt{3}P', \quad \bar{P}_{7c6c} = i\frac{1}{\sqrt{3}}P', \\
&\bar{P}_{8c8v} = -\frac{2}{3}Q, \quad \bar{P}_{8c7v} = -2Q, \quad \bar{P}_{7c8v} = -2Q, \\
&\bar{P}_{6c8v} = \sqrt{3}P, \quad \bar{P}_{6c7v} = -\frac{1}{\sqrt{3}}P, \\
&\bar{P}_{8v8v} = \frac{2}{\sqrt{3}}C_k, \quad \bar{P}_{8c8c} = \frac{2}{\sqrt{3}}C_k', \\
&\Delta_{8c8v} = +\frac{1}{3}\Delta^-, \quad \Delta_{7c7v} = -\frac{2}{3}\Delta^-.
\end{aligned} \tag{2.7}$$

The k-linear spin splitting parameter C_k' of the Γ_{8c} band has no discernible impact on the band structure close to the band gap and is neglected in the following. As noted before, the band-offsets E_{8c} through E_{7v} at $\mathbf{k} = 0$ contain the intra-band spin-orbit coupling only. Clearly, experimentally measured values for the band gaps contain all spin-orbit splitting implicitly. However, the impact of the intra-band spin-orbit coupling on the band gaps is very small. It is thus not necessary to correct the band gaps although we formally excluded the intra-band spin-orbit coupling from these values.

The momentum matrix elements P, P', Q, and C_k and the spin-orbit coupling Δ^- are defined with respect to the basis of the according Γ_5 representations. In terms of the matrix elements of the Cartesian basis functions the parameters read [Kan57, Win03]

$$P = \frac{\hbar}{m_0}\langle S^c|\pi_x|X^v\rangle, \tag{2.8}$$

$$P' = \frac{1}{i}\frac{\hbar}{m_0}\langle S^c|\pi_x|X^c\rangle, \tag{2.9}$$

$$Q = \frac{\hbar}{m_0}\langle X^v|\pi_y|Z^c\rangle, \tag{2.10}$$

$$C_k = \frac{\hbar}{m_0}\langle X^v|\pi_y|Z^v\rangle, \tag{2.11}$$

$$\Delta_0 = -\frac{3i\hbar}{4m_0^2c^2}\langle X^v|[(\nabla V)\times\boldsymbol{\pi}]_y|Z^v\rangle, \tag{2.12}$$

$$\Delta_0' = -\frac{3i\hbar}{4m_0^2c^2}\langle X^c|[(\nabla V)\times\boldsymbol{\pi}]_y|Z^c\rangle, \tag{2.13}$$

$$\Delta^- = -\frac{3\hbar}{4m_0^2c^2}\langle X^v|[(\nabla V)\times\boldsymbol{\pi}]_y|Z^c\rangle, \tag{2.14}$$

where V is the crystal potential from Eq. (1.1). Again, v and c label the valence bands and conduction bands, respectively. The inter-band spin-orbit matrix element

between the p-like conduction and valence bands is denoted by Δ^-. The intra-band spin-orbit matrix elements Δ_0 and Δ_0' relate to the p-like valence and conduction bands, respectively.

The k-linear spin splitting parameter C_k is only due to the small relativistic spin-orbit part of the kinematic momentum $\hat{\boldsymbol{\pi}}$ in Eq. (1.14) because the matrix element of the canonical momentum $\hat{\mathbf{p}}$ vanishes identically irrespectively of the lack of inversion asymmetry.

Together with the fundamental band gap E_0, band offsets read [MR91]

$$\begin{aligned} E_{7v} &= E_{VBO} - 2\Delta_0/3, && (2.15)\\ E_{8v} &= E_{VBO} + \Delta_0/3, && (2.16)\\ E_{6c} &= E_{VBO} + \Delta_0/3 + E_0, && (2.17)\\ E_{7c} &= E_{VBO} + \Delta_0/3 + E_0', && (2.18)\\ E_{8v} &= E_{VBO} + \Delta_0/3 + E_0' + \Delta_0', && (2.19) \end{aligned}$$

where E_{VBO} denotes the material-dependent relative valence band offset. [VdW89]

Note that we use the standard phase convention: The Cartesian basis of bonding bands is purely real and the Cartesian basis of anti-bonding bands purely imaginary. [MR91, Win03] In contrast to Ref. [MR91], however, we define P' and Δ^- as the imaginary part of the according matrix elements such that all material constants are real following Ref. [JSdAeSLR05]. Consequently, the imaginary unit appears explicitly as a prefactor before these parameters in $\bar{P}_{8c6c}$, $\bar{P}_{8c6c}$, Δ_{8c8v}, and Δ_{7c7v} instead.

2.3.2 Operator ordering in the envelope function approximation

The real space Hamiltonian is obtained from the k-space Hamiltonian Eq. (2.6) by the substitution $\mathbf{k} \to \hat{\mathbf{k}} = -i\nabla$ and by introducing position-dependent material parameters. [Bur94, For96, For98] This results in the real-space envelope function approximation (EFA) Hamiltonian $H(\mathbf{k}) \to \hat{H}(\mathbf{r}, \hat{\mathbf{k}})$ that depends on the position vector $\mathbf{r}$ and the differential operator $\hat{\mathbf{k}}$.

In the presence of a magnetic field $\mathbf{B}$, the k-operator becomes $\hat{\mathbf{k}} \to \hat{\mathbf{K}} = -i\nabla + (e/\hbar)\mathbf{A}(\mathbf{r})$ with the corresponding vector potential $\mathbf{A}(\mathbf{r})$. The components of $\hat{\mathbf{K}}$ do not commute and fulfill the commutation relation

$$\left[\hat{K}_i, \hat{K}_j\right] = -i\epsilon^{ijk}\frac{e}{\hbar}B_k. \qquad (2.20)$$

Even without a magnetic field, the differential operator $\hat{\mathbf{k}}$ does not commute with the material parameters in heterostructures. Clearly, the ordering of material parameters and operators is no longer arbitrary as in the case of a bulk semiconductor without a magnetic field.

It has been shown that there are two valid orderings in which material parameters and first-order operators may appear. [For97] First-order operators appear either left or right of the parameters. In contrast, a symmetrized ordering has been shown to produce unphysical interface states.

Here, we choose a particular operator ordering that enables us to construct the spurious solution free variational envelope function space in Ch. 3. Explicitly, the first-order 14-band EFA Hamiltonian in the Luttinger-Kohn representations, i.e. without remote-band contributions, reads [MR91, Win03]

$$
\begin{aligned}
\hat{H}^{LK}_{8c8c}(\mathbf{r},\hat{\mathbf{k}}) &= \left(E_{8c}(\mathbf{r}) + \frac{\hbar^2}{2m_0}\hat{\mathbf{k}}^\dagger\hat{\mathbf{k}}\right)\mathbf{1}_4,\\
\hat{H}^{LK}_{7c7c}(\mathbf{r},\hat{\mathbf{k}}) &= \left(E_{7c}(\mathbf{r}) + \frac{\hbar^2}{2m_0}\hat{\mathbf{k}}^\dagger\hat{\mathbf{k}}\right)\mathbf{1}_2,\\
\hat{H}^{LK}_{6c6c}(\mathbf{r},\hat{\mathbf{k}}) &= \left(E_{6c}(\mathbf{r}) + \frac{\hbar^2}{2m_0}\hat{\mathbf{k}}^\dagger\hat{\mathbf{k}}\right)\mathbf{1}_2,\\
\hat{H}^{LK}_{8v8v}(\mathbf{r},\hat{\mathbf{k}}) &= \left(E_{8v}(\mathbf{r}) + \frac{\hbar^2}{2m_0}\hat{\mathbf{k}}^\dagger\hat{\mathbf{k}}\right)\mathbf{1}_4\\
&\quad + \frac{2}{\sqrt{3}}C_k\left(\{J_y,J_z\}k_x + \{J_z,J_x\}k_y + \{J_x,J_y\}k_z\right),\\
\hat{H}^{LK}_{7v7v}(\mathbf{r},\hat{\mathbf{k}}) &= \left(E_{7v}(\mathbf{r}) + \frac{\hbar^2}{2m_0}\hat{\mathbf{k}}^\dagger\hat{\mathbf{k}}\right)\mathbf{1}_2,\\
\hat{H}^{LK}_{8c6c}(\mathbf{r},\hat{\mathbf{k}}) &= -i\sqrt{3}P'(\mathbf{r})(\hat{k}_x U_x + \hat{k}_y U_y + \hat{k}_z U_z),\\
\hat{H}^{LK}_{7c6c}(\mathbf{r},\hat{\mathbf{k}}) &= i\frac{1}{\sqrt{3}}P'(\mathbf{r})(\hat{k}_x\sigma_x + \hat{k}_y\sigma_y + \hat{k}_z\sigma_z),\\
\hat{H}^{LK}_{8c8v}(\mathbf{r},\hat{\mathbf{k}}) &= -\frac{2}{3}Q(\mathbf{r})(\{J_y,J_z\}\hat{k}_x + \{J_z,J_x\}\hat{k}_y + \{J_x,J_y\}\hat{k}_z)\\
&\quad + \frac{1}{3}\Delta^-(\mathbf{r})\mathbf{1}_4,\\
\hat{H}^{LK}_{8c7v}(\mathbf{r},\hat{\mathbf{k}}) &= -2Q(\mathbf{r})(\hat{k}_x U_{yz} + \hat{k}_y U_{zx} + \hat{k}_z U_{xy}),\\
\hat{H}^{LK}_{7c8v}(\mathbf{r},\hat{\mathbf{k}}) &= -2Q(\mathbf{r})(\hat{k}_x T_{yz} + \hat{k}_y T_{zx} + \hat{k}_z T_{xy}),\\
\hat{H}^{LK}_{7c7v}(\mathbf{r},\hat{\mathbf{k}}) &= -\frac{2}{3}\Delta^-(\mathbf{r})\mathbf{1}_2,\\
\hat{H}^{LK}_{6c8v}(\mathbf{r},\hat{\mathbf{k}}) &= \sqrt{3}(\hat{k}_x^\dagger T_x + \hat{k}_y^\dagger T_y + \hat{k}_z^\dagger T_z)P(\mathbf{r}),\\
\hat{H}^{LK}_{6c7v}(\mathbf{r},\hat{\mathbf{k}}) &= -\frac{1}{\sqrt{3}}(\hat{k}_x^\dagger\sigma_x + \hat{k}_y^\dagger\sigma_y + \hat{k}_z^\dagger\sigma_z)P(\mathbf{r}),
\end{aligned}
\tag{2.21}
$$

where U_{ij} is the conjugate transpose of T_{ij}.

To make the operator ordering unambiguous, we distinguish between operators that act on the right and on the left in the variational formulation of the Hamiltonian eigenvalue problem: The daggered operator $\hat{\mathbf{k}}^\dagger$ acts on the left and the operator $\hat{\mathbf{k}}$ on

the right, irrespectively of where the operators appear in a term. Thus,

$$\langle F_i^c|\hat{\mathbf{k}}^\dagger a(\mathbf{r})\hat{\mathbf{k}}|F_j^{c'}\rangle \equiv \langle F_i^c|a(\mathbf{r})\hat{\mathbf{k}}^\dagger\hat{\mathbf{k}}|F_j^{c'}\rangle \equiv \langle \hat{\mathbf{k}}F_i^c|a(\mathbf{r})|\hat{\mathbf{k}}F_j^{c'}\rangle, \tag{2.22}$$

for the c and c' components of two envelope functions F_i and F_j respectively and a position-dependent parameter function $a(\mathbf{r})$. The action of individual components of $\hat{\mathbf{k}}^\dagger$ and $\hat{\mathbf{k}}$ is defined analogous. This slight abuse of notation will substantially simplify the expressions for the perturbative remote-band contributions in the following sections. Moreover, we will always consider the EFA Hamiltonian and skip the explicit dependencies on $\mathbf{r}$ and $\hat{\mathbf{k}}$ in the following.

2.3.3 Coupling of the free electron spin to a magnetic field

It is apparent from Pauli-Schrödinger equation (1.1) that the free electron spin couples directly to a magnetic field. [1] This coupling is trivial in the Cartesian basis since the basis functions are products of the single group basis functions and the basis of spin. From this, we obtain the coupling in the angular momentum basis by the transformations Eq. (2.4) and Eq. (2.5).

Hence, the magnetic interaction Hamiltonian of Γ_6^c reads

$$\hat{H}^B_{6c6c} = \mu_B \frac{g_0}{2}\boldsymbol{\sigma}\cdot\mathbf{B}, \tag{2.23}$$

where $\boldsymbol{\sigma} = (\sigma_x, \sigma_y, \sigma_z)^T$ is the vector of Pauli matrices.

The magnetic interaction Hamiltonian of the Γ_7 and Γ_8 in obtained from the magnetic Hamiltonian of the reducible $\Gamma_5 \times D_{1/2}$ representation. As before, we require that the Γ_7 and Γ_8 basis can be constructed from the same Γ_5 basis. The magnetic Hamiltonian of Γ_{5Dc} thus reads

$$\hat{H}^B_{5Dc5Dc} = \mu_B \frac{g_0}{2}(\boldsymbol{\sigma}\cdot\mathbf{B}) \times \mathbf{1}_3. \tag{2.24}$$

Here, "$\times$" denotes the Kronecker product. Applying Eq. (2.4), we obtain the magnetic interaction Hamiltonian of $\Gamma_{7c} + \Gamma_{8c}$ as

$$\begin{aligned}
\hat{H}^B_{8c8c} &= \frac{2}{3}\mu_B\frac{g_0}{2}\left(J_xB_x + J_yB_y + J_zB_z\right), && (2.25)\\
\hat{H}^B_{7c8c} &= -2\mu_B\frac{g_0}{2}\left(T_xB_x + T_yB_y + T_zB_z\right), && (2.26)\\
\hat{H}^B_{8c7c} &= \hat{H}^\dagger_{7c8c}, && (2.27)\\
\hat{H}^B_{7c7c} &= -\frac{1}{3}\mu_B\frac{g_0}{2}\left(\sigma_xB_x + \sigma_yB_y + \sigma_zB_z\right). && (2.28)
\end{aligned}$$

The analogous Hamiltonian is obtained for $\Gamma_{7v} + \Gamma_{8v}$. The angular momentum matrices σ_i, T_i, and J_i are given in the appendix B.

[1] Here, the coupling of the *free* electron spin is to be understood as opposed to the *effective* coupling within the crystal potential.

2.3.4 Perturbative coupling to remote bands

In order to represent the band structure close to the band gap accurately, the remote bands not included in the 14-band model need to be taken into account perturbatively. To this end, we employ Loewdin's perturbation theory (1.40) to derive perturbative terms up to second-order in $\hat{\mathbf{k}}$.

Here, we consider second-order intra-band terms within the Γ_{6c} and the $\Gamma_{7v}+\Gamma_{8v}$ representations only. Second-order intra-band terms within the $\Gamma_{7c}+\Gamma_{8c}$ representations are neglected because they have no substantial influence on the bands close to the band gap. Further, all second-order inter-band terms are neglected for the same reason.

We discuss the perturbative contributions to the Γ_{6c} intra-band Hamiltonian explicitly. The contributions from remote Γ_6, Γ_7, and Γ_8 are directly derived from the complete Luttinger-Kohn Hamiltonian (2.2) by Loewdin's perturbation theory and read

$$\hat{H}^{6}_{6c6c} = \sum_{\alpha\neq c} \frac{\hat{H}^{LK\dagger}_{6\alpha6c}\hat{H}^{LK}_{6\alpha6c}}{E_{6c}-E_{6\alpha}} = 0, \tag{2.29}$$

$$\begin{aligned}
\hat{H}^{7}_{6c6c} &= \sum_{\alpha\neq c,v} \frac{\hat{H}^{LK\dagger}_{7\alpha6c}\hat{H}^{LK}_{7\alpha6c}}{E_{6c}-E_{7\alpha}} \\
&= \sum_{\alpha\neq c,v} \frac{|\bar{P}_{6c7\alpha}|^2}{E_{6c}-E_{7\alpha}} (k_x\sigma_x+k_y\sigma_y+k_z\sigma_z)^{\dagger}(k_x\sigma_x+k_y\sigma_y+k_z\sigma_z) \\
&= \sum_{\alpha\neq c,v} \frac{|\bar{P}_{6c7\alpha}|^2}{E_{6c}-E_{7\alpha}} (\hat{\mathbf{k}}^{\dagger}\hat{\mathbf{k}}\mathbf{1}_2 + i[(\hat{k}^{\dagger}_x\hat{k}_y-\hat{k}^{\dagger}_y\hat{k}_x)\sigma_z + c.p.]),
\end{aligned} \tag{2.30}$$

$$\begin{aligned}
\hat{H}^{8}_{6c6c} &= \sum_{\alpha\neq c,v} \frac{\hat{H}^{LK\dagger}_{8\alpha6c}\hat{H}^{LK}_{8\alpha6c}}{E_{6c}-E_{8\alpha}} \\
&= \sum_{\alpha\neq c,v} \frac{|\bar{P}_{6c8\alpha}|^2}{E_{6c}-E_{8\alpha}} (\frac{2}{9}\hat{\mathbf{k}}^{\dagger}\hat{\mathbf{k}}\mathbf{1}_2 - \frac{i}{9}[(\hat{k}^{\dagger}_x\hat{k}_y-\hat{k}^{\dagger}_y\hat{k}_x)\sigma_z + c.p.]).
\end{aligned} \tag{2.31}$$

Note again that the daggered operators always act on the left irrespective of their appearance in the terms. The abbreviation "*c.p.*" denotes the cyclic permutations of the indices x, y, and z of the previous terms.

For the bulk semiconductor in the presence of a mangetic field, we have that $(\hat{k}^{\dagger}_x\hat{k}_y-\hat{k}^{\dagger}_y\hat{k}_x) \rightarrow [K_x,K_y] = -i\frac{e}{\hbar}B_z$. Terms of this type thus contribute to the effective coupling to a magnetic field. This coupling is mediated by the orbital motion of remote band basis states and is thus conceptually different from the coupling of the free electron g-factor to the magnetic field.

We can gather the perturbative terms in two material parameters. The first

parameter

$$\bar{A}' = \sum_{\alpha\neq c,v} \frac{|\bar{P}_{6c7\alpha}|^2}{E_{6c}-E_{7\alpha}} + \frac{2}{9}\sum_{\alpha\neq c,v} \frac{|\bar{P}_{6c8\alpha}|^2}{E_{6c}-E_{8\alpha}}, \tag{2.32}$$

and the second parameter

$$\frac{\hbar^2}{2m_0}\bar{g}'_* = 2\sum_{\alpha\neq c,v} \frac{|\bar{P}_{6c7\alpha}|^2}{E_{6c}-E_{7\alpha}} - \frac{2}{9}\sum_{\alpha\neq c,v} \frac{|\bar{P}_{6c8\alpha}|^2}{E_{6c}-E_{8\alpha}}, \tag{2.33}$$

contribute to the effective mass and the effective g-factor of the Γ_{6c}, respectively. They are related to the common derived Luttinger-like parameters A' and g'_* of the Γ_{6c} band by [For97, TRR79]

$$\bar{A}' = A' - \frac{\hbar^2}{2m_0} = \frac{\hbar^2}{2m_0}\left(\frac{m_0}{m'_*}-1\right), \tag{2.34}$$

$$\bar{g}'_* = g'_* - g_0, \tag{2.35}$$

where m'_* is the derived effective mass of the Γ_{6c} band.

The Luttinger-Kohn Hamiltonian (2.6) together with these perturbative contributions results in the second-order $k\cdot p$ intra-band Hamiltonian of the Γ_{6c} band

$$\hat{H}^{k\cdot p}_{6c6c} = \left(E_{6c}(\mathbf{r}) + \frac{\hbar^2}{2m_0}\hat{\mathbf{k}}^\dagger\hat{\mathbf{k}}\right) + \hat{H}^6_{6c6c} + \hat{H}^7_{6c6c} + \hat{H}^8_{6c6c} \tag{2.36}$$

$$= \frac{\hbar^2}{2m_0}A'\hat{\mathbf{k}}^\dagger\hat{\mathbf{k}}\mathbf{1}_2 + i\frac{\hbar^2}{2m_0}\frac{g'_*-g_0}{2}\left[(\hat{k}^\dagger_x\hat{k}_y - \hat{k}^\dagger_y\hat{k}_x)\sigma_z + c.p.\right] + \mu_B\frac{g_0}{2}\boldsymbol{\sigma}\cdot\mathbf{B}. \tag{2.37}$$

In the bulk limit, we have that $\hat{\mathbf{k}} \to \mathbf{K} = \mathbf{k} + (e/\hbar)\mathbf{A}$ and the Γ_{6c} Hamiltonian reduces to

$$H^{k\cdot p}_{6c6c}(k) \to E_{6c}\mathbf{1}_2 + \frac{\hbar^2}{2m'_*}\mathbf{K}^2\mathbf{1}_2 + \mu_B\frac{g'_*}{2}\boldsymbol{\sigma}\cdot\mathbf{B}, \tag{2.38}$$

in agreement with the literature. [TRR79]

The contribution of remote bands to the perturbative $\Gamma_{8v}+\Gamma_{7v}$ Hamiltonian is derived analogously. However, the explicit expressions are cumbersome and we present our results only. The Γ_{8v} intra-band $k\cdot p$ Hamiltonian results in

$$\begin{aligned}\hat{H}^{k\cdot p}_{8v8v} = {} & E_{8v}\mathbf{1}_4 - \frac{\hbar^2}{2m_0}\Big((\bar{\gamma}'_1+1)\hat{\mathbf{k}}^\dagger\hat{\mathbf{k}}\mathbf{1}_4 \\ & -2\gamma'_2[(J_x^2-\frac{1}{3}J^2)\hat{k}^\dagger_x\hat{k}_x + \ldots] - 2\gamma'_3[\{J_x,J_y\}(\hat{k}^\dagger_x\hat{k}_y + \hat{k}^\dagger_y\hat{k}_x) + c.p.] \\ & +2i\bar{\kappa}'[J_z(\hat{k}^\dagger_x\hat{k}_y - \hat{k}^\dagger_y\hat{k}_x) + c.p.] + 2iq'[J_z^3(\hat{k}^\dagger_x\hat{k}_y - \hat{k}^\dagger_y\hat{k}_x) + c.p.]\Big) \\ & +\frac{2}{3}\mu_B\frac{g_0}{2}\left(J_xB_x + J_yB_y + J_zB_z\right) \\ & +\frac{2}{\sqrt{3}}C_k\left(\{J_y,J_z\}k_x + \{J_z,J_x\}k_y + \{J_x,J_y\}k_z\right),\end{aligned} \tag{2.39}$$

where the remote-band contributions $\bar{\gamma}_1'$ and $\bar{\kappa}'$ are related to the derived Luttinger γ_1' and κ' parameters by

$$\bar{\gamma}_1' = \gamma_1' - 1, \bar{\kappa}' = \kappa' + \frac{g_0}{6}. \tag{2.40}$$

We chose the numerical prefactors of the above terms such that γ_1', γ_2', γ_3', κ', and q' are identical to the derived Luttinger parameters. [Lut56, MR91] Analogously, the second-order Γ_{7v} and $\Gamma_{8v} - \Gamma_{7v}$ $k \cdot p$ Hamiltonians read

$$\begin{aligned} H_{7v7v}^{k\cdot p}(\mathbf{k}) &= E_{7v}\mathbf{1}_2 - \frac{\hbar^2}{2m_0}\Big((\bar{\gamma}_1'+1)\hat{\mathbf{k}}^\dagger\hat{\mathbf{k}}\mathbf{1}_2 - 2i\bar{\kappa}'[\sigma_z(\hat{k}_x^\dagger\hat{k}_y - \hat{k}_y^\dagger\hat{k}_x) + c.p.]\Big) \\ &\quad -\frac{1}{3}\mu_B\frac{g_0}{2}\left(\sigma_x B_x + \sigma_y B_y + \sigma_z B_z\right), \qquad (2.41) \\ H_{8v7v}^{k\cdot p}(\mathbf{k}) &= -\frac{\hbar^2}{2m_0}\Big(-6\gamma_2'[U_{xx}\hat{k}_x^\dagger\hat{k}_x + \ldots] - 6\gamma_3'[U_{xy}(\hat{k}_x^\dagger\hat{k}_y + \hat{k}_y^\dagger\hat{k}_x) + c.p.] \\ &\quad -3i\bar{\kappa}'[U_z(\hat{k}_x^\dagger\hat{k}_y - \hat{k}_y^\dagger\hat{k}_x) + c.p.]\Big) \\ &\quad -2\mu_B\frac{g_0}{2}\left(U_x B_x + U_y B_y + U_z B_z\right). \qquad (2.42) \end{aligned}$$

In the bulk limit, these Hamiltonians reduce to the expressions found in the literature. [TRR79, MR91]

The perturbative material parameters that occur in $\hat{H}_{7v7v}^{k\cdot p}$, $\hat{H}_{8v7v}^{k\cdot p}$, and $\hat{H}_{8v8v}^{k\cdot p}$ are in general not the same. This is because the energy denominators in the Loewdin's perturbation theory (1.40) differs by the spin-orbit splitting for the Γ_{7v} and Γ_{8v} bands. In this work, however, we are not interested in the details of the Γ_{7v} split-off bands. Like Ref. [MR91], we thus use the parameters of the Γ_{8v} intra-band Hamiltonian $\hat{H}_{8v8v}^{k\cdot p}$ for $\hat{H}_{7v7v}^{k\cdot p}$ and $\hat{H}_{8v7v}^{k\cdot p}$ as well. This guarantees that the Γ_{8v} bands are represented accurately.

Note that, in contrast to Luttinger's work and this work, Dresselhaus obtained the remote-band contributions for the single group representations only. [Lut56, DKK55] Hence, the center of the Γ_{5v} band $E_{5v} = (2E_{8v} + E_{7v})/3$ entered Loewdin's perturbation theory (1.40) instead of the energy offsets of the Γ_{8v} and Γ_{7v} bands. This is a valid approximation for semiconductors with small spin-orbit coupling $\Delta_0 \ll E_0$ only. Otherwise, neither the dispersion of the Γ_{8v} nor of the Γ_{7v} is well-represented by the $k \cdot p$ Hamiltonian. Note that consequently no simple relation exists between the Dresselhaus parameters F, G, H_1 and H_2 and the derived Luttinger parameters used in this work.

2.4 Linear response theory of the g-tensor

In the following, we discuss the linear response of a spin-degenerate state to a magnetic field. For the sake of clarity, we discuss a magnetic field in the z-direction only and the basis of spin is quantized in the same direction. The following derivation

applies to other directions of the magnetic field and quantization axes of the spin analogously leading to perturbative formulas for all components of the g-tensor.

The g-factor of the electronic state of orbital index n with spin orientation $\uparrow$ or $\downarrow$ ($|n,\uparrow\rangle$ and $|n,\downarrow\rangle$) can be written as [KIR98]

$$g_n = g_0 + g_n^L, \tag{2.43}$$

where $g_0 \approx 2$ is the free electron Landé g-factor and g_n^L is the contribution to the g-factor due to the angular motion of the electron.

The interaction of a magnetic field $\delta\hat{H}$ with the orbital motion can be accounted for in first-order perturbation theory by [KIR98]

$$\delta\hat{H} \approx \delta\mathbf{A} \cdot \left.\frac{\partial\hat{H}}{\partial\mathbf{A}}\right|_{\mathbf{A}=\mathbf{0}} = e\delta\mathbf{A}\cdot\hat{\mathbf{V}}, \tag{2.44}$$

where $\delta\mathbf{A}$ is the vector potential corresponding to a differential magnetic field $\delta\mathbf{B}$. The $k\cdot p$ velocity operator is given by $\hat{\mathbf{V}} = \hat{\mathbf{P}}/m_0$ where $\hat{\mathbf{P}} = \frac{m_0}{\hbar}\nabla_{\mathbf{k}}\hat{H}(\mathbf{k})$ is the $k\cdot p$ momentum operator obtained by the approximate Hellmann-Feynman theorem (1.45).

Importantly, the Hamiltonian derived in Sec. 2.6 contains all perturbative remote-band contributions in terms of $\hat{\mathbf{K}} = \hat{\mathbf{k}} + \frac{e}{\hbar}\mathbf{A}$. Thus, all far-band contributions enter the momentum operator via the Hellmann-Feynman theorem. We want to emphasize that it is crucial to preserve the operator ordering inherited from the Hamiltonian.

From relation (2.44), we now derive the linear response of the energy levels to a magnetic field $\delta\hat{H}/\delta\mathbf{B}$. In the symmetric Coulomb gauge, $\delta\mathbf{A} = (\delta\mathbf{B}\times\mathbf{r})/2$, we may write

$$\delta\hat{H} = \frac{e}{2m_0}(\delta\mathbf{B}\times\mathbf{r})\cdot\hat{\mathbf{P}} = \frac{e}{2m_0}\delta\mathbf{B}\cdot(\mathbf{r}\times\hat{\mathbf{P}}) = \frac{e}{2m_0}\delta\mathbf{B}\cdot\mathbf{L}, \tag{2.45}$$

with the $k\cdot p$ orbital angular momentum operator $\hat{\mathbf{L}} = \mathbf{r}\times\hat{\mathbf{P}}$. Hence, the response to a magnetic field is

$$\left.\frac{\delta\hat{H}}{\delta\mathbf{B}}\right|_{\mathbf{B}=0} = \frac{e}{2m_0}\hat{\mathbf{L}} = \mu_B\frac{1}{\hbar}\hat{\mathbf{L}}. \tag{2.46}$$

For the magnetic field $\mathbf{B} = B\mathbf{e}_z$ and the spin quantized in the same direction, the perturbative contribution of the orbital angular motion to the g-factor thus results in

$$g_n^L = \frac{1}{\hbar}\Big(\langle n\uparrow|\hat{L}_z|n\uparrow\rangle - \langle n\downarrow|\hat{L}_z|n\downarrow\rangle\Big). \tag{2.47}$$

Consequently, the effective g-factor in linear response theory becomes

$$g_n = g_0 + \frac{1}{\hbar}\Big(\langle n\uparrow|\hat{L}_z|n\uparrow\rangle - \langle n\downarrow|\hat{L}_z|n\downarrow\rangle\Big). \tag{2.48}$$

Equation (2.48) is readily evaluated to compute the g-factor perturbatively *without* including the magnetic field in the Hamiltonian. To this end, $|n\uparrow\rangle$ and $|n\downarrow\rangle$

are selected from the n-th twofold spin-degenerate eigenstate of $\hat{H}(\mathbf{B}=0)$ by diagonalizing the spin projection operator of the free electron $\hat{S}_z$ in z-direction. The eigenvectors corresponding to the positive and negative eigenvalues of $\hat{S}_z$ yield the states $|n\uparrow\rangle$ and $|n\downarrow\rangle$, respectively. Note that $\hat{S}_z$ commutes with $\hat{H}(\mathbf{B}=0)$, thus both operators can be diagonalized at the same time.

Note importantly that the expectation value of the angular momentum operator is a well-defined observable for bound states. The expectation value *does not* depend on the origin of the coordinate system, although it depends on the position operator. This is due to the fact that the expectation value of momentum vanishes for bound states. Consequently, $\langle n|(\mathbf{r}-\mathbf{r}_0)\times\hat{\mathbf{P}}|n\rangle = \langle n|\mathbf{r}\times\hat{\mathbf{P}}|n\rangle$, since $\langle n|\mathbf{r}_0\times\hat{\mathbf{P}}|n\rangle = \mathbf{r}_0\times\langle n|\hat{\mathbf{P}}|n\rangle = 0$ for any translation of the coordinate system by the vector $\mathbf{r}_0$.

The complete g-tensor $\overleftrightarrow{G}_n$ of the n-th orbital state is obtained analogously as

$$(G_n)_{ij} = \delta_{ij}g_0 + \frac{1}{\hbar}\left(\langle n\uparrow_j|\hat{L}_i|n\uparrow_j\rangle - \langle n\downarrow_j|\hat{L}_i|n\downarrow_j\rangle\right), \tag{2.49}$$

where $i,j=x,y,z$ and $|n\uparrow_j\rangle$ and $|n\downarrow_j\rangle$ denote the eigenvectors of the spin projection operator $\hat{S}_j$ in the twofold spin-degenerate sub-space of the n-th orbital state.

The spin projection operator in the angular momentum basis is directly read from the magnetic interaction Hamiltonian of the free electron g-factor in Eqs. (2.23) and (2.28). This results in

$$(\hat{S}_i)_{6c6c} = \sigma_i, \tag{2.50}$$
$$(\hat{S}_i)_{8c8c} = \frac{2}{3}J_i, \tag{2.51}$$
$$(\hat{S}_i)_{7c8c} = -2T_i, \tag{2.52}$$
$$(\hat{S}_i)_{8c7c} = (\hat{S}_i)^\dagger_{7c8c}, \tag{2.53}$$
$$(\hat{S}_i)_{7c7c} = -\frac{1}{3}\sigma_i, \tag{2.54}$$

for the Γ_{6c} and $\Gamma_{7c}+\Gamma_{8c}$ conduction bands and analogously for the $\Gamma_{7v}+\Gamma_{8v}$ valence bands.

As noted before, it is crucial to preserve the operator ordering inherited from the Hamiltonian. The momentum operator contains first-order differential operators acting on the left ($\hat{\mathbf{P}}^{\leftarrow}$) and acting on the right ($\hat{\mathbf{P}}^{\rightarrow}$). Zero-th order terms in $\hat{\mathbf{P}}$ commute with $\mathbf{r}$ and can be included on either side. The definition of the angular momentum operator is thus to be understood in the sense of

$$\hat{L}_i = \epsilon^{ijk}r_j\hat{P}_k \equiv \epsilon^{ijk}(r_j\hat{P}^{\rightarrow}_k + \hat{P}^{\leftarrow}_k r_j). \tag{2.55}$$

We illustrate this on hands of the perturbative contribution to the g-factor of the Γ_{6c} bands. For the sake of clarity, we assume the parameter $\bar{g}_*$ to be position-independent. The far-band contribution to the magnetic interaction of the Γ_{6c} Hamiltonian (2.37) reads

$$\hat{H} = i\frac{\hbar^2}{2m_0}\frac{\bar{g}_*}{2}\left[(\hat{K}^\dagger_x\hat{K}_y - \hat{K}^\dagger_y\hat{K}_x)\sigma_z + c.p.\right]. \tag{2.56}$$

The matrix element between two envelope functions $F_{ns}(\mathbf{r})$ and $F_{n's'}(\mathbf{r})$, where n and n' indicate the orbital quantum numbers and s and s' the spin state, is

$$\begin{aligned} H_{ns,n's'} &= i\frac{\hbar^2}{2m_0}\frac{\bar{g}_*}{2}\int_\Omega \mathrm{d}r^3 \Big(\Big[\hat{K}_x F^*_{ns}(\mathbf{r})\Big] \Big[\hat{K}_y F_{n's'}(\mathbf{r})\Big] \\ &\qquad - \Big[\hat{K}_y F^*_{ns}(\mathbf{r})\Big] \Big[\hat{K}_x F_{n's'}(\mathbf{r})\Big] \Big) \sigma_z + c.p.\,. \end{aligned} \tag{2.57}$$

In the symmetric Coulomb gauge for $\mathbf{B} = B_z\mathbf{e}_z$, we have that

$$\hat{K}_x = \hat{k}_x - \frac{e}{2\hbar}B_z r_y, \tag{2.58}$$

$$\hat{K}_y = \hat{k}_y + \frac{e}{2\hbar}B_z r_x, \tag{2.59}$$

$$\hat{K}_z = \hat{k}_z. \tag{2.60}$$

Note that the terms in $H_{ns,n's'}$ involving σ_x and σ_y (implicitly denoted by "c.p.") vanish because $\hat{K}_z$ commutes with $\hat{K}_x$ and $\hat{K}_y$.

Hence, the linear response to the **B**-field results in

$$\begin{aligned} \left.\frac{\delta H_{ns,n's'}}{\delta B_z}\right|_{\mathbf{B}=0} &= \frac{i\mu_B\bar{g}_*}{4}\sigma_z\int_\Omega \mathrm{d}r^3 \\ &\quad \times \Big(-r_y F^*_{ns}(\mathbf{r})\Big[\hat{k}_y F_{n's'}(\mathbf{r})\Big] + r_x\Big[\hat{k}_x F^*_{ns}(\mathbf{r})\Big] F_{n's'}(\mathbf{r}) \\ &\quad + r_y\Big[\hat{k}_y F^*_{ns}(\mathbf{r})\Big] F_{n's'}(\mathbf{r}) - r_x F^*_{ns}(\mathbf{r})\Big[\hat{k}_x F_{n's'}(\mathbf{r})\Big]\Big). \end{aligned} \tag{2.61}$$

On the other hand, the momentum operator corresponding to $\hat{H}$ at $\mathbf{B} = 0$ is

$$\begin{aligned} \hat{\mathbf{P}} &= \frac{m_0}{\hbar}\nabla_{\mathbf{k}}\hat{H} = \frac{i\hbar\bar{g}_*}{4}\Big[\sigma_z(\hat{k}_x^\dagger\mathbf{e}_y + \hat{k}_y\mathbf{e}_x - \hat{k}_y^\dagger\mathbf{e}_x - \hat{k}_x\mathbf{e}_y) + c.p.\Big] \\ &= \hat{\mathbf{P}}^{\rightarrow} + \hat{\mathbf{P}}^{\leftarrow}, \end{aligned} \tag{2.62}$$

with

$$\begin{aligned} \hat{\mathbf{P}}^{\rightarrow} &= \frac{i\hbar\bar{g}_*}{4}\Big[\sigma_z(\hat{k}_y\mathbf{e}_x - \hat{k}_x\mathbf{e}_y) + c.p.\Big], \\ \hat{\mathbf{P}}^{\leftarrow} &= \frac{i\hbar\bar{g}_*}{4}\Big[\sigma_z(\hat{k}_x^\dagger\mathbf{e}_y - \hat{k}_y^\dagger\mathbf{e}_x) + c.p.\Big]. \end{aligned} \tag{2.63}$$

Therefore, the z-component of the angular momentum operator is

$$\hat{L}_z = r_x\hat{P}_y - r_y\hat{P}_x \equiv r_x\hat{P}_y^{\rightarrow} + \hat{P}_y^{\leftarrow}r_x - r_y\hat{P}_x^{\rightarrow} - \hat{P}_x^{\leftarrow}r_y, \tag{2.64}$$

and the according matrix element between $F_{ns}(\mathbf{r})$ and $F_{n's'}(\mathbf{r})$ yields

$$\begin{aligned}(L_z)_{ns,n's'} &= \frac{i\hbar\bar{g}_*}{4}\sigma_z \int_\Omega \mathrm{d}r^3 \\ &\quad \times \Big(-r_x F^*_{ns}(\mathbf{r}) \left[\hat{k}_x F_{n's'}(\mathbf{r})\right] + r_x \left[\hat{k}_x F^*_{ns}(\mathbf{r})\right] F_{n's'}(\mathbf{r}) \\ &\quad\quad + r_y \left[\hat{k}_y F^*_{ns}(\mathbf{r})\right] F_{n's'}(\mathbf{r}) - r_y F^*_{ns}(\mathbf{r}) \left[\hat{k}_y F_{n's'}(\mathbf{r})\right]\Big) \\ &= \frac{\hbar}{\mu_B} \left.\frac{\delta H_{ns,n's'}}{\delta B_z}\right|_{\mathbf{B}=0}. \end{aligned} \tag{2.65}$$

This verifies Eq. (2.46). It shows that the $k \cdot p$ angular momentum operator is indeed proportional to the linear response to a magnetic field in the z-direction. The response to a magnetic field in another direction and for all other terms in the $k \cdot p$ Hamiltonian follows analogously. Consequently, the linear response $\hat{H}'$ to a magnetic field $\mathbf{B}$ is

$$\hat{H}' \approx \mathbf{B} \cdot \left.\frac{\delta \hat{H}}{\delta \mathbf{B}}\right|_{\mathbf{B}=0} = \mu_B \mathbf{B} \cdot \frac{1}{\hbar}\hat{\mathbf{L}}. \tag{2.66}$$

Note that this relation can also be used to compute the diamagnetic shift ΔE_n^{dia} perturbatively by

$$\Delta E_n^{dia} = \frac{\mu_B}{\hbar}\frac{1}{2}\left(\langle n\uparrow|\mathbf{B}\cdot\hat{\mathbf{L}}|n\uparrow\rangle + \langle n\downarrow|\mathbf{B}\cdot\hat{\mathbf{L}}|n\downarrow\rangle\right), \tag{2.67}$$

where the spin quantization axis is arbitrary in this context.

2.5 Relation to $k \cdot p$ models with fewer bands

2.5.1 The eight-band model

If the lack of inversion symmetry is not relevant, the Γ_{7c} and Γ_{8c} conduction bands need to be taken into account only perturbatively. The subsequent application of Loewdin's perturbation theory yields an eight-band model of the Γ_{6c} conduction and the Γ_{7v} and Γ_{8v} valence bands.

Compared to the 14-band $k \cdot p$ Hamiltonian, no new material parameters are necessary since all relevant symmetry allowed remote-band contributions are already included. However, the derived Luttinger parameters for the eight-band model need to be corrected by the perturbative contribution from the Γ_{7c} and Γ_{8c} conduction

bands. Loewdin's perturbation theory (1.40) yields the so-called rescaling relations

$$\begin{aligned}
\gamma_1 &= \gamma_1' + \frac{1}{3}\frac{2m_0}{\hbar^2}\left(\frac{Q^2}{E_0'+\Delta_0'} + \frac{Q^2}{E_0'}\right), \\
\gamma_2 &= \gamma_2' - \frac{1}{6}\frac{2m_0}{\hbar^2}\frac{Q^2}{E_0'}, \\
\gamma_3 &= \gamma_3' + \frac{1}{6}\frac{2m_0}{\hbar^2}\frac{Q^2}{E_0'}, \\
\kappa &= \kappa' + \frac{1}{18}\frac{2m_0}{\hbar^2}\left(7\frac{Q^2}{E_0'+\Delta_0'} - 10\frac{Q^2}{E_0'}\right), \\
q &= q' + \frac{2}{9}\frac{2m_0}{\hbar^2}\left(-\frac{Q^2}{E_0'+\Delta_0'} + \frac{Q^2}{E_0'}\right),
\end{aligned} \tag{2.68}$$

for the derived eight-band Luttinger parameters γ_1, γ_2, γ_3, κ, and q. Further the rescaling relations for the dispersion parameter A and the perturbative contribution to the g-factor g_* of the Γ_{6c} conduction band read

$$\begin{aligned}
A &= A' + \frac{1}{3}\left(2\frac{P'^2}{E_0 - E_0' - \Delta_0'} + \frac{P'^2}{E_0 - E_0'}\right), \\
g_* &= g_*' + \frac{2}{3}\frac{2m_0}{\hbar^2}\left(-\frac{P'^2}{E_0 - E_0' - \Delta_0'} + \frac{P'^2}{E_0 - E_0'}\right).
\end{aligned} \tag{2.69}$$

We find that these relations are identical to those previously obtained in the bulk case. [Win03] This is because the operator ordering has no impact on the value of the parameters.

2.5.2 The single-band model of the conduction band

Considering the Γ_{7v} and Γ_{8v} as remote, Loewdin's perturbation theory results in an effective two-band model for the Γ_{6c} conduction bands. If no magnetic field is present, the Γ_{6c} bands are spin-degenerate. Thus, the $k \cdot p$ Schrödinger equation can be solved for one spin-orientation only. This leaves an effective single band model of the Γ_1^c conduction band. Note that the Rashba and Dresselhaus effect are not present in the single band and two-band model of second order in k. [Win03]

The effective conduction band mass and g-factor which we label as m_c and g_c, respectively, are related to A and g_* by

$$\begin{aligned}
\frac{\hbar^2}{2m_0}\frac{1}{m_c} &= A + \frac{1}{3}\left(2\frac{P^2}{E_0} + \frac{P^2}{E_0+\Delta_0}\right), \\
g_c &= g_* + \frac{1}{3}\frac{\hbar^2}{2m_0}\left(-\frac{P^2}{E_0} + \frac{P^2}{E_0+\Delta_0}\right),
\end{aligned} \tag{2.70}$$

again in agreement with the literature. [Win03] Commonly, m_c and g_c are tabulated and the rescaling relations are applied to yield the according eight- and 14-band parameters.

2.5.3 The six-band model of the valence band

In order to compute the valence band dispersion only, the Γ_{6c} bands are considered as remote. Loewdin's perturbation theory yields the rescaling relations

$$\begin{aligned}
\gamma_1^L &= \gamma_1 + \frac{1}{3}\frac{2m_0}{\hbar^2}\frac{P^2}{E_0}, \\
\gamma_2^L &= \gamma_2 + \frac{1}{6}\frac{2m_0}{\hbar^2}\frac{P^2}{E_0}, \\
\gamma_3^L &= \gamma_3 + \frac{1}{6}\frac{2m_0}{\hbar^2}\frac{P^2}{E_0}, \\
\kappa^L &= \kappa + \frac{1}{6}\frac{2m_0}{\hbar^2}\frac{P^2}{E_0}, \\
q^L &= q,
\end{aligned} \tag{2.71}$$

for the Luttinger parameters γ_1^L, γ_2^L, γ_3^L, κ^L, and q^L in agreement with the literature. [Win03] Again, the eight- and 14-band parameters can be computed from the commonly tabulated values of the six-band Luttinger parameters.

2.6 Cartesian representation of the $k \cdot p$ Hamiltonian

The perturbative contributions to the $k \cdot p$-Hamiltonian are most conveniently derived in the angular momentum basis. However, the symmetry adapted finite element method, which we present in Ch. 3, requires the Hamiltonian in the Cartesian representation. We use the transformation matrices $S_{78,5D}$ (2.4) and $S_{6,1D}$ (2.5) to obtain this Cartesian Hamiltonian from the Hamiltonian in the angular momentum basis. This yields the block Hamiltonians

$$\begin{aligned}
H_{5D\alpha 5D\beta} &= S^H_{78,5D} \begin{pmatrix} H_{8\alpha 8\beta} & H_{8\alpha 7\beta} \\ H_{7\alpha 8\beta} & H_{7\alpha 7\beta} \end{pmatrix} S_{78,5D}, \\
H_{5D\alpha 1D\beta} &= S^H_{78,5D} \begin{pmatrix} H_{8\alpha 6\beta} \\ H_{7\alpha 6\beta} \end{pmatrix} S_{6,1D}, \\
H_{1D\alpha 1D\beta} &= S^H_{6,1D} H_{6\alpha 6\beta} S_{6,1D}.
\end{aligned} \tag{2.72}$$

By this transformations, we obtain the 14-band $k \cdot p$ Hamiltonian

$$\begin{aligned}
\hat{H}_{14} &= \begin{pmatrix} \mathbf{1}_2 \times \hat{H}^k_{5c5c} & \mathbf{1}_2 \times \hat{H}^k_{5c1c} & \mathbf{1}_2 \times \hat{H}^k_{5c5v} \\ \mathbf{1}_2 \times \hat{H}^{k\dagger}_{5c1c} & \mathbf{1}_2 \times \hat{H}^k_{1c1c} & \mathbf{1}_2 \times \hat{H}^k_{1c5v} \\ \mathbf{1}_2 \times \hat{H}^{k\dagger}_{5c5v} & \mathbf{1}_2 \times \hat{H}^{k\dagger}_{1c5v} & \mathbf{1}_2 \times \hat{H}^k_{5v5v} \end{pmatrix} \\
&+ \hat{H}^{SO}_{14} + \hat{H}^{\epsilon}_{14} + \hat{H}^{B}_{14} - e\Phi.
\end{aligned} \tag{2.73}$$

Here, we used the fact that the matrices of the double group Hamiltonians can be split into a spin-degenerate part and the explicit spin-orbit coupling. The first term on the right hand side resembles this spin-degenerate part and $\mathbf{1}_2$ denotes the 2×2 identity matrix. The operator $\hat{H}_{14}^{SO}$ denotes the spin-orbit coupling and $\hat{H}_{14}^{B}$ the coupling of the free electron spin to a magnetic field. In addition to the $k \cdot p$ interactions, we introduced the strain deformation potentials $\hat{H}_{14}^{\epsilon}$ and the external electrostatic potential Φ.

The spin-degenerate inter-band terms are first-order in $\hat{\mathbf{k}}$ and read

$$\hat{H}_{1c5v}^{k} = \begin{pmatrix} \hat{k}_x^\dagger P & \hat{k}_y^\dagger P & \hat{k}_z^\dagger P \end{pmatrix}, \tag{2.74}$$

$$\hat{H}_{5c5v}^{k} = \begin{pmatrix} 0 & Q\hat{k}_z & Q\hat{k}_y \\ Q\hat{k}_z & 0 & Q\hat{k}_x \\ Q\hat{k}_y & Q\hat{k}_x & 0 \end{pmatrix}, \tag{2.75}$$

$$\hat{H}_{1c5c}^{k} = \begin{pmatrix} iP'\hat{k}_x & iP'\hat{k}_y & iP'\hat{k}_z \end{pmatrix}, \tag{2.76}$$

with the momentum matrix elements P, P', and Q given by Eqs. (2.8) to (2.10).

The intra-band terms up to second order in $\hat{\mathbf{k}}$ are given by

$$(\hat{H}_{5c5c}^{k})_{\mu,\nu} = \delta_{\mu,\nu} E_{5c} \tag{2.77}$$

$$\begin{aligned} \hat{H}_{1c1c}^{k} &= E_{1c} + \hat{\mathbf{k}}^\dagger A' \hat{\mathbf{k}} \\ &\quad + \frac{\hbar^2}{2m_0} \left(i\sigma_x \left[\hat{k}_y^\dagger \frac{g'_* - g_0}{2} \hat{k}_z - \hat{k}_z^\dagger \frac{g'_* - g_0}{2} \hat{k}_y \right] + \text{c.p.} \right), \end{aligned} \tag{2.78}$$

$$\begin{aligned} (\hat{H}_{5v5v}^{k})_{\mu,\nu} &= \delta_{\mu,\nu} E_{5v} \\ &\quad + \begin{cases} \hat{\mathbf{k}}^\dagger M' \hat{\mathbf{k}} + \hat{k}_\mu^\dagger (L' - M') \hat{k}_\mu & \text{if } \mu = \nu \\ \hat{k}_\mu^\dagger N'_+ \hat{k}_\nu + \hat{k}_\nu^\dagger N'_- \hat{k}_\mu & \text{if } \mu \neq \nu \end{cases} \\ &\quad + (\hat{H}_{5Dv,5Dv}^{C_k})_{\mu,\nu} + (\hat{H}_{5Dv,5Dv}^{q})_{\mu,\nu}, \end{aligned} \tag{2.79}$$

where E_{5c}, E_{1c}, and E_{5v} are band offset parameters without spin-orbit interaction, and μ and ν denote the Cartesian directions x, y, z. These band offsets are obtained from tabulated values of the band gaps E_0, E'_0, the spin-orbit splittings Δ_0, Δ'_0 and the relative valence band offset E_{VBO}. [WZ98] Here, E_0 denotes the band gap between the Γ_{1c} and Γ_{5v} bands and E'_0 denotes the band gap between the Γ_{5c} and Γ_{5v} bands. The band offsets E_{5c}, E_{1c}, and E_{5v} are related to these parameters by

$$E_{5v} = E_{VBO}, \tag{2.80}$$

$$E_{1c} = E_{VBO} + E_0 + \tfrac{1}{3}\Delta_0, \tag{2.81}$$

$$E_{5c} = E_{VBO} + E'_0 + \tfrac{1}{3}\Delta_0 + \tfrac{2}{3}\Delta'_0. \tag{2.82}$$

The parameters L', M', N'_+, N'_-, A', and g'_* take into account remote bands perturbatively. [DKK55, For97] They are related to the derived Luttinger parameters γ'_1,

γ_2', γ_3', and κ' by [BP74, For97, AMV08]

$$\begin{aligned} L' &= \frac{\hbar^2}{2m_0}(-\gamma_1' - 4\gamma_2'), \\ M' &= \frac{\hbar^2}{2m_0}(-\gamma_1' + 2\gamma_2'), \\ N_+' &= \frac{\hbar^2}{2m_0}(-3\gamma_3' - 3\kappa' - 1), \\ N_-' &= \frac{\hbar^2}{2m_0}(-3\gamma_3' + 3\kappa' + 1). \end{aligned} \tag{2.83}$$

The parameters A' and $(g_*' - g_0)$ are remote-band contributions to the effective Γ_{1c} dispersion and g-factor, respectively.

The $\hat{\mathbf{k}}$-linear spin-splitting Hamiltonian of the valence band is caused by the lack of inversion symmetry [CCF88] and reads

$$\hat{H}^{C_k}_{5Dv,5Dv} = \sqrt{\frac{3}{4}} C_k \times \begin{pmatrix} 0 & 0 & \hat{k}_x & 0 & i\hat{k}_x + \hat{k}_y & -\hat{k}_z \\ 0 & 0 & -\hat{k}_y & i\hat{k}_x + \hat{k}_y & 0 & -i\hat{k}_z \\ \hat{k}_x & -\hat{k}_y & 0 & -\hat{k}_z & -i\hat{k}_z & 0 \\ 0 & -i\hat{k}_x + \hat{k}_y & -\hat{k}_z & 0 & 0 & -\hat{k}_x \\ -i\hat{k}_x + \hat{k}_y & 0 & i\hat{k}_z & 0 & 0 & \hat{k}_y \\ -\hat{k}_z & i\hat{k}_z & 0 & -\hat{k}_x & \hat{k}_y & 0 \end{pmatrix}. \tag{2.84}$$

with the parameter C_k defined by Eq. (2.11). The g-factor anisotropy of the Γ_{8v} bands assumes a very cumbersome form in the Cartesian basis and is best expressed implicitly as

$$\hat{H}^{q}_{5Dv,5Dv} = S^{H}_{78,5D} \left(-\frac{\hbar^2}{2m_0} 2i[J_z^3(\hat{k}_x^\dagger q' \hat{k}_y - \hat{k}_y^\dagger q' \hat{k}_x) + c.p.] \right) S_{78,5D}, \tag{2.85}$$

with the g-factor anisotropy parameter q'.

As before, perturbative second-order contributions to the Γ_5^c bands are neglected because they have no substantial impact on the band structure close to the band gap.

The spin-orbit Hamiltonian reads

$$\hat{H}^{SO}_{14} = \begin{pmatrix} \frac{\Delta_0'}{3}\hat{H}^{SO} & \mathbf{0} & \frac{i\Delta^-}{3}\hat{H}^{SO} \\ \mathbf{0} & \mathbf{0} & \mathbf{0} \\ \left(\frac{i\Delta^-}{3}\hat{H}^{SO}\right)^\dagger & \mathbf{0} & \frac{\Delta_0}{3}\hat{H}^{SO} \end{pmatrix}, \tag{2.86}$$

with

$$\hat{H}^{SO} = \begin{pmatrix} 0 & -i & 0 & 0 & 0 & 1 \\ i & 0 & 0 & 0 & 0 & -i \\ 0 & 0 & 0 & -1 & i & 0 \\ 0 & 0 & -1 & 0 & i & 0 \\ 0 & 0 & -i & -i & 0 & 0 \\ 1 & i & 0 & 0 & 0 & 0 \end{pmatrix}, \tag{2.87}$$

and Δ_0, Δ_0', and Δ^- given by Eqs. (2.12-2.14). The bold $\mathbf{0}$ denote blocks of zeros with appropriate dimension.

The deformation potential does not depend on spin and reads [BP74]

$$\hat{H}^{\epsilon}_{14} = \begin{pmatrix} \mathbf{0} & \mathbf{0} & \mathbf{0} \\ \mathbf{0} & \mathbf{1}_2 \times \hat{H}^{\epsilon}_{ss} & \mathbf{0} \\ \mathbf{0} & \mathbf{0} & \mathbf{1}_2 \times \hat{H}^{\epsilon}_{vv} \end{pmatrix}, \tag{2.88}$$

where the deformation potentials of the Γ_{5c} bands and between different bands are neglected. The intra-band terms read

$$\hat{H}^{\epsilon}_{ss} = a\bar{\epsilon}, \tag{2.89}$$

$$(\hat{H}_{vv})_{\mu,\nu} = \begin{cases} m\bar{\epsilon} + (l-m)\epsilon_{\mu\mu} & \text{if } \mu = \nu \\ n(\epsilon_{\mu\nu} + \epsilon_{\nu\mu})/2 & \text{if } \mu \neq \nu \end{cases}, \tag{2.90}$$

$$\bar{\epsilon} = \epsilon_{xx} + \epsilon_{yy} + \epsilon_{zz}, \tag{2.91}$$

with the strain tensor $\overleftrightarrow{\epsilon}$ and the deformation potentials a, l, m, and n. These parameters are linked to other common parameter sets by the relations [TRR79, BP74]

$$a' = a = C_1, \tag{2.92}$$

$$a'' = \frac{l+2m}{3} = D_d, \tag{2.93}$$

$$b = \frac{l-m}{3} = -\frac{2}{3}D_u, \tag{2.94}$$

$$d = \frac{n}{\sqrt{3}} = -\frac{2}{\sqrt{3}}D_u'. \tag{2.95}$$

The coupling of the free electron spin to a magnetic field is

$$\hat{H}^{B}_{14} = \begin{pmatrix} \hat{H}^{B}_{cc} & \mathbf{0} & \mathbf{0} \\ \mathbf{0} & \hat{H}^{B}_{ss} & \mathbf{0} \\ \mathbf{0} & \mathbf{0} & \hat{H}^{B}_{vv} \end{pmatrix}, \tag{2.96}$$

$$\hat{H}^{B}_{ss} = \mu_B \frac{g_0}{2} \boldsymbol{\sigma} \cdot \mathbf{B}, \tag{2.97}$$

$$\hat{H}^{B}_{cc} = \hat{H}^{B}_{vv} = \mu_B \frac{g_0}{2} \boldsymbol{\sigma} \cdot \mathbf{B} \times \mathbf{1}_3, \tag{2.98}$$

with the magnetic field $\mathbf{B}$, the 3-vector of Pauli matrices $\boldsymbol{\sigma}$, the Bohr magneton μ_B, and the g-factor of the free electron $g_0 \approx 2$.

The contributions of the remote bands to the effective g-factors are included in the parameters $(g'_* - g_0)$, N'_+, N'_-, and q' implicitly. For the Γ_{5Dc} bands, the according remote band contributions are neglected.

2.7 Material parameters of the $k \cdot p$ Hamiltonian

2.7.1 Elliptic parameter sets

The eight-band and 14-band models are susceptible to so-called wing-band solutions. [WS81, SM86, Szm96, Bur98] Depending on the material parameters, unphysical large-k-vector solutions to the $k \cdot p$ Hamiltonian can appear close to the band-edges or even within the fundamental band gap. They occur if the intra-band part of the Hamiltonian is not elliptic for both the valence and the conduction band. [CTM03, VSW07] In k-space, one can simply redeem this issue by restricting the k-vectors used in the calculation to a valid range. [WR93] This is not possible for a real space basis since its basis functions are not compactly supported in k-space. This problem can be resolved by modifying the Kane parameter P in such a way that Eqs. (2.68), (2.69), (2.71) and (2.70) yield rescaled parameters that fulfill the ellipticity conditions [For97, VSW07]

$$A \geq 0,\ M - N^- < 0,\ M + N^- < 0,\ L - N^+ < 0,\ L + 2N^+ < 0. \tag{2.99}$$

This approach is justified by the fact that the $k \cdot p$ band structure is not sensitive to small changes of the Kane parameters as long as the rescaling relations are observed. [For97, For07] In general, we adjust P such that $A = 1$. We find that this choice also fulfills the remaining conditions in Eqs. (2.99) for semiconductors and semiconductor alloys studied in this work.

2.7.2 Temperature dependency

Semiconductor heterostructures operate at various temperatures ranging from a almost zero up to several hundred Kelvin. However, only very little is known about the temperature dependence of the $k \cdot p$ parameters. We thus observe the two most important temperature effects on the band structure only. Firstly, the fundamental band gap depends on the temperature. The empirical Varshni form of this dependency reads [Var67]

$$E_0(T) \quad = \quad E_0 - \frac{\alpha T^2}{T + \beta}, \tag{2.100}$$

where α and β are tabulated material parameters. [VMRM01] Secondly, the temperature dependency of the lattice constant is well known and indirectly affects the

electronic structure via strain and deformation potentials. The linear temperature dependency of the lattice constant reads [VMRM01]

$$a(T) = a + a_T T, \tag{2.101}$$

where a is the lattice constant at 0 K and a_T is the linear expansion coefficient of the crystal lattice.

2.7.3 Interpolation of ternary alloys

Heterostructure commonly consist of semiconductor alloys. Only for a few particular alloys, parameter sets can be measured directly or computed theoretically. Thus, the elastic, the electrostatic and the $k \cdot p$ material parameters have to be interpolated. Commonly, quadratic interpolation formulas are employed. [VMRM01]

Here, we consider only ternary alloys of pure binary (group III-V and II-VI) constituents. For a ternary alloy $A_x B_{1-x} C$ consisting of AC and BC, the quadratic interpolation formula for a generic material parameter τ reads

$$\tau_{A_x B_{1-x} C} = x\tau_{AC} + (1-x)\tau_{BC} - x(1-x)\tau_{ABC}. \tag{2.102}$$

Here, τ_{AB} and τ_{AC} are the parameters of AC and BC, respectively, and τ_{ABC} is the so-called bowing of parameter τ of ABC alloys. This applies analogously to alloys of the type $AB_x C_{1-x}$ consisting of AB and AC.

We employ bowing to material parameters if available in the literature. An exception are the $k \cdot p$ parameters that represent remote-band contributions. Since it is not clear how these bowing parameters have to be rescaled to the eight- and 14-band models, we first compute the according 14-band parameters for the pure semiconductors by employing the rescaling relations Eqs. (2.68), (2.69), (2.70), and (2.71). The remote-band contributions in the 14-band model are small and thus no substantial bowing is expected. These parameters are then interpolated linearly and finally rescaled to the model used in the calculations.

This has to be contrasted with the common procedure where remote-band contribution are interpolated quadratically first and then rescaled. [VMRM01] We note that for semiconductor alloys with small are even vanishing band gap this method fails. For example, the band gap E_0 vanishes for a certain $\mathrm{Hg}_x\mathrm{Cd}_{1-x}\mathrm{Te}$ alloy. [CC73] In this case, the rescaling relations Eqs. (2.70) and (2.71) diverge. In contrast, our procedure still yield reasonable eight- and 14-band parameters because the band gap is non-zero for HgTe and CdTe resulting in well-defined rescaling relations.

2.8 Rotations of the $k \cdot p$ Hamiltonian

For heterostructures grown along a direction different from the [001] direction, the Hamiltonian has to be rotated. By convention, we rotate the crystal while the coordinate system of the heterostructure is left unchanged.

The rotation matrix [BS98]

$$R(\theta,\mathbf{w}) = \begin{pmatrix} w_x^2\,(1-\cos\theta)+\cos\theta & w_x w_y\,(1-\cos\theta)-w_z\sin\theta & w_x w_z\,(1-\cos\theta)+w_y\sin\theta \\ w_y w_x\,(1-\cos\theta)+w_z\sin\theta & w_y^2\,(1-\cos\theta)+\cos\theta & w_y w_z\,(1-\cos\theta)-w_x\sin\theta \\ w_z w_x\,(1-\cos\theta)-w_y\sin\theta & w_z w_y\,(1-\cos\theta)+w_x\sin\theta & w_z^2\,(1-\cos\theta)+\cos\theta \end{pmatrix}, \tag{2.103}$$

which represents a proper rotation about the normalized axis $\mathbf{w}$ by the angle θ, transforms the single group quantities as [Nye85]

$$\mathbf{r} = R(\theta,\mathbf{w})\mathbf{r}', \tag{2.104}$$
$$\hat{\mathbf{k}} = R(\theta,\mathbf{w})\hat{\mathbf{k}}', \tag{2.105}$$
$$\mathbf{B} = R(\theta,\mathbf{w})\mathbf{B}', \tag{2.106}$$
$$\overleftrightarrow{\epsilon} = R(\theta,\mathbf{w})\,\overleftrightarrow{\epsilon}'\,R^T(\theta,\mathbf{w}). \tag{2.107}$$

Here, the primed quantities correspond to the new coordinate system. These relations are also valid for improper rotations, except for the transformation of the pseudovector $\mathbf{B}$ which transforms as $\mathbf{B} = -R_i\mathbf{B}'$ under an improper rotation R_i.

The 1/2-spinor is transformed by the corresponding $SU(2)$ matrix [BP74]

$$D_{1/2}(\theta,\mathbf{w}) = \mathbf{1}_2\cos\left(\frac{\theta}{2}\right) - i\boldsymbol{\sigma}\cdot\frac{\mathbf{w}}{|\mathbf{w}|}\sin\left(\frac{\theta}{2}\right). \tag{2.108}$$

The transformation matrix U_{5D} of the Γ_{5D} representation is thus the Kronecker product

$$U_{5D}(\theta,\mathbf{w}) = D_{1/2}(\theta,\mathbf{w}) \times R(\theta,\mathbf{w}). \tag{2.109}$$

For $\Gamma_7+\Gamma_8$ this yields

$$U_{78}(\theta,\mathbf{w}) = S_{78,5D}U_{5D}(\theta,\mathbf{w})S_{5D,78}. \tag{2.110}$$

Note that $U_{78}(\theta,\mathbf{w})$ is block diagonal for all rotations, since Γ_8 and Γ_7 are compatible with the full rotational groups of 3/2 and 1/2 angular momentum, respectively. We may thus split $U_{78}(\theta,\mathbf{w})$ into the blocks $U_8(\theta,\mathbf{w})$ and $U_7(\theta,\mathbf{w})$ for the rotations of Γ_8 and Γ_7, respectively. For Γ_6 we simply have

$$U_{1D}(\theta,\mathbf{w}) = U_6(\theta,\mathbf{w}) = D_{1/2}(\theta,\mathbf{w}). \tag{2.111}$$

Each block Hamiltonian transforms into

$$\begin{aligned} \hat{H}_{i\alpha,j\beta}(\mathbf{r},\hat{\mathbf{k}},\mathbf{B},\overleftrightarrow{\epsilon}) &\rightarrow H'_{i\alpha,j\beta}(\mathbf{r}',\hat{\mathbf{k}}',\mathbf{B}',\overleftrightarrow{\epsilon}') \\ &= U_i^H\hat{H}_{i\alpha,j\beta}(R\mathbf{r},R\hat{\mathbf{k}},R\mathbf{B},R\overleftrightarrow{\epsilon}R^T)U_j, \end{aligned} \tag{2.112}$$

where the indices $(i\alpha)$ and $(j\beta)$ correspond to the representations $\Gamma_{i\alpha}$ and $\Gamma_{j\beta}$, respectively. We employ the simple term rewriting system described in appendix D to perform these transformations symbolically prior to discretization.

Note that the definition of the spin basis is arbitrary. It is thus not necessary to transform the spin at all since we may just choose another arbitrary definition after the rotation is performed. In the presence of an external magnetic field, however, it is convenient to transform the spin space along with the real space. Otherwise, the Pauli matrices which couple the magnetic field vector to the spin need to be transformed and assume a non-standard form. This, however, is counter-intuitive and error prone.

Moreover, the explicit rotation of spin space has the advantage that we may check the symmetry as well as the correctness of rotations of the Hamiltonian automatically. This automatic check exploits the fact that the Hamiltonian is invariant under symmetry operation in T_d such that $\hat{H} - \hat{H}' = 0$ for these operations. This is tested straightforwardly by the term rewriting system. If the spin space is not rotated explicitly, H and H' are identical up to a unitary transformation only which is much more difficult to verify.

Chapter 3

Novel Symmetry Adapted Finite Element method (SAFE)

3.1 Introduction

In this chapter, we make use of the symmetry of the Hamiltonian to construct a real-space EFA method that is manifestly free of spurious solutions. This robust and numerically efficient scheme is based on a variational representation of the EFA problem in terms of symmetry adapted finite elements. Therefore, we name this method the *symmetry adapted finite element method* (SAFE). Importantly, it permits the gauge-invariant incorporation of magnetic fields naturally, which is a costly procedure in standard EFA implementations. [GU98, PF06, AMV08]

In Sec. 3.2.1, we illustrate and explain the origin of the problem of spurious solutions due to the ill-representation of the first-order derivative in real-spaces bases. In Sec. 3.2.2, we develop the method of symmetry adapted finite elements that inherently solves this issue and illustrate it for White's two-band Hamiltonian. Section 3.2.3 is devoted to the generalization to eight- and 14-band envelope function Hamiltonians. A gauge-invariant formulation of the symmetry adapted finite element method is developed in Sec. 3.2.4. In Sec. 3.3, we present results for the exciton g-factor in self-assembled quantum dots and compare the results obtained with the present SAFE method to those previously obtained by standard techniques. The proof of the correct continuum limit for the gauge-invariant symmetry adapted finite element method is deferred to Appendix A.

3.2 Method

3.2.1 The problem: spurious solutions in discrete effective mass theory

The problem we address in the following is the appearance of spurious solutions related to the ill-representation of first-order derivatives in envelope function approach (EFA) Hamiltonians in standard real-space bases. For sake of clarity, we start the discussion of spurious solutions with the help of White's two-band $\mathbf{k}\cdot\mathbf{p}$-Hamiltonian describing the coupling of a single electron band with a single light hole band in one dimension. [WS81] In k-space, the Hamiltonian reads

$$H_2(k_x) = \begin{pmatrix} E_0 + \frac{\hbar^2}{2m_0}Ak_x^2 & Pk_x \\ Pk_x & -\frac{\hbar^2}{2m_0}Ak_x^2 \end{pmatrix}, \tag{3.1}$$

with the band gap E_0, the Luttinger parameter A and the Kane parameter P. The substitution $k_x \to -i\partial_x$ leads to first- and second-order derivatives in the real-space EFA Hamiltonian

$$\hat{H}_2 = \begin{pmatrix} E_0 - \frac{\hbar^2}{2m_0}\partial_x^\dagger A\partial_x & i\partial_x^\dagger P \\ -iP\partial_x & \frac{\hbar^2}{2m_0}\partial_x^\dagger A\partial_x \end{pmatrix}, \tag{3.2}$$

which must both be well approximated in order to preserve the k-space spectrum. The spatial derivative operators are already ordered appropriately with the daggered operators acting to the left hand side. [For97] Nevertheless, this mapping is known to lead to spurious solutions because standard parameters for many relevant semiconductors (InAs, GaAs, GaSb, etc.) lead to negative values for the parameter A. This induces unphysical solutions within the band gap for large $\mathbf{k}$ vectors. [WS81, For97, VSW07] Fortunately, this problem can be redeemed in various ways, e.g. by rescaling the effective mass parameters such that $A = 0$. [For97]

There is another cause for spurious solutions, however, that is not easy to resolve. For realistic three-dimensional multi-material nanostructures, the real-space Hamiltonian (3.2) can only be solved by discretizing position space in some way or, equivalently, by choosing a small variational real-space basis. The simplest scheme is to use a finite difference method with symmetric first-order differences, i.e. $\partial_x F = [F(x+h) - F(x-h)]/(2h)$ with grid spacing h. This scheme has been identified earlier to be the cause of unphysical solutions for many semiconductor nanostructures, [CTM03] but no easy remedy is known.

The problem comes from the dominance of the first-order term in the off-diagonal element of Eq. (3.2) for most semiconductors. Assume for the moment that $A = 0$ altogether. Then, a symmetric first-order discretization decomposes the Hamiltonian into its portions from the even (0,2,4,...) and odd (1,3,5,...) nodes *with no coupling between them* so that any combination of the even and odd solutions becomes a solution as well. This problem persists for small second-order terms A as long as

$A \lesssim E_P/E_0$ and disappears only in the limit of decoupled bands making the multi-band formulation pointless. Neither can it be healed by choosing an asymmetric first-order differencing scheme (e.g. a combination of forward and backward differencing) since this breaks the symmetry of the Hamiltonian. The failure of the finite difference method is illustrated explicitly in Fig. 3.1 for the case of Eq. (3.2). Here, typical parameters for III-V semiconductors, similar to GaSb in this case, have been used, [VMRM01] namely an energy gap E_0 of 1 eV and Kane's energy $2m_0P^2/\hbar^2$ of 26 eV ($P = 1$ eVnm). We have set the constant A equal to 0 in order to make sure that spurious modes are not just caused by ill-suited parameters.

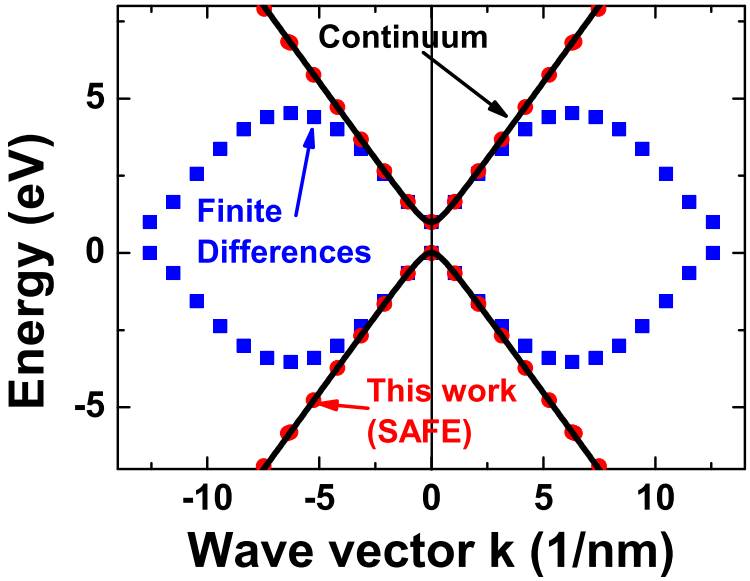

Figure 3.1: Electronic band structure of the White Hamiltonian with the parameters $E_0 = 1$ eV, $P = 1$ eVnm, and $A = 0$. The black line is the calculated continuum dispersion in k-space. The squares (blue) and circles (red) are real-space solutions on a periodic 6 nm grid of 0.25 nm spacing. The squares result from the finite difference method, whereas the circles represent the presently proposed symmetry adapted finite element method (SAFE).

3.2.2 The solution: the SAFE method

The problem illustrated vividly in Fig. 3.1 can be solved in a robust, reliable and numerically efficient manner. The method we have developed is based on the concept of finite elements [BS08] and guarantees a minimal real-space basis that manifestly represents the solution space. We illustrate this method for the simple 2×2 example first. We denote the finite variational space of the two-component envelope function

as

$$\Psi = \{ \begin{pmatrix} F^S \\ F^{LH} \end{pmatrix} | F^S \in V^S,\, F^{LH} \in V^{LH} \}, \tag{3.3}$$

with the finite variational spaces V^S and V^{LH} for the electron (S for s-like) and the light hole (LH) component, respectively. In contrast to first-order derivatives, the second-order derivatives are always well-behaved for elliptic problems and do not need special consideration. [BS08] By contrast, the first-order terms in the EFA Hamiltonian Eq. (3.2) are of the type $\left\langle \partial_x F^S \right| P \left| F^{LH} \right\rangle$. These matrix elements are represented exactly by the variational basis functions only if the derivatives of the functions F^S can be expressed in terms of the functions F^{LH}, i.e. if the function spaces obey the relation

$$V^{LH} = \partial_x V^S = \{ \partial_x F^S | F^S \in V^S \}. \tag{3.4}$$

This can be guaranteed by requiring that V^{LH} be continuous yet V^S to be continuously differentiable. One may easily verify that this is *not the case for standard discretization schemes* such as the centered finite differences method or the standard finite element method where the same basis is chosen for each wave function component.

We now define a piecewise polynomial basis with small support on a regular grid that guarantees the crucial requirement of Eq. (3.4), as well as scalability and a sparse discrete Hamilton matrix. To this end, we define a uniform grid with grid cells $\{R_I | I = 1 \ldots N\}$ and grid-spacing $R_{I+1} - R_I = h$, and expand the envelope functions of the components $F^S \in V^S$ and $F^{LH} \in V^{LH}$ on this grid in terms of basis functions,

$$F^S(x) = \sum_{R_I} \sum_{k=0 \ldots p^S} a^S_{k,R_I} u^S_{k,R_I}(x), \tag{3.5}$$

$$F^{LH}(x) = \sum_{R_I} \sum_{k=0 \ldots p^{LH}} a^{LH}_{k,R_I} u^{LH}_{k,R_I}(x), \tag{3.6}$$

where the functions $\{u^S_{k,R_I}(x) | k = 1, \ldots, p^S\}$ and $\{u^{LH}_{k,R_I}(x) | k = 1, \ldots, p^{LH}\}$ form a polynomial basis of degree p^S and p^{LH}, respectively, that are localized within grid cell R_I and zero outside. We note that these basis functions are the same in each cell, i.e. for all cells R_I, R_J we have $u_{k,R_I}(x) = u_{k,R_J}(x + R_J - R_I)$. The expansion coefficients are denoted by a_{k,R_I}. Because the function space V^{LH} consists of the derivatives of the functions in V^S, the polynomial degree p^{LH} of V^{LH} is one less than the polynomial degree p^S of V^S. In addition, the local basis functions $\{u_{k,R_I}\}$ should be chosen in such a way that simple boundary conditions for the coefficients a_{k,R_I} at the cell boundaries suffice to yield globally continuously differentiable and continuous functions F^S and F^{LH}, respectively. It turns out that an ideal choice for the S-band basis functions $\{u^S_{k,R_I}\}$ are the so-called Hermite interpolating polynomials of first and second kind with the two boundary points in each grid cell as nodal points. [BSV68, CR72] This choice yields four linearly independent polynomials of degree

$p^S = 3$ and the following simple constraints on the left and right boundary of each cell,

$$\begin{aligned} a^S_{0,R_I} &= a^S_{1,R_{I-1}}, \\ a^S_{2,R_I} &= a^S_{3,R_{I-1}}, \end{aligned} \tag{3.7}$$

guaranteeing the C^1 continuity of F^S in Eq. (3.5). Accordingly, a suitable local basis $\{u^{LH}_{k,R_I}\}$ for V^{LH} are the so-called Lagrange interpolating polynomials of degree $p^{LH} = 2$. One obtains three linearly independent polynomials by using the cell boundary and mid points as nodal points and obtains the constraint

$$a^{LH}_{0,R_I} = a^{LH}_{2,R_{I-1}}, \tag{3.8}$$

for continuous F^{LH} in Eq. (3.6). Explicitly, the local basis functions for $\{u^S_{k,0}|k = 0\ldots3\}$ for the cell at the coordinate origin $R_I = 0$ read

$$\begin{aligned} u^S_{0,0}(x) &= 1 - 3(x/h)^2 + 2(x/h)^3, \\ u^S_{1,0}(x) &= 3(x/h)^2 - 2(x/h)^3, \\ u^S_{2,0}(x) &= (x/h) - 2(x/h)^2 + (x/h)^3, \\ u^S_{3,0}(x) &= -(x/h)^2 + (x/h)^3, \end{aligned} \tag{3.9}$$

and for $\{u^{LH}_{k,0}|k = 0\ldots2\}$

$$\begin{aligned} u^{LH}_{0,0}(x) &= 1 - 3(x/h) + 2(x/h)^2, \\ u^{LH}_{1,0}(x) &= 4(x/h) - 4(x/h)^2, \\ u^{LH}_{2,0}(x) &= -(x/h) + 2(x/h)^2. \end{aligned} \tag{3.10}$$

With this local basis for V^S and V^{LH}, the real-space EFA Hamiltonian Eq. (3.2) gets converted into a discrete, generalized constrained eigenvalue problem of the dimension $(4+3)N$. A generalized constraint eigenvalue problem is difficult to solve in practice since the corresponding overlap matrix is highly singular. Fortunately, it can easily be converted into an unconstrained eigenvalue problem: The actual degrees of freedom are the number of variables minus the number of constraints. We may therefore define $(2+2)N$ new basis functions for Ψ by incorporating the $(2+1)N$ continuity constraints Eqs. (3.7) and (3.8) into new basis functions. These basis functions are then continuous (continuously differentiable) across cell boundaries and require no additional constraints on the expansion coefficients. A suitable basis with small support (two neighboring cells) contains only two basis functions per grid cell and is given explicitly by

$$\begin{aligned} v^S_{0,R_I}(x) &= u^S_{0,R_I}(x) + u^S_{1,R_{I-1}}(x), \\ v^S_{1,R_I}(x) &= u^S_{2,R_I}(x) + u^S_{3,R_{I-1}}(x), \end{aligned} \tag{3.11}$$

$$\begin{aligned} v^{LH}_{0,R_I}(x) &= u^{LH}_{0,R_I}(x) + u^{LH}_{2,R_{I-1}}(x), \\ v^{LH}_{1,R_I}(x) &= u^{LH}_{1,R_I}(x), \end{aligned} \tag{3.12}$$

for V^S and V^{LH}, respectively. The condition $V^{LH} = \partial_x V^S$ holds since

$$\partial_x v^S_{0,R_I}(x) = -\frac{3}{2h}\,[v^{LH}_{1,R_I}(x) - v^{LH}_{1,R_{I-1}}(x)], \tag{3.13}$$

$$\partial_x v^S_{1,R_I}(x) = \frac{1}{h} v^{LH}_{0,R_I}(x) - \frac{1}{4h}\,[v^{LH}_{1,R_I}(x) + v^{LH}_{1,R_{I-1}}(x)]. \tag{3.14}$$

Figure 3.2 illustrates these basis functions at $R_I = 0$ for $h = 1$.

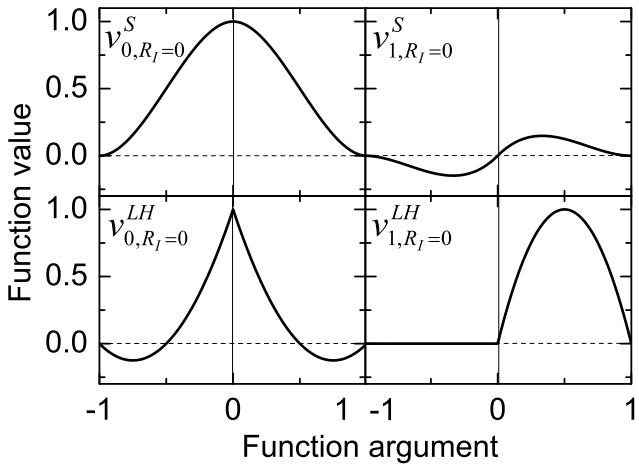

Figure 3.2: Finite element basis functions of the S-like and LH-like band for $R_I = 0$ and $h = 1$. The bold vertical line indicates the element boundary between the $(I-1)$-th and the I-th element.

We can now calculate the spectrum of the EFA Hamiltonian Eq. (3.2) for the bulk semiconductor on a discrete periodic grid in terms of our symmetry adapted finite element basis and compare it to the continuum spectrum of the Hamiltonian Eq. (3.1). The results are shown in Fig. 3.1. For larger k-values, the finite difference results deviate strongly from the continuum spectrum that is indicated by the full lines. In contrast, the present finite element method approximates the continuum spectrum up to the maximum k-values possible on the discrete grid. No spurious solutions appear in the spectrum.

3.2.3 SAFE method for eight- and 14-band Hamiltonians

The generalization of this method to the realistic eight- and 14-band zincblende $\mathbf{k}\cdot\mathbf{p}$ Hamiltonians turns out to be rather straightforward. It suffices to discuss the latter case since the eight-band components are a subset of the 14-band terms.

The complete real-space zincblende $\mathbf{k}\cdot\mathbf{p}$ Hamiltonian operator is given in Sec. 2.6. The intra-band terms $\hat{H}^k_{5Dc,5Dc}$, $\hat{H}^k_{1Dc,1Dc}$, and $\hat{H}^k_{5Dv,5Dv}$ are dominated by second-order terms in $\hat{k}$. Hence, only the inter-band couplings contain first-order terms and

need to be considered in the following. The inter-band term $\hat{H}^k_{5Dc,1Dc}$ is only due to inversion asymmetry and therefore small for most III-V and II-VI semiconductors. [JSdAeSLR05]

Hence, only the following terms from Sec. 2.6 are relevant for the well-posedness of the Hamiltonian eigenvalue problem,

$$\hat{H}^k_{1Dc5Dv} = \left(\begin{array}{ccc} \hat{k}_x^\dagger P & \hat{k}_y^\dagger P & \hat{k}_z^\dagger P \end{array} \right), \tag{3.15}$$

$$\hat{H}^k_{5Dc5Dv} = \left(\begin{array}{ccc} 0 & Q\hat{k}_z & Q\hat{k}_y \\ Q\hat{k}_z & 0 & Q\hat{k}_x \\ Q\hat{k}_y & Q\hat{k}_x & 0 \end{array} \right). \tag{3.16}$$

Analogously to White's Hamiltonian Eq. (3.2), $\hat{H}_{1Dc5Dv}$ and $\hat{H}_{5Dc5Dv}$ represent their momentum space counterpart exactly only if the envelope function spaces for the different components V_S for the Γ_{1c} bands, V_X, V_Y, and V_Z for the Γ_{5v} bands and $V_{X'}$, $V_{Y'}$, and $V_{Z'}$ for the Γ_{5c} bands obey the following set of conditions,

$$\begin{aligned} V_X &= \partial_x V_S,\, V_Y = \partial_y V_S,\, V_Z = \partial_z V_S, \\ V_{X'} &= \partial_y V_Z = \partial_z V_Y, \\ V_{Y'} &= \partial_z V_X = \partial_x V_Z, \\ V_{Z'} &= \partial_x V_Y = \partial_y V_X. \end{aligned} \tag{3.17}$$

They are derived from the particular matrix elements occurring in Eqs. (3.15) and (3.16). Consider now a uniform tensor grid $\{\mathbf{R}_j\}$ with grid-spacing h in each direction. Three-dimensional bases that obey the conditions of Eqs. (3.17) can easily be constructed from tensor product functions of the one-dimensional basis functions in Eqs. (3.9) and (3.10) that we defined earlier. Let us relabel the set of polynomial functions $\{u^S\}$ in Eq. (3.9) as $\{u^V\}$ and the set $\{u^{LH}\}$ in Eq. (3.10) as $\{u^W\}$, respectively. Likewise, the one-dimensional variational spaces V^S and V^{LH} are relabeled as V and W, respectively. Then, the component spaces for the S-like conduction band and the X-like valence band, for example, are given by $V_S = V \times V \times V$ and $V_X = W \times V \times V$, respectively, and obey the condition $V_X = \partial_x V_S$ as one can easily verify. Correspondingly, the local polynomial basis functions in cell $\mathbf{R}_I = (x_I, y_I, z_I)^T$ read

$$u^S_{K,\mathbf{R}_I}(\mathbf{r}) = u^V_{K_1,x_I}(x) u^V_{K_2,y_I}(y) u^V_{K_3,z_I}(z), \tag{3.18}$$

$$u^X_{K,\mathbf{R}_I}(\mathbf{r}) = u^W_{K_1,x_I}(x) u^V_{K_2,y_I}(y) u^V_{K_3,z_I}(z), \tag{3.19}$$

with $\mathbf{r} = (x, y, z)^T$. Here, we have lumped the three polynomial function indices into a single index $K = (K_1, K_2, K_3)$. These functions constitute a basis for V^S and V^X, respectively. Analogously to the one-dimensional case, constraints for the three-dimensional expansion coefficients can be derived that guarantee the required continuity in each direction. Again, numerically efficient basis functions may be

Table 3.1: Tensor product spaces for envelope function components.

Component	Tensor product space
Γ_{1c} conduction band S	$V \times V \times V$
Γ_{5v}-like valence band X	$W \times V \times V$
Γ_{5v}-like valence band Y	$V \times W \times V$
Γ_{5v}-like valence band Z	$V \times V \times W$
Γ_{5c}-like conduction band X'	$V \times W \times W$
Γ_{5c}-like conduction band Y'	$W \times V \times W$
Γ_{5c}-like conduction band Z'	$W \times W \times V$

constructed that intrinsically obey these constraints. This basis can be written in terms of the one-dimensional basis functions Eq. (3.11) and (3.12) as

$$\begin{aligned} v^S_{K,\mathbf{R}_I}(\mathbf{r}) &= v^V_{K_1,x_I}(x) v^V_{K_2,y_I}(y) v^V_{K_3,z_I}(z), \\ v^X_{K,\mathbf{R}_j}(\mathbf{r}) &= v^W_{K_1,x_I}(x) v^V_{K_2,y_I}(y) v^V_{K_3,z_I}(z), \end{aligned} \tag{3.20}$$

where $\mathbf{R}_I = (x_I, y_I, z_I)^T$ is a grid point and the index K labels the function indices. The complete set of product spaces that obeys the conditions in Eq. (3.17) is summarized in Table 3.1.

Thus, the present symmetry adapted finite element method guarantees the faithful representation of $\mathbf{k}$-space and manifestly avoids spurious solutions caused by discretization. There is another major advantage in using continuous basis functions. In contrast to the finite difference or finite volume methods, any material parameters and the electrostatic potential in the Hamiltonian Eq. (2.73) are not tacitly assumed to be cell-wise constant but can be arbitrary functions of position themselves. This allows a significantly more precise modeling of heterostructure shapes and alloy profiles, while admitting fewer grid lines and much smaller matrix dimensions than corresponding finite difference methods. Finally, we note that the basis functions in the SAFE method are not orthogonal, which leads to a generalized eigenvalue problem. Fortunately, highly efficient schemes for the solution of the generalized eigenvalue problem are available, e.g. the shift-invert Arnoldi iteration summarized in Sec. 4.4.

3.2.4 Gauge-invariant SAFE method for magnetic fields

Magnetic fields are commonly incorporated into the envelope function approach by invoking the substitution $\hat{\mathbf{k}} \to -i\nabla + (e/\hbar)\mathbf{A}$. This poses no problem for the present finite element method since matrix elements with the vector potential $\mathbf{A}(\mathbf{r})$ can be calculated straightforwardly. However, the resulting Hamilton matrix depends on the chosen gauge and this can lead to substantial errors if the gauge is unfit for the problem. [GU98] Therefore, it is desirable to formulate the discrete envelope function Hamiltonian eigenvalue problem in a gauge-invariant manner.

A gauge-invariant formulation of the general multi-band envelope function theory, based on lattice gauge theory, has been developed recently. [AMV08] This method, however, relies strongly on the finite difference scheme. In addition, the commutation relations of the covariant derivatives

$$\mathbf{D} = \nabla + (ie/\hbar)\mathbf{A}, \tag{3.21}$$

$$[D_\mu, D_\nu] = \epsilon^{\mu\nu\lambda} i \frac{e}{\hbar} B_\lambda. \tag{3.22}$$

converge slowly to the continuum limit. This is illustrated in Fig. 3.3 that compares the exact expectation value of the commutator $1/i\,[D_x, D_y]$ for the lowest Landau level of a free electron system at $B_z = 25$ T with the one predicted by the method of Ref. [AMV08].

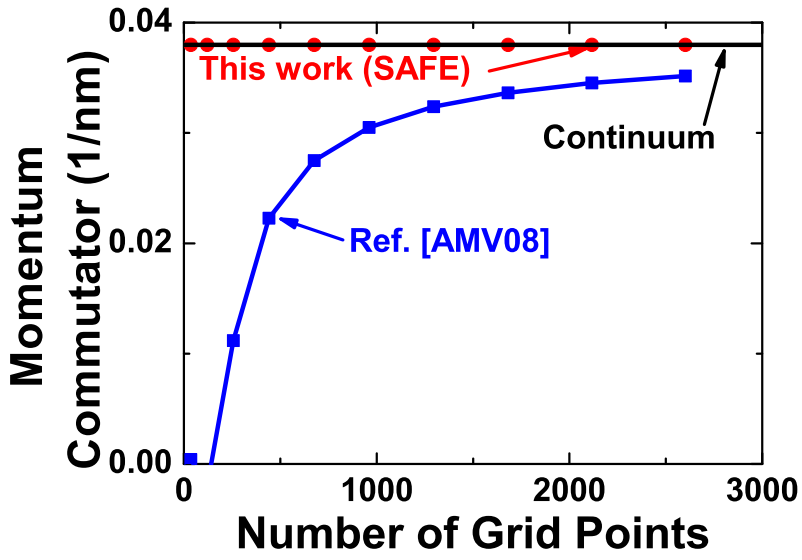

Figure 3.3: Calculated ground state expectation value of the momentum commutator for a free two-dimensional electron gas in a vertical magnetic field of 25 T. The full line indicates the exact continuum result. The circles (red) are results obtained in terms of the present SAFE method, whereas the squares (blue) have) have been obtained by a previous gauge-invariant finite difference method (Ref. [AMV08]).

Within the framework of finite elements, we have developed a robust, numerically more efficient, as well as gauge-invariant formulation of envelope function theory by generalizing an old method of Luttinger for Wannier functions. [Lut51] In contrast to the original theory, we can evaluate all matrix elements involving the position operator exactly and do not need any of the approximations required in Luttinger's method. The basic idea of our adaptation is to multiply the local basis functions $\{v^C_{K,\mathbf{R}_I}(\mathbf{r}) | C = S, X, Y, Z, X', Y', Z'\}$ with a position-dependent phase function $U_{\mathbf{R}_I}$ that already accounts for most of the action of the magnetic field. The magnetic field

adapted basis functions are defined as

$$\widetilde{v}^C_{K,\mathbf{R}_I}(\mathbf{r}) = U_{\mathbf{R}_I}(\mathbf{r}) v^C_{K,\mathbf{R}_I}(\mathbf{r}), \tag{3.23}$$

$$U_{\mathbf{R}_I}(\mathbf{r}) = \exp\left[-i\frac{e}{\hbar}\int_{\sigma(\mathbf{R}_I,\mathbf{r})} \mathrm{d}\mathbf{l}\cdot\mathbf{A}(\mathbf{l})\right]. \tag{3.24}$$

Here, the path integration is performed along the straight line segment $\sigma(\mathbf{R}_I, \mathbf{r})$ from $\mathbf{R}_I$ to $\mathbf{r}$. We point out that any integration path is admissible that vanishes in the limit of vanishing grid spacing. This would lead to a slightly different but equivalent formulation of the problem with the same correct continuum limit. The straight line path has the advantage of leading to a particular simple result. The action of the covariant derivative on the basis functions is given by

$$\left[\nabla + i\frac{e}{\hbar}\mathbf{A}(\mathbf{r})\right]\widetilde{v}^C_{K,\mathbf{R}_I}(\mathbf{r}) = U_{\mathbf{R}_I}(\mathbf{r})\left[\nabla + i\frac{e}{\hbar}\mathbf{A}^{loc}_{\mathbf{R}_I}(\mathbf{r})\right] v^C_{K,\mathbf{R}_I}(\mathbf{r}), \tag{3.25}$$

where the gauge-invariant local residual potential is given by

$$\mathbf{A}^{loc}_{\mathbf{R}_I}(\mathbf{r}) = \int_0^1 \lambda \mathrm{d}\lambda\, \mathbf{B}(\mathbf{r},\lambda)\times(\mathbf{r}-\mathbf{R}_I), \tag{3.26}$$

$$\mathbf{B}(\mathbf{r},\lambda) = \nabla\times\mathbf{A}[\mathbf{R}_I + \lambda(\mathbf{r}-\mathbf{R}_I)]. \tag{3.27}$$

For constant magnetic fields $\mathbf{B}$, this expression simplifies to

$$\mathbf{A}^{loc}_{\mathbf{R}_I}(\mathbf{r}) = \frac{1}{2}\mathbf{B}\times(\mathbf{r}-\mathbf{R}_I), \tag{3.28}$$

We note that $\mathbf{A}^{loc}_{\mathbf{R}_I}$ depends only on the integration path but not on the gauge of $\mathbf{A}$. Also note that matrix elements of this residual potential with the local basis functions are of the order of $|\mathbf{B}|h$ and thus tend to zero in the continuum limit. Using Eq. (3.25), the matrix elements in the envelope function Hamiltonian Eq. (2.73) can be evaluated that are zero-th, first, and second order in $\hat{\mathbf{k}}$, respectively. The zero-th order matrix elements between the components C and C' become

$$\left\langle \widetilde{v}^C_{K,\mathbf{R}_I}\right| \gamma(\mathbf{r}) \left|\widetilde{v}^{C'}_{K',\mathbf{R}_J}\right\rangle = \left\langle v^C_{K,\mathbf{R}_I}\right| U^*_{\mathbf{R}_I}(\mathbf{r})U_{\mathbf{R}_J}(\mathbf{r})\gamma(\mathbf{r}) \left|v^{C'}_{K',\mathbf{R}_J}\right\rangle, \tag{3.29}$$

where $\gamma(x)$ is the position-dependent term in the Hamiltonian. The first-order matrix elements are

$$\begin{aligned}&\left\langle \widetilde{v}^C_{K,\mathbf{R}_I}\right| \gamma(\mathbf{r}) D_x \left|\widetilde{v}^{C'}_{K',\mathbf{R}_J}\right\rangle \\ &= \left\langle v^C_{K,\mathbf{R}_I}\right| U^*_{\mathbf{R}_I}(\mathbf{r})U_{\mathbf{R}_J}(\mathbf{r})\gamma(\mathbf{r}) \left[\nabla + i\frac{e}{\hbar}\mathbf{A}^{loc}_{\mathbf{R}_J}(\mathbf{r})\right]_x \left|v^{C'}_{K',\mathbf{R}_J}\right\rangle,\end{aligned} \tag{3.30}$$

and the second-order matrix elements are given by

$$\begin{aligned}&\left\langle \widetilde{v}^C_{\mathbf{R}_I}\right| \mathbf{D}^\dagger\gamma(\mathbf{r})\mathbf{D} \left|\widetilde{v}^{C'}_{\mathbf{R}_J}\right\rangle \\ &= \left\langle v^C_{K,\mathbf{R}_I}\right| \left[\nabla + i\frac{e}{\hbar}\mathbf{A}^{loc}_{\mathbf{R}_I}(\mathbf{r})\right]^\dagger U^*_{\mathbf{R}_I}(\mathbf{r})U_{\mathbf{R}_J}(\mathbf{r})\gamma(\mathbf{r}) \\ &\cdot \left[\nabla + i\frac{e}{\hbar}\mathbf{A}^{loc}_{\mathbf{R}_J}(\mathbf{r})\right] \left|v^{C'}_{K',\mathbf{R}_J}\right\rangle.\end{aligned} \tag{3.31}$$

One may easily verify that these matrix elements are invariant under the gauge transformation

$$\begin{aligned}
\mathbf{A}(\mathbf{r}) &\rightarrow \mathbf{A}(\mathbf{r}) + \nabla\Lambda(\mathbf{r}), && (3.32)\\
v^C_{\mathbf{R}_I}(\mathbf{r}) &\rightarrow \mathrm{Exp}\left[-i\frac{e}{\hbar}\Lambda(\mathbf{R}_I)\right] v^C_{\mathbf{R}_I}(\mathbf{r}), && (3.33)\\
\widetilde{v}^C_{\mathbf{R}_I}(\mathbf{r}) &\rightarrow \mathrm{Exp}\left[-i\frac{e}{\hbar}\Lambda(\mathbf{r})\right] \widetilde{v}^C_{\mathbf{R}_I}(\mathbf{r}). && (3.34)
\end{aligned}$$

Importantly, the momentum commutation relation is fulfilled independently of the grid spacing h since

$$\begin{aligned}
&\left\langle \widetilde{v}^C_{K,\mathbf{R}_I} \right| [D_\mu, D_\nu] \left| \widetilde{v}^{C'}_{K',\mathbf{R}_J} \right\rangle \\
&= \left\langle v^C_{K,\mathbf{R}_I} \right| U^*_{\mathbf{R}_I} U_{\mathbf{R}_J} \left[\partial_\mu + i\frac{e}{\hbar}\left(\mathbf{A}^{loc}_{\mathbf{R}_J}\right)_\mu, \partial_\nu + i\left(\frac{e}{\hbar}\mathbf{A}^{loc}_{\mathbf{R}_J}\right)_\nu \right] \left| v^{C'}_{K',\mathbf{R}_J} \right\rangle, \quad (3.35)
\end{aligned}$$

and

$$\begin{aligned}
&[\partial_\mu + i\frac{e}{\hbar}\left(\mathbf{A}^{loc}_{\mathbf{R}_J}\right)_\mu, \partial_\nu + i\frac{e}{\hbar}\left(\mathbf{A}^{loc}_{\mathbf{R}_J}\right)_\nu] \\
&= i\frac{e}{\hbar}\partial_\mu \left(\mathbf{A}^{loc}_{\mathbf{R}_J}\right)_\nu - i\frac{e}{\hbar}\partial_\nu \left(\mathbf{A}^{loc}_{\mathbf{R}_J}\right)_\mu \\
&= \frac{ie}{2\hbar}\partial_\mu \left[\mathbf{B} \times (\mathbf{r} - \mathbf{R}_J)\right]_\nu - \frac{ie}{2\hbar}\partial_\nu \left[\mathbf{B} \times (\mathbf{r} - \mathbf{R}_J)\right]_\mu \\
&= i\frac{e}{\hbar}\epsilon^{\mu\nu\lambda}B_\lambda. \quad (3.36)
\end{aligned}$$

It can be shown that this gauge-invariant finite element method converges to the continuum limit with $O(h|\mathbf{B}|)$ in the presence of magnetic fields. This is the best order of convergence one may expect since the residual potential Eq. (3.27) vanishes in the continuum limit $\propto h|\mathbf{B}|$ on the support of the basis function. The proof of this continuum limit is outlined in Appendix A.

3.3 Results

We have applied the present method to the exciton g-factor and its electric field dependence in dilute self-assembled InAs-GaAs quantum dots embedded in GaAs. This structure has been investigated theoretically before, [JEK+11] employing a finite difference scheme. [AMV08] While these results are in good agreement with experiment, we will show here that they are actually plagued by an admixture of spurious modes to the real wave functions which masks important findings.

In experiment, the quantum dots (QDs) were grown as a single layer with a nominal In-composition of 50% at a high growth temperature leading to lower than nominal In-concentrations. [JEK+11] The QDs were modeled as having a truncated lens shape with a diameter of $D = 24$ nm, a height of 6 nm above the wetting layer of 0.18 nm thickness and an inverse trumpet-like In-compositional profile.

[OKW+05, MCFJ02, KCB+10] The In-concentration of the InGaAs alloy was set to 0.2 at the base and side of the dot, and values of $0.2-0.9$ at the dot apex. [MCFJ02] The electronic structure calculations in Ref. [JEK+11] invoked the eight-band envelope function method. The magnetic field was incorporated in terms of lattice gauge theory in a gauge invariant manner and spatial finite volume discretization, [AMV08] combined with the correct operator ordering. [For97, Bur99] Strain fields were included using continuum elasticity theory and their electronic effect was taken into account via deformation potentials and the linear piezoelectric effect. [SGB99] The direct Coulomb interaction was included by employing lowest order perturbation theory.

The electrical tunability Δg of the g-factor was defined as the difference of g-factors for a vertical electric field of 60 kV/cm and zero electric field, both at a magnetic field of 10 T. [JEK+11] An important prediction in this paper was that pronounced hole g-factor tuning can only be expected for In-dilute quantum dots, while the electron g-factor responds weaker to the electric field.

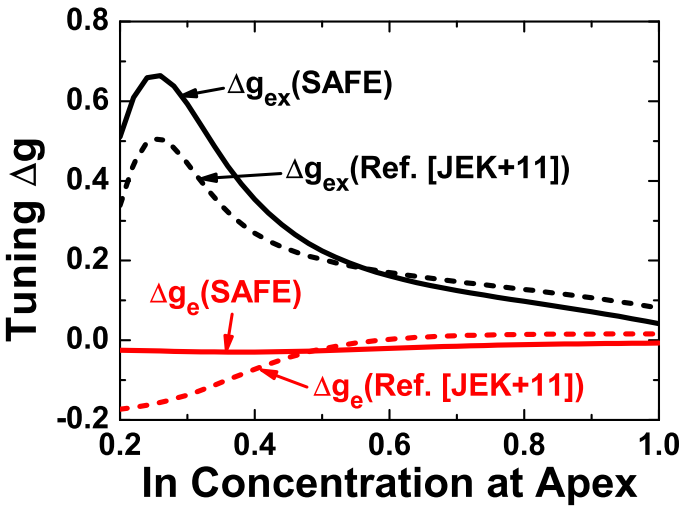

Figure 3.4: Calculated dependence of the electric tuning of the electron and exciton Landé factors g_e and g_{ex}, respectively, of an InAs/GaAs embedded quantum dot as a function of the In-concentration at the dot apex. The dotted lines indicate numerical results from a gauge-invariant finite differences method (Ref. [JEK+11]). The full lines indicate the present (SAFE) results.

We have repeated this calculation, using exactly the same geometry and material parameters, yet invoking the present symmetry adapted finite element method and the gauge-invariant incorporation of magnetic fields outlined above. Figure 3.4 compares the calculated value of Δg obtained by the present method (solid lines) and the previous calculations (dashed lines) for different In-concentrations at the QD apex. Our calculations indicate that there is almost no tuning of the electron g-factor and consequently a significantly larger tuning of the exciton g-factor $g_{ex} = g_e - g_h$ than

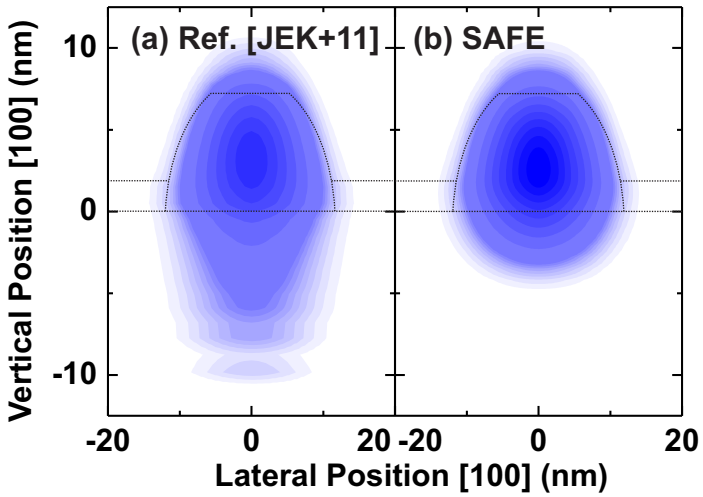

Figure 3.5: Contour graph of the electron density in the (010) plane in an InAs/GaAs embedded quantum dot through the dot center. There is an applied vertical electric field of 60 kV/cm. The left panel shows the finite difference calculations of Ref. [JEK$^+$11]. The right panel shows the calculated density obtained by the present (SAFE) method.

predicted previously. We can trace the result of the previous calculations to an admixture of spurious modes in the electron wave function. This is illustrated in Fig. 3.5, which depicts a cross section of the density of the bound electron ground state in the (010) plane at the center of the QD for a vertical electric field of 60 kV/cm. The dotted lines indicate the shape of the QD and the wetting layer. Figure 3.5(a) shows results from Ref. [JEK$^+$11]. The oscillatory behavior of the bound state density beneath the QD is unphysical. This alters the g-factor and artificially increases the electron tuning. The present results (Fig. 3.5(b)) show no such oscillations and the bound state is confined to the QD.

Note that in addition, the SAFE method requires only about 1/16 of the degrees of freedom (dimension of the discrete Hamiltonian) required by the finite difference method in order to obtain results of comparable accuracy. First, this is due to the fact that no degrees of freedom are wasted on spurious modes. Second, stronger continuity conditions and higher order polynomials lead to a basis that is well suited to accurately representing smooth envelope functions.

3.4 Summary

In summary, we have presented the symmetry adapted finite elements method for the discrete real-space $\mathbf{k} \cdot \mathbf{p}$ envelope function Hamiltonian. The method is suitable for large mesoscopic heterostructure and is inherently free form spurious solutions caused by the ill-representation of first-order derivatives that plagues previous real-space

discretization schemes. The method exploits the symmetry of the EFA Hamiltonian and yields a real-space basis that represents the relevant first-order terms in the Hamiltonian exactly. In addition, we have presented a gauge-invariant extension of this method that shows very fast convergence to the correct continuum limit. As an application of the method, we predict the exciton g-factor tuning in single InAs/GaAs to be significantly larger than previously expected. In conclusion, we believe the present method to be an effective systematic improvement of electronic structure calculations of mesoscopic semiconductor heterostructures.

Chapter 4

Concrete numerical implementation

4.1 Introduction

In the previous chapter, we have introduced the *symmetry adapted finite element* (SAFE) method for the numerical discretization of the $k \cdot p$ Hamiltonian. We used a few specific basis functions on a uniform tensor-product grid to clarify the concept of the SAFE method. Further, we used a notation similar to that of the tight-binding method since we believe this notation to be more intuitive than the abstract finite element framework. In Sec. 4.2, we generalize this simplified scheme and provide our concrete implementation of the abstract finite element method. This implementation is optimized for the efficient discretization of the multi-band Hamiltonian, material parameters of arbitrary position dependence and the so-called isoparametric elements that allow to adjust the tensor-product mesh to the shape of the nanostructure. In Sec. 4.3, we briefly summarize the so-called *direct* approach to solve linear systems of equations that we applied to the stiffness equation and to Poisson's equation. Section 4.4 finally deals with the solution of the generalized inner eigenvalue problem obtained from the operator eigenvalue problem of the $k \cdot p$-Hamiltonian discretized by the SAFE method.

4.2 Implementation of the finite element method

In the following, we summarize our implementation of the finite element method. Section 4.2.1 outlines the construction of the non-uniform tensor-product finite element space and its basis in which we compute the discrete operator bilinear forms of the $k \cdot p$ Hamiltonian, the stiffness equation and Poisson's equation. In Sec. 4.2.2, we introduce the so-called isoparametric finite elements which generalize the tensor-product finite elements to more flexible, non-rectangular domain shapes. Next, we address the efficient computation of operator bilinear forms in the finite element space

in Sec. 4.2.3. To this end, we perform the integration of differential operators efficiently using basic linear algebra operations for which optimized program libraries (BLAS libraries) exists. In Sec. 4.2.4, the general Hermite elements are discussed, which constitute the C^1 conforming space of continuously differential functions. As indicated in Ch. 3, we employed these elements in the SAFE method for some or all Cartesian directions depending on the component of the envelope function. Finally, the numerical realization of Dirichlet and Neumann boundary conditions is treated in Sec. 4.2.5.

4.2.1 Finite element space

In the following, we apply the abstract finite element framework, which is comprehensively discussed in the literature, [BS08] to obtain a concrete discretization scheme which is suitable for the semiconductor equations relevant to this work. We begin with the one-dimensional element which we extend to more dimension via tensor products. This yields a simple rectangular tensor-product grid and thus circumvents the problem of mesh generation that is encountered for triangular or tetrahedral elements.

Here, we will not present any proofs of uniqueness and existence of solutions, of approximability or of conformity, all of which can be found in the standard finite element literature. [BS08]

In one-dimensional space, the so-called Lagrange element is defined by an interval $K =]a, b[$, the polynomial space $P_n = \{p(x) | \text{degree}\, p(x) \leq n\}$ of degree n, and the set of $n+1$ nodal variables $\Sigma = \{L_i | i = 1 \ldots (n+1)\}$. The nodal variable are pairwise disjoint linear forms on P_n that constitute the *local* basis $\{u_i(x)\}$ of the Lagrange element by

$$L_i[u_j] = \delta_{ij}. \tag{4.1}$$

Since the polynomial space $P_n(K)$ has dimension $n+1$, the $n+1$ linear forms determine the $n+1$ local basis functions $u_i(x)$ that span P_n uniquely. For Lagrange interpolation, each nodal variable is simply an evaluation of a function f at that node, namely

$$L_i[f] = f(x_i). \tag{4.2}$$

The pairwise disjoint nodes are labeled $x_i \in \bar{K}$, where $\bar{K} = [a, b]$ denotes the closure of K. Hence, the basis functions have the property

$$u_j(x_i) = \delta_{ij}. \tag{4.3}$$

The local basis of the Lagrange element can be obtained explicitly from the canonical basis $\{1, x, x^2, \ldots, x^n\}$ of P_n by

$$u_i(x) = (V^{-T})_{i,j}\, x^j, \tag{4.4}$$

where V is the Vandermonde matrix

$$V = \begin{pmatrix} 1 & x_1 & \dots & x_1^n \\ 1 & x_2 & \dots & x_2^n \\ \vdots & \vdots & \ddots & \vdots \\ 1 & x_{n+1} & \dots & x_{n+1}^n \end{pmatrix}, \tag{4.5}$$

and V^{-T} its transpose inverse. For polynomial spaces of higher degree, the Vandermonde matrix becomes ill-conditioned thus increasing arithmetic error. This can be redeemed by using an orthonormal basis like the Legendre polynomials instead of the canonical basis. [HW10] Hence, we use the Legendre polynomials $l_0, l_1, \dots$ on $[a, b]$ to define the basis functions as

$$u_i(x) = (N^{-T})_{i,j}\, l_j(x), \tag{4.6}$$

with the nodal matrix

$$N = e_i e_j^T L_i[l_j] = \begin{pmatrix} l_0(x_1) & l_1(x_1) & \dots & l_n(x_1) \\ l_0(x_2) & l_1(x_2) & \dots & l_n(x_2) \\ \vdots & \vdots & \ddots & \vdots \\ l_0(x_{n+1}) & l_1(x_{n+1}) & \dots & l_n(x_{n+1}) \end{pmatrix}. \tag{4.7}$$

The evaluation and differentiation of Legendre polynomials can be performed recursively and the polynomial coefficients need not be known explicitly. [HW10]

Next, the construction of the global finite element space from these local elements is discussed. The global finite element space consists of a set of finite elements $\{(K_m, P_m, \Sigma_m)\}$. The set of disjoint local finite element domains $K_m =]a_m, b_m[$ is a complete partition of the global domain Ω, on which the partial differential equations are to be solved, namely

$$\Omega = \bigcup_m \bar{K}_m, \tag{4.8}$$

where the intervals are not required to be uniform.

In order to construct a global conforming basis, the first ($i = 1$) and last ($i = n+1$) nodes of the m-th element are chosen on the element boundaries such that

$$L_{m,1}[f] = f(a_m) \text{ and } L_{m,n+1}[f] = f(b_m). \tag{4.9}$$

This guarantees that

$$u_{m,1}(a_m) = 1,\ u_{m,n+1}(b_m) = 1, \tag{4.10}$$

and

$$u_{m,2}(a_m) = \dots = u_{m,n+1}(a_m) = u_{m,1}(b_m) = \dots = u_{m,n}(b_m) = 0. \tag{4.11}$$

Consequently, the nodal variables at the element boundaries of neighboring elements can be identified. Suppose, for example that the $(m-1)$-th element is directly left

of the m-th element. Then, $L_{m-1,n+1} = L_{m,1}$ constitutes the global nodal variable $\tilde{L}_{\mathrm{l2g}(m,1)}$, where the function $\mathrm{l2g}(m,i)$ is the so-called local-to-global mapping and maps the element index and the local index of a nodal variable to a global index of the global finite element space. Clearly, we have that $\mathrm{l2g}(m-1,n+1) = \mathrm{l2g}(m,1)$ and thus a global basis function across element boundaries is defined by

$$v_{\mathrm{l2g}(m,1)}(x) = \begin{cases} u_{m-1,n+1}(x) & \text{if } a_{m-1} < x \leq a_m \\ u_{m,1}(x) & \text{if } a_m < x < b_m \\ 0 & \text{otherwise} \end{cases} . \tag{4.12}$$

This clearly implies, that $n \geq 1$ in order to construct a non-trivial global finite element space.

For $n > 1$, there are $n-1$ interior basis functions that correspond to global function by

$$v_{\mathrm{l2g}(m,i)}(x) = \begin{cases} u_{m,i}(x) & \text{if } a_m < x < b_m \\ 0 & \text{otherwise} \end{cases} , \tag{4.13}$$

for $i = 2, \ldots, n$. The nodes corresponding to these interior nodal variables can be chosen arbitrarily in the interval $]a,b[$. For convenience, we place them uniformly over the interval

$$x_{m,i} = \frac{i-1}{n-1}(b_m - a_m) + a_m, \tag{4.14}$$

for and $1 < i < n+1$.

The resulting global basis $\{v_j\}$ is piecewise polynomial and is continuous across element boundaries. It is thus said to be $C^0(\Omega)$-conforming, where, in this context, $C^0(\Omega)$ denotes the set of Lipschitz continuous functions on Ω. It can be shown within the theory of Sobolev spaces that elliptic differential operators of second order can be represented on complete Lipschitz continuous spaces exactly. [BS08] Moreover, elliptical operators are well-approximated on finite Lipschitz continuous spaces.

We construct an n-dimensional basis simply by tensor products of one-dimensional bases. In three dimensions, the local domains, variables and basis functions become

$$\begin{aligned} K_m &=]a_m^x, b_m^x[\times]a_m^y, b_m^y[\times]a_m^z, b_m^z[, & (4.15)\\ L_{m,(ijk)}[f] &= f(x_i, y_j, z_k), & (4.16)\\ u_{m,(ijk)}(x,y,z) &= u_{m,i}^x(x) u_{m,j}^y(y) u_{m,k}^z(z), & (4.17) \end{aligned}$$

where the nodes are given by $\mathbf{r}_{(ijk)} = (x_i, y_j, z_k)^T$. Here, we use the same polynomial degree n in all directions and thus $1 \leq i \leq n+1$, $1 \leq j \leq n+1$, and $1 \leq k \leq n+1$ in the above relations. The construction of the global finite element space proceeds completely analogously to the one-dimensional case. The local-to-global mapping is thus

$$\mathrm{l2g} : m, (ijk) \mapsto (i'j'k'), \tag{4.18}$$

and the global $C^0(\Omega)$-conforming basis is $\{v_{(i'j'k')}\}$ with

$$v_{(i'j'k')}(x,y,z) = v_{i'}^x(x) v_{j'}^y(y) v_{k'}^z(z). \tag{4.19}$$

For convenience, we denote the triple index vectors as **i**, **j**, **k** and so on. The converse mapping of l2g is not uniquely defined. Still it is useful to define the global-to-local mapping

$$\mathrm{g2l} : \mathbf{i} \mapsto \{(m, \mathbf{k}) \,|\, \mathrm{l2g}(m, \mathbf{k}) = \mathbf{i}\}, \tag{4.20}$$

which maps a global index to a set of element and local indices. With this notation, the matrix A corresponding to the operator bilinear form of the operator $\hat{L}$ can simply be written as the sum over purely local integrals

$$A_{\mathbf{i},\mathbf{j}} = \sum_{(m,\mathbf{k})\in g2l(\mathbf{i})} \sum_{(m,\mathbf{l})\in g2l(\mathbf{j})} \int_{K_m} \mathrm{d}^3 r \; u^*_{m,\mathbf{k}}(\mathbf{r}) \hat{L} u_{m,\mathbf{l}}(\mathbf{r}). \tag{4.21}$$

Although, here, all basis functions are real, we still preserve the general form valid for complex basis functions in view of the Luttinger phase functions in Sec. 3.2.4.

Note that differential operators are to be understood in the sense of variational calculus. A differential operator $\hat{L} = \partial_i a(\mathbf{r}) \partial_j$ with a generic parameter function $a(\mathbf{r})$ is integrated as [BS08]

$$\int_{K_m} \mathrm{d}^3 r \; u^*_{m,\mathbf{k}}(\mathbf{r}) \hat{L} u_{m,\mathbf{l}}(\mathbf{r}) = - \int_{K_m} \mathrm{d}^3 r \; a(\mathbf{r}) \left[\partial_i u^*_{m,\mathbf{k}}(\mathbf{r})\right] \left[\partial_j u_{m,\mathbf{l}}(\mathbf{r})\right]. \tag{4.22}$$

We illustrate this method on the concrete example of Poisson's equation

$$-\nabla \varepsilon_0 \varepsilon_r(\mathbf{r}) \nabla \Phi(\mathbf{r}) = \rho(\mathbf{r}). \tag{4.23}$$

In the variational formulation on the finite element space, this partial differential equation becomes a system of linear equations

$$A\mathbf{x} = \mathbf{b}. \tag{4.24}$$

The matrix A is given by

$$A_{\mathbf{i},\mathbf{j}} = - \sum_{(m,\mathbf{k})\in g2l(\mathbf{i})} \sum_{(m,\mathbf{l})\in g2l(\mathbf{j})} \int_{K_m} \mathrm{d}^3 r \; \varepsilon_0 \varepsilon_r(\mathbf{r}) \left[\nabla u_{m,\mathbf{k}}(\mathbf{r})\right] \cdot \left[\nabla u_{m,\mathbf{l}}(\mathbf{r})\right], \tag{4.25}$$

where the basis functions $u_{m,\mathbf{k}}(\mathbf{r})$ are purely real. The Hilbert-space product of the finite element basis functions with the charge density $\rho(\mathbf{r})$ results in the right-hand-side

$$\mathbf{b}_\mathbf{i} = \sum_{(m,\mathbf{k})\in g2l(\mathbf{i})} \int_{K_m} \mathrm{d}^3 r \; u_{m,\mathbf{k}}(\mathbf{r}) \rho(\mathbf{r}). \tag{4.26}$$

The solution vector $\mathbf{x}$ provides the expansion coefficient of the approximated electrostatic potential

$$\Phi^h(\mathbf{r}) = \sum_m \sum_\mathbf{k} \mathbf{x}_{\mathrm{l2g}(m,\mathbf{k})} u_{m,\mathbf{k}}(\mathbf{r}). \tag{4.27}$$

A polynomial basis of degree n yields an error order of h^n for first and second-order differential operators. [BS08] The approximation of zero-th order operators has an error order of h^{n+1}. [BS08] In this context, h is the maximal diameter of all local element domains K_m.

4.2.2 Isoparametric finite elements

In order to accurately compute strain fields and electrostatic potentials, the tensor grid can be adjusted to match the shape of the nanostructure. Especially, in the case of the quadratic piezoelectric effect in truncated pyramidal quantum dots, we find that a rectangular tensor product grid does not lead to sufficiently accurate results with reasonable computational effort.

The so-called isoparametric finite elements present a simple extension to the tensor-product finite elements. [BS08] Given a non-rectangular domain K and an invertible polynomial map $\boldsymbol{\phi} : \tilde{K} \to K$ from the cubic reference domain $\tilde{K} = [-1, 1]^3$ to the domain K, the finite element basis $\{u_\mathbf{i}\}$ on K is defined by

$$u_\mathbf{i}(\mathbf{r}) = [\tilde{u} \circ \boldsymbol{\phi}^{-1}](\mathbf{r}) = \tilde{u}_\mathbf{i}(\boldsymbol{\phi}^{-1}(\mathbf{r})), \tag{4.28}$$

in terms of the standard tensor-product basis $\{\tilde{u}_\mathbf{i}\}$ on $\tilde{K}$. Likewise, a set of nodal variables $\{L_\mathbf{i}\}$ on K is defined by

$$L_\mathbf{i}[f] = \tilde{L}_\mathbf{i}[f \circ \boldsymbol{\phi}] = f[\phi(\tilde{\mathbf{r}}_\mathbf{i})], \tag{4.29}$$

in terms of the nodal variables $\tilde{\Sigma} = \{\tilde{L}_\mathbf{i}\}$ with the nodes $\tilde{\mathbf{r}}_\mathbf{i}$ on the reference domain $\tilde{K}$.

The mapping ϕ is required to be regular, i.e. the Jacobian $J = \partial\boldsymbol{\phi}/\partial\tilde{\mathbf{r}}$ must be invertible on $\tilde{K}$. Moreover, the set of finite element domains $\{K\}$ must be a complete partition of the domain Ω.

On the element (K, P, Σ), the operator bilinear form of the differential operator $\partial_i a(\mathbf{r})\partial_j$ can then be evaluated in terms of basis functions on the reference domain by variable substitution as

$$\begin{aligned}
&\int_K \mathrm{d}^3r\; u^*_\mathbf{k}(\mathbf{r})\partial_i a(\mathbf{r})\partial_j u_\mathbf{l}(\mathbf{r}) \\
&= -\int_K \mathrm{d}^3r\; a(\mathbf{r})\; [\partial_i u^*_\mathbf{k}](\mathbf{r})\; [\partial_j u_\mathbf{l}](\mathbf{r}) \\
&= -\int_{\tilde{K}} \mathrm{d}^3\tilde{r}\; |J(\tilde{\mathbf{r}})|\; a(\boldsymbol{\phi}(\tilde{\mathbf{r}}))\; \left[(J^{-T}(\tilde{\mathbf{r}}))_{i,i'}\partial_{i'}\tilde{u}^*_\mathbf{k}(\tilde{\mathbf{r}})\right]\; \left[(J^{-T}(\tilde{\mathbf{r}}))_{j,j'}\partial_{j'}\tilde{u}_\mathbf{l}(\tilde{\mathbf{r}})\right] \\
&\approx -\sum_\mathbf{h} w_\mathbf{h}|J_\mathbf{h}|\; a_\mathbf{h}\; (J^{-T}_\mathbf{h})_{i,i'}\,[\partial_{i'}\tilde{u}^*_\mathbf{k}(\mathbf{q}_\mathbf{h})]\; (J^{-T}_\mathbf{h})_{j,j'}\,[\partial_{j'}\tilde{u}_\mathbf{l}(\mathbf{q}_\mathbf{h})]\,(\mathbf{q}_\mathbf{h}),
\end{aligned} \tag{4.30}$$

where $|J(\tilde{\mathbf{r}})|$ denotes the Jacobi determinant at position $\tilde{\mathbf{r}}$. In the last line, the integral is approximated by a sum. The numerical quadrature points in the reference domain are $\mathbf{q}_\mathbf{h}$ and the quadrature weights are $w_\mathbf{h}$ and, correspondingly, $a_\mathbf{h} = a(\boldsymbol{\phi}(\mathbf{q}_\mathbf{h}))$ and $J_\mathbf{h} = J(\mathbf{q}_\mathbf{h})$.

In our calculation we employ tensor-product Gauss-Legendre quadrature where

$$\mathbf{q}_{(i,i,k)} = (q^1_i, q^1_j, q^1_k)^T, \tag{4.31}$$

and

$$\mathbf{w}_{(i,i,k)} = w_i^1 w_j^1 w_k^1, \tag{4.32}$$

with $1 \leq i, j, k \leq M$. The one-dimensional M-th order Gauss-Legendre quadrature points $q_1^1, \ldots, q_M^1$ and weights $w_1^1, \ldots, w_M^1$ are tabulated for the interval $]-1, 1[$ in the literature. [PTVF07] Differential operators of order $\partial_i a(\mathbf{r})$, $a(\mathbf{r})\partial_j$, and $a(\mathbf{r})$ are integrated analogously.

The error order of isoparametric finite element is the same as for the tensor-grid finite elements. [BS08] However, the error is also proportional to the norm of the inverse Jacobi matrix of the mapping $\boldsymbol{\phi}$ within in the finite element domain. Clearly, the Jacobi matrix must not be singular or near singular in this domain.

4.2.3 Efficient implementation

It is common for finite element methods that the discretization may take a similar amount of time as the numerical solution of the resulting matrix equation. [HW10] Especially, the discretization of the multi-band $k \cdot p$ Hamiltonian requires the evaluation of a large number of integrals. A naive implementation may easily take by a factor ten to a hundred more time than an optimized implementation. It is, however, not desirable to optimize the scientific source code itself since optimization is always error-prone, reduces the readability of the code and can in extreme cases lead to poorly structures incomprehensible code. Instead of optimizing our own code, we reformulate the numerical integration (4.30) in matrix form. In this form, highly optimized linear algebra (or BLAS) packages like Intel's Math Kernel Library can be employed while the scientific program code is kept clean and readable.

First, we bring the integral for the rectangular tensor-product elements (4.25) in an analogous form to Eq. (4.30). To this end, note that the non-uniform tensor grid is a special case of isoparametric finite elements with the mapping

$$\boldsymbol{\phi}(\tilde{r}) = \begin{pmatrix} a^x \\ a^y \\ a^z \end{pmatrix} + \frac{1}{2} \begin{pmatrix} (b^x - a^x)(\tilde{r}_x + 1) \\ (b^y - a^y)(\tilde{r}_y + 1) \\ (b^z - a^z)(\tilde{r}_z + 1) \end{pmatrix}, \tag{4.33}$$

for a domain $K =]a^x, b^x[\times]a^y, b^y[\times]a^z, b^z[$. In this case, the Jacobi matrix is diagonal and constant within the element. It reads

$$J = \frac{1}{2} \begin{pmatrix} b^x - a^x & 0 & 0 \\ 0 & b^y - a^y & 0 \\ 0 & 0 & b^z - a^z \end{pmatrix}. \tag{4.34}$$

Hence, the operator bilinear form is simply

$$\begin{aligned} &\int_K \mathrm{d}^3 r \; u_{\mathbf{k}}^*(\mathbf{r}) \partial_i a(\mathbf{r}) \partial_j u_{\mathbf{l}}(\mathbf{r}) \\ &\approx -4 \sum_{\mathbf{h}} |J| w_{\mathbf{h}} \; a_{\mathbf{h}} \; \frac{\partial_{i'} \tilde{u}_{\mathbf{k}}^*(\mathbf{q}_{\mathbf{h}})}{b^i - a^i} \; \frac{\partial_{j'} \tilde{u}_{\mathbf{l}}(\mathbf{q}_{\mathbf{h}})}{b^j - a^j}, \end{aligned} \tag{4.35}$$

with the constant Jacobi determinant $|J| = (b^x - a^x)(b^y - a^y)(b^z - a^z)/8$. Bilinear forms of other differential operators follow analogously. The numerical bilinear forms of the rectangular and isoparametric elements are now expressed in the same way.

Next, we define the matrices

$$\begin{aligned}
(\tilde{F}_0)_{k,h} &= \tilde{u}_k(\mathbf{q}_h), && (4.36)\\
(\tilde{F}_x)_{k,h} &= [\partial_{\tilde{x}}\tilde{u}_k](\mathbf{q}_h), && (4.37)\\
(\tilde{F}_y)_{k,h} &= [\partial_{\tilde{y}}\tilde{u}_k](\mathbf{q}_h), && (4.38)\\
(\tilde{F}_z)_{k,h} &= [\partial_{\tilde{z}}\tilde{u}_k](\mathbf{q}_h), && (4.39)
\end{aligned}$$

where k and h are linearized vector indices for the sake of clarity. The linear indices are obtained by some bijective map $\{\mathbf{k}\} \to \{1, 2, \ldots, N_\mathbf{k}\}$ with $N_\mathbf{k} = \mathrm{card}\{\mathbf{k}\}$. Further, the first-order derivatives for each Cartesian direction $i = x, y, z$ of the global coordinate system results by variable substitution and the chain rule in the matrices

$$(F_i)_{k,h} = (J_h^{-T})_{i,x}(\tilde{F}_x)_{k,h} + (J_h^{-T})_{i,y}(\tilde{F}_y)_{k,h} + (J_h^{-T})_{i,z}(\tilde{F}_z)_{k,h}, \tag{4.40}$$

and for the "zero-th order derivative" $i = 0$ in

$$(F_0)_{k,h} = (\tilde{F}_0)_{k,h}. \tag{4.41}$$

Hence, each local integral in Eq. (4.21) becomes a common matrix-matrix-product

$$\begin{aligned}
\int_K \mathrm{d}^3 r\; u^*_\mathbf{k}(\mathbf{r})\partial_i a(\mathbf{r})\partial_j u_\mathbf{l}(\mathbf{r}) &\approx -(F_i)^*_{k,h}|J_h|a_h w_h (F_j)_{l,h}\\
&= -F_i^* \cdot G_j^T, && (4.42)
\end{aligned}$$

with the matrix

$$(G_j)_{l,h} = |J_h|a_h w_h (F_j)_{l,h}, \tag{4.43}$$

incorporating the parameter function a_h, the Jacobi-determinants $|J_h|$ and the integration weights w_h. Likewise, we have that

$$\begin{aligned}
\int_K \mathrm{d}^3 r\; u^*_\mathbf{k}(\mathbf{r})a(\mathbf{r})\partial_j u_\mathbf{l}(\mathbf{r}) &= F_0^* \cdot G_j^T, && (4.44)\\
\int_K \mathrm{d}^3 r\; u^*_\mathbf{k}(\mathbf{r})\partial_i a(\mathbf{r}) u_\mathbf{l}(\mathbf{r}) &= -F_i^* \cdot G_0^T, && (4.45)\\
\int_K \mathrm{d}^3 r\; u^*_\mathbf{k}(\mathbf{r})a(\mathbf{r}) u_\mathbf{l}(\mathbf{r}) &= F_0^* \cdot G_0^T. && (4.46)
\end{aligned}$$

Note that Eqs. (4.36) to (4.39) need only to be evaluated once since the reference basis is the same for all elements. Further, the evaluation of Eqs. (4.40, 4.43) requires only $O(N_\mathbf{k} N_\mathbf{h})$ floating point operations (FLOPS), where $N_\mathbf{k}$ and $N_\mathbf{h}$ are the number of local basis functions and integration points, respectively. Commonly more than one integral has to be computed for the same element and the result of Eq. (4.40)

can be reused. In contrast, the matrix products Eq. (4.42), (4.44), (4.45), and (4.46), which can be evaluated using optimized BLAS packages, take the most computational time, namely $O(N_{\mathbf{k}}^2 N_{\mathbf{h}})$ FLOPS. The number of basis functions per element is up to 64 in the SAFE method such that $N_{\mathbf{k}}^2 N_{\mathbf{h}} \gg N_{\mathbf{k}} N_{\mathbf{h}}$.

A substantial amount of computational effort can be saved by performing integrals that differ by a numerical prefactor only once. Note that there are many such integrals in the $k \cdot p$-Hamiltonian for example all terms involving Δ_0. To sort terms accordingly, we use a simple term rewriting system (TRS) outlined in appendix D. The TRS also allows us to set up the operators in a concise way and to automatically test for invariance under crystal symmetry operations.

4.2.4 Hermite finite elements

We have noted that the Lagrange finite element space is $C^0(\Omega)$-conforming. All function in this space are thus Lipschitz continuous. The SAFE methods, however, requires global differentiability for some or all Cartesian directions depending on the particular band, so-called $C^1(\Omega)$-conformity. Such a $C^1(\Omega)$-conforming space is spanned by the Hermite elements. For the sake of clarity, we briefly discuss these elements in one dimension. The extension to more-dimensional tensor-product spaces is straightforward. The C^1 continuity across element boundaries is obtained in a similar fashion as the C^0 continuity for the Lagrange elements. At each boundary point of the finite element domain $\bar{K} = [a, b]$ we define two nodal variables [BS08]

$$
\begin{aligned}
L_1[f] &= f(a), && (4.47)\\
L_2[f] &= f'(a), && (4.48)\\
L_n[f] &= f(b), && (4.49)\\
L_{n+1}[f] &= f'(b), && (4.50)
\end{aligned}
$$

which correspond to the evaluation of a function $f(x)$ and its derivative on the element boundaries. The polynomial degree for the Hermite element is $n \geq 3$, since there are at least four nodal variables. For $n > 3$, the remaining interior nodal variables are again of the form $L_i[f] = f(x_i)$ for $2 < i < n$ with the nodes x_i, which are equally distributed over the interval $]a, b[$.

There are two global nodal variables at the boundary between two neighboring element domains K_{m-1} and K_m where without restriction K_{m-1} is left of K_m. These global nodal variables read $L_{m-1,n} = L_{m,1}$ and $L_{m-1,n+1} = L_{m,2}$. The basis functions are constructed analogously to Eq. (4.7) with the appropriate nodal variables.

Note that, the basis functions corresponding to the derivative nodal variables $u_2(x)$ and $u_n(x)$ read in terms of the reference basis functions

$$
\begin{aligned}
u_2(x) &= \frac{2}{b-a}\tilde{u}_2(\phi^{-1}(x)),\\
u_n(x) &= \frac{2}{b-a}\tilde{u}_n(\phi^{-1}(x)), && (4.51)
\end{aligned}
$$

with the mapping $\phi(\tilde{x}) = a + (b-a)(\tilde{x}+1)/2$ from the reference domain $]-1,1[$ to the element domain $]a,b[$. The factor $2/(b-a)$ is necessary to guarantee that

$$\begin{aligned} L_2[u_2(x)] &= 1, \\ L_n[u_n(x)] &= 1, \end{aligned} \tag{4.52}$$

for arbitrary domains $K =]a,b[$ and thus the $C^1(\Omega)$ conformity of the global basis. Note that in three dimensions, only *rectangular* tensor-product finite elements form a C^1 conforming space. [BS08]

4.2.5 Boundary conditions

On a finite computational domain the solution of a partial differential equation is not determined uniquely by the equation itself. For elliptic partial differential equations, either the derivative or the function value of the solution on the domain boundary has to be specified. We employ "force-free" Neumann boundary conditions to the stiffness equation, i.e. we require that the normal derivative of the displacement vanishes at the domain boundary. For Poisson's equation in the presence of gate electrodes, we use Dirichlet boundary conditions where the electrostatic potential assumes certain values on the domain boundary predetermined by the gate potential. In this work, we solve the $k \cdot p$ eigenvalue problem for bound states only and thus require the wave functions to vanish at the boundary.

Periodic boundary conditions are constructed by identifying the nodal variables at the opposite boundaries of the computational domain. This approach is straightforward and will not be discussed in more detail.

Note that Neumann and Dirichlet boundary conditions in general encompass some kind of approximation since the partial differential equations are cut-off at the boundary and are not solved consistently beyond the boundary. It is thus appropriate to choose the computational domain large enough such that the interesting physics occur far away from these boundaries. To achieve this, we employ an inhomogeneous grid spacing that becomes increasingly larger away from the region of interest.

The finite element method approximates the partial differential equation

$$\hat{L} f(\mathbf{r}) = g(\mathbf{r}), \tag{4.53}$$

by a discrete linear system of equations

$$A\mathbf{x} = \mathbf{b}. \tag{4.54}$$

The matrix A assembled using Eq. (4.21) naturally implements Neumann boundary conditions. [BS08] Neumann boundary condition require that the normal derivative of the solution vanishing on the domain boundary

$$\mathbf{n}(\mathbf{r}) \cdot \nabla f(\mathbf{r})|_{\partial\Omega} = 0, \tag{4.55}$$

where $\partial\Omega$ is the boundary of the computational domain Ω, $\mathbf{n}$ is the normal vector of the boundary surface and the function f is the solution of the partial differential equation.

In contrast, Dirichlet boundary conditions require that the solution has a specific value on the boundary, namely

$$f(\mathbf{r})|_{\partial\Omega} = f_0(\mathbf{r}), \tag{4.56}$$

where the function $f_0(\mathbf{r})$ represents the so-called Dirichlet values. In order to apply Dirichlet boundary conditions, we introduce a restriction matrix R that restricts the total set of m variables to the n interior variables and projects the $(m-n)$ boundary variables to zero. [1] Further, Q is the complement of R and restricts the m variables to the $m-n$ boundary variables whereas the n interior variables are projected to zero. The values of the boundary variables $\mathbf{x}_0$ are obtained from the Dirichlet values $f_0(\mathbf{r})$ by evaluating the nodal variables at the boundary

$$(\mathbf{x}_0)_{\mathrm{l2g}(m,i)} = L_{m,i}[f_0]. \tag{4.57}$$

The restricted system of equations reads

$$\bar{A}\bar{\mathbf{x}} = \bar{\mathbf{b}}. \tag{4.58}$$

with the restricted matrix and right-hand side

$$\bar{A} = RAR^T, \tag{4.59}$$
$$\bar{\mathbf{b}} = R\mathbf{b} - RAQ^TQ\mathbf{x}_0. \tag{4.60}$$

The solution is then

$$\mathbf{x} = R^T\bar{\mathbf{x}} + Q^T\mathbf{x}_0. \tag{4.61}$$

Consequently, the solution $\mathbf{x}$ solves the linear system of equations projected on the *interior* nodes and has the values $\mathbf{x}_0$ at the *boundary* nodes.

Dirichlet boundary conditions are applied to the eigenvalue problem analogously.

4.3 Solution of linear systems of equations

To solve a sparse system of linear equations that result from the finite element discretization

$$A\mathbf{x} = \mathbf{b}, \tag{4.62}$$

we employ a direct factorization approach. The matrix A is permuted by a permutation matrix P and factorized into

$$PAP^T = LDL^H, \tag{4.63}$$

[1] A general $n \times m$ $(n \leq m)$ restriction matrix R is given by $R_{ij} = P_{ii'}\delta_{i'j'}P'_{j'j}$ with some permutation matrices P and P' of dimension $n \times n$ and $m \times m$, respectively.

where L is a lower triangular and D a diagonal matrix. Here, we used that all linear systems that occur in our calculations are real symmetric or complex hermitian. Non-hermitian matrices can be factored similarly into LU where U is upper triangular. In contrast to a Cholesky decomposition of the form LL^H, the factorization LDL^H is also valid for indefinite matrices A. [PTVF07]

Given the factorization, the linear system is solved by

$$\mathbf{x} = (P^T L D L^H P)^{-1}\mathbf{b} = P^T L^{-H} D^{-1} L^{-1} P\mathbf{b}, \tag{4.64}$$

where the matrices are multiplied consecutively from right to left to the vector $\mathbf{b}$. The triangular matrices are not inverted directly. Instead, matrix products of the form $\mathbf{y} = L^{-1}\mathbf{z}$ and $\mathbf{y} = L^{-H}\mathbf{z}$ are solved by forward and backward substitution of $L\mathbf{y} = \mathbf{z}$ and $L^H\mathbf{y} = \mathbf{z}$, respectively. [PTVF07]

The factor L is obtained by the IKJ-variant of Gauss elimination. [Saa00] We use the optimized and parallelized linear solver package PARDISO to perform this factorization as well as the forward/backward substitution. [SBR08] The implementation in this package also employs Bunch-Kaufmann pivoting which guarantees a stable factorization of indefinite matrices. Even singular matrices can be factorized as long as the null-space is not too large. This is the case for the Stiffness equation: the elastic energy is independent of global translations and rotations. The three-dimensional stiffness equation thus has an at least five-dimensional null-space.

Note that the permutation matrix P is of cardinal importance. The number of non-zeros, the so-called fill-ins, in the factor L and thus time and memory consumption depends critically on the choice of P. [SBR08] In general, it is a hard combinatory problem to find the optimal fill-in reducing ordering. However, efficient heuristic algorithms exist that are known to find a "good" fill-in reducing ordering. We employ the graph-theoretical nodal-bisection algorithm that is implemented in the open-source METIS package. [KK99]

We prefer the direct method over iterative methods for the following reason. The convergence of the common iterative methods like the conjugate gradient (CG) method and flexible general minimal residual (FGMRes) method depend on the condition number of the matrix which is given by the modulus of the quotient of the eigenvalue that is largest by the eigenvalue that is smallest in magnitude. [Saa00] The larger the condition number, the worse is the convergence. For singular and indefinite problems, iterative methods thus often show slow convergence or do not converge at all. Although convergence can be improved by preconditioning, the most efficient preconditioning techniques are only well-behaved for positive definite matrices. [Saa00] In contrast, singular and indefinite matrices commonly lead to unstable preconditioners. As noted before, the stiffness equation is singular and thus especially troublesome to solve with iterative methods.

4.4 Solution of eigenvalue problems

There are various methods for solving interior generalized eigenvalue problems

$$(A - \lambda B)\mathbf{x} = 0, \tag{4.65}$$

for a hermitian matrix A and a positive definite hermitian matrix B corresponding to a so-called matrix pencil (A, B). In this work, we employ a variant of the shift-invert Arnoldi iteration. The Arnoldi iteration is known to converge to extremal eigenvalue linearly, where the speed of convergence depends on the separation between the target eigenvalue from the remainder of the spectrum. [Saa92] Since only the eigenvalues closest to the band gap are of interest, an interior eigenvalue problem has to be solved for multi-band $k \cdot p$ models. This can be stated as the problem of finding the closest eigenvalue above or below a shift σ that is chosen within the band gap. Fortunately, it is possible to transform the interior generalized eigenvalue problem to an extremal standard eigenvalue problem.

To this end, the generalized eigenvalue problem is transform into an equivalent standard eigenvalue problem by multiplying Eq. (4.65) by B^{-1} from the left [Saa92]

$$(B^{-1}A - \lambda \mathbf{1})\mathbf{x} = 0. \tag{4.66}$$

Note that B is invertible because it is positive definite. Next, the interior eigenvalue problem is cast to an extremal eigenvalue problem by introducing the shift-invert operator

$$M = (B^{-1}A - \sigma \mathbf{1})^{-1} = (A - \sigma B)^{-1}B. \tag{4.67}$$

The eigenvalue problem

$$(M - \tau \mathbf{1})\mathbf{x} = 0, \tag{4.68}$$

is solved by the same eigenvectors as the original problem. The eigenvalue λ of (A, B) is related to the eigenvalue τ of the shift-invert system $(M, \mathbf{1})$ by $\lambda = \sigma + 1/\tau$. The extremal eigenvalue τ thus correspond to the eigenvalue λ closest to σ. Note that M is not hermitian within the standard inner product $(y, x) = y^H x$. It is, however, hermitian within the B-inner product $(y, x)_B = y^H B x$ because

$$(\mathbf{y}, M\mathbf{x})_B = \big(\mathbf{y}, B(A - \sigma B)^{-1}B\mathbf{x}\big) = \big(B(A - \sigma B)^{-1}B\mathbf{y}, \mathbf{x}\big) = (M\mathbf{y}, \mathbf{x})_B\,. \tag{4.69}$$

Since B is positive definite, the B-inner product establishes a valid norm $|\mathbf{x}|_B = \sqrt{(x, x)_B}$ on the vector space. Hence, the standard hermitian variant of the Arnoldi iteration for extremal eigenvalues can be applied immediately to the matrix pencil $(M, \mathbf{1})$ where the all standard inner products in the algorithm have to be replaced with B-inner products. [Saa92] We employ the ARPACK program library to perform this Arnoldi iteration [LCY98] and the PARDISO direct solver to compute the matrix-vector products of the shift-invert operator M. [SBR08]

We note that other, potentially more efficient methods for the solution of generalized eigenvalue problems exist. Recently, the density projection method was proposed

that can obtain large numbers of eigenvalues and eigenvectors simultaneously within very few iterations. [Pol09] This method exploits the fact that a closed complex σ-contour integral over the Green's function $(A - \sigma B)^{-1}$ represents a projection onto the invariant subspace of A that corresponds to eigenvalues within the contour integral. This contour integral can be conducted numerically with only a few evaluations of the Green's function. For this approach to be efficient, it is critical, however, that the Green's function can be quickly applied to vectors. A sparse factorization of $(A - \sigma B)$ for each integration point appears to be the most promising way to achieve this. These factorizations, however, are costly. We find the shift-invert Arnoldi iteration to be more efficient if only a few eigenvalues are required since only one such factorization needs to be computed.

An iterative method that promises fast, up to cubic, convergence for generalized interior eigenvalue problems is the QZ Jacobi-Davidson method. [SVdV00] This method, however, depends on the availability of an efficient approximate solution of the correction equation that resembles a linear system of equations very similar to the shift-invert operator M. In contrast to the shift-invert Arnoldi iteration and the density projection method, only a coarse approximate solution with a relative residuum $\lesssim 0.1$ is required. Although this method has the potential to be highly efficient, additional research is required to find such an approximation. Possible candidates are incomplete factorization, approximate inverse, multi-grid, and domain decomposition methods. [Saa00]

Part II

Results

Chapter 5

New insights to the symmetry lifting in InGaAs/GaAs quantum dots

5.1 Introduction

It is known from fundamental symmetry arguments that InGaAs/GaAs quantum dots grown along the [001] direction exhibit at most C_{2v} symmetry as a consequence of the inversion asymmetry of the zincblende crystal. [BZ05] However, the inversion asymmetry effects are rather small for this material system and the Hamiltonian is clearly dominated by terms of C_{4v} and higher symmetry. [Win03] Still, the lifting of C_{4v} symmetry by C_{2v} terms influences many physical properties like the optical polarization anisotropy, [BAK$^+$10] the in-plane g-tensor anisotropy, [AV09] and the fine structure splitting of the X^0 exciton. [BNZ03] The origin of this symmetry lifting, however, is still unclear and controversial.

Only a few experimental observables can gauge the magnitude of the C_{2v} symmetry terms directly. Most prominently, the energy splitting of the first two excited electronic states in self-assembled InGaAs/GaAs quantum dots (QDs) grown along [001] is directly related to the lifting of C_{4v} symmetry by these C_{2v} terms and allows to examine its origin. These p-shaped states (further denoted as p-states) are degenerate in C_{4v} symmetry, [1] where in this context "p-shaped" relates to the shape of the envelope part of the wave function while the Bloch part still has dominant Γ_1 (s-like) character. This degeneracy is lifted in C_{2v} symmetry and the p-states split in energy. Moreover, this splitting can be measured unambiguously by polarization

[1] In fact, the p-states are not exactly degenerate: Together with spin, there are four p-states but the only irreducible double-group representation of C_{4v} is two-dimensional. This results in a splitting of the p-states already in C_{4v}. However, the impact of the spin-orbit interaction is very small for the lowest electronic states. [SWB07] Therefore, the p-states belong within good approximation to the irreducible single-group representation E of dimension two. [BP74] Together with the twofold spin degeneracy, all four p-states are thus degenerate within this approximation.

resolved PL: [SBL+02, ZWG+04, CZS+06] The optical transition from the s-shaped electronic ground state (s-state) to the p-state aligned in the [110] direction (p^+-state) is observed at higher energy than the transition to the p-state aligned in the $[1\bar{1}0]$ plane (p^--state).

In experiment, the two transitions can be identified with polarization filters since the s to p transitions are strongly anisotropic: The s-p^+ and s-p^- transitions are predominantly observed for ϵ^+ light with $\mathbf{E}\|[110]$ and ϵ^- light with $\mathbf{E}\|[1\bar{1}0]$, respectively. [ZWG+04] This pronounced anisotropy is caused by the weak influences of the spin-orbit coupling to the lowest electronic states. [SWB07] The p^+ and p^--states thus represent in good approximation the irreducible spin-degenerate single group representations B^+ and B^- of C_{2v}, respectively. [BP74, SWB07] Linearly polarized ϵ^+ and ϵ^- light also belongs to the irreducible representations B^+ and B^-, respectively. Since the s-state belongs to A^+, strict optical selection rules follow from $B^+ \times B^+ = A^+$, $B^- \times B^- = A^+$ and $B^+ \times B^- = A^- \neq A^+$. The latter relation implies that a s-p^+ transitions by ϵ^--polarized light and a s-p^- transitions by ϵ^+-polarized light is forbidden. [2] These relations directly follow from the character tables of C_{2v}. [BP74] Figure 5.1 illustrates the experimentally observed levels and the polarization resolved transitions from the singly occupied s-like ground state.[CZS+06]

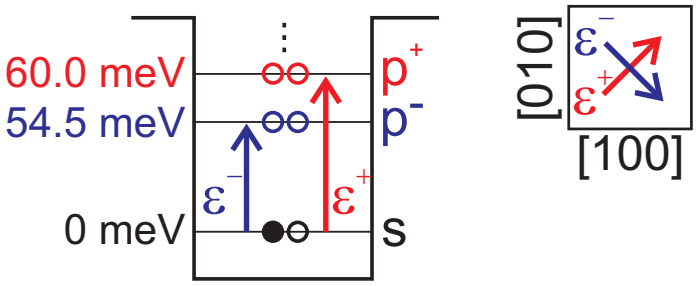

Figure 5.1: (left) Level scheme and symmetry allowed optical transitions of the lowest electronic states in InGaAs/GaAs QDs. The relative energy scales resembles experimental data from Ref. [CZS+06]. (*right*) Definition of the E-field polarization direction of ϵ^+ and ϵ^- polarized light as seen from the top of the QD.

Various conflicting theoretical models have been proposed to explain the p-level splitting including the linear piezoelectric effect (LPE), [SGB99] the more recently proposed quadratic piezoelectric effect (QPE), [BZWV06, SWB07] atomic asymmetry (AAS) [BZ05] and a systematic shape anisotropy (SAS) [JKBJ01, KKO+06] and combinations thereof. Moreover, it has been claimed that the issue of the p-level

[2] For any operator $\hat{A}$, the matrix element $\langle f|\hat{A}|i\rangle$ between two states $|i\rangle$ and $|f\rangle$ can be non-zero only if $\Gamma_1 \in \Gamma_i \times \Gamma_A \times \Gamma_f$ where Γ_i, Γ_f and Γ_A are the irreducible representations of the states $|i\rangle$ and $|f\rangle$ and the operator $\hat{A}$, respectively. In this context, Γ_1 denotes the unit representation. The condition $\Gamma_1 \in \Gamma_i \times \Gamma_A \times \Gamma_f$ is equivalent to $\Gamma_f \in \Gamma_i \times \Gamma_A$ since it is always the case that $\Gamma_1 \in \Gamma_f \times \Gamma_f$.

splitting even questions the validity of the $k \cdot p$ envelope function approximation. [WWZ$^+$00, BZ05]

In this chapter, we aim to resolve this issue in the light of recent experimental insight on the shape and alloy composition of InGaAs/GaAs quantum dots. We further critically review previous work on this topic.

A comprehensive theoretical study on the impact of the LPE, the QPE, and SAS was performed in Ref. [SWB07] within the $k \cdot p$ envelope function approximation. In addition, the AAS together with the LPE and the QPE was examined in empirical pseudo-potential calculations in Ref. [BZWV06]. It was found in both works that the linear and quadratic term of the QPE cancel inside QDs with *homogeneous* In-profile. Moreover, the AAS appears to be too small (2 to 3 meV) [BZ05] to account for the experimentally observed splittings (3.7 to 7 meV). [ZWG$^+$04, SBL$^+$02] In addition, in both works, the LPE was found to produce a p-level splitting with a sign *opposite* to experiment. These results led to the conclusion that only the SAS can cause the experimentally observed energy splitting. [SWB07]

Note importantly that in *both* Ref. [BZWV06] and Ref. [SWB07] the sign of the piezoelectric potential was reversed. [Sch, Bes] In contrast to these works, we show in detail in Sec. 5.3.3 that the LPE produces the correct sign in agreement with experiment on hands of the simplified analytic model of Ref. [Dav98a]. Yet independent of the overall sign the linear and quadratic term in the QPE were still found to cancel inside homogeneous QDs. Recent X-STM measurements and outward relaxation analyses, however, show strong evidence for a graded In:Ga-profile. [OKW$^+$05, BVK$^+$02, MCFJ02] Moreover, it was shown that a homogeneous In-profile cannot correctly account for the permanent dipole of the X^0 exciton. [FIM$^+$00] An inverse-trumpet shaped In-profile was found to be in best agreement with X-STM measurements and X^0 dipole moments. [FIM$^+$00, MCFJ02, OKW$^+$05] We find that such a In-profile substantially reduces strain fields within and around the QD. This reduction of strain clearly has a stronger impact on the quadratic terms than on the linear terms. Consequently, these terms do not cancel and the QPE is only a minor correction compared to the LPE.

Further, we want to note that currently there are several open questions concerning the QPE. The currently available QPE coefficients were fitted to density functional theory calculations. [BWVZ06, BWPB11] However, neither details on the model used in the calculation nor original data nor the deviation of the fitted quadratic relation from the original data were published. Further, the calculations appear to be performed in the limit of zero electric field. [BWPB11] This, we believe, requires more profound theoretical justification since the QPE can lead to extremely large local dipole fields.

The AAS was found to be large only for very small pure InAs QDs. [BZ05] It encompasses two distinct effects: First, the bulk inversion asymmetry (BIA) of the T_d crystal and second atomic interface effects. The latter is caused by the non-equivalent atomic configuration at the material interface of the four $\{101\}$ facets of the pyramidal

QDs. [BZ05] It was shown only recently that this interface effect can be included in the $k \cdot p$ envelope function approximation (EFA). [TV11] This, however, requires a sophisticated treatment of the material interfaces and it is unclear how to adapt this method to a graded In-profile. Moreover, we do not expect a large contribution of the atomic interface asymmetry effect for graded In-profiles anyway since there are no extended InAs-GaAs interfaces in contrast to pure InAs QDs in a pure GaAs matrix. On the other hand, we examine the impact of the BIA by employing a 14-band model.

Section 5.2 provides details on the calculations, the alloy profile and the quantum dot shape. The results of our calculations are presented in Sec. 5.3. Firstly, in Sec. 5.3.1 the p-level splittings resulting from the various contributions presented and compared with experiment. Next, the $[1\bar{1}0]$ elongation is discussed separately in Sec. 5.3.2. In Sec. 5.3.3, the numerical results are validated against the analytical solution of the inclusion problem. Moreover, we provide intuitive qualitative arguments that support the correctness of the sign of the piezoelectric effect in our calculations. Finally, Sec. 5.4 summarizes our results.

5.2 Method

We employed the eight-band $k \cdot p$ envelope function approximation together with the SAFE method to compute the electronic structure. To examine the effect of BIA we also utilized the 14-band model which includes inversion asymmetry terms. Strain effects are accounted for via the deformation potentials. Further, the LPE (1.66) and the QPE (1.68) were used as indicated in the results.

Isoparametric Lagrange finite elements were employed to compute strain fields to a high accuracy. This was found to be necessary since the QPE turned out to vary strongly even for small deviations in the strain. Forth order polynomial tensor product finite elements were transformed by trilinear maps to conform with the truncated pyramidal shape exactly. A cross section of the resulting finite element mesh is shown in Fig. 5.2 for the (010) plane through the QD center.

Note that we followed the standard convention for the orientation of crystal axes, i.e. the vector $a(\frac{1}{4}, \frac{1}{4}, \frac{1}{4})$ points from an cation to the nearest anion where a is the side length of a conventional crystal cell in the zincblende structure. In this convention, the linear piezoelectric constant e_{14} of every $\mathrm{In}_x\mathrm{Ga}_{1-x}\mathrm{As}$ alloy is negative. [Mar72]

Further, note that all states are spin-degenerate. This has no influence on our results and argumentation. Consequently, we refer to a *single* s-state and *two* distinct p-states in the following although all of theses states are two-times spin-degenerate. We do so also for the calculation carried out at a magnetic field up to 12 T since the Zeeman splitting is much smaller that the p-level splitting. We averaged over the two spin states in this case.

In agreement with X-STM measurements, we modeled our QD as truncated pyramids of 18 nm base length and 6 nm height above the wetting layer with an inverse-trumpet In:Ga-profile. [OKW$^+$05, MCFJ02] Consistently with Ref. [MCFJ02], we

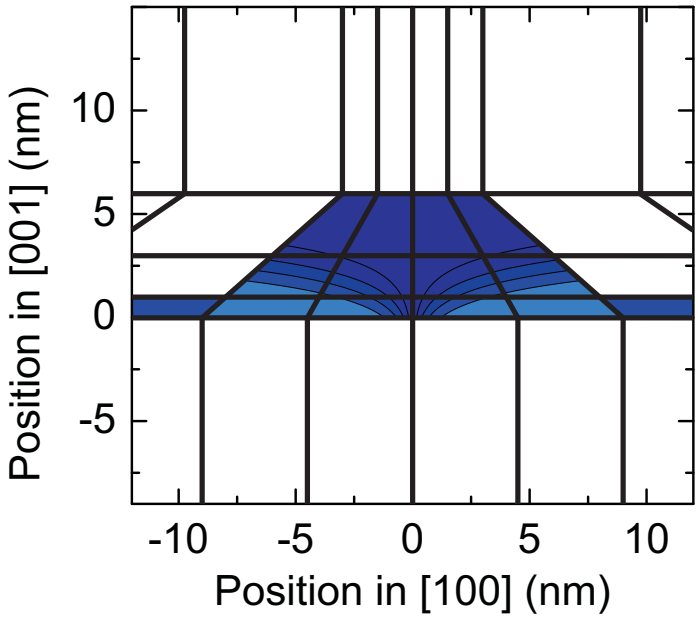

Figure 5.2: Cross section of the isoparametric finite element mesh (bold lines) and the inverse trumpet alloy profile in the {010} plane through the center of the QD. In the alloy profile, dark blue indicates areas with high In-concentration, lighter blue areas with lower In-concentration and white areas with no In.

used the In-profile

$$x_{In}(x,y,z) = x_{min} + (x_{max} - x_{min}) \exp\left\{ -\frac{\sqrt{x^2+y^2}\exp(-|z|/z_0)}{\rho_0} \right\}, \qquad (5.1)$$

with $x_{min} = 0.3$, $x_{max} = 0.8$, $z_0 = 1.0$ nm, and $\rho_0 = 0.75$ nm. The coordinates $\mathbf{r} = (x,y,z)^T$ are relative to the center of the QD base and x, y, and z correspond to the [100], [010], and [001] direction, respectively. The In-concentration at the base x_{min} and at the apex x_{max} were taken from Ref. [MCFJ02]. The parameters z_0 and ρ_0, however, were not published and we chose these values such that they result in a rather "soft" In gradient. We believe, this to be more consistent with the X-STM measurements in Ref. [BVK$^+$02], which show an almost linear In-profile in the z-direction. The wetting layer was modeled with a thickness of 1 nm and an In-concentration of 0.5. [MCFJ02] The resulting In-profile is illustrated in Fig. 5.2. In the calculation a temperature of 4.2 K was used.

For the elongated QDs, an affine transformation was applied to the shape as well as the In-profile while the overall volume and the overall In-content was kept constant. The elongation is denoted as the aspect ratio between the diagonal of the QD base in $[1\bar{1}0]$ and the [110] direction. A $2:1$ elongated QD is thus stretched by a factor of $\sqrt{2}$ in the $[1\bar{1}0]$ and compressed by a factor of $1/\sqrt{2}$ in the [110] direction.

5.3 Results and discussion

5.3.1 p-Level splitting

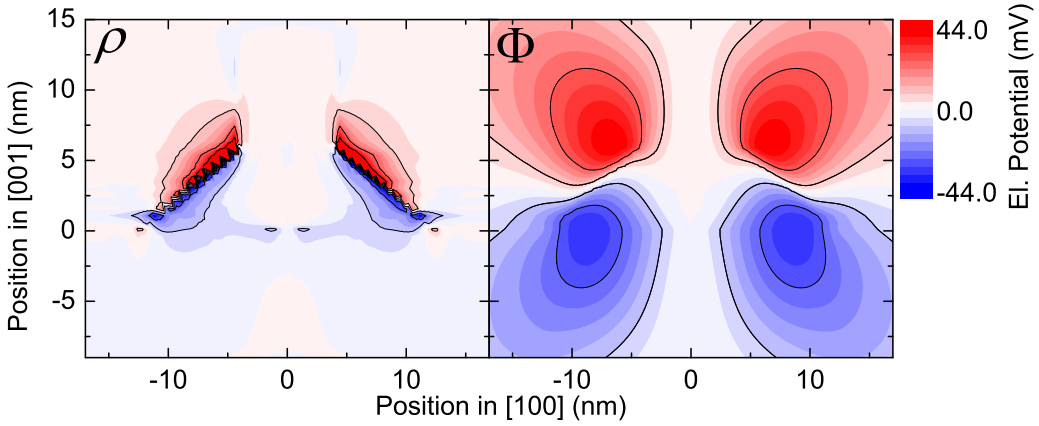

Figure 5.3: (*left*) Calculated piezoelectric charge in the $(1\bar{1}0)$ plane through the center of the QD, where the blue and the red shade indicates negative and positive charge, respectively. (*right*) Calculated piezoelectric potential in the $(1\bar{1}0)$ plane through the center of the QD. The blue and the red shade indicates negative and positive potential, respectively. The scale of the potential is indicated in the right.

Figure 5.3 shows the piezoelectric charge and the resulting electrostatic potential in the $(1\bar{1}0)$ plane through the center of the QD for the LPE. Inside the QD, the piezoelectric charge and potential are negative in this plane. Likewise, the piezoelectric charge and potential are positive in the (110) plane through the center of the QD. Consistently with experiment, the p^+-state aligned in the $(1\bar{1}0)$ plane is higher in energy than the p^--state aligned in the (110) plane. Note that the $(1\bar{1}0)$ plane is spanned by the [110] and [001] direction vectors.

Figure 5.4 compares the LPE with the QPE: the according piezoelectric potentials are shown in the (001) plane 2 nm above the QD base. Both the LPE and the QPE produce the same sign for the p-level splitting that is consistent with experiment. Inside the QD, which is indicated by the solid line, the QPE results in almost the same potential as the LPE. Only in the very center of the QD the quadratic and linear terms of the QPE actually cancel. The p-state wave functions, however, extend to the corners of the QD where they have substantial overlap with the electrostatic potentials for both the LPE and the QPE. This is illustrated by Fig. 5.5 which shows the density of the p-state wave functions in the same plane as the piezoelectric potential in Fig. 5.4. Not surprisingly, we find that the p-level splitting of 5.2 meV for the QPE is only reduced only by 1.8 meV compared to 7.0 meV for the LPE.

Table 5.1 summarizes the p^-- and p^+-state energy levels and the p-level splitting for various models and compares our calculated results with experiment. Firstly,

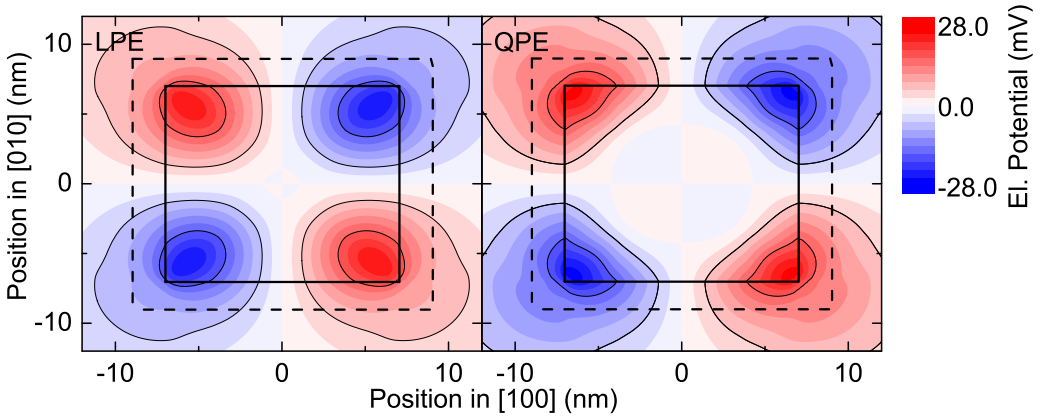

Figure 5.4: (*left*) Calculated piezoelectric potential for the LPE in the (001) plane 2 nm above the QD base. (*right*) Calculated piezoelectric potential for the QPE in the same plane. Both figures use the same scale indicated on the right. The blue and the red shade indicates negative and positive potential, respectively. The outline of the QD 2 nm above its base and at its base are indicates by the bold solid and dashed lines, respectively.

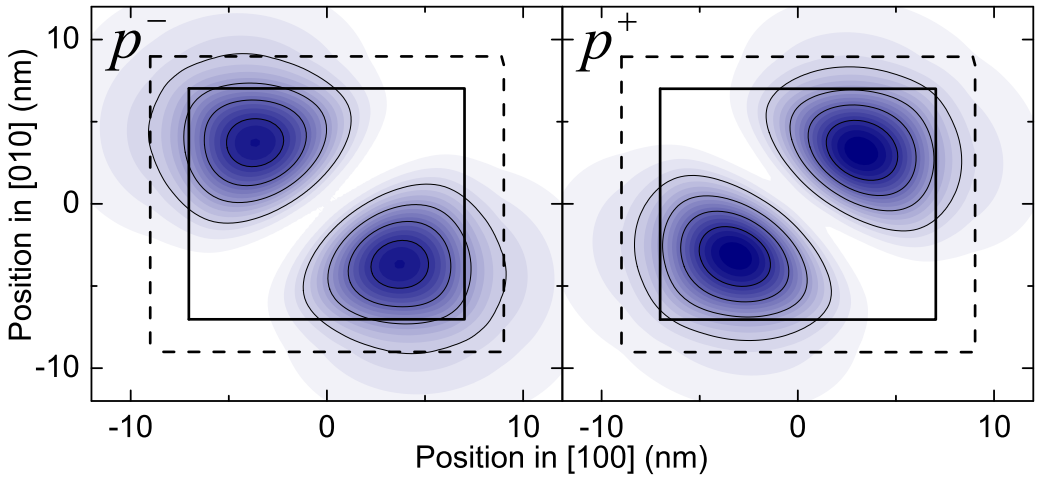

Figure 5.5: (*left*) Calculated density of the p^--state in the (001) plane 2 nm above the QD base. (*right*) Calculated density of the p^+-state in the same plane. The outline of the QD 2 nm above its base and at its base are indicates by the bold solid and dashed lines, respectively.

Model	p^--Level (meV)	p^+-Level (meV)	p-Level splitting (meV)
8-band $k \cdot p$ with LPE	58.1	65.0	7.0
8-band $k \cdot p$ with QPE	58.6	63.7	5.2
14-band $k \cdot p$ w/o PE	62.3	61.9	-0.4
14-band $k \cdot p$ with LPE	58.0	64.5	6.6
14-band $k \cdot p$ with QPE	58.5	63.2	4.7
Experiment Ref. [ZWG$^+$04]	50 to 55	54 to 61	3.7 to 5.5
Experiment Ref. [CZS$^+$06]	54.5	60.0	5.5
Experiment Ref. [SBL$^+$02]	56	63	7

Table 5.1: Calculated p-levels relative to the s-level and p-level splitting for various models compared to experimentally observed values.

the p-states are about 60 meV above the s-state for all models. This is in good agreement with experiment and points at the validity of our QD model. Secondly, the LPE is the dominant contribution to the p-level splitting. Both, the bulk inversion asymmetry, which is account for in the 14-band $k \cdot p$ model, and the QPE present minor corrections. In fact, the latter finding is consistent with calculations for graded In-profile in Ref. [SWB07]. Unfortunately, the incorrect sign of piezoelectric potential in this reference obfuscated this important result. Remarkably, the bulk inversion asymmetry *reduces* the p-level splitting. This is in sharp contrast to the AAS effect that increases the p-level splitting in pseudopotential calculations on QDs with *homogeneous* In-content. [BZ05] To our best knowledge, however, pseudopotential calculations have not yet been performed for QDs with a realistic graded In:Ga-profile. Such calculations could be highly illuminating since it appears to us that the discrepancies between $k \cdot p$ and pseudopotential calculations could stem from the abrupt material interfaces of the homogeneous alloy profile. Finally, we find that the p-level splittings from all models that encompass the LPE or the QPE are in the range of experimentally observed values.

Figure 5.6 shows the decrease of the degree of polarization (DoP) of the $s - p^-$ transition with an increasing vertical B-field calculated in the eight-band $k \cdot p$ model with the LPE. The relative decrease of the DoP in our calculations is in excellent agreement with experiment. The DoP of the optical $s - p^-$ transition is defined by

$$\mathrm{DoP} = \frac{I_{\epsilon^-} - I_{\epsilon^+}}{I_{\epsilon^-} + I_{\epsilon^+}}, \tag{5.2}$$

where I_{ϵ^-} and I_{ϵ^+} are the optical transition intensities (1.54) proportional to $|\langle s|\hat{P}_x + \hat{P}_y|p^-\rangle|^2$ and $|\langle s|\hat{P}_x - \hat{P}_y|p^-\rangle|^2$, respectively. Here, $\hat{\mathbf{P}} = \frac{m_0}{\hbar}\nabla_{\mathbf{k}}\hat{H}$ is the $k \cdot p$ momentum operator obtained by the approximate Hellmann–Feynman theorem in the $k \cdot p$ basis (1.45). The magnetic field lowers the symmetry from C_{2v} to C_2 where there are only two one-dimensional irreducible representations of the single group. [BP74] In

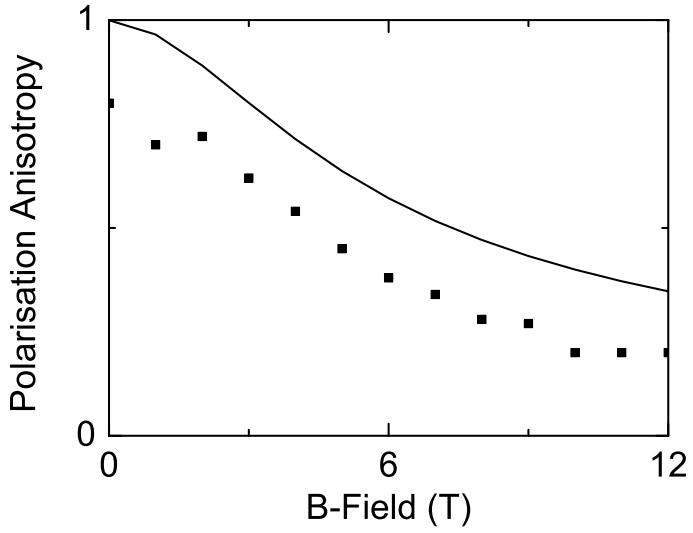

Figure 5.6: Calculated degree of polarization DoP of the optical $s - p^-$ transition as a function of the applied vertical B-field (solid line) in the eight-band $k \cdot p$ model with the LPE. Experimental data from Ref. [CZS$^+$06] is indicated by squares.

particular, both p^- and p^+ belong to the same irreducible representation in C_2. Consequently, the optical selection rules of C_{2v} symmetry become weaker with increasing magnetic field.

Experimentally, a maximum DoP of only 0.8 was observed. [CZS$^+$06] This can, for example, be caused by an asymmetric QD shape [CZS$^+$06] or near field effect in optical measurements caused by the small shadow mask used to select single QDs. [GBM$^+$04] In contrast, neither the QPE nor the AAS nor a $[1\bar{1}0]$ elongation of the QD can account for the low maximum DoP since these effects do not break C_{2v} symmetry.

As already mentioned, the QPE has conceptional issues that require further investigation. In addition, there are also practical issues. We find that the magnitude of QPE depends critically on the numerical accuracy and the exact shape of the alloy profile. In contrast, we find the LPE to be almost unaffected by details of the alloy profile and much more resilient to numerical error.

In conclusion, our results indicate that the LPE is sufficient to account for the lifting of C_{2v} symmetry within reasonable accuracy. More sophisticated effects lead only to small corrections or even artifacts and can be safely neglected.

5.3.2 Shape anisotropy

The incorrect sign of the piezoelectric potential and the homogeneous In-profile in previous work [BZWV06, SWB07] led to the conclusion that the piezoelectric effect in symmetric pyramidal and lense shapes QDs does not lead to the experimentally observed p-level splitting. In order to obtain the observed p-level splitting a sys-

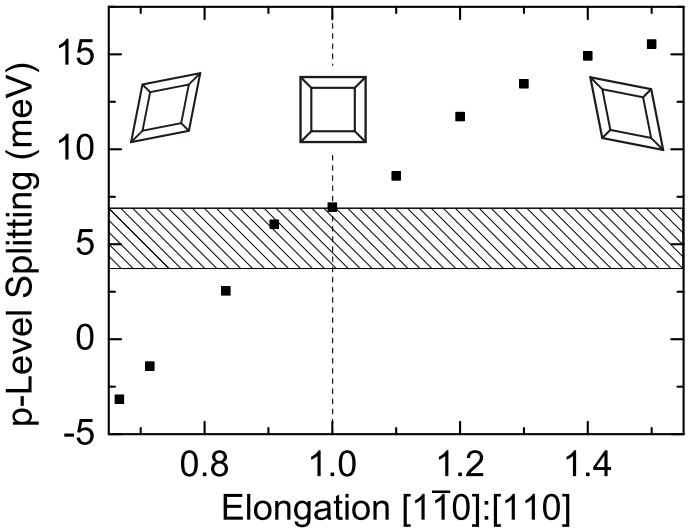

Figure 5.7: p-Level splitting calculated using eight-band $k \cdot p$ wit the LPE as a function of the elongation of the QD. The elongation is defined as the ratio of the $[1\bar{1}0]$ to the [110] diagonal. The hatched area represents the range of experimentally observed values. [SBL$^+$02, ZWG$^+$04, CZS$^+$06]

tematic shape anisotropy of the QDs, namely an elongation in the $[1\bar{1}0]$ direction, was proposed. [SWB07, JKBJ01] This elongation lowers the kinetic energy of the p^--energy-level aligned in the elongated direction compared to the p^+-energy-level aligned in the perpendicular direction. [SWB07] In fact, such an elongation was observed experimentally on InAs/GaAs QDs that were overgrown stepwise. [JKBJ01] After the deposition of each capping layer, the shape of the QD was examined with scanning tunneling microscopy. A large diagonal ration of $[1\bar{1}0] : [110] = 18 : 10$ was observed. Note, however, that the p-level splitting was not measured and it was shown that the growth condition including the growth rate have a profound impact on the optical spectra of QDs. [PLF$^+$07] In addition, the outward relaxation found in X-STM measurements on usually grown QDs was successfully modeled without an elongation of the QD. [MCFJ02, OKW$^+$05]

Our calculations shown in Fig. 5.7 clearly indicate that a substantial elongation of the QD is not compatible with experimentally observed p-level splittings. Even for a small elongation of 11 : 10, the p-level splitting increases to 8.6 meV which is already beyond the experimentally observed range. At an elongation of 15 : 10 we find a p-level splitting of 15.5 meV although a much larger elongation of 18 : 10 has been proposed. [JKBJ01] These results indicate that conventionally grown QDs have no or only a negligible systematic shape anisotropy.

5.3.3 Sign of the piezoelectric potential

Unfortunately, the sign of the piezoelectric potential was reversed in two recent comprehensive studies of the electronic structure of InGaAs/GaAs QDs: In the $k \cdot p$ calculations in Ref. [SWB07], the crystal axes were defined *converse* to the common convention. [Sch] Thus the [110] and $[1\bar{1}0]$ directions and consequently the p^+ and p^--states were exchanged. In the pseudopotential calculations in Ref. [BZWV06], the electrostatic potential was computed correctly and the crystal axes were also aligned conventionally. However, the electrostatic potential was added to the Hamiltonian with a *positive* charge thus effectively reversing the piezoelectric potential. [Bes] The coinciding results from both works led to substantial confusion about the impact of the piezoelectric effect on the electronic structure.

As shown above, our numerical results indicate that the LPE produces a p-level splitting with the correct sign. Because of the importance of this finding and the contrasting results in the above-mentioned works, we give additional evidence in this section. We compare our numerical results with the results from the analytic formula in Ref. [Dav98a] and, in addition, give qualitative arguments that support our findings.

The analytic solution employs the following central approximations: [Dav98a] Firstly, the medium is assumed to be isotropic. Secondly, the elastic, piezoelectric and electrostatic constants are the same everywhere. Thirdly, the strain is measured with respect to the same lattice constant, namely the lattice constant of the matrix material. Finally, the QD composition is homogeneous.

Under these approximations the solution to the inclusion problem is given by [DFO97, Dav98a]

$$\mathbf{u}(\mathbf{r}) = \frac{\epsilon^0}{4\pi}\frac{1+\nu}{1-\nu}\oint \frac{\mathrm{d}\mathbf{S}(\mathbf{r}')}{|\mathbf{r}-\mathbf{r}'|}, \tag{5.3}$$

$$\epsilon_{ij}^{rel}(\mathbf{r}) = -\frac{\epsilon^0}{4\pi}\frac{1+\nu}{1-\nu}\oint \frac{(r_i - r_i')\mathrm{d}S_j(\mathbf{r}')}{|\mathbf{r}-\mathbf{r}'|^3}, \tag{5.4}$$

where ϵ^0 is the mismatch strain of the homogeneous QD material with respect to the matrix material and ν the isotropic Poisson ratio. The surface integral is conducted over the surface of the QD. As expected, Eq. (5.3) shows that the displacement $\mathbf{u}$ points away from the QD surface and vanishes asymptotically away from the QD. The strain given by ϵ_{ij}^{rel} is relative to the mismatch strain. Since the mismatch strain has no shear components, Eq. (5.4) immediately yields the shear strain.

Moreover, the piezoelectric potential was also given analytically by [Dav98a]

$$\Phi(\mathbf{r}) = \frac{9e_{14}\epsilon^0}{4\pi\varepsilon_0\varepsilon_r}\frac{1+\nu}{1-\nu}\oint (x-x')(y-y')(z-z')\frac{(\mathbf{r}-\mathbf{r}')\mathrm{d}\mathbf{S}(\mathbf{r}')}{|\mathbf{r}-\mathbf{r}'|^5}, \tag{5.5}$$

where e_{14} is the piezoelectric constant and ϵ_r the relative dielectric constant.

The analytic Eqs. (5.3), (5.4) and (5.5) can be readily evaluated. To this end, however, we employ numerical Gauss-Legendre quadrature of order 30 for the evaluation of the surface integrals. Still, we call the results "*analytical*" to distinguish them from the *numerical* solution of the stiffness Eq. (1.64).

There are various steps in the calculation of the piezoelectric potential and the electronic states where the sign of the piezoelectric effect can be wrongly reversed in a fully numerical calculation. Further, it is difficult to validate the fully numerical solution directly. We thus proceed in three steps. Firstly, we verify the sign of the shear strain obtained from the analytic solution Eq. (5.4) by qualitative arguments. Secondly, we show the consistency between the analytical and numerical results and further show that the sign of the piezoelectric charge is consistent with qualitative arguments. Finally, we present the resulting electrostatic potential both from the fully numerical and the analytical calculation. We show that this potential is consistent with the piezoelectric charge and leads to the experimentally observed p-level splitting.

Here, we considered the LPE only and compared the numerical and analytical results for a homogeneous $In_{0.5}Ga_{0.5}As/GaAs$ QD. We used the same truncated-pyramidal shape as before, namely as base length of 18 nm and a height of 6 nm. However, we neglected the wetting layer because this simplifies the evaluation of analytical equations substantially. For the uniform material constants we used the values of GaAs, namely, $e_{14} = -0.16\mathrm{C/m}^2$, [dGBR89] $\nu = 0.31$, [Dav98a] and $\epsilon_r = 12.9$. [MSH82] The mismatch strain in this context is defined as $\epsilon^0 = a_{\mathrm{In_{0.5}Ga_{0.5}As}}/a_{\mathrm{GaAs}} - 1$. With the lattice constants $a_{\mathrm{In_{0.5}Ga_{0.5}As}} = (6.06\mathring{A} + 5.65\mathring{A})/2 = 5.86\mathring{A}$ and $a_{\mathrm{GaAs}} = 5.65\mathring{A}$ this yields $\epsilon^0 = 3.6\%$. [VMRM01]

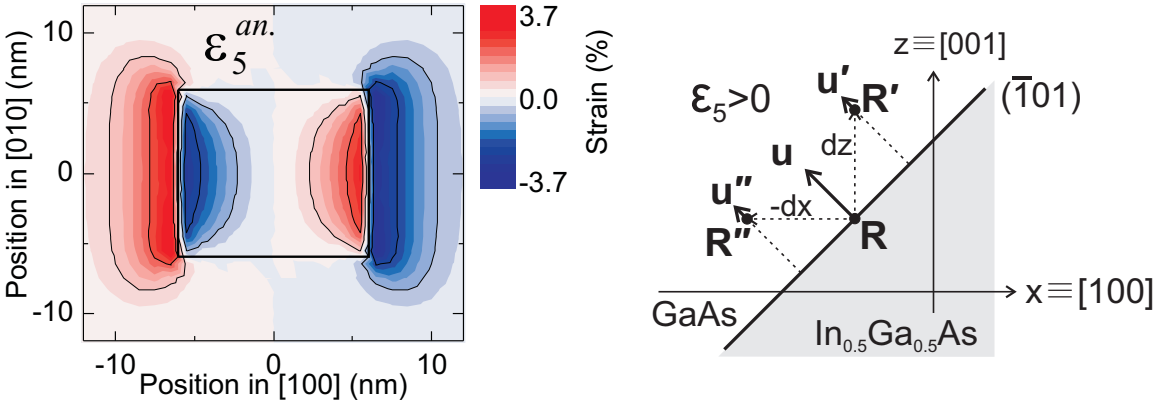

Figure 5.8: (*left*) Analytically computed shear strain component $\epsilon_5^{an.}$ in the (001) plane 3 nm above the QD base. The outline of the QD in this plane is indicated by the solid line. (*right*) Sketch of the displacement at a point $\mathbf{R}$ on the $(\bar{1}01)$ facet and at differentially shifted points $\mathbf{R}' = \mathbf{R} + \mathrm{d}z\mathbf{e}_z$ and $\mathbf{R}'' = \mathbf{R} - \mathrm{d}x\,\mathbf{e}_x$ shown in the (010) plane. The x- and z-direction correspond to the [100] and [001] crystallographic directions, respectively.

First, we give qualitative evidence for the correctness of the sign of the shear strain components obtained from Eq. (5.4). Figure 5.8(*left*) shows the analytically obtained shear strain component $\epsilon_5^{an.}$ in the (001) plane 3 nm above the QD base. The sign of the shear strain can be verified by a simple qualitative argument where we use the fact that the displacement decreases away from the QD. This is illustrated in Fig. 5.8(*right*): For the sake of argument, consider the region above the center $\mathbf{R}$ of the $(\bar{1}01)$ facet. This region corresponds to the region left of the QD outline in Fig. 5.8(*left*). Close to the QD interface we may approximate the displacement by the contribution from the $(\bar{1}01)$ facet only. At the point $\mathbf{R}$ directly on the facet, the displacement $\mathbf{u}$ point away from the QD and is approximately perpendicular to the facet. With increasing distance to the facet, the magnitude of the displacement decreases due to the finite size of the facet. In particular, we have that $|u_x'| < |u_x|$ and $|u_z''| < |u_z|$ at the points $\mathbf{R}'$ and $\mathbf{R}''$, respectively. Considering the sign of the components this yields $u_x' > u_x$ and $u_z'' < u_z$. Here, the points $\mathbf{R}' = \mathbf{R} + \mathbf{e}_z \mathrm{d}z$ and $\mathbf{R}'' = \mathbf{R} - \mathbf{e}_x \mathrm{d}x$ are differentially shifted relative to $\mathbf{R}$ by $+\mathrm{d}z$ and $-\mathrm{d}x$ along the unit vectors $\mathbf{e}_z$ and $\mathbf{e}_x$, respectively. The shear strain component ϵ_5 is $\epsilon_5 = \partial_z u_x + \partial_x u_z$. Since $u_x' > u_x$ and $\mathbf{R}'$ lies relative to $\mathbf{R}$ in the positive z-direction, we have that $\partial_z u_x > 0$. Because $u_z'' < u_z$ and $\mathbf{R}''$ lies relative to $\mathbf{R}$ in the *negative* x-direction, we also have that $\partial_x u_z > 0$. The shear strain component ϵ_5 is thus positive directly above the $(\bar{1}01)$ QD facet. This is consistent with the results from Eq. (5.4). The sign of the shear strain components at the various $\{\bar{1}01\}$ facets inside and outside the QD can be verified analogously.

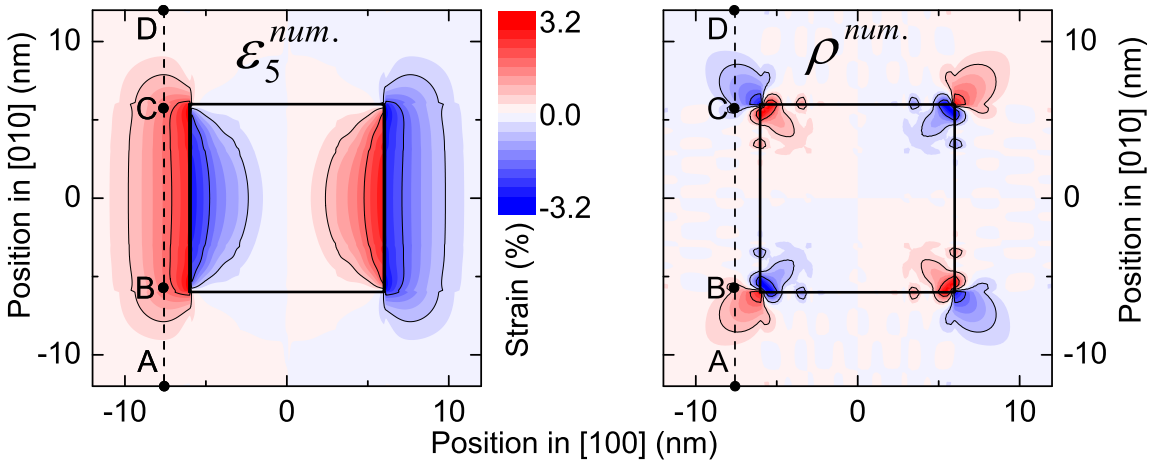

Figure 5.9: (*left*) Numerically calculated shear strain component $\epsilon_5^{num.}$ in the (001) plane 3 nm above the QD base. (*right*) The numerically calculated piezoelectric charge distribution $\rho^{num.}$ in the same plane where blue and red indicate negative and positive charge, respectively. The bold line indicates the outline of the QD in this plane.

Secondly, we show that (a) the shear strain components obtained numerically and

analytically are consistent and (b) that this shear strain results in the correct sign of the piezoelectric charge. The first point is illustrated by Fig. 5.9(*left*): The shear strain component $\epsilon_5^{num.}$ obtained by a fully numerical solution of the stiffness equation is apparently consistent with the analytical result in Fig. 5.8(*left*). Now we consider the sign of the piezoelectric charge. The piezoelectric charge is

$$\rho = -\partial_x e_{14}\epsilon_4 - \partial_y e_{14}\epsilon_5 - \partial_z e_{14}\epsilon_6, \tag{5.6}$$

where the piezoelectric material constant e_{14} is negative for InGaAs alloys in the standard convention. [Mar72] For the sake of argument, we assume e_{14} to be constant everywhere. To validate the sign of the calculated piezoelectric charge shown in Fig. 5.9(*right*), we consider the contribution form ϵ_5 along the dashed line in Fig. 5.9(*left*) in positive y-direction along [010]. Starting from point A, ϵ_5 increases towards point B and thus $\partial_y\epsilon_5|_A^B > 0$. Between the points B and C ϵ_5 is almost constant ($\partial_y\epsilon_5|_B^C \approx 0$) and then decreases towards point D ($\partial_y\epsilon_5|_C^D < 0$). Since the minus in Eq. (5.6) cancels with the negative sign of e_{14}, the piezoelectric charge has the same sign as $\partial_y\epsilon_5$. Consequently, the charge is positive along the line from A to B, zero between B and C and negative between C and D. This is consistent with the fully numerically calculated piezoelectric charge shown in Fig. 5.9(*right*).

Analogous arguments apply as well to the ϵ_4 shear strain component as to the regions above and below the various {101} facets. Our numerical calculations indicate that the shear strain components ϵ_4 and ϵ_5 together contribute dominantly to the piezoelectric charge. In a similar way, it can be argued that our numerical results are also consistent with the qualitative contribution of the ϵ_6 shear strain component.

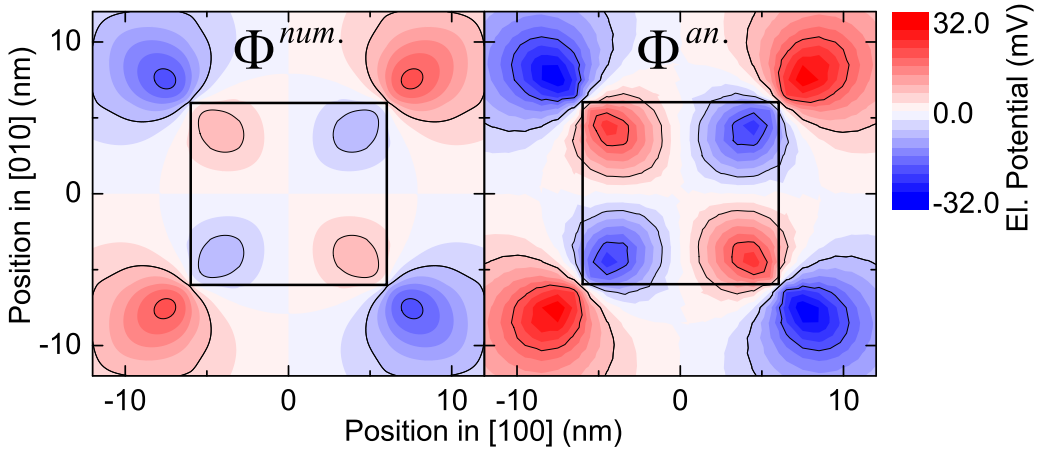

Figure 5.10: (*left*) Numerically and (*right*) analytically calculated piezoelectric potential $\Phi^{num.}$ and $\Phi^{an.}$, respectively, in the (001) plane 3 nm above the QD base. The bold line indicates the outline of the QD in this plane.

Finally, Fig. 5.10 shows that the analytically (*right*) and fully numerically (*left*) calculated piezoelectric potential are consistent and the piezoelectric potential clearly

corresponds to the piezoelectric charge distribution shown in Fig. 5.9(*right*). Note that we used the piezoelectric constant of GaAs for the analytical calculations. Hence, the analytically computed piezoelectric potential is larger in magnitude than the numerically obtained potential since the piezoelectric constant of $In_{0.5}Ga_{0.5}As$ is considerably smaller in magnitude that the piezoelectric constant of GaAs which was used in the analytical calculation for the entire structure. The sign of the potential, however, is consistent inside and outside the QD.

The p^+-state aligned along the [110] diagonal and the p^--state aligned along the $[1\bar{1}0]$ diagonal thus overlap with a negative and a positive electrostatic potential, respectively. Consequently, the p^+-state is higher in energy than the p^--state. Therefore, the LPE leads to a sign of the p-level splitting that agrees with experiment.

5.4 Summary

For a realistic QD model with graded In:Ga-profile, we have shown that the LPE causes the experimentally observed p-level splitting of 5 to 7 meV. The QPE, on the other hand, only leads to a minor correction compared to the LPE because of the reduced strain due to the graded alloy profile. Further, the impact of the bulk inversion asymmetry contributes only -0.6 meV to the p-level splitting. Finally, we have shown that a systematic elongation of the QD in $[1\bar{1}0]$ dramatically increases the p-level splitting. Combined with the LPE, this results in a splitting too large to be compatible with current experimental data. Our results thus indicate that the LPE is the dominant contribution to the lifting of C_{4v} symmetry. All other contributions are either negligible or incompatible with experiment.

Chapter 6

Prediction of strong electrical g-Factor tuning in In-dilute quantum dots

6.1 Introduction

In this chapter, we examine the very strong electrical tunability of the X^0 exciton g-factor that was observed experimentally in InGaAs/GaAs self-assembled QDs. [JEK+11] By performing realistic eight-band $\mathbf{k}\cdot\mathbf{p}$ simulations using a QD size, shape and In-composition determined by scanning tunneling microscopy, we quantitatively account for experimental results and obtain new insight into the origin of the effect. Our theoretical findings are in excellent agreement with experiment; exciton transition energy, the g-factor at zero E-field and g-factor tunability all being simultaneously reproduced our calculations using dots with a diameter $D = 25$ nm, height $d = 6$ nm and a maximum In-composition of $x_{In} \sim 35\%$ near the dot apex. We show that the g_{ex} tunability is dominated by the *hole* (g_h), the electron (g_e) contributing only weakly. Most interestingly, the electric field-induced perturbation of the hole wave function is shown to impact upon g_h principally via orbital angular momentum quenching. [PF06] In contrast, the valence band mixing and the change of the In:Ga composition inside the envelope function plays only a minor role. The results show that the strength of the electrical tunability *increases* as the In-alloy content at the dot apex (x_{In}^{apex}) *reduces*, explaining why strong electrical g_{ex} tunability is observed for the particular sample in Ref. [JEK+11].

Surprisingly, we find that the g-factor calculated in linear response theory form wave functions at zero B-field is in excellent agreement with the g-factor obtained from the full non-perturbative calculation including the B-field in the Hamiltonian. This finding implies a simple method for approximation of g-factors that circumvents the practical issues presented by the gauge-invariant discretization of the vector potential.

Moreover, we validate the single particle approximation to the exciton g-factor

that has been used in previous work. [AV09] In this approximation, the impact of the electron-hole Coulomb interaction on the exciton g-factor is neglected.

The experimental results shown in this chapter were obtained for QDs that were grown with a nominal In-content of $x_{In} = 50\%$ under the unusually high growth temperature of 595°C. Due to the combined effects of In-desorption [HH03b] and inter-diffusion with the GaAs matrix material during capping, [HH03a] this is expected to lead to a lower than nominal average In-content in the dots. Cross sectional STM measurements [KCB+10] indicate that the resulting dots have a lateral size of $D = 26 \pm 8$ nm and height of $h = 6 \pm 2$ nm. The experimental data was recorded using photoluminescence measurements at low electric field (< 25 kV/cm) and photo current at high electric field (> 27 kV/cm). Both measurements were conducted with σ^+ and σ^- circularly polarized laser light to unambiguously identify the two Zeeman branches and thus the sign of the exciton g-factor. More details on the growth conditions and the experimental setup are published in Ref. [JEK+11].

Note that theoretical results, which we published in Ref. [JEK+11], were calculated using the state-of-the-art $k \cdot p$ method for incorporating magnetic fields *at that time*. In contrast, the results presented in this chapter have been calculated with our novel SAFE method, which we expect to yield more accurate results. Hence, there are a few quantitative discrepancies between results in this work and Ref. [JEK+11]. The arguments and the central propositions, however, are consistent and stay intact.

Section 6.2 gives details on the quantum dot model and the theoretical methods employed in this chapter. In Sec. 6.2.1, the electron-hole Coulomb interaction is discussed. Next, the sign convention of the exciton g-factor is treated in Sec. 6.2.2. The impact of the g-factor anisotropy is briefly discussed in Sec. 6.2.3. In Sec. 6.3, the results of our numerical calculations are presented. We first compare the calculated electrical g-factor tuning to experimental data in Sec. 6.3.1 and provide an intuitive explanation of the observed tuning in Sec. 6.3.2. In Sec. 6.3.3 we propose the design of an universal all electrical single qubit gate. The results are summarized in Sec. 6.4.

6.2 Method

We performed electronic structure calculations using the eight-band $\mathbf{k} \cdot \mathbf{p}$ envelope function approximation (EFA) Hamiltonian. The discretization of the Hamiltonian was performed using the SAFE method presented in Ch. 3. Strain fields were computed in continuum elasticity theory and their impact on the electronic structure was taken into account via deformation potentials and the linear piezoelectric effect.

We modeled our QDs as having a truncated lens shape with a diameter varying from $D = 16 - 48$ nm, a height of 6 nm above the wetting layer and a realistic inverse trumpet-like In-compositional profile (5.1). [OKW+05, MCFJ02] The In-concentration of the InGaAs alloy was taken to be $x_{In} = 0.2$ at the base and side of the dot increasing to $x_{In}^{apex} = 0.2{-}0.8$ at the dot apex. [MCFJ02] This range of parameters are fully consistent with the results of cross sectional STM measurements performed

on samples grown under the same conditions, from which we also determined the wetting layer thickness (2 nm) and $x_{In}^{WL} = 0.18$. [KCB$^+$10]

6.2.1 Electron-hole Coulomb interaction

In the literature, the impact of the Coulomb interaction on the exciton g-factors was previously neglected and the exciton g-factor was computed from the single particle electron and hole energies. [AV09] A vertical electric field, however, separates holes and electrons spatially [SHB$^+$03] and the attractive direct Coulomb interaction thus counteracts the external electric field. Hence, we performed self-consistent calculation to examine the validity of the single particle approximation in the presence of an external electric field. We only consider the direct Coulomb interaction, because the electron-hole exchange interaction active for the bright X^0 exciton states is expected to be small for large QDs. [BOS$^+$02]

We computed the electronic state self-consistently in the electric potential produced by the hole state and vice versa. To this end, we solved the coupled system of equations

$$\begin{aligned}
(\hat{H} - e\Phi_e(\mathbf{r}) - E_h^{SC}\mathbf{1})F_h^{SC}(\mathbf{r}) &= 0, && (6.1)\\
-\nabla(\varepsilon_0\varepsilon_r(\mathbf{r}))\nabla\Phi_h(\mathbf{r}) &= +e\sum_i |F_{h,i}^{SC}(\mathbf{r})|^2, && (6.2)\\
(\hat{H} - e\Phi_h(\mathbf{r}) - E_e^{SC}\mathbf{1})F_e^{SC}(\mathbf{r}) &= 0, && (6.3)\\
-\nabla(\varepsilon_0\varepsilon_r(\mathbf{r}))\nabla\Phi_e(\mathbf{r}) &= -e\sum_i |F_{e,i}^{SC}(\mathbf{r})|^2, && (6.4)
\end{aligned}$$

where $\hat{H}$ is the single particle Hamilton operator and ε_0 and $\varepsilon_r(\mathbf{r})$ are the vacuum and relative dielectric constants, respectively. The self-consistent pairs of energy and envelope function of the hole and of the electron Hamiltonian are denoted as (E_h^{SC}, F_h^{SC}) and (E_e^{SC}, F_e^{SC}), respectively. The sums run over all components i of the envelope function.

The electrostatic potentials Φ_h and Φ_e were calculated by solving Poisson's equation with asymptotic boundary conditions. These were represented by Dirichlet boundary conditions on the boundary of the computational domain Ω with the Dirichlet values

$$\Phi_i^{Dir}(\mathbf{r}) = \int_\Omega \mathrm{d}r'^3 \, \frac{1}{4\pi\varepsilon_0\varepsilon_r^{GaAs}} \frac{q_i|F_i(\mathbf{r}')|^2}{|\mathbf{r}-\mathbf{r}'|}, \qquad (6.5)$$

with $i = e, h$ and the charges $q_e = -e$ and $q_h = +e$. For computing the Dirichlet value, the constant relative dielectric constant $\varepsilon_r^{\mathrm{GaAs}}$ of GaAs is used. This approximation is expected to yield reasonable results, first, because the InAs-content in the dot is low and, second, because we chose the domain Ω large enough such that the values on the boundary are small. Consequently, the error of approximating the relative dielectric constant is also small.

Table 6.1: Exciton g-factor calculated in various approximations.

Exciton g-factor g_{ex}	at 0 kV/cm and 10 T	at 60 kV/cm and 10 T
Self-Consistent	0.625	1.112
Single Particle	0.635	1.199

The system of equations was solved by iteratively inserting the result of one equation into the next until convergence. The iteration was started with $\Phi_e = 0$ and was terminated when the difference between the current and the previous exciton energy was less than 10^{-8} eV. Only a small number of iterations (three to four) was required because the potential produced by the carriers is one order of magnitude smaller than the confining potential. More efficient and sophisticated methods to improve convergence were thus not required.

The self-consistent exciton energy was then calculated by

$$E_{ex}^{SC} = E_e^{SC} - E_h^{SC} - \frac{1}{2}(\langle F_e^{SC}| - e\Phi_h|F_e^{SC}\rangle - \langle F_h^{SC}| - e\Phi_e|F_h^{SC}\rangle), \tag{6.6}$$

where the interaction potential must be subtracted once since it is contained in both E_e and E_h.

Note that in this approach, the electron and the hole Hamiltonian are not the same and the eigenfunction are thus not exactly orthogonal. We find, however, that the loss of orthogonality is very small due to the large effective band gap (≈ 1300 meV).

Table 6.1 shows that the difference between exciton g-factors of the single particle and of the self-consistent calculation is negligible at zero external electric field, namely $g_x^{SP}(0\text{ kV/cm}) - g_x^{SC}(0\text{ kV/cm}) \approx 0.01$. As expected, the effect of the external electric field of 60 kV/cm is counteracted by the Coulomb interaction. Consequently, the discrepancy, $g_x^{SP}(60\text{ kV/cm}) - g_x^{SC}(60\text{ kV/cm}) \approx 0.09$, is larger in the presence of an electric field. This is, however, still comparable to deviations from other sources, e.g. different sets of material parameters. We thus conclude that the additional effort of a self-consistent calculation is not justified and we will only consider the single particle approximation throughout this work. To this end, we calculate exciton transition energies in first-order perturbation theory by

$$E_{ex} = E_e - E_h + \frac{1}{2}(\langle F_e| - e\Phi_h|F_e\rangle - \langle F_h| - e\Phi_e|F_h\rangle), \tag{6.7}$$

where all terms are obtained from the solution of the single particle Hamiltonian.

6.2.2 Sign convention of the g-factor

There has been much confusion concerning the sign of the bright X^0 exciton g-factor and various seemingly contradicting relations can be found in the literature: $g_{ex} \stackrel{?}{=} g_e + g_h$, [BKF+99, AV09] $g_{ex} \stackrel{?}{=} g_e - g_h$, and $g_{ex} \stackrel{?}{=} -g_e + g_h$. [NSTA04] To

make our results unambiguous, we clarify the convention used in this work. In the following, we will only discuss a magnetic field in the growth direction [001], denoted as z-direction. This is also the quantization direction of the spin. The basis functions of spin $|\uparrow\rangle$ and $|\downarrow\rangle$ are thus defined with respect to the positive [001] direction. The definitions apply to other directions of the magnetic field analogously.

In the electron-hole picture it is natural to define the electron g-factor as

$$g_e^{nat} = \frac{E(e\uparrow) - E(e\downarrow)}{\mu_B B} = g_c, \tag{6.8}$$

and the hole g-factor as

$$g_h^{nat} = \frac{E(h\uparrow) - E(h\downarrow)}{\mu_B B} = \frac{-E(v\downarrow) + E(v\uparrow)}{\mu_B B} = g_v, \tag{6.9}$$

respectively, in terms of the g-factors of the conduction band state g_c and the valence band state g_v in the purely electronic picture. The terms $E(e\uparrow/\downarrow)$, $E(h\uparrow/\downarrow)$,and $E(v\uparrow/\downarrow)$ denote the spin $\uparrow/\downarrow$ energy levels of electron, valence band, and hole state, respectively. Note that $E(h\uparrow/\downarrow) = -E(v\downarrow/\uparrow)$ when changing form the purely electronic to the electron-hole picture.

The g-factor of an excitation is most naturally defined as the g-factor of the excited minus the g-factor of the ground state. The natural definition of the bright X^0 exciton g-factor is thus

$$g_{ex}^{nat} = g_e^{nat} - g_h^{nat} = g_c - g_v. \tag{6.10}$$

In the QD literature, however, the exciton g-factor is conventionally defined as [NSTA04]

$$\begin{aligned} g_{ex}^{conv} &= \frac{E(\sigma^+) - E(\sigma^-)}{\mu_B B} \\ &= \frac{E(c\downarrow) - E(v\downarrow) - (E(c\uparrow) - E(v\uparrow))}{\mu_B B} = -g_c + g_v, \end{aligned} \tag{6.11}$$

where $E(\sigma^+)$ and $E(\sigma^-)$ denote the transition energies for the absorption of σ^+ and σ^- circularly polarized light with angular momentum projection $l = +1$ and $l = -1$, respectively. The absorption processes relate to the two optical transitions that preserve angular momentum: Firstly, a $j = +3/2$ heavy hole-like valence band electron is excited by absorbing a σ^- photon with $l = -1$ to a $j = +1/2$ s-like conduction band electron. Secondly, a $j = -3/2$ heavy hole-like valence band electron is excited by absorbing a σ^+ photon with $l = +1$ to a $j = -1/2$ s-like conduction band electron.

Moreover, the relation $g_{ex}^{conv} = g_e^{conv} + g_h^{conv}$ is commonly used in the QD literature. [SBM+92, BKF+99, AV09] This requires that

$$g_e^{conv} = -g_c \text{ and } g_h^{conv} = +g_v. \tag{6.12}$$

Consistently, with the QD literature, we will use this conventional definition of the electron, hole, and exciton g-factors throughout this work.

6.2.3 Valence band g-factor anisotropy

There are two Luttinger parameters that directly contribute to the Zeeman splitting of the Γ_{8v} valence bands. [Lut56] These parameters κ^L and q^L correspond to the two independent invariants of the Γ_{8v} Hamiltonian that are first order in B. [TRR79] Previous work has only focused on the role of κ^L in the magnetic response. [AV09] Although values for q^L are small, it contributes to the heavy hole g-factor with a large prefactor of 13.5. This immediately results from the Γ_{8v} Hamiltonian. [Lut56, Win03] For $\mathbf{B}\|[001]$ and equivalent directions, the inspection of this Hamiltonian yields

$$g_{\mathrm{HH}} = -6\kappa^L - \frac{27}{2}q^L. \tag{6.13}$$

In the literature, values of q^L range from 0.04 [Law71] to 0.39 [Win03] for InAs. The contribution to the heavy hole g-factor is thus -0.54 to -5.3.

Note that a high value for q^L of 0.39 in InAs appears implausible, since the major perturbative contribution to q^L comes from the Γ_{8c} and Γ_{7c} valence bands. [Win03] For InAs and GaAs this amounts to 0.048 and 0.032 by Eq. (2.68), respectively. We use exactly these values in our calculation. They are consistent with Ref. [Law71], where $q^L(\mathrm{GaAs}) = q^L(\mathrm{InAs}) = 0.04$. It appears that more accurate values for q^L are currently not available.

6.3 Results and discussion

6.3.1 E-Field dependence of the exciton g-factor

The dependence of g_{ex} on the electric field is summarized in Fig. 6.1. The calculated exciton g-factor is strongly E-field-dependent and increases from 0.01 to 1.20 for the field ranging from -60 kV/cm to 60 kV/cm. The calculated values are in excellent agreement with the experimental data for two representative QDs labeled QD_A and QD_B. Moreover, the perturbative result of the exciton g-factor is in remarkably good agreement with the exact calculation over the whole range of the E-field.

Figures 6.2(*left*) and 6.2(*right*) show contour plots of the exciton transition energy E_{ex} and the exciton g-factor g_{ex}, respectively. The exciton transition energy was obtained at 7 kV/cm and 10 T and the Coulomb interaction was included perturbatively via Eq. (6.7). The exciton g-factor was calculated at 0 kV/cm and $B = 10$ T. The measured values of these quantities for QD_A are represented by the bold contours on the figure, showing that they are reproduced in the D and x_{In}^{apex} parameter space probed. More importantly, both contours intersect at $D = 24 \pm 2$ nm and $x_{In}^{apex} = 0.35 \pm 0.02$, as indicated by the open circles on the panels of Fig. 6.2. We note that we also calculated very different X^0 g-factors for small ($D \leq 16$ nm), InAs rich (x_{In}^{apex}) dots, in very good agreement with previous experiments and calculations. [NSTA04]

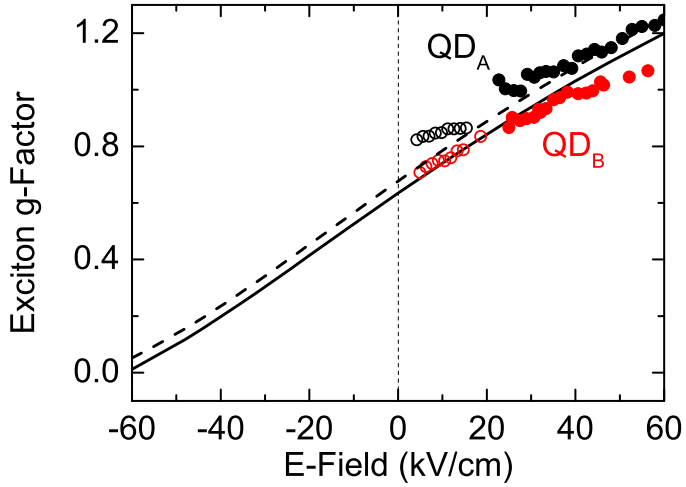

Figure 6.1: Experimentally obtained excitonic g-factor as a function of the applied electric field for two representative QDs, QD_A and QD_B, at 10 T (black and red circles, respectively). The open and closed circles indicate photoluminescence and photo current measurement, respectively. The solid line shows the result of the full 8-band $\mathbf{k} \cdot \mathbf{p}$ calculation at 10 T using the dot size and composition parameters described in the manuscript. The dashed line shows the g-factor that was calculated perturbatively from wave functions at 0 T using Eq. (2.48).

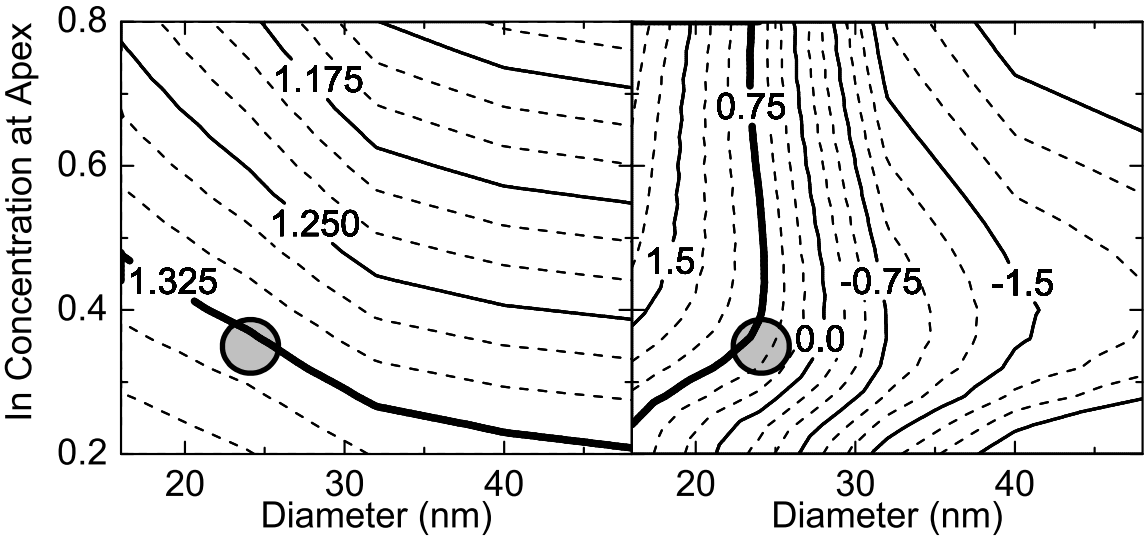

Figure 6.2: The following properties were obtained by varying QD diameter and InAs content in our calculations: (*left*) The X^0 exciton energy (eV) at 7 kV/cm and 10 T, and (*right*) the exciton g-factor at zero electric field and 10 T. The circles indicate the QD parameters used in g-factor calculations (Fig. 6.1 and Fig. 6.3) and the bold lines indicate experimentally measured values. The experimental values have been slightly rounded for the sake of clarity.

The electron and hole g-factors in self-assembled dots have been investigated in previous theoretical works; primary contributions arising from (i) strain-induced band mixing, [NST+05] (ii) modification of Roth's formula by the effective band gap [RLZ59, PF06] and (iii) orbital angular momentum quenching. [KIR98, LMR85, PF06] Electric field-induced changes in the alloy overlap, i.e. the In-Ga content within the envelope function, have been shown to be important mostly for very extended electronic states in weakly confined dots. [PF06, NSTA04] However, while each of the effects (i)-(iii) have been reported to contribute to g_{ex}, the microscopic origin of the strong electrical g_{ex} tunability in our samples is not at all obvious. We now demonstrate that the observed effects can be directly traced to strong electric field induced changes of the *hole* g-factor (g_h), the electron g-factor (g_e) being much more weakly influenced by the electric field.

The left panel of Fig. 6.3 shows representative calculations of g_h, and g_e for $B = 10$ T using the model dot parameters deduced from Fig. 6.2 ($D = 24$ nm and $x_{In}^{apex} = 0.35$). Clearly, g_e varies only weakly over the range of electric fields investigated ($g_e = 0.56$ to 0.63), while g_h is much more strongly affected ($g_h = -0.55$ to 0.63). Further, g_h crosses 0 at almost zero electric field.

6.3.2 Orbital angular momentum quenching

We now show that quenching of the orbital angular momentum in zero dimensional structures (mechanism - (iii)) is primarily responsible for the observed electrical tunability.

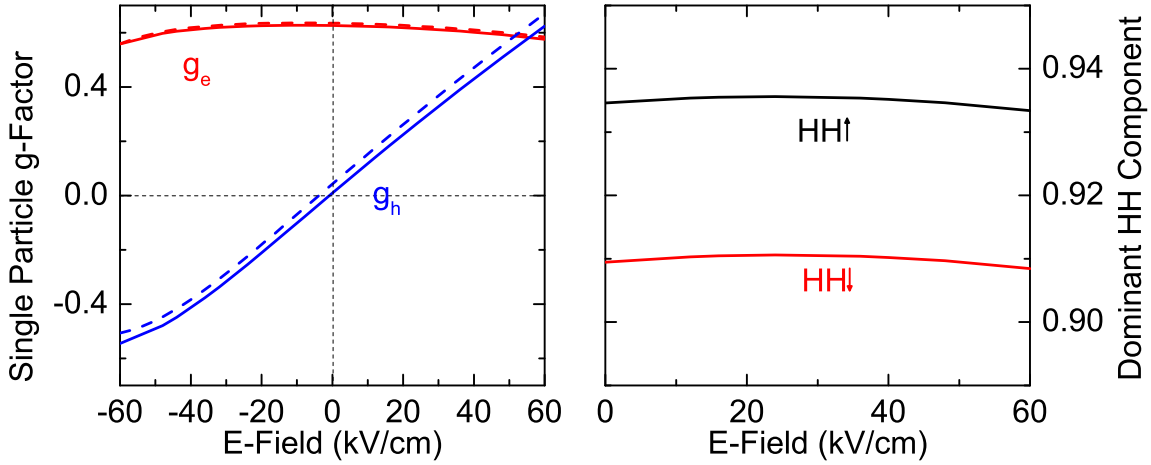

Figure 6.3: (*left*) Calculated electron and hole g-factor as a function of the electric field (solid line) at 10 T. The dashed line show results that were calculated perturbatively from wave functions at 0 T from Eq. (2.48). (*right*) $HH\uparrow$ component of the predominantly $HH\uparrow$-like ground state (black) and $HH\downarrow$ component of the predominantly $HH\downarrow$-like ground state (red) as a function of the electric field.

Firstly, the left panel of Fig. 6.3 compares the calculated value of $g_{e/h}$ (solid lines) and the contributions of the orbital angular momentum obtained from Eq. (2.48) (dashed lines). The electric field tuning of g_h is almost entirely due to the angular momentum contribution. In comparison, g_L plays a much less important role for the electrical modification of g_e.

It has been speculated that the change in alloy overlap may induce HH-LH mixing that could be responsible for the observed strong electrical tunability, [KJK+10] since the HH and LH g-factors differ strongly. However, we find that the electrically induced mixing of the valence bands is weak.This is illustrated in the right panel of Fig. 6.3: the change of the $HH\downarrow$-component of the predominantly $HH\downarrow$-like hole state and $HH\uparrow$-component of the predominantly $HH\uparrow$-like hole state is almost unaffected by the electric field. Unlike the hole g-factor, the magnitude of the dominant HH-component does not vary monotonously over the range of the electric field. This clearly indicates that HH-LH mixing cannot account for the g-factor tuning.

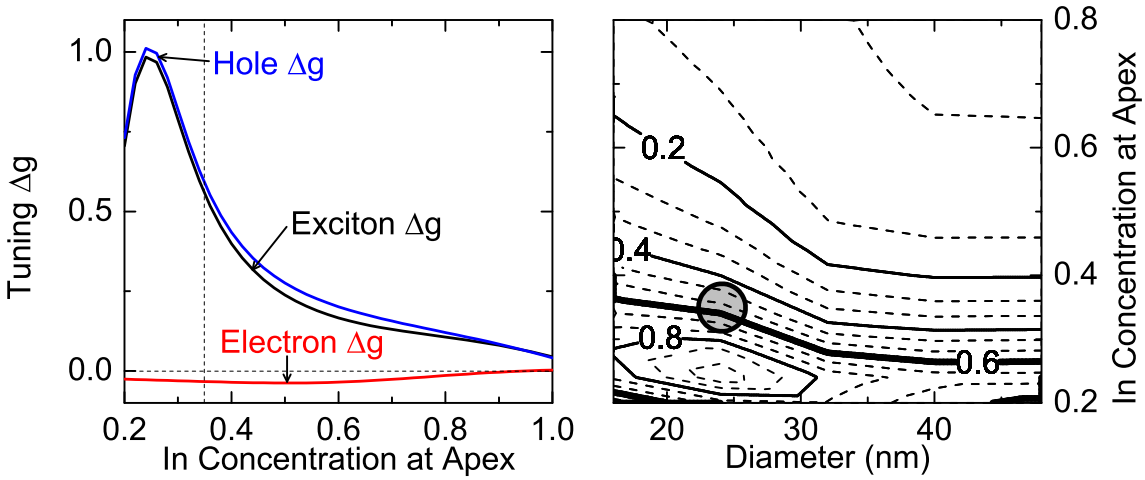

Figure 6.4: (*left*) Calculated dependency of the electric tuning of g_e, g_h and g_{ex} as a function of In-concentration at the dot apex. The electric tuning is defined as g-factor at 60 kV/cm minus g-factor at 0 kV/cm. (*right*) The electric g-factor tuning of g_{ex} as defined above obtained by varying QD diameter and InAs content in our calculations. The circle indicates the QD parameters used in g-factor calculations (Fig. 6.1 and Fig. 6.3) and the bold lines indicate experimentally measured value.

Secondly, the left panel of Fig. 6.4 shows the g-factor tuning

$$\Delta g_{e/h} = g_{e/h}(60kV/cm) - g_{e/h}(0kV/cm), \tag{6.14}$$

obtained from our full calculation for $0.2 \leq x_{In}^{apex} \leq 1.0$. There is a clear maximum in the tunability of g_h for *low* In-concentrations at the dot apex ($0.25 \leq x_{In}^{apex} \leq 0.35$). In addition, the right panel of Fig. 6.4 shows the exciton g-factor tuning over a wide range of dot diameter and In-content. This indicates that the tunability of the hole g-factor also reduces with increasing diameter of the QDs.

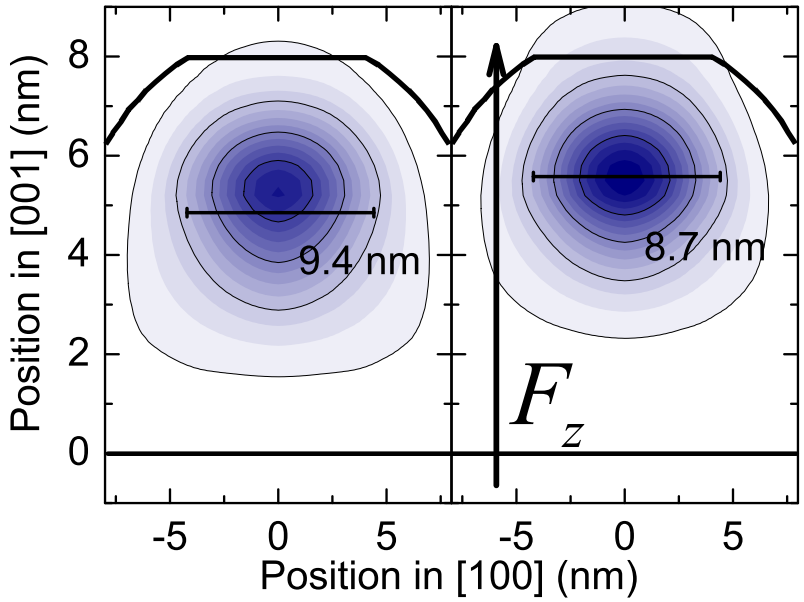

Figure 6.5: Sheet density of the hole wave function at zero electric field (*left*) and at 60 kV/cm (*right*) in the (010) plane. The bold line indicates the outline of the QD through its center. The mean diameter of the wave function is given explicitly and indicated by the horizontal line which is positioned vertically at the center of gravity of the wave function.

There are two interfering contributions to the total angular momentum of the electron and hole states: the angular momentum of the Bloch function and the angular momentum of the envelope function. Since no field-dependent valence band mixing is observed in our calculations, only the latter contributes to the field-dependent angular momentum quenching of the hole ground state. In a qualitative picture, the hole ground state is pushed to the apex of the dot for positive fields. This effectively compresses the wave function laterally since the dot is narrowing towards its apex. Because the dot diameter is comparable to the magnetic length, the cyclotron motion of the hole and thus its angular motion is suppressed. Figure 6.5 shows the sheet density of the hole wave function at zero electric field (*left*) and at 60 kV/cm (*right*) in the (010) plane. The electric field clearly pushes the wave function to the apex of the QD. This can be seen on hand of the horizontal line which indicates the mean diameter of the wave function and is positions vertically at its center of gravity. The lateral compression due to the electric field is also evident. Note that the angular momentum contribution g_L to the g-factor is negative for materials with positive spin-orbit splitting. [Win03] Consequently, the suppression of the angular motion is equivalent to the increase of the hole g-factor. The converse effect is observed for negative fields. In this case, the hole wave function is pushed to the base of dot and into the wetting layer, where it can extend laterally. On the other hand, the electric field impacts the electron states only weakly due to their large kinetic energy. Hence,

the suppression of angular momentum is much less effective.

Similarly, the electric field leads to no substantial change of the In:Ga alloy content within the hole envelope function. We calculated that for $x_{In}^{apex} = 0.35$ and $D = 24$ nm, the In-alloy overlap changes by $\approx 0.14\%$ or $\approx -2.2\%$ for the hole and electron, respectively. This small change cannot significantly contribute to the observed electric field tunability. In addition, note that the change in the alloy overlap impacts the effective g-factor dominantly by inducing valence band mixing due to the position dependence of the spin-orbit splitting. As shown before, there is no substantial change in the valence band mixing.

Our calculations show weak electric tunability for conventional In-rich QDs: the confining potential in such dots is much stronger for both electrons and holes compared to the external electrostatic potential. The strongly bound ground states are therefore nearly unaffected by the field.

The tunability also reduces for a very low In-concentration (≤ 0.25). In this case, both the electron and the hole are weakly bound in the dot and leak into the wetting layer. Even with the electric field increasing the hole state becomes only weakly confined in the top of the dot. Therefore, the angular momentum does not reduce as strongly as for slightly higher In-concentrations.

6.3.3 Universal single-qubit gate

It has been shown that the E-field dependence of the g-tensor of the hole ground state can be exploited to realize single qubit gate operations in quantum dot molecules. [AV09, REVP10] To manipulate the qubit represented by the spin of a hole in the ground state, a constant magnetic field and a time-dependent microwave field are applied. The microwave field modulates the g-tensor and in turn controls its precession in the static magnetic field. It has been shown that reliable universal single-qubit operations based on this principle are technically feasible. [REVP10] Here, we show that single QDs can provide a system with comparable potential.

To this end, we need to examine the complete g-tensor and its electric field dependence. In C_{2v} symmetry the g-tensor of the hole ground state has three independent components, namely $g_h^{[001]}$, $g_h^{[110]}$, and $g_h^{[1\bar{1}0]}$ where the superscript denotes the principal axis to which the g-factor corresponds. We derived the principal axes and the number of independent components from symmetry properties of symmetric rank-2-tensors of the group C_{2v}. [Nye85, BP74] This finding agrees with previous results for quantum dot molecules with the same symmetry class. [AV09] The g-tensor reads

$$\overleftrightarrow{G} = \begin{pmatrix} \left(g_h^{[110]} + g_h^{[1\bar{1}0]}\right)/2 & \left(g_h^{[110]} - g_h^{[1\bar{1}0]}\right)/2 & 0 \\ \left(g_h^{[110]} - g_h^{[1\bar{1}0]}\right)/2 & \left(g_h^{[110]} + g_h^{[1\bar{1}0]}\right)/2 & 0 \\ 0 & 0 & g_h^{[001]} \end{pmatrix}, \tag{6.15}$$

in the Cartesian coordinate system spanned by the [100], [010], and [001] unit vectors.

The spin precession vector is [PPF11]

$$\mathbf{\Omega} = \frac{\mu_B}{\hbar} \overleftrightarrow{G} \mathbf{B}, \tag{6.16}$$

where $|\mathbf{\Omega}|$ is the angular precession frequency and $\mathbf{\Omega}_0 \equiv \mathbf{\Omega}/|\mathbf{\Omega}|$ is the precession axis.

Note that a magnetic field breaks the C_{2v} symmetry of the system. This, in general, leads to a magnetic field-dependent non-linear g-tensor. In the low field limit, however, the C_{2v} symmetry is lifted only weakly. The good agreement of the g-factors obtained by the linear response theory (2.48) with the g-factors calculated including the magnetic field up to 10 T indicates that the non-linear contributions are small. It is shown in Ch. 7 that this is no longer the case for dots with a diameter substantially larger than the magnetic length.

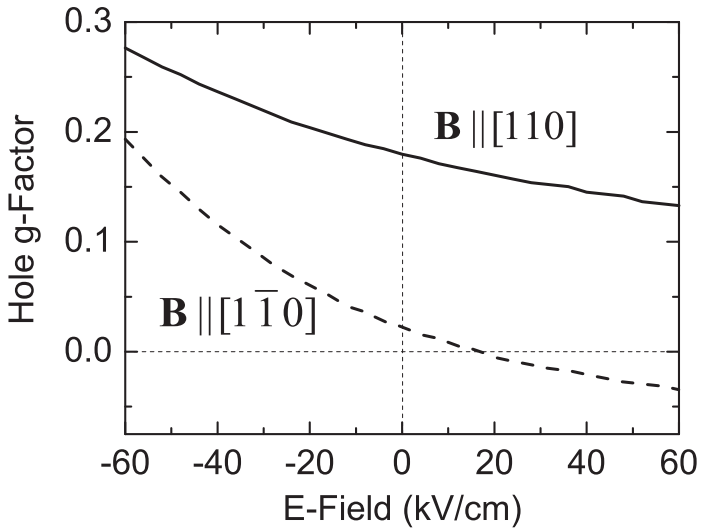

Figure 6.6: Calculated g-factor $g_h^{[110]}$ (solid line) and $g_h^{[1\bar{1}0]}$ (dashed line) of the hole ground state as a function of the electric field for a magnetic field of 10 T along the [110] and $[1\bar{1}0]$ direction, respectively.

Figure 6.6 depicts the electric field dependence of the g-tensor components $g_h^{[110]}$ and $g_h^{[1\bar{1}0]}$ of the hole ground state. The pronounced anisotropy between the two components is due to the piezoelectric potential, which induces an additional quenching of the g-factor in $[1\bar{1}0]$ direction. The vertical electric field controls the overlap of the hole ground state with the piezoelectric potential and in turn tunes the $[1\bar{1}0]$ g-factor. The piezoelectric potential is analogous to that of the truncated pyramidal QDs discussed in Ch. 5. It is largest at the base of the QD and smallest at the apex. The vertical electric field shifts the vertical position of the hole ground state and thus controls the overlap with the piezoelectric potential. The [110] g-factor is tuned by the vertical electric field analogously. However, our calculations indicate that the ratio between tuning and the magnitude at zero electric field is much smaller for the [110] g-factor than for the $[1\bar{1}0]$ g-factor.

It is convenient to use a polynomial fit of the g-factors for the further analysis. We find that a quadratic fit accurately resembles the g-factors with a maximal absolute error of about 10^{-4} in the electric field range of interest. The polynomial fits are

$$\tilde{g}_h^{[110]}(F_z) = 0.17951 - 0.00115\,\tilde{F}_z + 7.12425 \times 10^{-6}\,\tilde{F}_z^2, \quad (6.17)$$

$$\tilde{g}_h^{[1\bar{1}0]}(F_z) = 0.02203 - 0.00163\,\tilde{F}_z - 1.51404 \times 10^{-5}\,\tilde{F}_z^2, \quad (6.18)$$

$$\tilde{g}_h^{[001]}(F_z) = 0.00756 + 0.01075\,\tilde{F}_z - 1.43386 \times 10^{-6}\,\tilde{F}_z^2, \quad (6.19)$$

where $\tilde{F}_z$ is the magnitude of the vertical electric field F_z divided by the unit kV/cm.

We find in analogy to Ref. [REVP10] that the most promising setup for single spin-qubit gate operations would be a low static magnetic field of about 10 mT in the [111] direction and a vertically polarized microwave field ranging from -24 to 24 kV/cm. For this direction of the magnetic field, only the [001] and the [110] g-factor contribute to the precession vector. In the electric field range of -24 to 24 kV/cm, the [001] g-factor ranges from -0.25 to 0.26 while the [110] g-factor is almost constant and ranges from 0.21 to 0.16. At the extremal fields, the precession axes are orthogonal and read

$$\mathbf{\Omega}_0(F_z = -24\ \text{kV/cm}) = (0.541, 0.541, -0.644)^T, \quad (6.20)$$

$$\mathbf{\Omega}_0(F_z = +24\ \text{kV/cm}) = (0.453, 0.453, 0.768)^T. \quad (6.21)$$

Two orthogonal precession axes offer the freedom required for universal single qubit gate operations. [REVP10] The precession frequency $\nu = |\mathbf{\Omega}|/(2\pi)$ is linear in the magnetic field and is of the order of 40 MHz for a field of 10 mT. Consequently, a pulse shaping with a precision below $1/\nu \approx 25$ ns is required. Note, however, that a detailed study of an optimal control pulse sequence including spin lifetime and spin decoherence in analogy to Ref. [REVP10] will be necessary to fully assess the capability of this system to function as an universal single qubit gate.

6.4 Summary

In summary, we identified the microscopic origin of pronounced electrical tunability of the exciton g-factor in composition engineered InGaAs/GaAs self-assembled QDs. We demonstrated that the g_{ex} tunability is dominated by g_h, g_e contributing only weakly. The electric field-induced perturbation of the hole wave function was shown to impact upon g_h principally via orbital angular momentum quenching, the HH-LH mixing and the change of the In:Ga composition inside the wave function playing only a minor role. The strength of the electrical tunability was shown to be strong only for dots with a low In-alloy content. Our results provide significant scope for morphological and structural tailoring self-assembled QDs to allow all electrical universal spin qubit gates via the g-tensor modulation. [PPF08, REVP10] Moreover, we showed that the simple perturbative method to compute g-factors *without* including the magnetic

field in the Hamiltonian in Sec. 2.4 is in remarkable agreement with the fully detailed non-perturbative method in the low field limit.

Chapter 7

Explanation of the non-linear Zeeman splitting in large quantum dots

7.1 Introduction

In this chapter, we predict and explain strong magnetic field-induced tuning of the bright X^0 exciton g-factor in large In-dilute InGaAs/GaAs self-assembled quantum dots (QDs). By comparing experimental results with realistic eight-band $\mathbf{k} \cdot \mathbf{p}$ simulations performed using quantum dot size, shape and compositional information obtained from cross-sectional scanning tunneling microscopy (X-STM), we identify the origins of the magnetic field-dependence of the g-factor. Our results show that magnetic fields influence the excitonic g-factor via a mechanism that differs fundamentally from the case of static electric fields that was examined in the previous chapter. In particular, the combination of the rather dilute In-composition ($x < 0.4$) and comparatively large lateral size of the dots ($40 - 50$ nm) is found to lead to spin selective mixing of the heavy hole (HH) and light hole (LH) orbital states, the strength of which varies with magnetic field. This gives rise to a quadratic $\propto B^2$ contribution to the Zeeman energy gap - a phenomenon previously observed only in semiconductor quantum wells and super lattices. [SBM$^+$92, WNS$^+$93]

In the following, we give a brief summary of the sample growth and experimental results from Ref. [JEK$^+$12]. The non-linear Zeeman splitting was observed experimentally for two different types of QDs. Both samples were produced using molecular beam epitaxy under nominally identical growth conditions. The first sample was grown utilizing the conventional Stranski-Krastanov growth, while in the second was utilized the partially covered island (PCI) "In-flushing" method. [FWA$^+$99] The QD layer nominally consisted of 8 ML of $In_xGa_{1-x}As$ with an In-content of $x = 0.50$. The comparatively high growth temperature of 590 °C is expected to lead to an average In-content lower than the nominal $x = 0.50$, due to the combined

effects of In-desorption, [HH03b] interdiffusion with the GaAs matrix material and In-segregation. [HH03a]

X-STM measurements of representative dots revealed that the QDs exhibit graded In:Ga-profiles with a large diameter of $40-50$ nm and a height of $4-8$ nm and a In-concentration in the apex of $x^{apex} = 0.3-0.35$, reducing to $x^{min} = 0.22$ near the base of the dot. [JEK+12] These data provide the basis for the dot size, shape and composition used in our calculations.

Experimental photoluminescence (PL) spectra are presented in Fig. 7.1 from the neutral exciton X^0 of four representative QDs from the *non-flushed*, as well as from the *flushed* sample. The polarization-resolved PL spectra reveal a substantially different behavior of the Zeeman splitting with increasing magnetic field. This can be clearly seen in Fig. 7.2 where the Zeeman energy, defined as $\Delta E_Z = E(\sigma^+_{det}) - E(\sigma^-_{det}) = g_{ex}\mu_B B$, is plotted for the four dots presented in Fig. 7.1, as well as for many other dots examined in Ref. [JEK+12]. Positive, negative as well as zero excitonic Zeeman splittings were observed for different dots from the same samples.

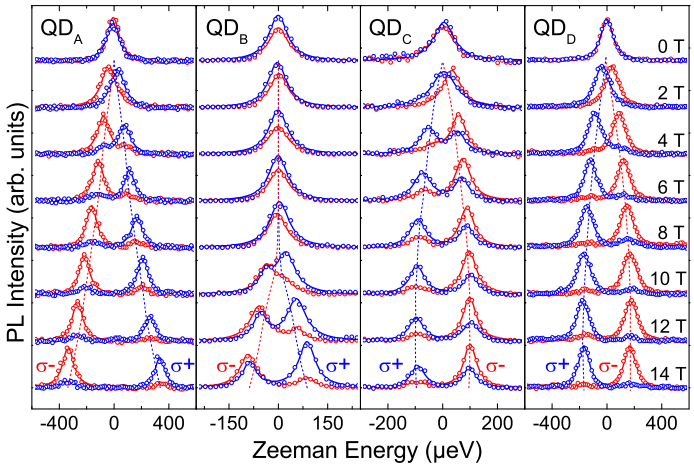

Figure 7.1: Experimentally measured polarization resolved photoluminescence of four representative quantum dots from Ref. [JEK+12].

A striking feature of the Zeeman splittings presented in Fig. 7.2 is the non-linear dependence of ΔE_Z on the magnetic field – a magnetic *field-dependent* exciton g-factor; $g_{ex} = g_e + g_h = g^0_{ex} + g^1_{ex}B$. The best fit to the Zeeman splittings of QD_A, QD_B, QD_C and QD_D was obtained using quadratic functions, as depicted by the solid lines presented in Fig. 7.2. The solid lines for the other QDs interpolate the experimental data. For all of the QDs investigated, the observed Zeeman splittings for the negatively charged trion X^{-1} were identical to those of the corresponding neutral excitons X^0. Hence, the pronounced non-linear dependence of ΔE_Z on B can be attributed to a strongly magnetic field-dependent *hole* g-factor g_h for QDs with particular lateral size and In-composition profiles, as will be explained in detail below.

At this point, note that the observation of a non-linear Zeeman splitting is not directly correlated with the degrees of circular polarization DoP = $(I_{\sigma^+} - I_{\sigma^-})/(I_{\sigma^+} + I_{\sigma^-})$ of the emission. This can be clearly seen by comparing the data recorded from QD_C and QD_D presented in Fig. 7.1. Both of these dots exhibit similar behavior; a negative Zeeman splitting that saturates at higher magnetic fields > 10 T. However, despite the similarity in the observed behavior the two dots exhibit degrees of circular polarization that are both very different from each other and magnetic field independent. The dot QD_C exhibits a rather low degree of circular polarization of 37 ± 1 % while QD_D has DoP of 87 ± 2 %, respectively. A large fraction of the dots investigated (≥ 60 %) showed the expected circularly polarized transitions at elevated magnetic field, regardless of the type of Zeeman splitting they exhibited. However, the low degree of circular polarization for QD_B and QD_C is not in accord with theoretical expectations and we believe that it arises from the experimental geometry used. For example, Au-dielectric shadow mask apertures with a size close to the optical wavelength in free space (≈ 1 μm) were used, the position of the dot under the aperture is highly likely to influence the polarization of the emitted light into the far field. [GBM+04] For any situation other than a dot located in the center of the aperture, the reduction of the symmetry of the local dielectric environment may perturb the polarization of the emitted light, leading to the observed complex behavior. Similar effects are well known for the emission of quantum dots in elliptical micropillars [GGL+98] or, in an extreme case, the emission from semiconductor nanowires with sub-wavelength lateral dimensions. [vWAK+09] Thus, it is difficult to draw quantitative conclusions from the measured degree of circular polarization. In contrast, the Zeeman splitting is a robust experimental quantity and we continue by exploring the microscopic origins of the rich behavior exhibited in Figs 7.1 and 7.2.

More details on the growth process and on the measurements are published in Ref. [JEK+12].

7.2 Model

To understand the microscopic origin of the observed non-linear Zeeman splitting we performed three-dimensional electronic structure calculations using the eight-band $\mathbf{k} \cdot \mathbf{p}$ envelope function approximation. In order to include the B-field we used the gauge-invariant SAFE method that accurately accounts for valence band couplings. Strain fields were included using continuum elasticity theory and their impact on the electronic structure was fully taken into account via deformation potentials and the linear piezoelectric effect. [SGB99] As mentioned before, the exchange interaction is expected to be of minor importance for the neutral exciton for large QDs. [BOS+02] The direct Coulomb interaction was found to have a negligible influence on the exciton g-factor and is therefore also neglected in our simulations.

To obtain quantitative results for the X^0 g-factor, the eight-band $\mathbf{k} \cdot \mathbf{p}$-model was employed. We modeled our QDs as having a truncated lens shape with a diameter

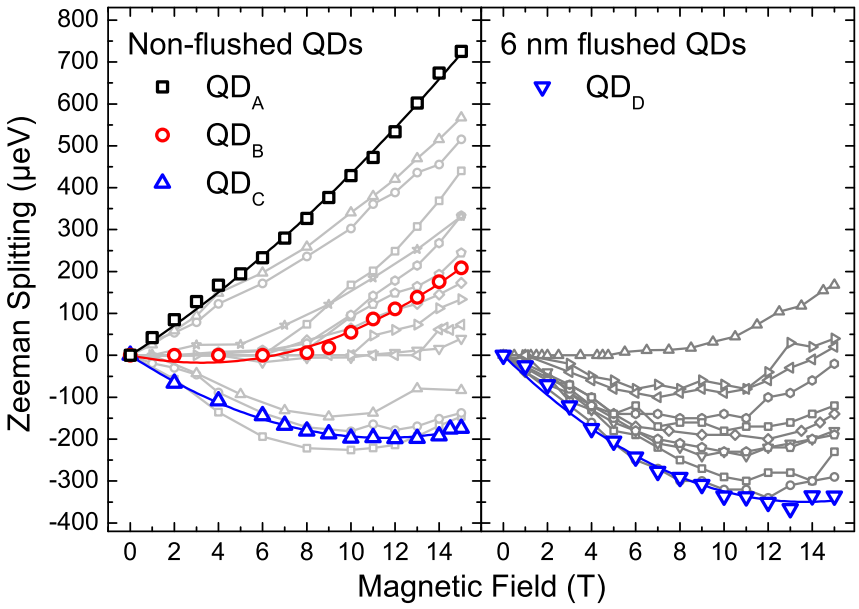

Figure 7.2: Experimentally measured Zeeman splitting of the neutral exciton in several QDs grown without (left) and with the partially covered island flushing technique (right) from Ref. [JEK+12].

varying from $D = 25 - 50$ nm, a height of 4 nm above the wetting layer (WL) and an inverse trumpet-like In-compositional profile (5.1) with $\rho_0 = 0.3$ nm and $z_0 = 1.5$ nm. The In-concentration of the $In_xGa_{1-x}As$ alloy was taken to be $x^{min} = 0.2$ at the base and side of the dot increasing to $x^{apex} = 0.4 - 0.5$ at the dot apex. These parameters are consistent with the results of X-STM measurements, from which we also determined the thickness and In-content of the wetting layer to be 2 nm and $x^{WL} = 0.18$, respectively. [KCB+10]

7.3 Results and discussion

7.3.1 Non-linear Zeeman splitting

A weak non-linear dependence of the electron Zeeman splitting on the magnetic field was first reported for GaAs-AlGaAs quantum wells and super lattices subject to very high magnetic fields. [DKW88] Similar quadratic magnetic field dependencies of the hole Zeeman splitting have been reported for GaAs-InGaAs superlattices and quantum wells and attributed to a magnetic field-induced mixing of HH and LH states. [WNS+93, THW95, KRBF01]

For bulk semiconductors in a magnetic field, the analytic solution of the eight-band $k \cdot p$ Hamiltonian in the axial approximation reveals that the components of the envelope function resemble Landau Levels. [PB66] Further, a B-field-dependent

mixing of the valence bands is observed which accounts for the non-linear Zeeman splitting. In quantum wells, an analytic solution is not possible. However, a perturbative approach also indicates a non-linear Zeeman splitting that is caused by valence band mixing. [KRBF01] This approach is based on a factorization of the envelope functions into quantum well envelope functions in the vertical and Landau Levels in the lateral direction. [KRBF01] The HH and LH components of the envelope function predominantly correspond to a specific Landau Level and the coupling between the the HH and LH bands is found to be proportional to the raising and lowering operator of the Landau Levels.

To illustrate the essential effects, we consider the action of the magnetic field on the four band Γ_{8v} Hamiltonian only. This Hamiltonian represents the interaction of HH and LH bands, whereas all other bands enter only via the Luttinger parameters γ_1^L, γ_2^L, γ_3^L, κ^L, and q^L. In the following, we drop the superscript L. The Γ_{8v} Hamiltonian in the presence of a magnetic field $\mathbf{B}$ along the [001] direction has been given in Ref. [TRR79]. We split this Hamiltonian in into the magnetically induced *inter-band* Hamiltonian

$$\begin{aligned}\hat{H}_{interband} &= \mu_B B \Big[4\gamma_3(\{J_3 J_+\}\hat{a} + \{J_3 J_-\}a^\dagger)\lambda\hat{k}_z + (\gamma_2+\gamma_3)(J_+^2\hat{a}^2 + J_-^2\hat{a}^{\dagger\,2}) \\ &\quad +(\gamma_2-\gamma_3)(J_+^2\hat{a}^{\dagger\,2} + J_-^2 a^2)\Big]\,, \end{aligned} \tag{7.1}$$

and the diagonal intra-band Hamiltonian

$$\begin{aligned}\hat{H}_{intraband} &= \mu_B B \Big[-2\gamma_1 \mathbf{1}_4 \left(\hat{a}^\dagger\hat{a} + \tfrac{1}{2} + \tfrac{1}{2}(\lambda\hat{k}_z)^2\right) \\ &\quad -2\gamma_2\left(J_z^2 - \tfrac{5}{4}\mathbf{1}_4\right)\left(\hat{a}^\dagger\hat{a} + \tfrac{1}{2} - (\lambda\hat{k}_z)^2\right) - \kappa J_z - q J_z^3\Big]\,. \end{aligned} \tag{7.2}$$

Here, $J_+ = J_x + iJ_y$ and $J_- = J_x - iJ_y$ are the raising and lowering operators of 3/2-spin of the Γ_8 representation, respectively. The k-operator along [001] is labeled $\hat{k}_z$. Consistently with Ref. [SH74], the raising and lowering operators of the in-plane Landau Levels are defined as

$$\hat{a}^\dagger = \frac{\lambda}{\sqrt{2}}(\hat{K}_x + i\hat{K}_y) \;\text{ and }\; \hat{a} = \frac{\lambda}{\sqrt{2}}(\hat{K}_x - i\hat{K}_y), \tag{7.3}$$

respectively, with the gauge covariant in-plane k-operators $\hat{K}_x = \hat{k}_x + (e/\hbar)A_x$ and $\hat{K}_y = \hat{k}_y + (e/\hbar)A_y$ for the vector potential $\mathbf{A}$ and the magnetic length $\lambda = \sqrt{\hbar/(eB)}$. With this definition, the Landau quantum number N (= 0, 1, 2, ...) corresponding to the eigenvalues of $\hat{a}^\dagger\hat{a}$ coincides with the angular momentum projection of the Landau oscillator state. [SH74] Note that in contrast to bulk and quantum wells, there is no second "good" Landau quantum number due to the lack of lateral translation symmetry in the dots.

We continue with the discussion of the qualitative implications of the magnetically induced band mixing resulting from Eq. (7.1) for the predominantly HH-like ground states in quantum wells. To this end we use the factorization approach of the envelope

functions into vertical quantum well states and lateral Landau Levels. [KRBF01] We denote the basis states as $|N, n_z, m_j\rangle$, where N is the Landau quantum number, n_z the index on the quantum well state and m_j the angular momentum project of the Bloch function.

The HH ↑- and HH ↓-like ground state are predominantly composed of the functions $|0, 0, \frac{3}{2}\rangle$ and $|0, 0, -\frac{3}{2}\rangle$, respectively. The magnetic field induces a coupling of the HH ↑ state $|0, 0, \frac{3}{2}\rangle$ to the LH ↑ state $|1, 1, \frac{1}{2}\rangle$ and to the LH ↓ state $|2, 0, -\frac{1}{2}\rangle$. The strength of this coupling is proportional to $\gamma_3 \hat{k}_z \sqrt{B}$ and $(\gamma_2 + \gamma_3)B$ for the LH ↑ and LH ↓ sub-bands, respectively. This B-field-dependent mixing causes the non-linear Zeeman splitting because the response of the various heavy hole and light hole components to the magnetic field given by Eq. (7.2) is vastly different.

On the other hand, since $\hat{a}|0, 0, -\frac{3}{2}\rangle = 0$, the HH ↓ state $|0, 0, -\frac{3}{2}\rangle$ couples only to the LH ↑ state $|2, 0, +\frac{1}{2}\rangle$ via an interaction with a strength proportional to $(\gamma_2 - \gamma_3)B$. Since $\gamma_2 \approx \gamma_3$ for $In_xGa_{1-x}As$ alloys, [VMRM01] the latter coupling is normally negligible and, consequently, the HH ↓ ground state has an almost pure HH ↓ character, independent of the magnetic field.

Next, we discuss how these results from quantum wells relate to the quantum dots examined in this work. It was found that the coupling of the HH ↑ ground state to the light hole bands leads to a HH g-factor that varies linearly with the square of the in-plane wave vector, i.e. $g_h \propto k_\parallel^2$. [KRBF01] For quantum well Landau levels, $k_\parallel^2$ itself varies linearly with magnetic field leading to the experimentally observed quadratic Zeeman splitting. On the other hand, in small, strongly confined quantum dots $k_\parallel^2$ varies with $\propto 1/D^2$ where D is the dot diameter. As a result, one would expect that the hole g-factor in strongly confined dots (i.e. small D) should be unaffected by the magnetic field. These qualitative considerations indicate that the presently studied, large QDs with dilute In-composition produce effects that fall in a regime between the expectations for quantum wells ($g_h = g_h^0 + g_h^1 B$) and quantum dots (g_h independent of B). We continue by developing these ideas quantitatively to explain the experimental observations.

The leftmost panel of Fig. 7.3 shows the calculated exciton Zeeman spin splitting as a function of the magnetic field for three model dots having different size and In-composition consistent with the range obtained from our X-STM measurements. These representative QDs have been chosen in order to reproduce the generic behavior of QD_A, QD_B, and QD_C, representing the full range of behaviors observed in experiment. The In-concentration decreases from $x^{apex} = 0.50$ to $x^{apex} = 0.40$, the data labeled (i) to (iii) in Fig. 7.3, while the lateral size is increased from 25 nm (i) to 50 nm (iii) in order to reproduce the experimentally observed range of exciton transition energies ($1310 - 1365$ meV). The curve labeled (i) in the leftmost panel of Fig. 7.3 shows an almost purely linear Zeeman splitting (B-field independent g-factor) while (iii) exhibits a clear quadratic dependence. In comparison, the model QD (ii) exhibits a behavior that is intermediate between the linear and quadratic regimes. The quadratic dependence of the exciton Zeeman splitting stems entirely from the

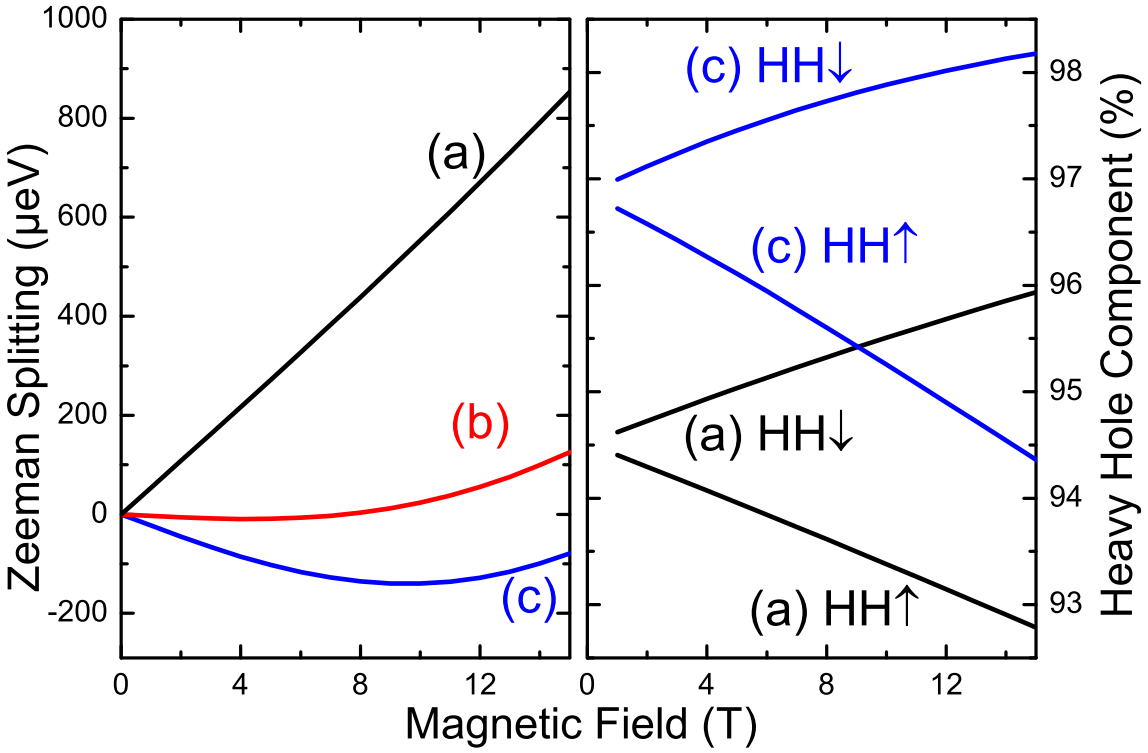

Figure 7.3: (left) Calculated Zeeman spin splitting of the neutral exciton in three QDs with the same height of 6 nm but different diameter and In-concentration at the apex x^{apex} as a function of the magnetic field: (i) 25 nm diameter and $x^{apex} = 0.50$, (ii) 45 nm diameter and $x^{apex} = 0.45$, (iii) 50 nm diameter and $x^{apex} = 0.40$. (right) Calculated heavy hole character of the lowest hole orbital levels having spin-up HH $\uparrow$ and spin-down HH $\downarrow$ character, respectively.

HH-like groundstate of the valence band. For all QDs presented in Fig. 7.3 (i) to (iii), the valence band Zeeman splitting varies quadratically with magnetic field, namely,

$$\Delta E_Z^h = \mu_B g_h^0 B + \mu_B g_h^1 B^2, \tag{7.4}$$

where the B-field is applied along the growth direction, μ_B is the Bohr magneton and, g_h^0 and g_h^1 are the linear and quadratic components of the hole g-factor, respectively.

	$g_e^0 + g_h^0$	g_h^1 (T^{-1})
$\mathrm{QD_A}$	0.58 ± 0.02	0.016 ± 0.002
$\mathrm{QD_B}$	-0.19 ± 0.03	0.028 ± 0.002
$\mathrm{QD_C}$	-0.59 ± 0.01	0.026 ± 0.001
$\mathrm{QD_D}$	-0.89 ± 0.03	0.032 ± 0.002

Table 7.1: Linear ($g_e^0 + g_h^0$) and quadratic (g_h^1) components of the experimentally observed exciton g-factor for $\mathrm{QD_A}$, $\mathrm{QD_B}$, $\mathrm{QD_C}$ and $\mathrm{QD_D}$ presented in Figs. 7.1 and 7.2.

	$g_e^0 + g_h^0$	g_h^1 (T^{-1})
(a)	0.91	0.004
(b)	-0.13	0.017
(c)	-0.50	0.026

Table 7.2: Linear ($g_e^0 + g_h^0$) and quadratic (g_h^1) components of the calculated exciton g-factors (a)-(c) in Fig. 7.2.

By fitting quadratic function to the experimentally observed Zeeman splittings in Fig. 7.2 for $\mathrm{QD_A}$ to $\mathrm{QD_D}$, we extracted both the linear ($g_e^0 + g_h^0$) and quadratic (g_h^1) components of the exciton g-factor. The results of this analysis are presented in Table 7.1. Our calculation yield perfectly quadratic behavior summarized in Table 7.2. In our calculation, we find the full range of almost linear to dominantly quadratic behavior that was also observed in experiment.

The strong quadratic character of the hole Zeeman splitting arises from the combination of the comparatively large diameter, small height and dilute In-content in the dots investigated. Firstly, the dot diameter ($D = 40 - 50$ nm) is larger than the magnetic length over the entire range of magnetic fields of interest. Secondly, the low, almost homogeneous In-concentration induces only a weak confinement potential in the core of the QDs. As a result, the quantum states that are formed in the magnetic field resemble somewhat 2D Landau levels and, consequently, the HH ground states behave in a manner similar to what is known for quantum wells. Moreover, the small dot height of 6 nm (including the wetting layer) introduces a strong field-induced coupling of HH $\uparrow$ and LH $\uparrow$ states, as in narrow quantum wells. [THW95] The quantum well-like dependence of the Zeeman spin splitting on magnetic field is especially

pronounced for the large, In-dilute QD (iii) as illustrated in Fig. 7.3. The HH-like ground state has only a weak LH admixture (< 6 %) at zero magnetic field that is caused by the QD shape, In-Ga alloy profile and inhomogeneous strain fields. This is illustrated quantitatively in the rightmost panel of Fig. 7.3 that shows the magnetic field dependence of the HH-like ground states. Unlike the HH $\uparrow$, the HH $\downarrow$-like ground state effectively decouples from the LH bands as the magnetic field increases and, thus, its LH character weakens at higher fields.

7.3.2 Degree of polarization

The observed B-field-induced HH-LH mixing discussed in the previous section has no effect on the degree of circular polarization since a magnetic field applied along the growth direction of the QDs does not lower the rotational symmetry of the Hamiltonian. This expectation was confirmed by the results of our calculations which revealed negligible and magnetic field independent reduction of the degree of polarization ($\approx 10^{-7}$) for magnetic fields up to B = 15 T. This can be clearly seen from the calculated absorption spectra for $\sigma^{\pm}$ polarized light that are presented in Fig. 7.4a for a lens-shaped model dot with diameter of 50 nm and inverse trumpet-like In-composition with $x^{apex} = 0.40$ and $x^{min} = 0.20$, chosen to represent a dot similar to QD_C or QD_D in Figs 7.1 and 7.2. For clarity, the spectra are centered around the mean energy of the two bright exciton ground states. The spectra clearly show that the polarization of the QD levels is unaffected by the elevated external magnetic field, in accord with our expectations.

The negligible loss of degree of polarization originates from terms in the Hamiltonian that lower the symmetry from C_4 to C_2 and from C_{4v} to C_{2v} with and without external magnetic fields, respectively. A strong breaking of C_4 symmetry has been observed for elongated GaAs/AlGaAs [BAK+10] and CdTe-ZnTe [LBMM07] quantum dots, as well as for GaAs/AlGaAs QDs which were grown along the reduced symmetry [111] direction. [SUG+11] In contrast, in symmetrically shaped InGaAs/GaAs QDs grown on a [001] surface the primary symmetry breaking term stems from the piezoelectric field as shown in Ch. 5. In the large, In-dilute QDs studied here, the strain field is weak with almost axial symmetry and the piezoelectric field is negligible, especially in the center of the QD where the HH-like ground state is localized. In C_4 symmetry, the optical selection rules for circularly polarized light are strict. This has been shown in detail for hole bands of bulk Ge in the presence of uniaxial strain and magnetic fields. [SH74] The results are based on symmetry arguments alone and can readily be applied to QDs with the same symmetry class. Our calculations show that, even a 2 : 1 elongation of the QDs in the plane leads only to an extremely small reduction of the degree of polarization of the order of $\sim 10^{-3}$. This reduction is so tiny due to the large size of our QDs: The ground state wave functions are localized in the center of the QDs and shape anisotropy in the dot periphery has only a very weak influence on the orbital states. A more intuitive picture is obtained for full axial symmetry which is almost realized in near perfect lens-shaped QDs since

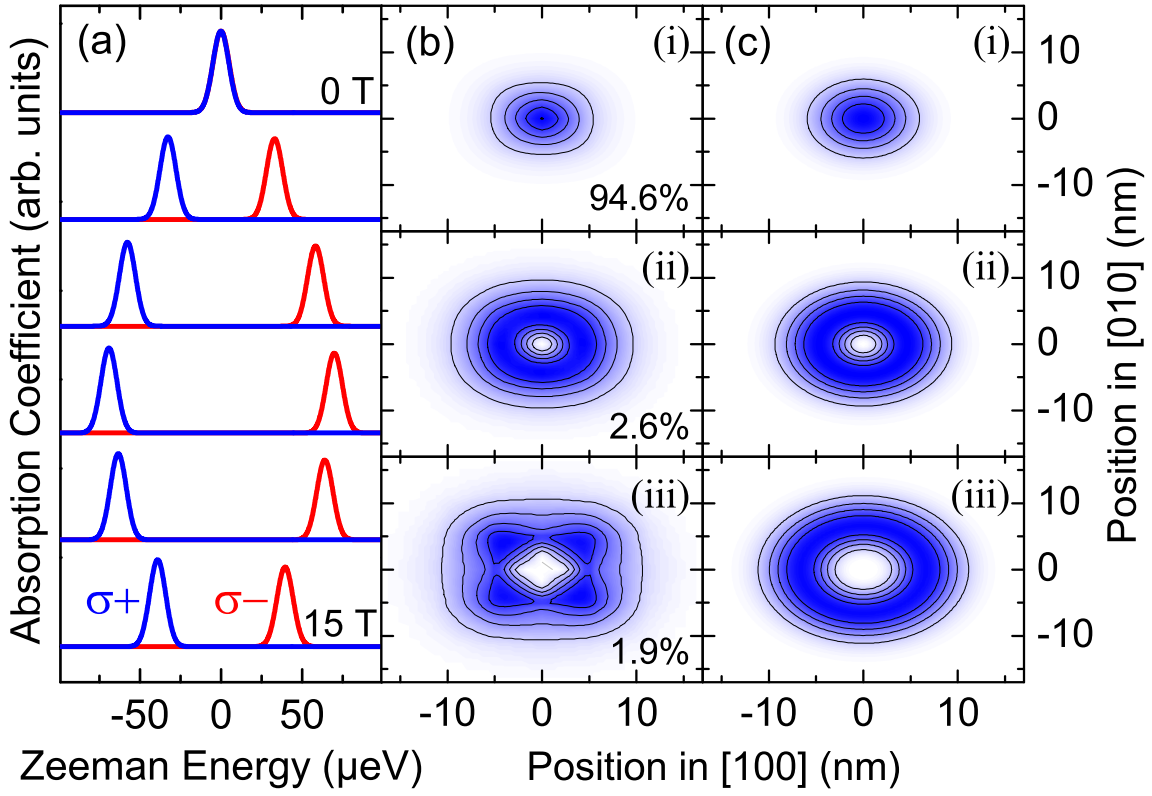

Figure 7.4: (a) Polarization resolved ground state absorption spectra for a QD of the type $QD_{C/D}$ as the magnetic field increases from $0 - 15$ T. (b) In-plane envelope function probability density looking along the QD growth direction of the (i) HH $\uparrow$, (ii) LH $\uparrow$, and (iii) LH $\downarrow$ component of the predominantly HH $\uparrow$ ground state for the full Hamiltonian. The numbers in the lower right corner of each panel indicate the total contribution to the wave function. (c) Probability density along the confinement direction for quantum well Landau Levels corresponding in the axial approximation to the components (b (i)-(iii)) of the full Hamiltonian.

$\gamma_2 \approx \gamma_3$. [LB70] In this case, the projection of total angular momentum m_J is a good quantum number. Moreover, selection rules for $\sigma^{\pm}$ transitions are strict and become $\Delta m_J = \pm 1$. If in addition the magnetic length is smaller than the QD radius, the components of the QD ground states increasingly resemble combinations of Landau-Levels with HH/LH-Bloch functions in the lateral directions. [Lut56, SH74] This is realized for our QDs for magnetic fields above 5 T where the magnetic length is $\lambda = \sqrt{\hbar/(eB)} \lesssim 11$ nm. In the presence of a magnetic field the rotational symmetry is preserved and only states having the same total angular momentum projection are mixed.

The total angular momentum projection of the states $m_J = m_j + N$ is a combination of the Landau oscillator state (N) and the angular momentum projection m_j of the Bloch function, namely $\pm 3/2$ and $\pm 1/2$ for heavy holes and light holes, respectively.

Figure 7.4b (i)-(iii) and Fig. 7.4c (i)-(iii) compare the admixture of different band spin states, namely HH $\uparrow$, LH $\uparrow$ and LH $\downarrow$, in the predominantly HH $\uparrow$-like ground state wave function. In this comparison, we consider only the lateral wave function for the sake of clarity. To a very good approximation, it is composed of $|N, m_j\rangle = |0, \frac{3}{2}\rangle$, $|1, \frac{1}{2}\rangle$, and $|2, -\frac{1}{2}\rangle$ states, each of which combine to produce $m_J = 3/2$. The HH $\uparrow$ component $|0, \frac{3}{2}\rangle$ and the LH $\uparrow$ component $|1, \frac{1}{2}\rangle$, shown in Figs 7.4b (i) and 7.4b (ii), respectively, were obtained by detailed calculations and show good agreement with the corresponding Landau Levels (Figs 7.4c (i) and 7.4c (ii)) in the axial approximation. The small LH $\downarrow$ component $|2, -\frac{1}{2}\rangle$ (Fig. 7.4b (iii)) is affected substantially by C_4 symmetry terms in the Hamiltonian. However, it contributes only 1.9 % to the total wave function and, as noted before, C_4 symmetry is enough to guarantee full polarization.

7.4 Summary

In summary, strongly magnetic field-dependent exciton g-factors were explained in InGaAs/GaAs self-assembled QDs. The microscopic origin of non-linear Zeeman splitting was accounted for by eight-band $\mathbf{k} \cdot \mathbf{p}$ simulations using realistic parameters (size and In-composition) that were directly extracted from X-STM measurements. The combined effect of dilute In-composition and relatively large lateral size was shown to result in strong field-induced mixing of the HH-LH orbital states in high magnetic fields. This mixing manifests itself as a quadratic variation of the hole Zeeman splitting on the external magnetic field. Similar effects are negligible for the electron and have previously been observed only in thin two dimensional systems.

Part III

Appendices

Appendix A

Continuum limit of the gauge-invariant SAFE method

Let Ω be the subspace of $\mathbb{R}^3$ that contains the grid. In the following, we derive a global error bound $\|D_\mu(F^C - \widetilde{F}^{C\,h})\|_{\max}$ for the gauge covariant derivative $D_\mu = \partial_\mu + i(e/\hbar)A_\mu$ in the direction μ in a constant magnetic field with $|\mathbf{B}| = B$. Here, $F^C \equiv f$ is the component of the normalized envelope function. In addition,

$$\widetilde{F}^{C\,h} \equiv \widetilde{f}^h = \sum_{\mathbf{R}_I, K} a^C_{K,\mathbf{R}_J} U_{\mathbf{R}_J} v^C_{K,\mathbf{R}_I}, \tag{A.1}$$

is its approximation in the basis $\{\widetilde{v}^C_{K,\mathbf{R}_I}\}$ of gauge-invariant symmetry adapted finite elements given in Eq. (3.23). The $a^C_{K,\mathbf{R}_J}$ are the expansion coefficients of the envelope function. For simplicity, we derive the result for the maximum norm since convergence with this norm implies convergence in $L^2(\Omega)$. In the following, we set $e/\hbar = 1$ and denote the component functions F^C as f for the sake of simplicity.

First, the global error clearly equals the maximum error within the individual grid cells,

$$\|D_\mu(f - \widetilde{f}^h)\|_{\max} = \max_{\mathbf{R}_I} \|D_\mu(f - \widetilde{f}^h)\|_{\max,\Omega_I}, \tag{A.2}$$

where Ω_I denotes the cell of grid point $\mathbf{R}_I$. In the following, the norm $\|\cdot\|$ always indicates the maximum norm on Ω_I. Assume the error to be maximal within grid cell Ω_I for some index I. Since the error is independent of the particular gauge, we choose a symmetric Coulomb gauge centered at $\mathbf{R}_I$,

$$\mathbf{A}(\mathbf{r}) = \frac{1}{2}\mathbf{B} \times (\mathbf{r} - \mathbf{R}_I). \tag{A.3}$$

This choice guarantees that the vector potential $\mathbf{A}$ is bound by $\|\mathbf{A}\| < B\,h$ within the cell Ω_I. Next, the error on the grid cell Ω_I can be split into the common interpolation error of finite elements δ_I and the error δ_B because the phase function $U_{\mathbf{R}_I}$ deviates from unity on the finite grid. This gives

$$\|D_\mu(f - \widetilde{f}^h)\| \leq \delta_I + \delta_B. \tag{A.4}$$

The finite element interpolation error is given by [BS08]

$$\delta_I = \|D_\mu(f - f^h)\| \propto h^m \|\partial_\mu^{m+1} f\|. \tag{A.5}$$

Here, f^h is the approximate envelope function for the gauge in Eq. (A.3) without a phase function and we have used the boundedness of $\mathbf{A}$. The polynomial order m of the basis functions is 2 or 3 depending on the direction μ and the component C leading to an error order of $\mathrm{O}(h^2)$ and $\mathrm{O}(h^3)$, respectively. The error δ_B due to the phase function is given by

$$\begin{aligned}
\delta_B &= \|D_\mu(f^h - \widetilde{f}^h)\| \\
&= \|(\partial_\mu + iA_\mu) \sum_{\mathbf{R}_J,K} a^C_{K,\mathbf{R}_J}(1 - U_{\mathbf{R}_J}) v^C_{K,\mathbf{R}_J}\| \\
&\leq \sum_{\mathbf{R}_J,K} |a^C_{K,\mathbf{R}_J}| \|(\partial_\mu + iA_\mu)(1 - U_{\mathbf{R}_J}) v^C_{K,\mathbf{R}_J}\| \\
&\leq N a_{\max} \max_{K,\mathbf{R}_J} \|(\partial_\mu + iA_\mu)(1 - U_{\mathbf{R}_J}) v^C_{K,\mathbf{R}_J}\|,
\end{aligned} \tag{A.6}$$

where we used the fact that only a small number N of basis functions $\{v^C_{K,\mathbf{R}_J}\}$ is non-zero within the grid cell Ω_I. The constant $a_{\max}$ is the maximum of the moduli of the expansion coefficients which are bounded due to the normalization of the envelope function. The maximum on the right hand side of Eq. (A.6) can be further estimated as

$$\begin{aligned}
& \|(\partial_\mu + iA_\mu)(1 - U_{\mathbf{R}_J}) v^C_{K,\mathbf{R}_J}\| \\
= \; & \|(\partial_\mu - U_{\mathbf{R}_J}\partial_\mu + iA_\mu - iU_{\mathbf{R}_J} A^{loc}_{J,\mu}) v^C_{K,\mathbf{R}_J}\| \\
\leq \; & \|1 - U_{\mathbf{R}_J}\| \|\partial_\mu v^C_{K,\mathbf{R}_J}\| \\
& + \|A_\mu - U_{\mathbf{R}_J} A^{loc}_{J,\mu}\| \|v^C_{K,\mathbf{R}_J}\|,
\end{aligned} \tag{A.7}$$

where we have used Eq. (3.25). Since the distance of the grid point $\mathbf{R}_J$ to the center of the gauge $\mathbf{R}_I$ is $|\mathbf{R}_J - \mathbf{R}_I| \leq \sqrt{3}h$ in the phase function $U_{\mathbf{R}_J}$, the bounds of the individual terms in the gauge Eq. (A.3) are obtained by means of Taylor expansions of $U_{\mathbf{R}_J}$ and $A^{loc}_{J,\mu}$ around $\mathbf{R}_I$ as

$$\|1 - U_{\mathbf{R}_J}\| \propto B\, h^2, \tag{A.8}$$

$$\|\partial_\mu v^C_{K,\mathbf{R}_J}\| \propto \frac{1}{h}, \tag{A.9}$$

$$\|A_\mu - U_{\mathbf{R}_J} A^{loc}_{J,\mu}\| \propto B\, h, \tag{A.10}$$

$$\|v^C_{K,\mathbf{R}_J}\| \propto 1. \tag{A.11}$$

Consequently, the error δ_B and hence the overall error is of order $\mathcal{O}(B\, h)$.

Appendix B

Angular momentum matrices of T_d

Here, we summarize the matrices used to construct the Hamiltonian in the angular momentum basis. [BP74, Win03] The common Pauli matrices are denoted as σ_x, σ_y, and σ_z. They present the angular momentum matrices of the Γ_{6c}, Γ_{7c} and Γ_{7v} representations. The matrices J_x, J_y, and J_z are the angular momentum matrices of the Γ_{8c} and Γ_{8v} representations. The U_i and T_i are coupling matrices of the Γ_{8c} and Γ_{8v} representations with the Γ_{6c}, Γ_{7c} and Γ_{7v} representations.

$$\sigma_x = \begin{pmatrix} 0 & 1 \\ 1 & 0 \end{pmatrix}, \quad \sigma_y = \begin{pmatrix} 0 & -i \\ i & 0 \end{pmatrix}, \quad \sigma_z = \begin{pmatrix} 1 & 0 \\ 0 & -1 \end{pmatrix}, \quad \mathbf{1}_2 = \begin{pmatrix} 1 & 0 \\ 0 & 1 \end{pmatrix},$$

$$J_x = \tfrac{1}{2} \begin{pmatrix} 0 & \sqrt{3} & 0 & 0 \\ \sqrt{3} & 0 & 2 & 0 \\ 0 & 2 & 0 & \sqrt{3} \\ 0 & 0 & \sqrt{3} & 0 \end{pmatrix}, \qquad J_y = \tfrac{i}{2} \begin{pmatrix} 0 & -\sqrt{3} & 0 & 0 \\ \sqrt{3} & 0 & -2 & 0 \\ 0 & 2 & 0 & -\sqrt{3} \\ 0 & 0 & \sqrt{3} & 0 \end{pmatrix},$$

$$J_z = \tfrac{1}{2} \begin{pmatrix} 3 & 0 & 0 & 0 \\ 0 & 1 & 0 & 0 \\ 0 & 0 & -1 & 0 \\ 0 & 0 & 0 & -3 \end{pmatrix}, \qquad \mathbf{1}_4 = \begin{pmatrix} 1 & 0 & 0 & 0 \\ 0 & 1 & 0 & 0 \\ 0 & 0 & 1 & 0 \\ 0 & 0 & 0 & 1 \end{pmatrix},$$

$$T_x = \tfrac{1}{3\sqrt{2}} \begin{pmatrix} -\sqrt{3} & 0 & 1 & 0 \\ 0 & -1 & 0 & \sqrt{3} \end{pmatrix}, \qquad T_y = \tfrac{-i}{3\sqrt{2}} \begin{pmatrix} \sqrt{3} & 0 & 1 & 0 \\ 0 & 1 & 0 & \sqrt{3} \end{pmatrix},$$

$$T_z = \tfrac{\sqrt{2}}{3} \begin{pmatrix} 0 & 1 & 0 & 0 \\ 0 & 0 & 1 & 0 \end{pmatrix},$$

$$T_{xx} = \tfrac{1}{3\sqrt{2}} \begin{pmatrix} 0 & -1 & 0 & \sqrt{3} \\ -\sqrt{3} & 0 & 1 & 0 \end{pmatrix}, \qquad T_{yy} = \tfrac{1}{3\sqrt{2}} \begin{pmatrix} 0 & -1 & 0 & -\sqrt{3} \\ \sqrt{3} & 0 & 1 & 0 \end{pmatrix},$$

$$T_{zz} = \tfrac{\sqrt{2}}{3} \begin{pmatrix} 0 & 1 & 0 & 0 \\ 0 & 0 & -1 & 0 \end{pmatrix},$$

$$T_{yz} = \frac{i}{2\sqrt{6}} \begin{pmatrix} -1 & 0 & -\sqrt{3} & 0 \\ 0 & \sqrt{3} & 0 & 1 \end{pmatrix}, \quad T_{zx} = \frac{1}{2\sqrt{6}} \begin{pmatrix} -1 & 0 & \sqrt{3} & 0 \\ 0 & \sqrt{3} & 0 & -1 \end{pmatrix},$$

$$T_{xy} = \frac{i}{\sqrt{6}} \begin{pmatrix} 0 & 0 & 0 & -1 \\ -1 & 0 & 0 & 0 \end{pmatrix},$$

$$(U_i) = (T_i)^H, (U_i j) = (T_i j)^H.$$

Appendix C

Material parameters of InGaAs

In this appendix we give the material parameters we used in our calculations. Note that all bowing parameters are from Ref. [VMRM01]. The volume deformation potentials a_c for the Γ_{6c} conduction band are calculated by $a_c = a_v + a_0$ where a_v is the Γ_{8v} valence band deformation potential and a_0 is the value of the deformation potential of the $\Gamma_{8v} - -\Gamma_{6c}$ band gap both tabulated in Ref. [WZ99]. The Γ^v_{5D} valence band offsets E_{VBO} are calculated from the Γ^v_8 valence band offsets Δ_{E_v} in [WZ98] by $E_{VBO} = \Delta_{E_v} - \Delta_0/3$ with the spin-orbit splitting Δ_0 from Ref. [Win03].

The valence band g-factor anisotropy q^L is calculated from the contribution of the Γ_{7c} and Γ_{8c} by Eq. (2.68) with $q' = 0$ since values in the literature are inconsistent. [Win03, Law71] Material parameters from Ref. [Win03] were used in this calculation.

Parameter	InAs	GaAs	InGaAs bowing [VMRM01]
a (A) [VMRM01]	6.0583	5.65325	–
a_T (A/K) [VMRM01]	$2.74e-5$	$3.88e-5$	–
C_{11} (GPa) [VMRM01]	83.29	122.1	–
C_{12} (GPa) [VMRM01]	45.26	56.6	–
C_{44} (GPa) [VMRM01]	39.59	60.0	–
e_{14} (C/m^2) [dGBR89]	-0.044	-0.160	–
e^q_{14} (C/m^2) [BWPB11]	-0.115	-0.238	–
B^q_{114} (C/m^2) [BWPB11]	-0.6	-0.4	–
B^q_{124} (C/m^2) [BWPB11]	-4.1	-3.8	–
B^q_{156} (C/m^2) [BWPB11]	0.2	-0.7	–
ε_r [MSH82]	15.15	12.91	–

Parameter	InAs	GaAs	InGaAs bowing [VMRM01]
E_0 (eV) [VMRM01]	0.417	1.519	0.477
α (meV/K) [VMRM01]	0.276	0.5405	–
β (K) [VMRM01]	93	204	–
E_{VBO} (eV) [WZ98]	1.390	1.346	−0.38
E_0' (eV) [Win03]	4.390	4.488	–
Δ_0 (eV) [Win03]	0.38	0.341	0.15
Δ_0' (eV) [Win03]	0.240	0.171	–
Δ_- (eV) [Win03]	0	−0.05	–
P (eVnm) [Win03]	0.9197	1.0493	[1]
P' (eVnm) [Win03]	0.0873	0.4780	–
Q (eVnm) [Win03]	0.8331	0.8165	–
m_c [Win03]	0.0229	0.0665	–
g_c [Win03]	−14.9	−0.44	–
γ_1^L [Win03]	20.40	6.85	–
γ_2^L [Win03]	8.30	2.10	–
γ_3^L [Win03]	9.10	2.90	–
κ^L [KKY01]	7.68	1.2	–
q^L	0.048	0.032	–
C_k (eVnm) [Win03]	−0.00112	−0.00034	–
a_1 (eV) [WZ99]	−6.66	−9.36	2.61
a_2 (eV) [WZ99]	−1.00	−1.21	–
b (eV) [VMRM01]	−1.8	−2.0	–
d (eV) [VMRM01]	−3.6	−4.8	–

Table C.1: Material parameters of InAs and GaAs and bowing parameters of InGaAs alloys.

Appendix D

Term rewriting system

The 14-band Hamiltonian has $14 * 14 = 196$ matrix entries, of which about 100 are not empty. Each entry may contain up to 16 different combinations of differential operators $1, a\partial_z, \ldots, a\partial_z, \partial_x a, \ldots, \partial_z a, \partial_x a\partial_x, \partial_x a\partial_y, \ldots, \partial_z a\partial_z$ with parameter functions a. The 14-band Hamiltonian thus has in about 500 terms at the various entries of various differential order for the coordinate axes along directions of high symmetry. The number increases above 2000 for arbitrary coordinate axes.

Hence, a term-by-term setup of the Hamiltonian would be highly error prone. Moreover, most standard references contain mistypings, e.g. T_{yz} in Ref. [Win03].

We implement a simple automated term rewriting system (TRS) to

- construct the Hamiltonian from concise matrix expressions,
- perform rotations of the coordinate system,
- test the Hamiltonian for invariance under symmetry operations,
- optimize the discretization process by computing equivalent matrix elements only once.

D.1 Definition of the TRS

We assume that all variables commute. We keep track of operator order by using $\hat{\mathbf{k}}^\dagger$ and $\nabla^\dagger$ for differential operators left of the parameter function

$$A(\mathbf{r})\hat{k}_i^\dagger\hat{k}_j = \hat{k}_j A(\mathbf{r})\hat{k}_i^\dagger = \text{all perm.} \equiv \hat{k}_i \left(A(\mathbf{r})\hat{k}_j\right). \tag{D.1}$$

The TRS is based on the following constructs. The atomic terms are real numbers, (complex) scalar variables, and functions. All other terms are compositions of these atomic terms. A special case of functions are constants which are represented by functions without arguments. Table D.1 summarizes all further functions used in the TRS. Products of scalars or of a matrix and a scalar are interpreted as commuting

products, whereas products of matrices are interpreted as non-commuting matrix products.

Function Symbol	Description
$I()$	the imaginary unit
$\mathrm{Sum}(a, b, c, \ldots)$	the sum $a + b + c + \ldots$
$\mathrm{Product}(a, b, c, \ldots)$	the product $a \cdot b \cdot c \cdot \ldots$
$\mathrm{Matrix}(n, m, a_{1,1}, a_{1,2}, \ldots, a_{n,m})$	the (n, m)-matrix $\begin{pmatrix} a_{1,1} & a_{1,2} & \ldots \\ \vdots & \ddots & \ddots \\ \ldots & \ldots & a_{n,m} \end{pmatrix}$
$\mathrm{KroneckerProduct}(A, B)$	the Kronecker product $A \times B$
$\mathrm{Conjugate}(a)$	the conjugate a^*
$\mathrm{Transpose}(a)$	the transpose a^T

Table D.1: Functions used in the TRS. The function arguments are indicated in brackets after the function symbols. a, b, c, $a_{i,j}$ are arbitrary terms, n and m are numbers and A and B are matrices.

Terms are simplified with the following reduction rules. These rules are applied recursively and repeatedly to a term until no more rules apply. After the simplification, a term is in the form of a scalar or a matrix of fully expanded sums of products.

In the following, we summarized the simplification rules. Here, l_i denotes a list of terms, and the binary operation "," concatenates two lists. A list can also be empty. For the sake of conciseness, ... indicate that a pattern applies analogously to subsequent terms of a list of arguments. Further, a, b, and c are arbitrary terms, A, and B are matrices and p, q, and r are real numbers. An n-fold product of a term a is denoted by a^n. The special function Num indicates that the operation enclosed in its argument is evaluated explicitly by the term rewriting system ($\mathrm{Num}(\mathrm{Sum}(2, 3)) = \mathrm{Num}(2 + 3) = 5$). Variables are denotes by Var(name, conj) with their name "name" and a boolean "conj" that indicates whether they are conjugate.

Unify Sum: $\mathrm{Sum}(l_1, \mathrm{Sum}(l_2), l_3) \to \mathrm{Sum}(l_1, l_2, l_3)$.

Unify Product: $\mathrm{Product}(l_1, \mathrm{Product}(l_2), l_3) \to \mathrm{Product}(l_1, l_2, l_3)$.

Expand: Apply the distributive law to fully expand products of sums.
$\mathrm{Product}(l_1, \mathrm{Sum}(a, b, \ldots), l_2) \to \mathrm{Sum}(\mathrm{Product}(l_1, a, l_2), \mathrm{Product}(l_1, b, l_2), \ldots)$.

Normalize Product: Simplify products and sort factors.

1. Contract n-fold product of imaginary unit $I()$.

$$I()^n \to I()^{n \bmod 2} \begin{cases} -1 & \text{if } n \bmod 4 \geq 2 \\ 1 & \text{otherwise} \end{cases}$$

2. Contract all numbers.

$$\text{Product}(l_1, p, l_2, q, l_3) \to \text{Product}(\text{Num}(pq\ldots), l_1, l_2, l_3).$$

If the resulting number is 1 and is not the only factor in product, remove the number from the argument list.

3. If a product has a single argument, replace the product by its argument.

$$\text{Product}(a) \to a$$

4. If a product contains the number $p = 0$ and all factors are scalar, replace the product by 0.

$$\text{Product}(l_1, p, l_2) \to 0$$

5. Multiply matrices and draw all scalar factors into the resulting matrix. Here, without restriction, l_1 and l_2 are lists of scalar expressions and n_A and m_A denote the number of rows and columns of A, respectively.

$$\begin{aligned}\text{Product}(l_1, A, l_2, B, \ldots) \;=\; &\text{Matrix}(n_A, m_B, \text{Product}(l_1, l_2, \text{Sum}(\\ &\text{Product}(A_{1,1}, B_{1,1}), \ldots,\\ &\text{Product}(A_{1,m_A}, B_{m_A,1}), \ldots)))\end{aligned}$$

6. Sort all factors in the following order: Number, I, Constants (sorted by Name), conjugate Variables (sorted by name), non-conjugate Variables (sorted by name), Functions (sorted by name then recursively by argument from back to front)

Normalize Sum: Simplify sums and contract summands that only differ by a number prefactor.

1. Remove summands $p = 0$.

$$\text{Sum}(l_1, p, l_2, \ldots) \to \text{Sum}(l_1, l_2, \ldots)$$

2. If only one summand remains, replace the sum by that summand.

$$\text{Sum}(a) \to a$$

3. If no summands remain, replace the sum by zero.

$$\text{Sum}() \to 0$$

4. Contract all scalar summands that differ by a number prefactor only.

$$\text{Sum}(\text{Product}(p, l_1), \text{Product}(q, l_1), \ldots) = \text{Sum}(\text{Product}(\text{Num}(p, q), l1), \ldots)$$

Sum Matrices: Sum matrices in an element-wise sum. The formal description is not shown here because it is straightforward but result in a cumbersome formal expression.

Flatten Matrices: Flatten a matrix of matrices in a matrix of scalars. Again, the formal notation is straightforward but cumbersome. Hence, we give the rule in matrix notation only.

$$\begin{pmatrix} A & B & \dots \\ C & D & \dots \\ \vdots & \vdots & \ddots \end{pmatrix} \rightarrow \begin{pmatrix} A_{1,1} & A_{1,2} & \dots & B_{1,1} & B_{1,2} & \dots \\ A_{2,1} & A_{2,2} & \dots & B_{2,1} & B_{2,2} & \dots \\ \vdots & \vdots & \vdots & \vdots & \vdots & \vdots \\ C_{1,1} & C_{1,2} & \dots & D_{1,1} & D_{1,2} & \dots \\ C_{2,1} & C_{2,2} & \dots & D_{2,1} & D_{2,2} & \dots \\ \vdots & \vdots & \vdots & \vdots & \vdots & \ddots \end{pmatrix}$$

Apply Conjugate: Apply the conjugate function recursively.

1. $\text{Conjugate}(\text{Var}(\text{name}, \text{conj})) \rightarrow \text{Var}(\text{name}, \text{not conj})$.
2. $\text{Conjugate}(\text{Conjugate}(a)) \rightarrow a$.
3. $\text{Conjugate}(p) \rightarrow p$.
4. $\text{Conjugate}(I()) \rightarrow \text{Product}(-1, I())$.
5. For other functions Func do
   $\text{Conjugate}(\text{Func}(a, b, \dots)) \rightarrow \text{Func}(\text{Conjugate}(a), \text{Conjugate}(b), \dots)$.
   Note that this is valid form all functions we consider here.

Apply Transpose: Apply the transpose function.

1. $\text{Transpose}(\text{Var}(v, conj)) \rightarrow \text{Var}(v, conj)$
2. $\text{Transpose}(\text{Transpose}(t)) \rightarrow t$
3. $\text{Transpose}(p) \rightarrow p$
4. $\text{Transpose}(I()) \rightarrow I()$
5. $\text{Transpose}(\text{Matrix}(n, m, l_1)) \rightarrow \text{Matrix}(m, n, l_2)$, where l_2 is the transposed of l_1. To this end all entries are transposed recursively.
6. $\text{Transpose}(\text{Sum}(a, \dots)) \rightarrow \text{Sum}(\text{Transpose}(a), \dots)$,
   and
   $\text{Transpose}(\text{Product}(a, \dots)) \rightarrow Product(\dots, \text{Transpose}(a))$.

Apply Kronecker Product: Apply the Kronecker product.

1. $\text{KroneckerProduct}(A, b) = \text{Product}(A, b)$,
   and $\text{KroneckerProduct}(a, B) = Product(a, B)$, if a and b are scalars, respectively.

2. KroneckerProduct$(A, B) = C$ where C is Kronecker Product of A and B.

Apply Conjugate Variable: If a variable is on the list of real variables, $\mathrm{Var}(\mathrm{name}, \mathrm{true}) = \mathrm{Var}(\mathrm{name}, \mathrm{false})$.

The result of this simplification process is fully expanded and readily serves as an input to the discretization methods. Applied to a scalar valued term, these rules yield a scalar that consists of a sum of products of atomic terms only. Applied to a matrix valued term, a matrix of scalar with the above property results.

D.2 Application of the TRS

We want to briefly illustrate an application of the TRS to point out its usefulness.

As an example we show the original source code used to setup the Γ_{6c}-Γ_{6c} Hamiltonian that already contains 17 entries of different differential operator combinations.

```
// sx, sy, sz: Pauli Matrices
// s0: 2*2 Identity
// I: imaginary unit
// Bx, By, Bz: B-Field
// g0: free-electron g-factor
// uS = hbar*hbar / (2 m0)
// muB = e*hbar / (2 m0)
// k2 = kxdag kx + kydag ky + kzdag kz
// kyz_com = kydag kz - kzdag ky; kzx_com = kzdag kx - kxdag kz;
// kxy_com = kxdag ky - kydag kx
// E6c: conduction band offset
// gstar: effective conduction band g-factor
// A: effective conduction band dispersion parameter

// G6c = G1Dc
H6c6c = E6c * s0
    + uS * A * k2 * s0
    + muB * (g0 / 2) * (sx * Bx + sy * By + sz * Bz)
    + uS * ((gstar - g0) / 2) * I
        * (sx * kyz_com + sy * kzx_com + sz * kxy_com);
```

Especially the last term of the Hamiltonian is cumbersome to setup entry by entry. The combinations of various signs and potencies of the imaginary unit is error prone. With the help of the TRS it can be clearly arranged and expressed in a concise way.

The intra-band Hamiltonian of the Γ_{5D}^{v} and the $\Gamma_{7v} + \Gamma_{8v}$ representation contains even more terms and a concise way to setup this Hamiltonian is highly important to avoid mistyping errors.

D.3 Optimization of the discretization

In higher order finite elements methods (polynomial degree>1), the discretization often takes comparable time to the numerical solutions of the resulting matrix problem. We can thus save computational time substantially by integrating each distinct term in the Hamiltonian only once. If constant prefactors are extracted from each term, even more terms coincide. The total number of terms that is distinct up to a prefactor may be only a fifth of the total number of terms in the Hamiltonian.

First, for all terms in all entries H_{ij} of the Hamiltonian matrix extract numerical prefactors and imaginary units. For each distinct remaining term t', safe all extracted prefactor z and position (i,j) of the according term in a set $\{(z,i,j)\}$. Second, discretize each t' and write the result times z in the block (i,j) of the discrete Hamilton matrix for each element in the according set $\{(z,i,j)\}$. This is illustrated in the following algorithm:

```
1.  do for each term t in all entries (i,j) of H
1.1   extract prefactor z, denote remaining term as t'
1.2   try to find t' in T
1.3   if found, update entry: T(t') -> T(t') & (z,i,j)
1.4   else add new entry: T -> T & (t', (z,i,j))
2.  do for each t' in T
2.1   discretize t'
2.2   for all (z,i,j) in T(t')
2.2.1   add result times z to final matrix at block (i,j)
```

Here, `H` denotes the (matrix) operator to discretize, `T` is a list of a terms. A set of prefactors and indices `T(t)` $=\{(z,i,j)\}$ is associated to each term `t` in `T`.

List of publications

- *Real-space multiband envelope-function approach without spurious solutions*, T. Eissfeller and P. Vogl, Phys. Rev. B **84**, 195122 (2011)
- *Observation and explanation of strong electrically tunable exciton g factors in composition engineered In(Ga)As quantum dots*, V. Jovanov, T. Eissfeller, S. Kapfinger, E. Clark, F. Klotz, M. Bichler, J. G. Keizer, P. M. Koenraad, G. Abstreiter and J. Finley, Phys. Rev. B **83**, 161303(R) (2011)
- *Highly nonlinear excitonic Zeeman spin splitting in composition-engineered artificial atoms*, V. Jovanov, T. Eissfeller, S. Kapfinger, E. Clark, F. Klotz, M. Bichler, J. G. Keizer, P. M. Koenraad, M. S. Brandt, G. Abstreiter and J. Finley, Phys. Rev. B **85**, 165433 (2012)
- *Electric g tensor control and spin echo of a hole-spin qubit in a quantum dot molecule*, R. Roloff, T. Eissfeller, P. Vogl and W. Pötz, New Journal of Physics **12**, 093012 (2010)
- *Origin of the symmetry lifting in InGaAs/GaAs quantum dots*, T. Eissfeller and P. Vogl, in preparation for Phys. Rev. B

Acknowledgments

At this point, I like to thank all people who contributed to the success of this work.

In particular, I like to thank Prof. Dr. Peter Vogl for offering me this doctorate thesis and his kind support and professional advice. Without the freedom, he gave me in interpreting the topic of this thesis, many parts of this work would not have been possible.

I like to thank all members of the group T33 for the kind and productive working atmosphere. Special thanks go to my predecessors Tobias Zibold and Till Andlauer who, in their work on the simulation of semiconductor devices, laid the foundations this work is based on. Moreover, I like to thank Christoph Schindler, Stefan Birner, Peter Greck and Thomas Grange for the productive discussions that helped me to clarify the concepts of my work. I also like to thank Tillman Kubis and Reinhard Scholz for introducing me to advanced topics of theoretical physics and Alexander Trellakis for introducing me to advanced numerical methods. I like to thank Veronika Enter and Joana Figueiredo who arranged contracts and business trips for me.

Moreover, I like to thank Prof. Jonathan James Finley, his group, and especially Vase Jovanov for the helpful discussions and the experimental data that, on the one hand, inspired parts of the applications presented in this work and, on the other hand, provided an experimental verification of the theoretical results.

Further, I like to thank all members of the WSI for the nice atmosphere and for the social gatherings at the WSI Sommerfest and the WSI Weihnachtsfeier.

I like to thank my parents for supporting me personally and financially. First and foremost, I thank my partner Judith for her loving and enduring support and my son Niklas for always brightening up the day.

In addition, I acknowledge the funding of this work by the Deutsche Forschungsgemeinschaft (SFB 631, SPP 1285), the Austrian Science Fund FWF (SFB IRON), and the Nanosystems Initiative Munich (NIM) and I acknowledge the infrastructure provided by the Technische Universität München.

Bibliography

[AEF85] M. Altarelli, U. Ekenberg, and A. Fasolino, *Calculations of hole subbands in semiconductor quantum wells and superlattices*, Phys. Rev. B **32** (1985), no. 8, 5138–5143.

[AMV08] T. Andlauer, R. Morschl, and P. Vogl, *Gauge-invariant discretization in multiband envelope function theory and g factors in nanowire dots*, Phys. Rev. B **78** (2008), no. 7, 075317.

[AS94] Claudio Aversa and J. E. Sipe, *General $k \cdot p$ theory of lattice-matched semiconductor heterostructures*, Phys. Rev. B **49** (1994), no. 20, 14542–14549.

[AV09] T. Andlauer and P. Vogl, *Electrically controllable g tensors in quantum dot molecules*, Phys. Rev. B **79** (2009), no. 4, 045307.

[BAK+10] T. Belhadj, T. Amand, A. Kunold, C.-M. Simon, T. Kuroda, M. Abbarchi, T. Mano, K. Sakoda, S. Kunz, X. Marie, and B. Urbaszek, *Impact of heavy hole-light hole coupling on optical selection rules in gaas quantum dots*, Applied Physics Letters **97** (2010), no. 5, 051111.

[Bes] G. Bester, *Private communication.*

[BKF+99] M. Bayer, A. Kuther, A. Forchel, A. Gorbunov, V. B. Timofeev, F. Schäfer, J. P. Reithmaier, T. L. Reinecke, and S. N. Walck, *Electron and hole g factors and exchange interaction from studies of the exciton fine structure in $in_{0.60}ga_{0.40}as$ quantum dots*, Phys. Rev. Lett. **82** (1999), no. 8, 1748–1751.

[BNZ03] G. Bester, S. Nair, and A. Zunger, *Pseudopotential calculation of the excitonic fine structure of million-atom self-assembled* $\mathrm{in}_{1-x}\mathrm{ga}_x\mathrm{As}/\mathrm{GaAs}$ *quantum dots*, Phys. Rev. B **67** (2003), 161306.

[BOS+02] M. Bayer, G. Ortner, O. Stern, A. Kuther, A. A. Gorbunov, A. Forchel, P. Hawrylak, S. Fafard, K. Hinzer, T. L. Reinecke, S. N. Walck, J. P. Reithmaier, F. Klopf, and F. Schäfer, *Fine structure of neutral and charged excitons in self-assembled in(ga)as/(al)gaas quantum dots*, Phys. Rev. B **65** (2002), no. 19, 195315.

[BP74] G. L. Bir and G. E. Pikus, *Symmetry and strain induced effects in semiconductors*, Wiley, 1974.

[BS98] I. N. Bronshtein and K. A. Semendyayev, *Handbook of mathematics*, Springer Berlin Heidelberg, 1998.

[BS08] S. C. Brenner and L. R. Scott, *The mathematical theory of finite element methods*, Texts in Applied Mathematics, vol. 15, Springer Science+Business Media, LLC, 2008.

[BSO+11] R. Brunner, Y.-S. Shin, T. Obata, M. Pioro-Ladrière, T. Kubo, K. Yoshida, T. Taniyama, Y. Tokura, and S. Tarucha, *Two-qubit gate of combined single-spin rotation and interdot spin exchange in a double quantum dot*, Phys. Rev. Lett. **107** (2011), 146801.

[BSV68] G. Birkhoff, M. Schultz, and R. Varga, *Piecewise hermite interpolation in one and two variables with applications to partial differential equations*, Numerische Mathematik **11** (1968), 232–256, 10.1007/BF02161845.

[BSW36] L. P. Bouckaert, R. Smoluchowski, and E. Wigner, *Theory of brillouin zones and symmetry properties of wave functions in crystals*, Phys. Rev. **50** (1936), 58–67.

[Bur92] M. G. Burt, *The justification for applying the effective-mass approximation to microstructures*, Journal of Physics: Condensed Matter **4** (1992), no. 32, 6651.

[Bur94] M. G. Burt, *Direct derivation of effective-mass equations for microstructures with atomically abrupt boundaries*, Phys. Rev. B **50** (1994), no. 11, 7518–7525.

[Bur98] ———, *Resolution of the out-of-zone solution problem in envelope-function theory*, Superlattices and Microstructures **23** (1998), no. 2, 531 – 534.

[Bur99] M. G. Burt, *Fundamentals of envelope function theory for electronic states and photonic modes in nanostructures*, Journal of Physics: Condensed Matter **11** (1999), no. 9, 53.

[BVK+02] D. M. Bruls, J. W. A. M. Vugs, P. M. Koenraad, H. W. M. Salemink, J. H. Wolter, M. Hopkinson, M. S. Skolnick, Fei Long, and S. P. A. Gill, *Determination of the shape and indium distribution of low-growth-rate inas quantum dots by cross-sectional scanning tunneling microscopy*, Journal of Applied Physics **81** (2002), no. 9, 1708–1710.

[BWPB11] A. Beya-Wakata, P.-Y. Prodhomme, and G. Bester, *First- and second-order piezoelectricity in iii-v semiconductors*, Phys. Rev. B **84** (2011), 195207.

[BWVZ06] G. Bester, X. Wu, D. Vanderbilt, and A. Zunger, *Importance of second-order piezoelectric effects in zinc-blende semiconductors*, Phys. Rev. Lett. **96** (2006), no. 18, 187602.

[BZ05] G. Bester and A. Zunger, *Cylindrically shaped zinc-blende semiconductor quantum dots do not have cylindrical symmetry: Atomistic symmetry, atomic relaxation, and piezoelectric effects*, Phys. Rev. B **71** (2005), no. 4, 045318.

[BZWV06] G. Bester, A. Zunger, X. Wu, and D. Vanderbilt, *Effects of linear and nonlinear piezoelectricity on the electronic properties of inas?gaas quantum dots*, Phys. Rev. B **74** (2006), no. 8, 081305.

[CC73] D. J. Chadi and Marvin L. Cohen, *Electronic structure of* $\mathrm{hg}_{1-x}\mathrm{cd}_x\mathrm{Te}$ *alloys and charge-density calculations using representative k points*, Phys. Rev. B **7** (1973), 692–699.

[CCF88] M. Cardona, N. E. Christensen, and G. Fasol, *Relativistic band structure and spin-orbit splitting of zinc-blende-type semiconductors*, Phys. Rev. B **38** (1988), no. 3, 1806–1827.

[CDG+10] J. M. Chow, L. DiCarlo, J. M. Gambetta, F. Motzoi, L. Frunzio, S. M. Girvin, and R. J. Schoelkopf, *Optimized driving of superconducting artificial atoms for improved single-qubit gates*, Phys. Rev. A **82** (2010), 040305.

[Chu95] S. L. Chuang, *Physics of optoelectronic devices*, John Wiley & Sons Inc., New York, 1995.

[CR72] P. G. Ciarlet and P. A. Raviart, *General lagrange and hermite interpolation in* r^n *with applications to finite element methods*, Archive for Rational Mechanics and Analysis **46** (1972), 177–199, 10.1007/BF00252458.

[CTM03] X. Cartoixà, D. Z.-Y. Ting, and T. C. McGill, *Numerical spurious solutions in the effective mass approximation*, Journal of Applied Physics **93** (2003), no. 7, 3974–3981.

[CZS+06] B. A. Carpenter, E. A. Zibik, M. L. Sadowski, L. R. Wilson, D. M. Whittaker, J. W. Cockburn, M. S. Skolnick, M. Potemski, M. J. Steer, and M. Hopkinson, *Intraband magnetospectroscopy of singly and doubly charged n -type self-assembled quantum dots*, Phys. Rev. B **74** (2006), no. 16, 161302.

[Dav98a] J. H. Davies, *Elastic and piezoelectric fields around a buried quantum dot: A simple picture*, Journal of Applied Physics **84** (1998), no. 3, 1358–1365.

[Dav98b] ———, *The physics of low-dimensional semiconductors: an introduction*, Cambridge University Press, New York, 1998.

[DFO97] J. R. Downes, D. A. Faux, and E. P. O'Reilly, *A simple method for calculating strain distributions in quantum dot structures*, Journal of Applied Physics **81** (1997), no. 10, 6700–6702.

[dGBR89] S. de Gironcoli, S. Baroni, and R. Resta, *Piezoelectric properties of iii-v semiconductors from first-principles linear-response theory*, Phys. Rev. Lett. **62** (1989), no. 24, 2853–2856.

[DKK55] G. Dresselhaus, A. F. Kip, and C. Kittel, *Cyclotron resonance of electrons and holes in silicon and germanium crystals*, Phys. Rev. **98** (1955), 368–384.

[DKW88] M. Dobers, K. v. Klitzing, and G. Weimann, *Electron-spin resonance in the two-dimensional electron gas of gaas-al$_x$ga$_{1-x}$as heterostructures*, Phys. Rev. B **38** (1988), no. 8, 5453–5456.

[DMG+09] L. DiCarlo, Chow J. M., J. M. Gambetta, Lev S. Bishop, B. R. Johnson, D. I. Schuster, J. Majer, A. Blais, L. Frunzio, S. M. Girvin, and R. J. Schoelkopf, *Demonstration of two-qubit algorithms with a superconducting quantum processor*, Nature **460** (2009), 240–244.

[DRS+10] L. DiCarlo, M. D. Reed, L. Sun, B. R. Johnson, J. M. Chow, J. M. Gambetta, L. Frunzio, S. M. Girvin, M. H. Devoret, and R. J. Schoelkopf, *Preparation and measurement of three-qubit entanglement in a superconducting circuit*, Nature **467** (2010), 574578.

[DSP+06] M. F. Doty, M. Scheibner, I. V. Ponomarev, E. A. Stinaff, A. S. Bracker, V. L. Korenev, T. L. Reinecke, and D. Gammon, *Electrically tunable g factors in quantum dot molecular spin states*, Phys. Rev. Lett. **97** (2006), 197202.

[Eis08] T. Eissfeller, *Linear optical response of semiconductor nanodevices*, Master's thesis, Walter-Schottky-Institut and Physics Department, Technische Universität München, 2008.

[ESC87] R. Eppenga, M. F. H. Schuurmans, and S. Colak, *New $k \cdot p$ theory for gaas/ga$_{1-x}$al$_x$as-type quantum wells*, Phys. Rev. B **36** (1987), no. 3, 1554–1564.

[Fey39] R. P. Feynman, *Forces in molecules*, Phys. Rev. **56** (1939), 340–343.

[FIM+00] P. W. Fry, I. E. Itskevich, D. J. Mowbray, M. S. Skolnick, J. J. Finley, J. A. Barker, E. P. O'Reilly, L. R. Wilson, I. A. Larkin, P. A. Maksym, M. Hopkinson, M. Al-Khafaji, J. P. R. David, A. G. Cullis, G. Hill, and J. C. Clark, *Inverted electron-hole alignment in inas-gaas self-assembled quantum dots*, Phys. Rev. Lett. **84** (2000), 733–736.

[For93] B. A. Foreman, *Effective-mass hamiltonian and boundary conditions for the valence bands of semiconductor microstructures*, Phys. Rev. B **48** (1993), no. 7, 4964–4967.

[For95] ———, *Exact effective-mass theory for heterostructures*, Phys. Rev. B **52** (1995), no. 16, 12241–12259.

[For96] ———, *Envelope-function formalism for electrons in abrupt heterostructures with material-dependent basis functions*, Phys. Rev. B **54** (1996), no. 3, 1909–1921.

[For97] ———, *Elimination of spurious solutions from eight-band $k\cdot p$ theory*, Phys. Rev. B **56** (1997), no. 20, R12748–R12751.

[For98] ———, *Connection rules versus differential equations for envelope functions in abrupt heterostructures*, Phys. Rev. Lett. **80** (1998), no. 17, 3823–3826.

[For00] Bradley A Foreman, *Theory of the effective hamiltonian for degenerate bands in an electric field*, Journal of Physics: Condensed Matter **12** (2000), no. 34, R435.

[For07] B. A. Foreman, *Choosing a basis that eliminates spurious solutions in $k \cdot p$ theory*, Phys. Rev. B **75** (2007), no. 23, 235331.

[FWA+99] S. Fafard, Z. R. Wasilewski, C. Ni. Allen, D. Picard, M. Spanner, J. P. McCaffrey, and P. G. Piva, *Manipulating the energy levels of semiconductor quantum dots*, Phys. Rev. B **59** (1999), 15368–15373.

[GBM+04] R. Gordon, A. G. Brolo, A. McKinnon, A. Rajora, B. Leathem, and K. L. Kavanagh, *Strong polarization in the optical transmission through elliptical nanohole arrays*, Phys. Rev. Lett. **92** (2004), 037401.

[GGL+98] B. Gayral, J. M. Gérard, B. Legrand, E. Costard, and V. Thierry-Mieg, *Optical study of gaas/alas pillar microcavities with elliptical cross section*, Applied Physics Letters **72** (1998), no. 12, 1421–1423.

[GKB10] O. Gywat, H. J. Krenner, and J. Berezovsky, *Spins in optically active quantum dots: Concepts and methods*, Wiley-VCH, 2010.

[GLY+10] Wei-Bo Gao, Chao-Yang Lu, Xing-Can Yao, Ping Xu, Otfried Gühne, Alexander Goebel, Yu-Ao Chen, Cheng-Zhi Peng, Zeng-Bing Chen, and Jian-Wei Pan, *Experimental demonstration of a hyper-entangled ten-qubit schrdinger cat state*, Nature Physics **6** (2010), 331 – 335.

[GM96] M. J. Godfrey and A. M. Malik, *Boundary conditions and spurious solutions in envelope-function theory*, Phys. Rev. B **53** (1996), no. 24, 16504–16509.

[GU98] M. Governale and C. Ungarelli, *Gauge-invariant grid discretization of the schrödinger equation*, Phys. Rev. B **58** (1998), no. 12, 7816–7821.

[GV95] M. Graf and P. Vogl, *Electromagnetic fields and dielectric response in empirical tight-binding theory*, Phys. Rev. B **51** (1995), no. 8, 4940–4949.

[HH03a] C. Heyn and W. Hansen, *Desorption of inas quantum dots*, Journal of Crystal Growth **251** (2003), 218.

[HH03b] ———, *Ga/in-intermixing and segregation during inas quantum dot formation*, Journal of Crystal Growth **251** (2003), no. 1-4, 140 – 144.

[HHR+05] H. Häffner, W. Hänsel, C. F. Roos, J. Benhelm, D. Chek-al kar, M. Chwalla, T. Körber, U. D. Rapol, M. Riebe, P. O. Schmidt, C. Becher, O. Gühne, W. Dür, and R. Blatt, *Scalable multiparticle entanglement of trapped ions*, Nature **438** (2005), 643–646.

[HKP+07] R. Hanson, L. P. Kouwenhoven, J. R. Petta, S. Tarucha, and L. M. K. Vandersypen, *Spins in few-electron quantum dots*, Rev. Mod. Phys. **79** (2007), 1217–1265.

[HSH+07] D. Heiss, S. Schaeck, H. Huebl, M. Bichler, G. Abstreiter, J. J. Finley, D. V. Bulaev, and D. Loss, *Observation of extremely slow hole spin relaxation in self-assembled quantum dots*, Phys. Rev. B **76** (2007), 241306.

[HW10] J. S. Hesthaven and T. Warburton, *Nodal discontinuous galerkin methods: Algorithms, analysis, and applications (texts in applied mathematics)*, vol. 54, Springer Science+Business Media, LLC, 2010.

[IP97] E. L. Ivchenko and G. E. Pikus, *Superlattices and other heterostructures: symmetry and optical phenomena*, vol. 110, Springer Verlag, 1997.

[JEK+11] V. Jovanov, T. Eissfeller, S. Kapfinger, E. C. Clark, F. Klotz, M. Bichler, J. G. Keizer, P. M. Koenraad, G. Abstreiter, and J. J. Finley,

Observation and explanation of strong electrically tunable exciton g factors in composition engineered in(ga)as quantum dots, Phys. Rev. B **83** (2011), no. 16, 161303.

[JEK+12] V. Jovanov, T. Eissfeller, S. Kapfinger, E. C. Clark, F. Klotz, M. Bichler, J. G. Keizer, P. M. Koenraad, M. S. Brandt, G. Abstreiter, and J. J. Finley, *Highly nonlinear excitonic zeeman spin splitting in composition-engineered artificial atoms*, Phys. Rev. B **85** (2012), 165433.

[JKBJ01] P. B. Joyce, T. J. Krzyzewski, G. R. Bell, and T. S. Jones, *Surface morphology evolution during the overgrowth of large inas/gaas quantum dots*, Applied Physics Letters **79** (2001), no. 22, 3615–3617.

[JSBB98] J.-M. Jancu, R. Scholz, F. Beltram, and F. Bassani, *Empirical spds∗ tight-binding calculation for cubic semiconductors: General method and material parameters*, Phys. Rev. B **57** (1998), no. 11, 6493–6507.

[JSdAeSLR05] J.-M. Jancu, R. Scholz, E. A. de Andrada e Silva, and G. C. La Rocca, *Atomistic spin-orbit coupling and $k \cdot p$ parameters in iii-v semiconductors*, Phys. Rev. B **72** (2005), no. 19, 193201.

[Kan57] E. O. Kane, *Band structure of indium antimonide*, Journal of Physics and Chemistry of Solids **1** (1957), no. 4, 249 – 261.

[KBT+06] F. H. L. Koppens, C. Buizert, K. J. Tielrooij, I. T. Vink, K. C. Nowack, T. Meunier, L. P. Kouwenhoven, and L. M. K. Vandersypen, *Driven coherent oscillations of a single electron spin in a quantum dot*, Nature **442** (2006), no. 7104, 766–771.

[KCB+10] J. G. Keizer, E. C. Clark, M. Bichler, G. Abstreiter, J. J. Finley, and P. M. Koenraad, *An atomically resolved study of ingaas quantum dot layers grown with an indium flush step*, Nanotechnology **21** (2010), no. 21, 215705.

[KDH+04] M. Kroutvar, Y. Ducommun, D. Heiss, M. Bichler, D. Schuh, G. Abstreiter, and J. J. Finley, *Optically programmable electron spin memory using semiconductor quantum dots*, Nature **432** (2004), 81–84.

[KDWS63] G. F. Koster, J. O. Dimmock, R. G. Wheeler, and H. Statz, *The properties of the thirty-two point groups*, MIT Press, 1963.

[KIR98] A. A. Kiselev, E. L. Ivchenko, and U. Rössler, *Electron g factor in one- and zero-dimensional semiconductor nanostructures*, Phys. Rev. B **58** (1998), no. 24, 16353–16359.

[KJK+10] F. Klotz, V. Jovanov, J. Kierig, E. C. Clark, D. Rudolph, D. Heiss, M. Bichler, G. Abstreiter, M. S. Brandt, and J. J. Finley, *Observation of an electrically tunable exciton g factor in ingaas/gaas quantum dots*, Applied Physics Letters **96** (2010), no. 5, 053113.

[KK99] G. Karypis and V. Kumar, *A fast and high quality multilevel scheme for partitioning irregular graphs*, SIAM Journal on Scientific Computing **20** (1999), no. 1, 359 – 392.

[KKO+06] V. Křápek, K. Kuldová, J. Oswald, A. Hospodková, E. Hulicius, and J. Humlíček, *Elongation of inas/gaas quantum dots from magnetophotoluminescence measurements*, Applied Physics Letters **89** (2006), no. 15, 153108.

[KKY01] A. A. Kiselev, K. W. Kim, and E. Yablonovitch, *In-plane light-hole g factor in strained cubic heterostructures*, Phys. Rev. B **64** (2001), no. 12, 125303.

[KLN03] K. I. Kolokolov, J. Li, and C. Z. Ning, *$k \cdot p$ hamiltonian without spurious-state solutions*, Phys. Rev. B **68** (2003), no. 16, 161308.

[KN00] A. V. Khaetskii and Y. V. Nazarov, *Spin relaxation in semiconductor quantum dots*, Phys. Rev. B **61** (2000), 12639–12642.

[KRBF01] R. Kotlyar, T. L. Reinecke, M. Bayer, and A. Forchel, *Zeeman spin splittings in semiconductor nanostructures*, Phys. Rev. B **63** (2001), 085310.

[KSP+09] D. Kim, W. Sheng, P. J. Poole, D. Dalacu, J. Lefebvre, J. Lapointe, M. E. Reimer, G. C. Aers, and R. L. Williams, *Tuning the exciton g factor in single inas/inp quantum dots*, Phys. Rev. B **79** (2009), 045310.

[KWB+08] M. Kroner, K. M. Weiss, B. Biedermann, S. Seidl, S. Manus, A. W. Holleitner, A. Badolato, P. M. Petroff, B. D. Gerardot, R. J. Warburton, and K. Karrai, *Optical detection of single-electron spin resonance in a quantum dot*, Phys. Rev. Lett. **100** (2008), 156803.

[L̈51] P.-O. Löwdin, *A note on the quantum-mechanical perturbation theory*, The Journal of Chemical Physics **19** (1951), no. 11, 1396–1401.

[Law71] P. Lawaetz, *Valence-band parameters in cubic semiconductors*, Phys. Rev. B **4** (1971), 3460–3467.

[LB70] N. O. Lipari and A. Baldereschi, *Angular momentum theory and localized states in solids. investigation of shallow acceptor states in semiconductors*, Phys. Rev. Lett. **25** (1970), 1660–1664.

[LBMM07] Y. Léger, L. Besombes, L. Maingault, and H. Mariette, *Valence-band mixing in neutral, charged, and mn-doped self-assembled quantum dots*, Phys. Rev. B **76** (2007), 045331.

[LCY98] R. B. Lehoucq, Sorensen D. C., and C. Yang, *Arpack users' guide: solution of large-scale eigenvalue problems with implicitly restarted arnoldi methods.*, SIAM, 1998.

[LK55] J. M. Luttinger and W. Kohn, *Motion of electrons and holes in perturbed periodic fields*, Phys. Rev. **97** (1955), no. 4, 869–883.

[LL91] L. D. Landau and E. M. Lifschitz, *Lehrbuch der theoretischen physik: Elastizitttstheorie*, vol. 7, Akademie Verlag GmbH, Berlin, 1991.

[LMR85] G. Lommer, F. Malcher, and U. Rössler, *Reduced g factor of subband landau levels in algaas/gaas heterostructures*, Phys. Rev. B **32** (1985), 6965–6967.

[Lut51] J. M. Luttinger, *The effect of a magnetic field on electrons in a periodic potential*, Phys. Rev. **84** (1951), no. 4, 814–817.

[Lut56] ———, *Quantum theory of cyclotron resonance in semiconductors: General theory*, Phys. Rev. **102** (1956), 1030–1041.

[Mad96] O. Madelung, *Semiconductors - basic data*, Springer Verlag Berlin, 1996.

[Mar72] R. M. Martin, *Piezoelectricity*, Phys. Rev. B **5** (1972), 1607–1613.

[MCFJ02] M. A. Migliorato, A. G. Cullis, M. Fearn, and J. H. Jefferson, *Atomistic simulation of strain relaxation in $in_xga_{1-x}as$/gaas quantum dots with nonuniform composition*, Phys. Rev. B **65** (2002), no. 11, 115316.

[MGO94] A. T. Meney, B. Gonul, and E. P. O'Reilly, *Evaluation of various approximations used in the envelope-function method*, Phys. Rev. B **50** (1994), no. 15, 10893–10904.

[MR91] H. Mayer and U. Rössler, *Spin splitting and anisotropy of cyclotron resonance in the conduction band of gaas*, Phys. Rev. B **44** (1991), 9048–9051.

[MSH82] O. Madelung, M. Schulz, and Weiss H. (eds.), *Landolt-börnstein: Zahlenwerte und funktionen aus naturwissenschaften und technik*, vol. 17a, Springer Berlin, Heidelberg, New York, 1982.

[NMR+08] P. Neumann, N. Mizuochi, F. Rempp, P. Hemmer, H. Watanabe, S. Yamasaki, V. Jacques, T. Gaebel, F. Jelezko, and J. Wrachtrup, *Multipartite entanglement among single spins in diamond*, Science **320** (2008), no. 5881, 1326–1329.

[NST+05] T. Nakaoka, T. Saito, J. Tatebayashi, S. Hirose, T. Usuki, N. Yokoyama, and Y. Arakawa, *Tuning of g-factor in self-assembled in(ga)as quantum dots through strain engineering*, Phys. Rev. B **71** (2005), 205301.

[NSTA04] T. Nakaoka, T. Saito, J. Tatebayashi, and Y. Arakawa, *Size, shape, and strain dependence of the g factor in self-assembled in(ga)as quantum dots*, Phys. Rev. B **70** (2004), 235337.

[NTA07] T. Nakaoka, S. Tarucha, and Y. Arakawa, *Electrical tuning of the g factor of single self-assembled quantum dots*, Phys. Rev. B **76** (2007), 041301.

[Nye85] J. F. Nye, *Physical properties of crystals: Their representation by tensors and matrices*, Oxford University Press, 1985.

[OKW+05] P. Offermans, P. M. Koenraad, J. H. Wolter, K. Pierz, M. Roy, and P. A. Maksym, *Atomic-scale structure and photoluminescence of inas quantum dots in gaas and alas*, Phys. Rev. B **72** (2005), no. 16, 165332.

[PB66] C. R. Pidgeon and R. N. Brown, *Interband magneto-absorption and faraday rotation in insb*, Phys. Rev. **146** (1966), 575–583.

[PF06] C. E. Pryor and M. E. Flatté, *Landé g factors and orbital momentum quenching in semiconductor quantum dots*, Phys. Rev. Lett. **96** (2006), no. 2, 026804.

[PLF+07] T. Passow, S. Li, P. Feinäugle, T. Vallaitis, J. Leuthold, D. Litvinov, D. Gerthsen, and M. Hetterich, *Systematic investigation into the influence of growth conditions on inas/gaas quantum dot properties*, Journal of Applied Physics **102** (2007), no. 7, 073511.

[Pol09] E. Polizzi, *Density-matrix-based algorithm for solving eigenvalue problems*, Phys. Rev. B **79** (2009), 115112.

[PPF08] J. Pingenot, C. E. Pryor, and M. E. Flatté, *Method for full bloch sphere control of a localized spin via a single electrical gate*, Applied Physics Letters **92** (2008), no. 22, 222502.

[PPF11] J. Pingenot, C. E. Pryor, and M. E. Flatté, *Electric-field manipulation of the landé g tensor of a hole in an $in_{0.5}ga_{0.5}as$/gaas self-assembled quantum dot*, Phys. Rev. B **84** (2011), 195403.

[PTVF07] W. H. Press, S. A. Teukolsky, W. T. Vetterling, and B. P. Flannery, *Numerical recipes 3rd edition: The art of scientific computing*, Cambridge University Press, 2007.

[PZ96] P. Pfeffer and W. Zawadzki, *Five-level $k \cdot p$ model for the conduction and valence bands of gaas and inp*, Phys. Rev. B **53** (1996), no. 19, 12813–12828.

[RAE+02] A. V. Rodina, A. Yu. Alekseev, Al. L. Efros, M. Rosen, and B. K. Meyer, *General boundary conditions for the envelope function in the multiband $k \cdot p$ model*, Phys. Rev. B **65** (2002), no. 12, 125302.

[REVP10] R. Roloff, T. Eissfeller, P. Vogl, and W. Pötz, *Electric g-tensor control and spin echo of a hole-spin qubit in a quantum dot molecule*, New Journal of Physics **12** (2010), no. 9, 093012.

[RLZ59] L. M. Roth, B. Lax, and S. Zwerdling, *Theory of optical magneto-absorption effects in semiconductors*, Phys. Rev. **114** (1959), 90–104.

[Saa92] Y. Saad, *Numerical methods for large eigenvalue problems*, Manchester University Press, 1992.

[Saa00] ———, *Iterative methods for sparse linear systems*, 2000.

[SBL+02] S. Sauvage, P. Boucaud, R. P. S. M. Lobo, F. Bras, G. Fishman, R. Prazeres, F. Glotin, J. M. Ortega, and J.-M. Gérard, *Long polaron lifetime in inas/gaas self-assembled quantum dots*, Phys. Rev. Lett. **88** (2002), 177402.

[SBM+92] M. J. Snelling, E. Blackwood, C. J. McDonagh, R. T. Harley, and C. T. B. Foxon, *Exciton, heavy-hole, and electron g factors in type-i gaas/$\mathrm{al}_x\mathrm{ga}_{1-x}$as quantum wells*, Phys. Rev. B **45** (1992), 3922–3925.

[SBR08] O. Schenk, M. Bollhöfer, and R. A. Römer, *On large-scale diagonalization techniques for the anderson model of localization*, SIAM REVIEW **50** (2008), no. 1, 91 – 112.

[Sch] A. Schliwa, *Private communication.*

[SGB99] O. Stier, M. Grundmann, and D. Bimberg, *Electronic and optical properties of strained quantum dots modeled by 8-band $k \cdot p$ theory*, Phys. Rev. B **59** (1999), no. 8, 5688–5701.

[SH74] K. Suzuki and J. C. Hensel, *Quantum resonances in the valence bands of germanium. i. theoretical considerations*, Phys. Rev. B **9** (1974), no. 10, 4184–4218.

[SHB+03] M. Sabathil, S. Hackenbuchner, S. Birner, J. A. Majewski, P. Vogl, and J. J. Finley, *Theory of vertical and lateral stark shifts of excitons in quantum dots*, physica status solidi (c) **0** (2003), no. 4, 1181–1184.

[SKE+01] G. Salis, Y. Kato, K. Ensslin, D. C. Driscoll, A. C. Gossard, and D. D. Awschalom, *Electrical control of spin coherence in semiconductor nanostructures*, Nature **414** (2001), no. 6864, 619–622.

[SKHG+03] F. Schmidt-Kaler, H. Häffner, S. Gulde, M. Riebe, G. P. T. Lancaster, T. Deuschle, C. Becher, W. Hänsel, J. Eschner, C. F. Roos, and R. Blatt, *How to realize a universal quantum gate with trapped ions*, Appl. Phys. B **77** (2003), 789796.

[SM86] D. L. Smith and C. Mailhiot, *$k\cdot p$ theory of semiconductor superlattice electronic structure. i. formal results*, Phys. Rev. B **33** (1986), no. 12, 8345–8359.

[StH85] M. F. H. Schuurmans and G. W. 't Hooft, *Simple calculations of confinement states in a quantum well*, Phys. Rev. B **31** (1985), no. 12, 8041–8048.

[SUG+11] G. Sallen, B. Urbaszek, M. M. Glazov, E. L. Ivchenko, T. Kuroda, T. Mano, S. Kunz, M. Abbarchi, K. Sakoda, D. Lagarde, A. Balocchi, X. Marie, and T. Amand, *Dark-bright mixing of interband transitions in symmetric semiconductor quantum dots*, Phys. Rev. Lett. **107** (2011), 166604.

[SVdV00] G. L. G. Sleijpen and H. A. Van der Vorst, *A jacobi-davidson iteration method for linear eigenvalue problems*, SIAM Review **42** (2000), no. 2, 267–293.

[SWB07] A. Schliwa, M. Winkelnkemper, and D. Bimberg, *Impact of size, shape, and composition on piezoelectric effects and electronic properties of in(ga)as/gaas quantum dots*, Phys. Rev. B **76** (2007), no. 20, 205324.

[Szm96] F. Szmulowicz, *Numerically stable hermitian secular equation for the envelope-function approximation for superlattices*, Phys. Rev. B **54** (1996), no. 16, 11539–11547.

[THW95] N. J. Traynor, R. T. Harley, and R. J. Warburton, *Zeeman splitting and g factor of heavy-hole excitons in* $\mathrm{in}_x\mathrm{ga}_{1-x}$*as/gaas quantum wells*, Phys. Rev. B **51** (1995), 7361–7364.

[TRR79] H.-R. Trebin, U. Rössler, and R. Ranvaud, *Quantum resonances in the valence bands of zinc-blende semiconductors. i. theoretical aspects*, Phys. Rev. B **20** (1979), no. 2, 686–700.

[TV11] S. Tomić and N. Vukmirović, *Symmetry reduction in multiband hamiltonians for semiconductor quantum dots: The role of interfaces and higher energy bands*, Journal of Applied Physics **110** (2011), no. 5, 053710.

[Var67] Y. P. Varshni, *Temperature dependence of the energy gap in semiconductors*, Physica **34** (1967), no. 1, 149 – 154.

[vBSK+11] J. van Bree, A. Y. Silov, P. M. Koenraad, M. E. Flatté, and C. E. Pryor, *g-Factors and diamagnetic coefficients of electrons, holes and excitons in InAs/InP quantum dots*, ArXiv e-prints (2011).

[VdW89] C. G. Van de Walle, *Band lineups and deformation potentials in the model-solid theory*, Phys. Rev. B **39** (1989), no. 3, 1871–1883.

[VMRM01] I. Vurgaftman, J. R. Meyer, and L. R. Ram-Mohan, *Band parameters for iii–v compound semiconductors and their alloys*, Journal of Applied Physics **89** (2001), no. 11, 5815–5875.

[VSW07] R. G. Veprek, S. Steiger, and B. Witzigmann, *Ellipticity and the spurious solution problem of $k \cdot p$ envelope equations*, Phys. Rev. B **76** (2007), no. 16, 165320.

[vWAK+09] M. H. M. van Weert, N. Akopian, F. Kelkensberg, U. Perinetti, M. P. van Kouwen, J. G. Rivas, M. T. Borgström, R. E. Algra, M. A. Verheijen, E. P. A. M. Bakkers, L. P. Kouwenhoven, and V. Zwiller, *Orientation-dependent optical-polarization properties of single quantum dots in nanowires*, Small **5** (2009), no. 19, 2134–2138.

[Win03] R. Winkler, *Spin-orbit coupling effects in two-dimensional electron and hole systems*, Springer Tracts in Modern Physics, vol. 191, Springer Berlin / Heidelberg, 2003.

[WNS+93] R. J. Warburton, R. J. Nicholas, S. Sasaki, N. Miura, and K. Woodbridge, *Superlattice modification of the valence-band spin splitting in* $\mathrm{in}_x\mathrm{ga}_{1-x}$*as/gaas superlattices up to 45 t*, Phys. Rev. B **48** (1993), 12323–12325.

[WR93] R. Winkler and U. Rössler, *General approach to the envelope-function approximation based on a quadrature method*, Phys. Rev. B **48** (1993), no. 12, 8918–8927.

[WS81] S. R. White and L. J. Sham, *Electronic properties of flat-band semiconductor heterostructures*, Phys. Rev. Lett. **47** (1981), no. 12, 879–882.

[WWZ+00] L. W. Wang, A. J. Williamson, A. Zunger, H. Jiang, and J. Singh, *Comparison of the* $\mathbf{k} \cdot \mathbf{p}$ *and direct diagonalization approaches to the electronic structure of inas/gaas quantum dots*, Applied Physics Letters **76** (2000), no. 3, 339–341.

[WXW06] H.-B. Wu, S. J. Xu, and J. Wang, *Impact of the cap layer on the electronic structures and optical properties of self-assembled inas/gaas quantum dots*, Phys. Rev. B **74** (2006), 205329.

[WZ98] S.-H. Wei and A. Zunger, *Calculated natural band offsets of all ii–vi and iii–v semiconductors: Chemical trends and the role of cation d orbitals*, Applied Physics Letters **72** (1998), no. 16, 2011–2013.

[WZ99] ———, *Predicted band-gap pressure coefficients of all diamond and zinc-blende semiconductors: Chemical trends*, Phys. Rev. B **60** (1999), no. 8, 5404–5411.

[ZWG+04] E. A. Zibik, L. R. Wilson, R. P. Green, G. Bastard, R. Ferreira, P. J. Phillips, D. A. Carder, J-P. R. Wells, J. W. Cockburn, M. S. Skolnick, M. J. Steer, and M. Hopkinson, *Intraband relaxation via polaron decay in inas self-assembled quantum dots*, Phys. Rev. B **70** (2004), 161305.

In der Schriftenreihe des Walter Schottky Instituts der Technischen Universität München sind bisher folgende Bände erschienen:

Vol. 1
Cornelia Engel
Si/SiGe basierende Phototransistoren
131 Seiten
ISBN 3-932749-01-4

Vol. 2
Peter Schittenhelm
Selbst-Organisation und Selbst-Ordnung in Si/SiGe-Heterostrukturen
151 Seiten
ISBN 3-932749-02-2

Vol. 3
Andreas Nutsch
Selektive Epitaxie von (GaIn)(AsP) Schichtstrukturen
129 Seiten
ISBN 3-932749-03-0

Vol. 4
Peter Baumgartner
Optische und elektronische Eigenschaften lasergeschriebener GaAs-Nanostrukturen
180 Seiten
ISBN 3-932749-04-9

Vol. 5
Walter Franz Rieger
Untersuchung der elektronischen und strukturellen Eigenschaften von GaNAlN und deren Legierungen
158 Seiten
ISBN 3-932749-05-7

Vol. 6
Markus Hauser
Oberflächenemittierende Laserdioden mit Mehrfachepitaxie
148 Seiten
ISBN 3-932749-06-5

Vol. 7
Markus Sexl
Verspannte und gitterrelaxierte In(GaAl)As Heterostrukturen
144 Seiten
ISBN 3-932749-07-3

Vol. 8
Christian Obermüller
Photolumineszenszspektroskopie mit optischen Nahfeldmethoden an GaAs-Nanostrukturen
140 Seiten
ISBN 3-932749-08-1

Vol. 9
Edilson Silveira
Inelastische Lichtstreuung an niedrig-dimensionalen Halbleiterstrukturen
104 Seiten
ISBN 3-932749-09-X

Vol. 10
Eberhard Christian Rohrer
Photoleitungs-Spektroskopie von Diamant
153 Seiten
ISBN 3-932749-10-03

Vol. 11
Thomas Wimbauer
Magnetische Resonanz-Untersuchungen an modernen Halbleitermaterialien
125 Seiten
ISBN 3-932749-11-1

Vol. 12
Herbert Verhoeven
Thermische Eigenschaften von CVD-Diamantschichten
154 Seiten
ISBN 3-932749-12-X

Vol. 13
Hans-Christoph Ostendorf
Trennung von Volumen- und Oberflächenrekombination in Silizium
128 Seiten
ISBN 3-932749-13-8

Vol. 14
Martin Städele
Dichtefunktionaltheorie mit exaktem Austausch für Halbleiter
202 Seiten
ISBN 3-932749-14-6

Vol. 15
Helmut Angerer
Herstellung von Gruppe III-Nitriden mit Molekularstrahlepitaxie
144 Seiten
ISBN 3-932749-15-4

Vol. 16
Wolfgang Heller
Spektroskopie einzelner Quantenpunkte in magnetischen und elektrischen Feldern
128 Seiten
ISBN 3-932749-16-2

Vol. 17
Molela Moukara
Pseudopotentiale mit exaktem Austausch
117 Seiten
ISBN 3-932749-17-0

Vol. 18
Ralph Oberhuber
Elektronische Struktur und Transport in verspannten Halbleiterschichtsystemen
110 Seiten
ISBN 3-932749-18-9

Vol. 19
Reiner Pech
High-Energy Boron-Implantation into Different Silicon Substrates
158 Seiten
ISBN 3-932749-19-7

Vol. 20
Christoph Martin Engelhardt
Zyklotronresonanz zweidimensionaler Ladungsträgersysteme in Halbleitern, Effekte der Elektron-Elektron-Wechselwirkung und Lokalisierung
317 Seiten
ISBN 3-932749-20-0

Vol. 21
Eduard Neufeld
Erbium-dotierte Si/SiGe-Lichtemitter und -Wellenleiter
136 Seiten
ISBN 3-932749-21-9

Vol. 22
Gert Schedelbeck
Optische Eigenschaften von Halbleiternanostrukturen hergestellt durch Überwachsen von Spaltflächen
154 Seiten
ISBN 3-932749-22-7

Vol. 23
Jürgen Zimmer
Optoelektronisches Verhalten von Dünnschichtbauelementen aus amorphem und mikrokristallinem Silizium
171 Seiten
ISBN 3-932749-23-5

Vol. 24
Berthold Schmidt
Leistungsoptimierung abstimmbarer InGaAsP/InP Halbleiterlaser
85 Seiten
ISBN 3-932749-24-3

Vol. 25
Jianhong Zhu
Ordering of self-assembled Ge and SiGe nanostructures on vicinal Si surfaces
120 Seiten
ISBN 3-932749-25-1

Vol. 26
Gerhard Groos
Herstellung und Charakterisierung von Silizium-Nanostrukturen
168 Seiten
ISBN 3-932749-26-X

Vol. 27
Uwe Hansen
Theorie der Reaktionskinetik an Festkörperoberflächen
119 Seiten
ISBN 3-932749-27-8

Vol. 28
Roman Dimitrov
Herstellung und Charakterisierung von AlGaN/GaN-Transistoren
196 Seiten
ISBN 3-932749-28-6

Vol. 29
Martin Eickhoff
Piezowiderstandsmechanismen in Halbleitern mit großer Bandlücke
151 Seiten
ISBN 3-932749-29-4

Vol. 30
Nikolai Wieser
Ramanspektroskopie an Gruppe III-Nitriden
161 Seiten
ISBN 3-932749-30-8

Vol. 31
Rainer Janssen
Strukturelle und elektronische Eigenschaften amorpher Silizium-Suboxide
275 Seiten
ISBN 3-932749-31-6

Vol. 32
Martin W. Bayerl
Magnetic resonance investigations of group III-nitrides
155 Seiten
ISBN 3-932749-32-4

Vol. 33
Martin Rother
Elektronische Eigenschaften von Halbleiternanostrukturen hergestellt durch Überwachsen von Spaltflächen
196 Seiten
ISBN 3-932749-33-2

Vol. 34
Frank Findeis
Optical spectroscopy on single self-assembled quantum dots
156 Seiten
ISBN 3-932749-34-0

Vol. 35
Markus Ortsiefer
Langwellige Vertikalresonator-Laser-dioden im Materialsystem InGaAlAs/InP
152 Seiten
ISBN 3-932749-35-9

Vol. 36
Roland Zeisel
Optoelectronic properties of defects in diamond and AlGaN alloys
140 Seiten
ISBN 3-932749-36-7

Vol. 37
Liwen Chu
Inter- und Intraband Spektroskopie an selbstorganisierten In(Ga)As/GaAs Quantenpunkten
124 Seiten
ISBN 3-932749-37-5

Vol. 38
Christian Alexander Miesner
Intra-Valenzbandspektroskopie an SiGe-Nanostrukturen in Si
100 Seiten
ISBN 3-932749-38-3

Vol. 39
Szabolcs Kátai
Investigation of the nucleation process of chemical vapour deposited diamond films
178 Seiten
ISBN 3-932749-39-1

Vol. 40
Markus Arzberger
Wachstum, Eigenschaften und Anwendungen selbstorganisierter InAs-Quantenpunkte
236 Seiten
ISBN 3-932749-40-5

Vol. 41
Markus Oliver Markmann
Optische Eigenschaften von Erbium in $Si/Si_{1-x}C_x$, $Si/Si_{1-x}Ge_x$ und Si/SiO_x Heterostrukturen
182 Seiten
ISBN 3-932749-41-3

Vol. 42
Rainer Alexander Deutschmann
Two dimensional electron systems in atomically precise periodic potential
210 Seiten
ISBN 3-932749-42-1

Vol. 43
Uwe Karrer
Schottky-Dioden auf Galliumnitrid: Eigenschaften und Anwendungen in der Sensorik
182 Seiten
ISBN 3-932749-43-X

Vol. 44
Günther Anton Johann Vogg
Epitaxial thin films of Si and Ge based Zintl phases and sheet polymers
169 Seiten
ISBN 3-932749-44-8

Vol. 45
Christian Strahberger
Vertikaler Transport und extreme Magnetfelder in Halbleitern
167 Seiten
ISBN 3-932749-45-6

Vol. 46
Jan Schalwig
Feldeffekt-Gassensoren und ihre Anwendung in Abgasnachbehandlungssystemen
125 Seiten
ISBN 3-932749-46-4

Vol. 47
Christopher Eisele
Novel absorber structures for Si-based thin film solar cells
126 Seiten
ISBN 3-932749-47-2

Vol. 48
Stefan Hackenbuchner
Elektronische Struktur von Halbleiter-Nanobauelementen im thermodynamischen Nichtgleichgewicht
213 Seiten
ISBN 3-932749-48-0

Vol. 49
Andreas Sticht
Herstellung und Charakterisierung von dünnen Silizium/Siliziumoxid-Schichtsystemen
166 Seiten
ISBN 3-932749-49-9

Vol. 50
Giuseppe Scarpa
Design and fabrication of Quantum Cascade Lasers
193 Seiten
ISBN 3-932749-50-2

Vol. 51
Jörg Frankenberger
Optische Untersuchungen an zweidimensionalen Ladungsträgersystemen
158 Seiten
ISBN 3-932749-51-0

Vol. 52
Doris Heinrich
Wavelength selective optically induced charge storage in self-assembled semiconductor quantum dots
144 Seiten
ISBN 3-932749-52-9

Vol. 53
Nicolaus Ulbrich
Entwurf und Charakterisierung von Quanten-Kaskadenlasern und Quantenpunktkaskaden
133 Seiten
ISBN 3-932749-53-7

Vol. 54
Lutz Carsten Görgens
Analyse stickstoffhaltiger III-V Halbleiter-Heterosysteme mit hochenergetischen schweren Ionen
116 Seiten
ISBN 3-932749-54-5

Vol. 55
Andreas Janotta
Doping, light-induced modification and biocompatibility of amorphous silicon suboxides
180 Seiten
ISBN 3-932749-55-3

Vol. 56
Sebastian Tobias Benedikt Gönnenwein
Two-dimensional electron gases and ferromagnetic semiconductors: materials for spintronics
198 Seiten
ISBN 3-932749-56-1

Vol. 57
Evelin Beham
Photostromspektroskopie an einzelnen Quantenpunkten
186 Seiten
ISBN 3-932749-57-X

Vol. 58
Po-Wen Chiu
Towards carbon nanotube-based molecular electronics
116 Seiten
ISBN 3-932749-58-8

Vol. 59
Tobias Graf
Spin-spin interactions of localized electronic states in semiconductors
194 Seiten
ISBN 3-932749-59-6

Vol. 60
Stefan Klein
Microcrystalline silicon prepared by hot wire CVD: preparation and characterisation of material and solar cells
157 Seiten
ISBN 3-932749-60-X

Vol. 61
Markus Krach
Frequenzverdreifacher mit Anti-Seriellem Schottky-Varaktor für den Terahertzbereich
156 Seiten
ISBN 3-932749-61-8

Vol. 62
Ralph Thomas Neuberger
AlGaN/GaN-Heterostrukturen als chemische Sensoren in korrosiven Medien
153 Seiten
ISBN 3-932749-62-6

Vol. 63
Sonia Perna
Wasserstoff-Passivierung von trikristallinem Silizium durch hydrogenisiertes Siliziumnitrid
136 Seiten
ISBN 3-932749-63-4

Vol. 64
Oliver Schumann
Einfluss von Stickstoff auf das Wachstum und die Eigenschaften von InAs-Quantenpunkten
148 Seiten
ISBN 3-932749-64-2

Vol. 65
Gerhard Rösel
Entwicklung und Charakterisierung von Typ-II-Heterostrukturen für die Abstimmregion in abstimmbaren Laserdioden
101 Seiten
ISBN 3-932749-65-0

Vol. 66
Angela Link
Zweidimensionale Elektronen- und Löcher-Gase in GaN/AlGaN Heterostrukturen
156 Seiten
ISBN 3-932749-66-9

Vol. 67
Matthias Sabathil
Opto-electronic and quantum transport properties of semiconductor nanostructures
156 Seiten
ISBN 3-932749-67-7

Vol. 68
Frank Fischer
Growth and electronic properties of two-dimensional systems on (110) oriented GaAs
139 Seiten
ISBN 3-932749-68-5

Vol. 69
Robert Shau
Langwellige oberflächenemittierende Laserdioden mit hoher Ausgangsleistung und Modulationsbandbreite
198 Seiten
ISBN 3-932749-69-3

Vol. 70
Andrea Baumer
Structural and electronic properties of hydrosilylated silicon surfaces
163 Seiten
ISBN 3-932749-70-7

Vol. 71
Andreas Florian Kreß
Manipulation of the Light-Matter-Interaction in Photonic Crystal Nanocavities
185 Seiten
ISBN 3-932749-71-5

Vol. 72
Markus Grau
Molekularstrahlepitaktische Herstellung von antimonidischen Laserdioden für die Gassensorik
138 Seiten
ISBN 3-932749-72-3

Vol. 73
Karin Buchholz
Microprocessing of silicon on insulator substrates and biofunctionalisation of silicon dioxide surfaces for sensing applications in fluids
170 Seiten
ISBN 3-932749-73-1

Vol. 74
Dominique Bougeard
Spektroskopische Charakterisierung von Germanium-Quantenpunkten in Silizium
154 Seiten
ISBN 3-932749-74-X

Vol. 75
Jochen Bauer
Untersuchungen zum kontrollierten Wachstum von InAs-Nanostrukturen auf Spaltflächen
140 Seiten
ISBN 3-932749-75-8

Vol. 76
Ingo Bormann
Intersubband Spektroskopie an Silizium-Germanium Quantenkaskadenstrukturen
124 Seiten
ISBN 3-932749-76-6

Vol. 77
Hubert Johannes Krenner
Coherent quantum coupling of excitons in single quantum dots and quantum dot molecules
160 Seiten
ISBN 3-932749-77-4

Vol. 78
Ulrich Rant
Electrical manipulation of DNA-layers on gold surfaces
249 Seiten
ISBN 3-932749-78-2

Vol. 79
René Todt
Widely tunable laser diodes with distributed feedback
152 Seiten
ISBN 3-932749-79-0

Vol. 80
Miroslav Kroutvar
Charge and spin storage in quantum dots
150 Seiten
ISBN 3-932749-80-4

Vol. 81
Markus Maute
Mikromechanisch abstimmbare Laser-Dioden mit Vertikalresonator
170 Seiten
ISBN 3-932749-81-2

Vol. 82
Frank Ertl
Anisotrope Quanten-Hall-Systeme, Vertikale Ultrakurzkanal- und Tunneltransistoren
170 Seiten
ISBN 3-932749-82-0

Vol. 83
Sebastian M. Luber
III-V semiconductor structures for biosensor and molecular electronics applications
212 Seiten
ISBN 978-3-932749-83-4

Vol. 84
Claudio Ronald Miskys
New substrates for epitaxy of group III nitride semiconductors: challenges and potential
207 Seiten
ISBN 978-3-932749-84-1

Vol. 85
Sebastian Friedrich Roth
n- and p-type transport in (110) GaAs substrates, single- and double-cleave structures
138 Seiten
ISBN 978-3-932749-85-8

Vol. 86
Mario Gjukic
Metal-induced crystallization of silicon-germanium alloys
309 Seiten
ISBN 978-3-932749-86-5

Vol. 87
Tobias Zibold
Semiconductor based quantum information devices: Theory and simulations
151 Seiten
ISBN 978-3-932749-87-2

Vol. 88
Thomas Jacke
Weit abstimmbare Laserdiode mit vertikal integriertem Mach-Zehnder-Interferometer
165 Seiten
ISBN 978-3-932749-88-9

Vol. 89
Nenad Ocelić
Quantitative near-field phonon-polariton spectroscopy
174 Seiten
ISBN 978-3-932749-89-6

Vol. 90
Kenji Arinaga
Control and manipulation of DNA on gold and its application for biosensing
111 Seiten
ISBN 978-3-932749-90-2

Vol. 91
Hans-Gregor Hübl
Coherent manipulation and electrical detection of phosphorus donor spins in silicon
162 Seiten
ISBN 978-3-932749-91-9

Vol. 92
Andrea Friedrich
Quanten-Kaskaden-Laser ohne Injektorbereiche
140 Seiten
ISBN 978-3-932749-92-6

Vol. 93
Oliver Dier
Das Materialsystem (AlGaIn) (AsSb): Eigenschaften und Eignung für GaSb-basierte Vertikalresonator-Laserdioden
174 Seiten
ISBN 978-3-932749-93-3

Vol. 94
Georg Steinhoff
Group III-nitrides for bio- and electrochemical sensors
197 Seiten
ISBN 978-3-932749-94-0

Vol. 95
Stefan Harrer
Next-generation nanoimprint lithography: Innovative approaches towards improving flexibility and resolution of nanofabrication in the sub-15-nm region
161 Seiten
ISBN 978-3-932749-95-7

Vol. 96
Stefan Ahlers
Magnetic and electrical properties of epitaxial GeMn
184 Seiten
ISBN 978-3-932749-96-0

Vol. 97
Emanuele Uccelli
Guided self-assembly of InAs quantum dots arrays on (110) surfaces
172 Seiten
ISBN 978-3-932749-97-1

Vol. 98
Shavaji Dasgupta
Growth optimization and characterization of high mobility two-dimensional electron systems in AlAs quantum wells
152 Seiten
ISBN 978-3-932749-98-8

Vol. 99
Werner Hofmann
InP-based long-wavelength VCSELs and VCSEL arrays for high-speed optical communication
142 Seiten
ISBN 978-3-932749-99-5

Vol. 100
Robert Lechner
Silicon nanocrystal films for electronic applications
227 Seiten
ISBN 978-3-941650-00-8

Vol. 101
Nebile Işık
Investigation of Landau level spin reversal in (110) oriented p-type GaAs quantum wells
114 Seiten
ISBN 978-3-941650-01-5

Vol. 102
Andreas Florian Härtl
Novel concepts for biosensors using diamond-based field effect transistors
255 Seiten
ISBN 978-3-941650-02-2

Vol. 103
Felix Florian Georg Hofbauer
Realization of electrically tunable single quantum dot nanocavities
160 Seiten
ISBN 978-3-941650-03-9

Vol. 104
Dominic F. Dorfner
Novel photonic biosensing based on silicon nanostructures
169 Seiten
ISBN 978-3-941650-04-6

Vol. 105
Till Andlauer
Optoelectronic and spin-related properties of semiconductor nanostructures in magnetic fields
157 Seiten
ISBN 978-3-941650-05-3

Vol. 106
Christoph Bihler
Magnetic semiconductors
190 Seiten
ISBN 978-3-941650-06-0

Vol. 107
Michael Huber
Tunnel-Spektroskopie im Quanten-Hall-Regime
164 Seiten
ISBN 978-3-941650-07-7

Vol. 108
Philipp Achatz
Metal-insulator transition and super-Conductivity in heavily boron-doped diamond and related materials
151 Seiten
ISBN 978-3-941650-08-4

Vol. 109
Sebastian Strobel
Nanoscale contacts to organic molecules based on layered semiconductor substrates
140 Seiten
ISBN 978-3-941650-09-1

Vol. 110
Ying Xiang
Semiconductor nanowires and templates for electronic applications
152 Seiten
ISBN 978-3-941650-10-7

Vol. 111
Michael Kaniber
Non-classical light generation in photonic crystal nanostructures
177 Seiten
ISBN 978-3-941650-11-4

Vol. 112
Martin Hermann
Epitaktische AlN-Schichten auf Saphir und Diamant
216 Seiten
ISBN 978-3-941650-12-1

Vol. 113
Dominik Heiss
Spin storage in quantum dot ensembles and single quantum dots
196 Seiten
ISBN 978-3-941650-13-8

Vol. 114
Tillmann Christoph Kubis
Quantum transport in semiconductor nanostructures
253 Seiten
ISBN 978-3-941650-14-5

Vol. 115
Lucia Steinke
Magnetotransport of coupled quantum Hall edges in a bent quantum well
194 Seiten
ISBN 978-3-941650-15-2

Vol. 116
Christian Lauer
Antimonid-basierte Vertikalresonator-Laserdioden für Wellenlängen oberhalb 2 μm
180 Seiten
ISBN 978-3-941650-16-9

Vol. 117
Simone Maria Kaniber
Optoelektronische Phänomene in hybriden Schaltkreisen aus Kohlenstoffnanoröhren und dem Photosystem I
136 Seiten
ISBN 978-3-941650-17-6

Vol. 118
Martin Heiß
Growth and properties of low-dimensional III-V semiconductor nanowire heterostructures
172 Seiten
ISBN 978-3-941650-18-3

Vol. 119
Sandro Francesco Tedde
Design, fabrication and characterization of organic photodiodes for industrial and medical applications
277 Seiten
ISBN 978-3-941650-19-0

Vol. 120
Danche Spirkoska Jovanov
Fundamental properties of self-catalyzed GaAs nanowires and related heterostructures
200 Seiten
ISBN 978-3-941650-20-6

Vol. 121
Jürgen Sailer
Materials and devices for quantum Information processing in Si/SiGe
158 Seiten
ISBN 978-3-941650-21-3

Vol. 122
Ilaria Zardo
Growth and raman spectroscopy studies of gold-free catalyzed semiconductor nanowires
184 Seiten
ISBN 978-3-941650-22-0

Vol. 123
Andre Rainer Stegner
Shallow dopants in nanostructured and in isotopically engineered silicon
185 Seiten
ISBN 978-3-941650-23-7

Vol. 124
Andreas J. Huber
Nanoscale surface-polariton spectroscopy by mid- and far-infrared near-field microscopy
144 Seiten
ISBN 978-3-941650-24-4

Vol. 125
Marco Andreas Höb
Funktionalisierung von Gruppe IV-Halbleitern
186 Seiten
ISBN 978-3-941650-25-1

Vol. 126
Daniel Claudio Pedone
Nanopore analytics – electro-optical studies on single molecules
114 Seiten
ISBN 978-3-941650-26-8

Vol. 127
Casimir Richard Simeon Katz
Multi-alloy structures for injectorless Quantum Cascade Lasers
131 Seiten
ISBN 978-3-941650-27-5

Vol. 128
Barbara Annemarie Kathrin Baur
Functionalization of group III-nitrides for biosensor applications
215 Seiten
ISBN 978-3-941650-28-2

Vol. 129
Arne Laucht
Semiconductor quantum optics with tailored photonic nanostructures
232 Seiten
ISBN 978-3-941650-29-9

Vol. 130
Jia Chen
Compact laser-spectroscopic gas sensors using Vertical-Cavity Surface-Emitting Lasers
150 Seiten
ISBN 978-3-941650-30-5

Vol. 131
Hans Leonhard Prechtel
Ultrafast Photocurrents and Terahertz Radiation in Gallium Arsenide and Carbon Based Nanostructures
160 Seiten
ISBN 978-3-941650-31-2

Vol. 132
Roland Enzmann
Technologieentwicklung für eine Einzelphotonenquelle
142 Seiten
ISBN 978-3-941650-32-9

Vol. 133
Alexander Bachmann
Antimonide-Based Vertical-Cavity Surface-Emitting Lasers
144 Seiten
ISBN 978-3-941650-33-6

Vol. 134
Markus Andreas Mangold
Two-Dimensional Gold Nanoparticle Arrays – A Platform for Molecular Optoelectronics
140 Seiten
ISBN 978-3-941650-34-3

Vol. 135
Stefan Birner
Modeling of semiconductor nanostructures and semiconductor–electrolyte interfaces
227 Seiten
ISBN 978-3-941650-35-0

Vol. 136
Christian Claus Jäger
Polycrystalline Silicon Thin Films for Electronic Applications
202 Seiten
ISBN 978-3-941650-36-7

Vol. 137
Gunther Christian Jegert
Modeling of Leakage Currents in High-κ Dielectrics
170 Seiten
ISBN 978-3-941650-37-4

Vol. 138
Shamsul Arafin
Electrically-Pumped GaSb-Based Vertical-Cavity Surface-Emitting Lasers
126 Seiten
ISBN 978-3-941650-38-1

Vol. 139
Norman Hauke
Enhanced spontaneous emission from silicon-based photonic crystal nanostructures
208 Seiten
ISBN 978-3-941650-39-8

Vol. 140
Christoph Schindler
Quantum spin transport in semiconductor nanostructures
175 Seiten
ISBN 978-3-941650-40-4

Vol. 141
Narayan Sircar
Group IV all-semiconductor spin-tronics: Materials aspects and optical spin selection rules
163 Seiten
ISBN 978-3-941650-41-1

Vol. 142
Alaa Abdellah
Scalable Thin-Film Manufacturing Technologies for Organic Electronics
162 Seiten
ISBN 978-3-941650-42-8

Vol. 143
Roland Dietmüller
Hybrid organic-inorganic heterojunctions for photovoltaic applications
179 Seiten
ISBN 978-3-941650-43-5

Vol. 144
Simon Hertenberger
Growth and Properties of In(Ga)As Nanowires on Silicon
152 Seiten
ISBN 978-3-941650-44-2

Vol. 145
Thomas Zabel
Study on silicon-germanium nanoislands as emitters for a monolithic silicon light source
152 Seiten
ISBN 978-3-941650-45-9

Vol. 146
Thomas Eißfeller
Theory of the Electronic Structure of Quantum Dots in External Fields
146 Seiten
ISBN 978-3-941650-46-6